NON-NEURONAL CELLS EDITOR'S PICK 2021

EDITED BY: Marie-Ève Tremblay

PUBLISHED IN: Frontiers in Cellular Neuroscience

frontiers Research Topics

ISSN 1664-8714
ISBN 978-2-88966-958-5
DOI 10.3389/978-2-88966-958-5

About Frontiers

Frontiers is more than just an open-access publisher of scholarly articles: it is a pioneering approach to the world of academia, radically improving the way scholarly research is managed. The grand vision of Frontiers is a world where all people have an equal opportunity to seek, share and generate knowledge. Frontiers provides immediate and permanent online open access to all its publications, but this alone is not enough to realize our grand goals.

Frontiers Journal Series

The Frontiers Journal Series is a multi-tier and interdisciplinary set of open-access, online journals, promising a paradigm shift from the current review, selection and dissemination processes in academic publishing. All Frontiers journals are driven by researchers for researchers; therefore, they constitute a service to the scholarly community. At the same time, the Frontiers Journal Series operates on a revolutionary invention, the tiered publishing system, initially addressing specific communities of scholars, and gradually climbing up to broader public understanding, thus serving the interests of the lay society, too.

Dedication to Quality

Each Frontiers article is a landmark of the highest quality, thanks to genuinely collaborative interactions between authors and review editors, who include some of the world's best academicians. Research must be certified by peers before entering a stream of knowledge that may eventually reach the public - and shape society; therefore, Frontiers only applies the most rigorous and unbiased reviews.
Frontiers revolutionizes research publishing by freely delivering the most outstanding research, evaluated with no bias from both the academic and social point of view. By applying the most advanced information technologies, Frontiers is catapulting scholarly publishing into a new generation.

What are Frontiers Research Topics?

Frontiers Research Topics are very popular trademarks of the Frontiers Journals Series: they are collections of at least ten articles, all centered on a particular subject. With their unique mix of varied contributions from Original Research to Review Articles, Frontiers Research Topics unify the most influential researchers, the latest key findings and historical advances in a hot research area! Find out more on how to host your own Frontiers Research Topic or contribute to one as an author by contacting the Frontiers Editorial Office: frontiersin.org/about/contact

NON-NEURONAL CELLS EDITOR'S PICK 2021

Topic Editor:
Marie-Ève Tremblay, University of Victoria, Canada

Citation: Tremblay, M.-È., ed. (2021). Non-Neuronal Cells Editor's Pick 2021. Lausanne: Frontiers Media SA. doi: 10.3389/978-2-88966-958-5

Table of Contents

frontiers in Cellular Neuroscience

ORIGINAL RESEARCH
published: 09 January 2019
doi: 10.3389/fncel.2018.00529

Idebenone Alleviates Neuroinflammation and Modulates Microglial Polarization in LPS-Stimulated BV2 Cells and MPTP-Induced Parkinson's Disease Mice

*Aijuan Yan†, Zhihua Liu†, Lu Song, Xijin Wang, Yu Zhang, Na Wu, Jingya Lin, Ying Liu and Zhenguo Liu**

Department of Neurology, Xinhua Hospital Affiliated to Shanghai Jiao Tong University School of Medicine, Shanghai, China

OPEN ACCESS

Edited by:
Shawn Hayley,
Carleton University, Canada

Reviewed by:
Jiro Kasahara,
Tokushima University, Japan
Archan Ganguly,
University of California, San Diego, United States

***Correspondence:**
Zhenguo Liu
liuzhenguo@xinhuamed.com.cn

† These authors have contributed equally to this work

Received: *21 August 2018*
Accepted: *21 December 2018*
Published: *09 January 2019*

Citation:
Yan A, Liu Z, Song L, Wang X, Zhang Y, Wu N, Lin J, Liu Y and Liu Z (2019) Idebenone Alleviates Neuroinflammation and Modulates Microglial Polarization in LPS-Stimulated BV2 Cells and MPTP-Induced Parkinson's Disease Mice. Front. Cell. Neurosci. 12:529. doi: 10.3389/fncel.2018.00529

Background: Idebenone is an antioxidant and a coenzyme Q10 analog that has been used to treat neurodegeneration disease. Some studies show idebenone exerts anti-inflammatory effects. However, whether idebenone can be used to reduce the neuroinflammation in Parkinson's disease (PD) has been little studied.

Methods: The study investigated the potential anti-inflammatory effects of idebenone *in vitro* and *in vivo*, using cell models of Lipopolysaccharide (LPS)-simulated BV2 cells and animal models of 1-methyl-4-phenyl-1,2,3,6-tetrahydropyridine (MPTP)-induced PD with or without idebenone. To verify how idebenone exerts its effects on the BV2 cell activation and PD model, we performed the mechanistic studies *in vitro* and *in vivo*.

Results: *In vitro* study showed that pretreatment with idebenone could attenuate the production of pro-inflammatory factors in LPS-stimulated BV2 cells and promoted a phenotypic switch from the M1 state to the M2 state. Mechanistically, idebenone reduced the activation of the MAPK and NF-κB signaling pathway upon LPS stimulation. Furthermore, *in vivo* experiments confirmed that pretreatment with idebenone could ameliorate MPTP-induced neurodegeneration and modulate microglia phenotypes through inhibition of the MAPK and NF-κB signaling pathway in the SN.

Conclusion: These results suggest that idebenone ameliorates the neurological deficits related to PD and this effect is partly mediated by inhibiting the neuroinflammation and modulating microglia phenotypes.

Keywords: idebenone, neuroinflammation, microglial polarization, Parkinson's disease, BV2 cells

INTRODUCTION

Parkinson's disease (PD) is a neurodegenerative disease that is caused by progressive loss of dopaminergic neurons, Lewy body formation, and mitochondrial dysfunction (Dauer and Przedborski, 2003). In addition to these pathophysiological mechanisms, there is some evidence from previous studies suggest that the neuroinflammatory response related to microglia cell activation participate in the progression of dopaminergic neuron cell death (Czlonkowska et al., 2002; Whitton, 2007; Brochard et al., 2009).

Microglia cells are the main glial cell type that participate in the neuroinflammatory response in the central nervous system (CNS) (Saijo and Glass, 2011; Lu et al., 2018). Under pathological conditions, microglia cells in the brain undergo changes in morphology to adopt an activated state in order to respond to the toxic environment (Song and Suk, 2017). One of the characteristics of microglia cell is the capacity to adopt two different states in response to the toxic substance they encounter. Microglial activation can be classified into two major phenotypes defined as classically M1 microglia or alternatively M2 microglia (Colton, 2009; Han et al., 2018). The M1 phenotype is associated with the release of proinflammatory factors, whereas M2 microglia execute an anti-inflammatory effect and contribute to regeneration and neuroprotection (Saijo et al., 2009; Colton and Wilcock, 2010). M1 microglia release proinflammatory factors such as interleukin-6 (IL-6), IL-1β, tumor necrosis factor-α (TNF-α) to recruit additional inflammatory cells (Giaume et al., 2007; Colton and Wilcock, 2010). M2 microglia produce anti-inflammatory cytokine including IL-4 and IL-10 and promote wound healing and tissue repair (Liu et al., 2006; Yan et al., 2016). The M1 and M2 activation state are critical in neuroinflammation-related neurodegeneration diseases including PD.

Idebenone (2,3-dimethoxy-5-methyl-6-(10-hydroxydecyl)-1,4-benzoquinone), a synthetic analog of coenzyme Q10, is an important antioxidant for cell membrane and an elementary constituent of the ATP-producing mitochondrial electron transport chain (Muscoli et al., 2002). One of the most important features of idebenone is its antioxidant capacity (Jaber and Polster, 2015). Beneficial effects of idebenone have been studied in the treatment of some neurodegeneration diseases, including Parkinson's disease (Horvath et al., 2003), Alzheimer's disease (Weyer et al., 1997), and dementia (Voronkova and Meleshkov, 2009). In addition, idebenone is also used in the treatment of Friedreich's Ataxia, which is a progressive neurodegenerative disease associated with cardiomyopathy and other features (Parkinson et al., 2013). Apart from its antioxidant properties, the study from Civenni et al. (1999) reported that idebenone exerted anti-inflammatory effects and behaved similar to indomethacin and piroxicam—two typical anti-inflammatory agents.

Taking these factors into consideration, we hypothesize that idebenone may have an inhibitory effect on neuro-inflammatory processes and microglial activation in PD. To test this hypothesis, we will investigate the anti-neuroinflammation and microglia modulating effects of idebenone in the BV2 microglial cell line and examine idebenone's efficacy on 1-methyl-4-phenyl-1,2,3,6-tetrahydropyridine (MPTP)-induced neurodegeneration and neuroinflammatory response in PD mice.

MATERIALS AND METHODS

Reagents

Idebenone was purchased from Qilu Pharmaceutical Co., Ltd., MPTP, dopamine and 3,4-dihydroxyphenylacetic acid (DOPAC) standards, dimethyl sulfoxide (DMSO), and Lipopolysaccharide (LPS) were purchased from Sigma-Aldrich (St. Louis, MO, United States).

Animals

Male C57BL/6 mice (mean weight = 22–25 g; mean age = 10–12 weeks) were purchased from Shanghai SLAG Laboratory Animal Corporation (Shanghai, China). The mice were individually housed at a temperature of 22 ± 1°C and relative humidity 50–60% under a 12-h/12-h light–dark cycle, with free access to food and water. Animals received four intraperitoneal injection of MPTP (20 mg/kg) at 2 h intervals, whereas control mice were treated with the same volume of saline. Idebenone was resuspended in corn oil and applied daily by oral gavage. 100 mg/kg idebenone or vehicle (corn oil) was administered daily starting at day 7 before MPTP administration (Abdel Baky et al., 2010). These mice were sacrificed at 3, and 7 days after MPTP treatment.

This study was carried out according to the guidelines of the National Institutes of Health and was approved by the Ethics Committee of Xin Hua Hospital affiliated to Shanghai Jiao Tong University School of Medicine.

Behavioral Tests

Open Field Test

Motor behavior was analyzed in an open-field test after 3 and 7 days of administration of MPTP. Open-field test is an important method for assessing spontaneous locomotor activity in mice model of PD (Yan et al., 2018). Mice were placed into the center of the case, and their behaviors were observed. The total distance and the number of gridline crossings were measured by an observer who was seated approximately 1.0 m away. The parameters were analyzed by the SuperMaze V2.0 software (Shanghai Xin Ruan, China) over a 5-min period: the total distance traveled and the number of gridline crossings.

Pole Test

The pole test is an available method to evaluate bradykinesia in PD mice model. We performed the pole test at 3 and 7 days after the last MPTP injection according to a previously described protocol (Wu et al., 2012). In brief, a rod with a length of 55 cm and a diameter of 10 mm was used to make the pole. The mice were put on the top of the pole.

Time taken by the animal to turn around was recorded as the T-turn (time to turn). The test was carried out three times for each mouse, and the mean time was calculated for statistical analysis.

Cell Culture

The BV2 microglial cell line was purchased from China Center for Type Culture Collection[1]. The SH-SY5Y cells were presented by Institute of Neurology, Rui Jin Hospital (Shanghai, China). The BV2 microglial cells and SH-SY5Y cells were cultured in Dulbecco's-modified Eagle's medium (DMEM) (Gibco; Thermo Fisher Scientific, Inc.) supplemented with 10% fetal bovine serum (FBS) (Gibco; Thermo Fisher Scientific, Inc.) and 1% penicillin/streptomycin at 37°C with an atmosphere of 5% CO_2. Idebenone was dissolved in DMSO as a 1 M stock solution, and dilutions were made in DMEM. The final concentration of DMSO in the DMEM was less than 0.05% which had no effect on cell growth.

Cell Viability Assay

The BV2 microglial cells were seeded in 96-well plates (4.0×10^3 cells/ml) and treated with idebenone concentrations (1, 2.5, 5, 7.5, 10, or 20 μM) for 24 h. Cell viability was examined by a CCK-8 assay kit (CCK-8; Dojindo, Tokyo, Japan) according to the manufacturer's instructions (Yan et al., 2017).

BV2 cells were seeded in 6-well plates (4.0×10^5 cells/ml) and treated with 5 μM idebenone for 2 h, followed by incubation with 100 ng/ml LPS for 24 h. Then, conditioned media of the BV2 cells was collected and applied to SH-SY5Y cells that has been seeded in 96-well plates. CCK-8 assay kit was used to assess the changes in SH-SY5Y cell viability after 24 h. Morphological change in the SH-SY5Y cells were examined by phase-contrast microscopy.

NO Measurement

The BV2 microglial cells were seeded in 24-well plates (1.0×10^5 cells/ml) and treated with various idebenone concentrations (1, 2.5, 5, 7.5, 10, or 20 μM) for 2 h, followed by 100 ng/ml LPS for 24 h. After 24 h, culture supernatant was collected, and the NO concentration in the supernatant was measured by an NO assay kit (Beyotime Institute of Biotechnology, Inc., Shanghai, China) according to the manufacturer's instructions (Yang et al., 2016).

Immunohistochemistry

Immunohistochemical staining of brain sections was carried out as previously described (Luster et al., 2005). Briefly, mice were transcardially perfused with PBS, followed by 4% paraformaldehyde (PFA) in 0.1 M PBS. The brains were removed and immersed for 24 h in 4% PFA, and then cryoprotected in a 30% sucrose solution in PBS (pH 7.4). Subsequently, serial coronal sections (cut thickness: 20 μm) were then prepared using a microtome. These brain sections were immersed with 0.3% H_2O_2 for 30 min and then were rinsed with PBS containing 0.3% Triton X-100. The coronal sections were immersed with serum for 1 h and then incubated overnight with a rabbit polyclonal anti-TH (cat. no. 41528, 1:500, Abcam) at 4°C. Staining was carried out using the ABC method (Vector Laboratories), with 3,3′-diaminobenzidine (DAB) as the peroxidase substrate. TH-positive DA neurons from the substantia nigra (SN) region were examined by light microscopy. Stereological counting of TH-positive neurons was used the method described in previous studies (Hunot et al., 2004; Brochard et al., 2009).

Brain sections were fixed with 4% PFA for 15 min and then rinsed with PBS containing 0.3% Triton X-100. Sections were blocked for 60 min in 10% donkey serum and incubated with primary antibody at 4°C overnight. Primary antibodies used were rabbit anti-Iba-1 (cat. no. 178847, 1:200 dilution, Abcam); goat anti-Arg-1 (cat. no. 18351, 1:100 dilution, Santa Cruz Biotechnology); mouse anti-CD16/32 antibody (cat. no. 553141, 1:200 dilution, BD Pharmingen, San Jose, CA, United States). After washing three times with PBS, brain sections were incubated with corresponding donkey anti-rabbit, donkey anti-goat, or donkey anti-mouse secondary antibodies conjugated to Alexa Fluor-488 and Alexa Fluor-594 fluorochrome (1:500 dilution, Life Technologies). 4,6-diamidino-2-phenylindole (DAPI) (1:1000 dilution, Beyotime Institute of Biotechnology, China) was used to stain the nuclei. The brain sections were examined by a microscope (Leica, Solms, Germany).

BV2 microglial cells were fixed with 4% PFA and stained overnight with rabbit anti-NF-κB antibody (cat. no. 32536, 1:300, Abcam) at 4°C, followed by incubation with the fluorescent conjugated secondary antibodies.

High-Performance Liquid Chromatography (HPLC) Analysis

The levels of dopamine and its metabolites (DOPAC) in the striatum were measured using an HPLC apparatus (Yu et al., 2017). Briefly, the striatum was weighed and quickly removed on ice. Striatum was homogenized in perchloric acid (0.1 mol/L). After lysis, samples were centrifuged at 10,000 *g* (4°C) for 10 min and the collected supernatants were then assayed for dopamine and DOPAC content through HPLC. The content of each neurotransmitter was expressed as pg/mg equivalent striatal tissue.

Reverse Transcription-Quantitative Polymerase Chain Reaction (RT-qPCR)

BV2 cells, seeded in 12-well plates, were pretreated with 5 μM idebenone for 2 h, followed by treatment with 100 ng/ml LPS for 12 h. Total RNA was extracted from BV2 microglial cells with Trizol reagent (Takara Bio, Inc., Otsu, Japan) and was reverse transcribed to cDNA using the PrimeScript RT Reagent kit (Takara Bio, Inc., Otsu, Japan), as previously described (Yan et al., 2017). RT-qPCR was carried out using an SYBR Green kit (Takara Bio, Inc., Otsu, Japan) with the following conditions: Denaturation at 95°C for 10 s, followed by 40 cycles at 95°C for 5 s and 60°C for 30 s. The data were

[1]http://www.cctcc.org

analyzed using the comparative threshold cycle (Ct) method. The outcome was expressed as fold-difference normalized to the ribosomal phosphoprotein P0 (Rplp0). RT-qPCR was detected using an ABI PRISM 7500 Sequence Detection system (Thermo Fisher Scientific, Inc.). The primers used in RT-qPCR were as follows:

IL-6 (F: TAGTCCTTCCTACCCCAATTTCC, R: TTGGTC CTTAGCCACTCCTTC); IL-1β (F: GCAACTGTTCCTGAA CTCAACT, R: ATCTTTTGGGGTCCGTCAACT); TNF-α (F: CCCTCACACTCAGATCATCTTCT, R: GCTACGACG TGGGCTACAG); iNOS (F: ATGTCCGAAGCAAACATCAC, R: TAATGTCCAGGAAGTAGGTG); CD 16 (F:TTTGGACACCC AGATGTTTCAG, R: GTCTTCCTTGAGCACCTGGATC); CD32 (F: AATCCTGCCGTTCCTACTGATC, R:GTGTCAC CGTGTCTTCCTTGAG); CD86 (F: TTGTGTGTGTTCTG GAAACGGAG, R: AACTTAGAGGCTGTGTTGCTGGG); Arg-1 (F: GAACACGGCAGTGGCTTTAAC, R: TGC TTAGCTCTGTCTGCTTTGC); CD206 (F: TCTTTGC CTTTCCCAGTCTCC, R: TGACACCCAGCGGAATTTC); YM (F: CAGGGTAATGAGTGGGTTGG, R: CACGG CA CCTCCTAAATTGT); Rplp0 (F: AGATTCGGGATATGCTGTT GGC, R: TCGG GTCCTAGACCAGTGTTC).

Western Blotting

Proteins were extracted from the BV2 cells and brain by homogenization in standard lysis buffer. The concentration of protein was measured using a BCA kit (Beyotime Institute of Biotechnology, Inc., Shanghai, China) according to the manufacturer's instructions (Cai et al., 2018). 40 μg of protein was separated by 10% SDS-PAGE and then transferred into nitrocellulose membranes (300 mA for 60 min). The membranes were blocked with 3% bovine serum albumin (BSA) for 1 h and immersed overnight in primary antibodies at 4°C. The primary antibodies used were as follows: p-ERK (cat. no. #4370), ERK (cat. no. #4695), p-p38 (cat. no. #4511), p-38 (cat. no. #8690), p-JNK (cat. no. #4668), JNK (cat. no. #9252), p-NF-κB (cat. no. #3033), NF-κB (cat. no. #8242) (1:1,000; Cell Signaling Technology, Inc., Danvers, MA, United States), a rabbit polyclonal anti-TH (cat. no. 41528, 1:500, Abcam). The membranes were washed three times with Tris-buffered saline and Tween 20 (Beyotime Institute of Biotechnology, Inc., Shanghai, China) and incubated with corresponding anti-rabbit Horseradish Peroxidase (HRP) IgGs (cat. no. #7074 diluted 1:1000, Santa Cruz Biotechnology, CA, United States) secondary antibody for 1 h. The bands were visualized by chemiluminescence (Thermo Scientific Inc.) and results were measured by a ChemiDoc^{TM} XRS+ imaging system (Bio-Rad Laboratories, Inc., Hercules, CA, United States).

Statistical Analysis

All data were analyzed by GraphPad Prism software, v6.0 (GraphPad Software, Inc., La Jolla, CA, United States). Comparison between the two groups was assessed with an unpaired *t*-test, while comparison among several groups was evaluated using one-way ANOVA followed by a Tukey's multiple comparisons test. Data were expressed as the mean ± standard error of the mean (SEM). *p*-values < 0.05 was considered statistically significant.

RESULTS

Idebenone Reduced NO Release and Expression of Proinflammatory Cytokines in LPS-Activated BV2 Cells

To detect the potential cytotoxicity of idebenone, we analyzed the dose-dependent effects of idebenone (1, 2.5, 5, 7.5, 10, and 20 μM) on the survival of BV2 microglial cells. The result demonstrated that idebenone was not cytotoxic to BV2 microglial cells at 1, 2.5, or 5 μM (**Figure 1A**). Activated microglia release various proinflammatory cytokines, NO and superoxide (Shao et al., 2013). We then investigated the effects of idebenone on LPS-activated BV2 cells. Our data showed that idebenone (1, 2.5, and 5 μM) dose-dependently decreased the LPS-stimulated production of NO ($p < 0.01$; **Figure 1B**) and suppressed the mRNA expression of IL-6, IL-1β, TNF-α, and iNOS in LPS-stimulated BV2 cells ($p < 0.05$; **Figure 1C**). As shown in **Figure 1**, the most inhibition was observed at the concentration of 5 μM, and we selected 5 μM idebenone in the following experiments.

Idebenone Suppressed LPS-Stimulated Microglial M1 Polarization and Promoted M2 Polarization in BV2 Cells

Lipopolysaccharide is regard as a classically M1 microglia inducer, which causes M1 phenotype to express pro-inflammatory cytokines (Yang et al., 2017). In our study, we showed that the expression of CD16, CD32, and CD86 (M1 markers) was increased in LPS-activated BV2 cells. Idebenone had little impact on microglia polarization in resting state, while it could suppress the expression of M1 markers ($p < 0.05$; **Figure 2A**) and promote activated microglia to alternatively M2 phenotype in conditions of inflammatory stimulation, as demonstrated by the increased expression of Arg-1, CD206, and YM (M2 markers) ($p < 0.05$; **Figure 2B**).

Conditioned Medium From Activated BV2 Cells Pretreated With Idebenone Could Increase SH-SY5Y Cells Viability

Conditioned medium from LPS-stimulated BV2 cells should contain proinflammatory cytokines and other toxic molecules (Yang et al., 2016). We designed the following experiment to test such impacts on human neuroblastoma SH-SY5Y (**Figure 3A**). SH-SY5Y, a neuronal cell line, was used to mimic neurons. BV2 microglial cells were treated with 100 ng/ml LPS for 24 h with or without idebenone (5 μM) pretreatment, and then the conditioned medium from BV2 microglial cells was collected. SH-SY5Y cells were incubated with the conditioned medium and cells viability was analyzed by CCK8 assay kit after 24 h. Conditioned medium from LPS-stimulated BV2 cells reduced

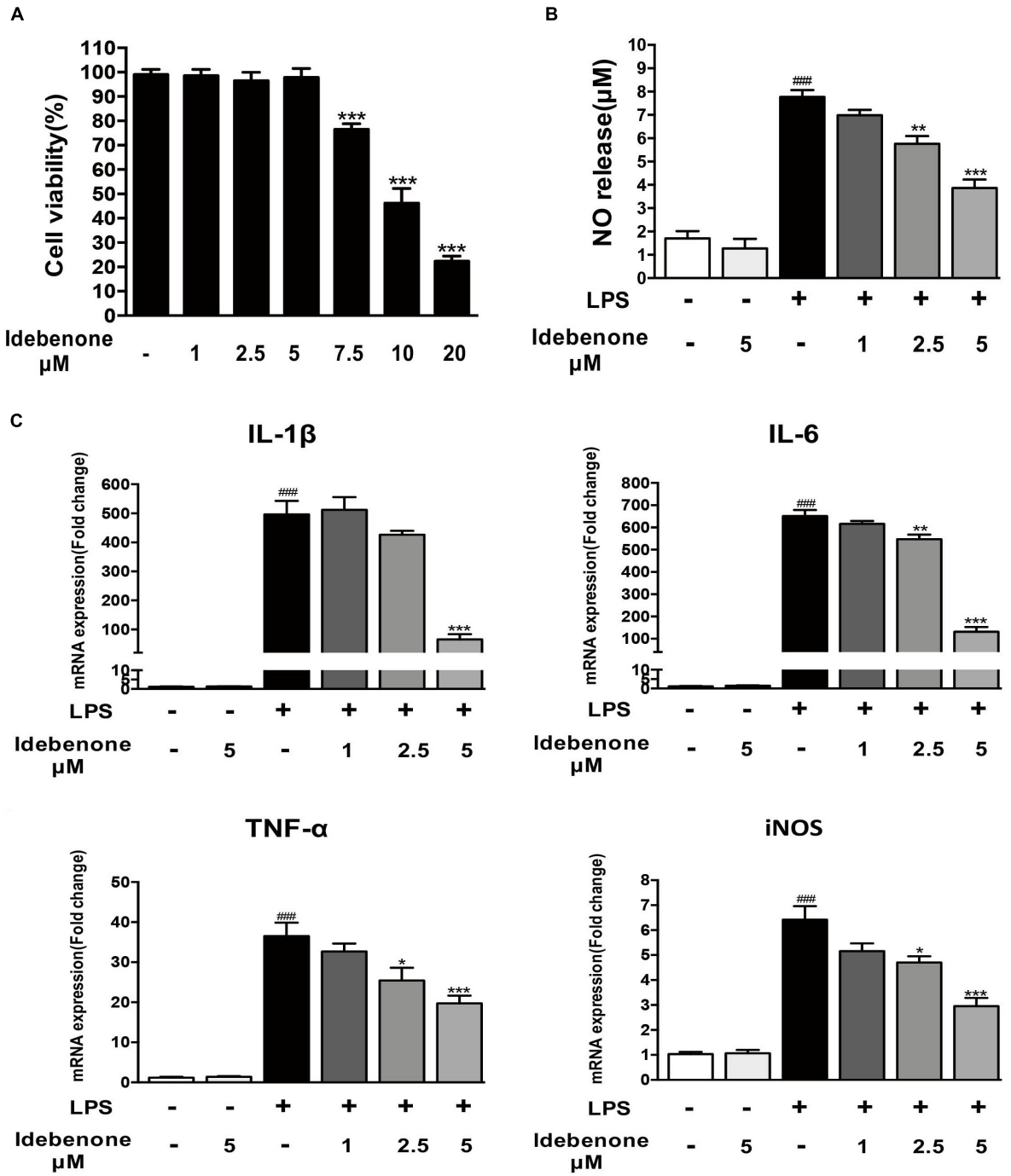

FIGURE 1 | Idebenone reduced LPS-induced NO release and expression of proinflammatory cytokines in BV2 cells. **(A)** Effects of different concentration of idebenone on BV2 microglial cell viability. $^{***}p < 0.001$, different concentration of idebenone vs. control. **(B)** The NO content of the supernatant was analyzed using NO assay kit. **(C)** The mRNA expression levels of IL-1β, IL-6, TNF-α, and iNOS were measured by RT-qPCR in different group. $^{*}p < 0.05$, $^{**}p < 0.01$, $^{***}p < 0.001$: idebenone + LPS vs. LPS; $^{###}p < 0.001$: LPS vs. vehicle.

SH-SY5Y cells viability, and caused morphological changes, while pretreatment with idebenone partially blocked the effect of LPS (**Figures 3B,C**). These results indicated that LPS could promote production of pro-inflammatory cytokines, which could explain the reduction of SH-SY5Y cells survival in the conditioned medium from activated BV2 cells. Pretreatment with idebenone could reverse the process of inflammation. To eliminate the possibility that reagents in conditioned medium may affect SH-SY5Y cells survival, idebenone and LPS were directly added to SH-SY5Y cells for 24 h. Results suggested that there was no

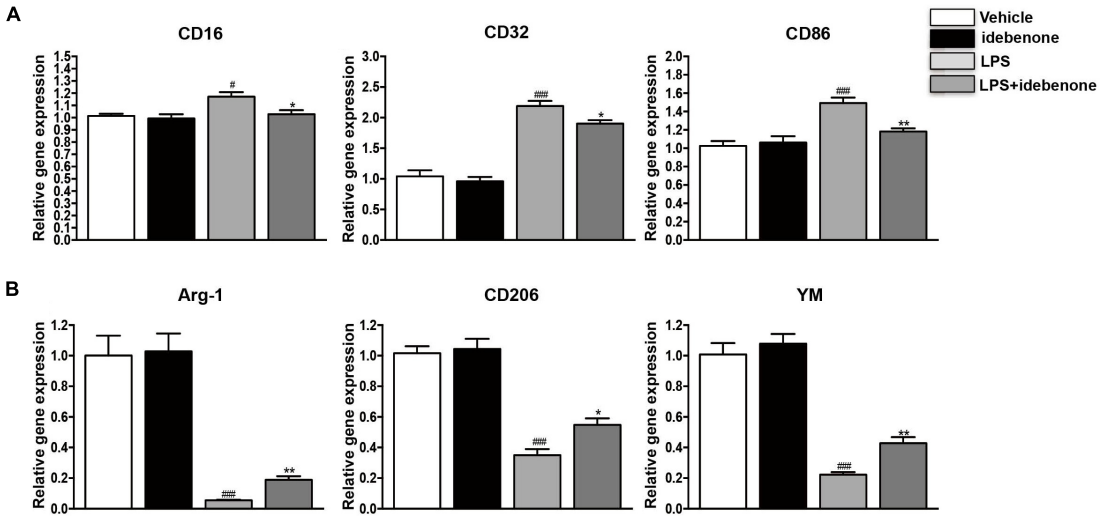

FIGURE 2 | Idebenone reduced the expression of M1 markers and promoted the expression of M2 markers in LPS-activated BV2 cells. **(A)** The expression of M1 markers (CD16, CD32, and CD86) as determined by RT-qPCR in the different groups. **(B)** The expression of M2 microglial markers (Arg-1, CD206, and YM) as determined by RT-qPCR in the different groups. $^{*}p < 0.05$, $^{**}p < 0.01$: idebenone + LPS vs. LPS; $^{\#}p < 0.05$, $^{\#\#\#}p < 0.001$: LPS vs. vehicle.

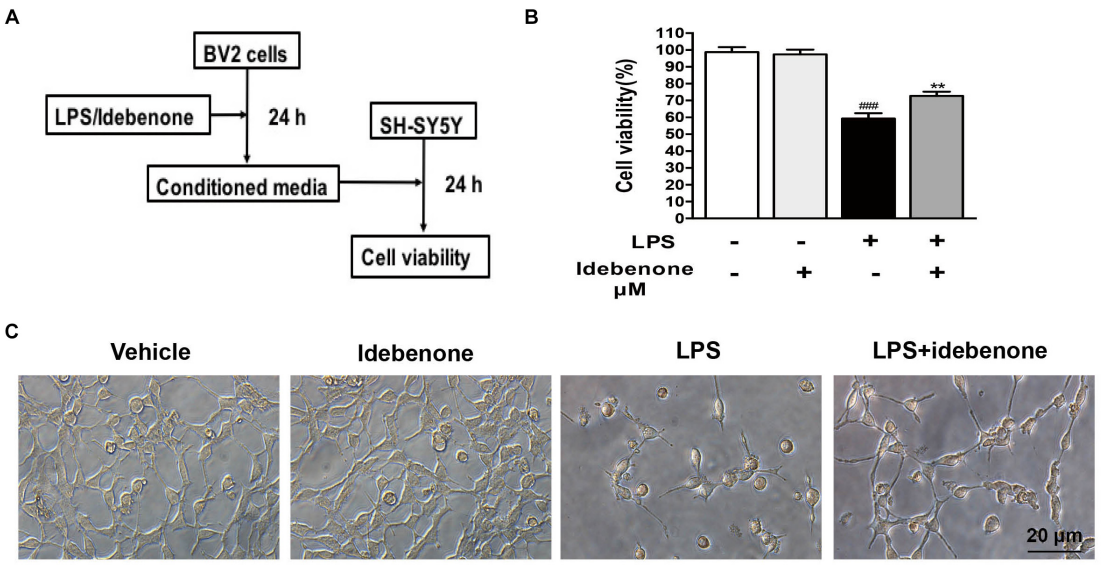

FIGURE 3 | Conditioned medium from idebenone in the pretreated group could increase SH-SY5Y cell viability. **(A)** The experimental design and procedure. **(B)**. The effects of mediated conditioned medium from the different groups on the SH-SY5Y cells were assessed by CCK-8 assay kit. **(C)** The effects of mediated conditioned medium from the different groups on SH-SY5Y cells were observed by microscopy. Scale bar = 20 μm. $^{**}p < 0.01$: idebenone + LPS vs. LPS; $^{\#\#\#}p < 0.001$: LPS vs. vehicle.

statistically significance among different groups (**Supplementary Figure S1**).

Idebenone Inhibited LPS-Induced Activation of Mitogen Activated Protein Kinases (MAPK) and NF-κB

Lipopolysaccharide, an inducer of M1 microglia (Fenn et al., 2012), especially acts on Toll-like receptors (TLRs) of cells, which can stimulate the activation of NF-κB/MAPK pathway. MAPKs are important regulators in the process of LPS-activated BV2 microglial cells (Yan et al., 2017). To detect the potential mechanisms of the idebenone-mediated reduction of inflammatory factors expression and modulation of microglial polarization, BV2 microglial cells were pretreated with or without idebenone for 2 h and then treated with 100 ng/ml LPS for 30 min. LPS induced an increase in the phosphorylation of ERK, p38, and JNK, which was inhibited by idebenone pretreatment ($p < 0.05$; **Figure 4A**).

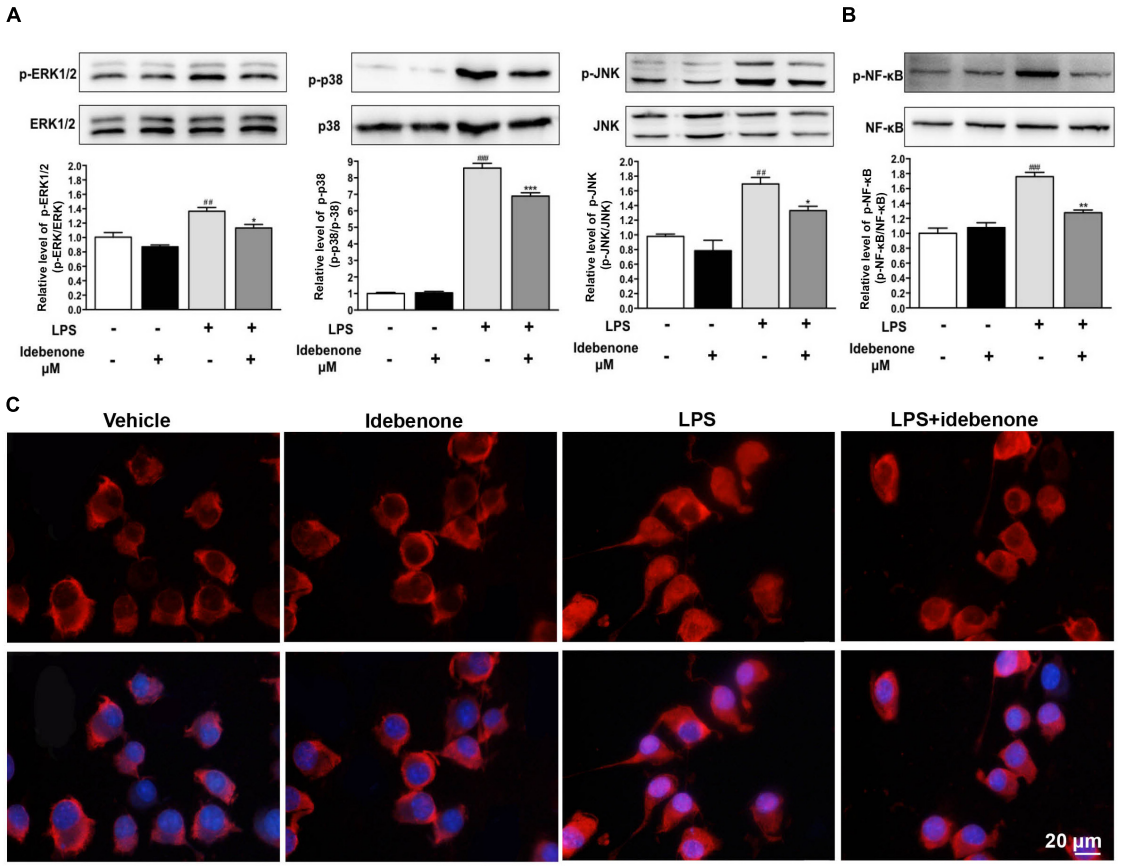

FIGURE 4 | Idebenone inhibited LPS-induced activation of MAPKs and NF-κB. **(A)** Expression levels of p-ERK, ERK, p-p38, P-38, p-JNK, and JNK were analyzed by western blotting. **(B)** Expression levels of p-NF-κB and NF-κB were analyzed by western blotting. **(C)** Idebenone inhibited LPS-caused translocation of p65 from cytosol to nucleus. BV2 microglial cells were immunostained with anti-NF-κB p65 antibodies and Alexa Fluor 594-conjugated secondary antibodies. Scale bar = 20 μm. Values are presented as the mean ± standard error. $^{*}p < 0.05$, $^{**}p < 0.01$, $^{***}p < 0.001$: idebenone + LPS vs. LPS; $^{\#\#}p < 0.01$, $^{\#\#\#}p < 0.001$: LPS vs. vehicle.

The NF-κB signaling pathway is also a significant mediator in LPS-activated BV2 microglial cells (Min et al., 2014). Thus, NF-κB pathway was evaluated as a potential mechanistic target for idebenone during inflammatory response. In the following study, the effect of idebenone on LPS-stimulated NF-κB activation was observed. The data showed that pretreatment with idebenone did not change the protein expression of NF-κB, but it inhibited LPS-induced expression of p-NF-κB in BV2 microglial cells ($p < 0.01$; **Figure 4B**). The result was confirmed by immunofluorescence study of NF-κB translocation from the cytosol to the nucleus in BV2 microglial cells (**Figure 4C**).

Idebenone Treatment Protected Against MPTP-Induced Motor Dysfunction and Reduced the Neuronal Death in the SN and in the Striatum of PD Mice

We sought to identify whether idebenone treatment affected MPTP-induced dopaminergic neuronal death and neurobehavioral deficits. According to previous studies, idebenone was treated at a dose of 100 mg/kg body weight (Abdel Baky et al., 2010; Fiebiger et al., 2013). Mice received idebenone showed no visible disorders such as reduced appetite, infection, or inhibition of motor activity. The open field test and pole test are useful methods for evaluating the motor dysfunction caused by PD. For open field test, we mapped the mice's paths on the 3rd and 7th days, which were recorded as the total distance mice traveled in 5 min. MPTP-treated mice that were pretreated with corn oil moved around the arena very little, compared with MPTP-treated mice that received idebenone (3 days: $p < 0.01$; 7 days: $p < 0.001$; **Figures 5A,B**). Corn oil-MPTP-treated mice demonstrated decreased locomotor activity, crossing fewer lines than corn oil-saline-treated mice (3 days: $p < 0.001$; 7 days: $p < 0.001$; **Figures 5A,C**). Idebenone-MPTP treated mice crossed more lines than corn oil-MPTP-treated mice (3 days: $p < 0.01$; 7 days: $p < 0.01$; **Figures 5A,C**). For the pole test, the time to descend for the corn oil-MPTP group was markedly prolonged compared with the corn oil-saline group (3 days: $p < 0.001$; 7 days: $p < 0.01$; **Figure 5D**). However, the time to descend of the idebenone-MPTP group was shortened to 8.69 ± 0.64 s (3 days, $p < 0.01$; **Figure 5D**), and 6.97 ± 0.54 s (7 days, $p < 0.05$; **Figure 5D**) compared with the corn oil-MPTP group.

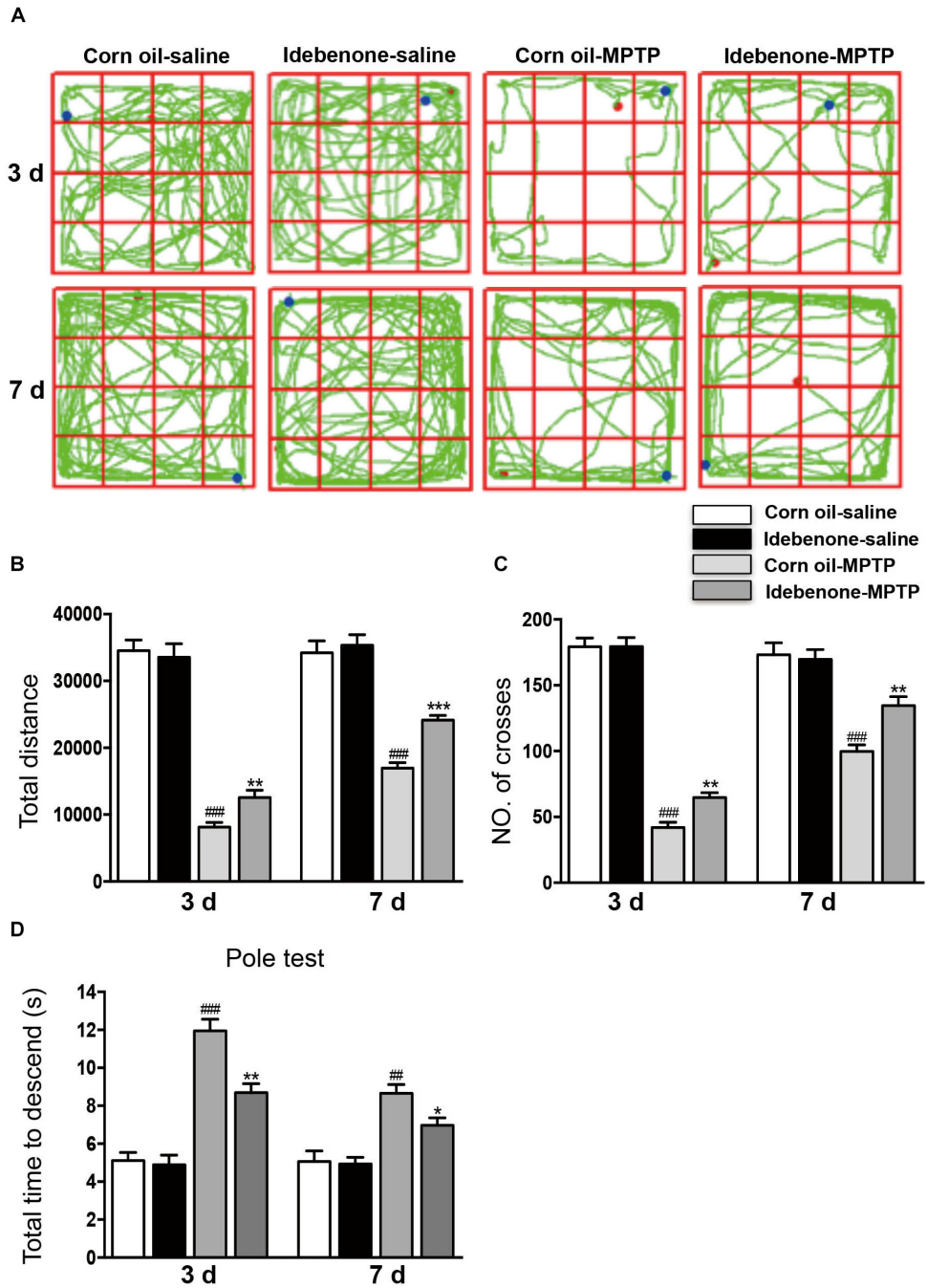

FIGURE 5 | Idebenone treatments ameliorated motor function in MPTP-treated mice. **(A)** Movement paths in the different experimental groups. **(B)** Total distance traveled in different experimental groups. **(C)** The number of squares crossed by mice. **(D)** For the pole test, the time for every mouse to reach the bottom of the pole was recorded and analyzed. Values are presented as the mean ± SEM. $^{*}p < 0.05$, $^{**}p < 0.01$, $^{***}p < 0.001$: idebenone-MPTP vs. corn oil-MPTP; $^{\#\#}p < 0.01$, $^{\#\#\#}p < 0.001$: corn oil-MPTP vs. corn oil-saline.

To determine whether idebenone in the PD model is beneficial or harmful to TH+ neurons in the SN, we compared the idebenone-MPTP group with its corn oil-MPTP group. The results showed that only 38% of TH+ neurons survived in the corn oil-MPTP group, while 66% of TH+ neurons survived in the idebenone-MPTP group ($p < 0.01$; **Figures 6Aa,b**). We also used western blotting to analyze the expression of TH in the SN. The results showed that expression of TH was downregulated in the SN of corn oil-MPTP-treated mice ($p < 0.001$; **Figure 6Ac**), whereas idebenone lessened the decline of TH in the SN, compared with corn oil-MPTP-treated mice ($p < 0.01$; **Figure 6Ac**).

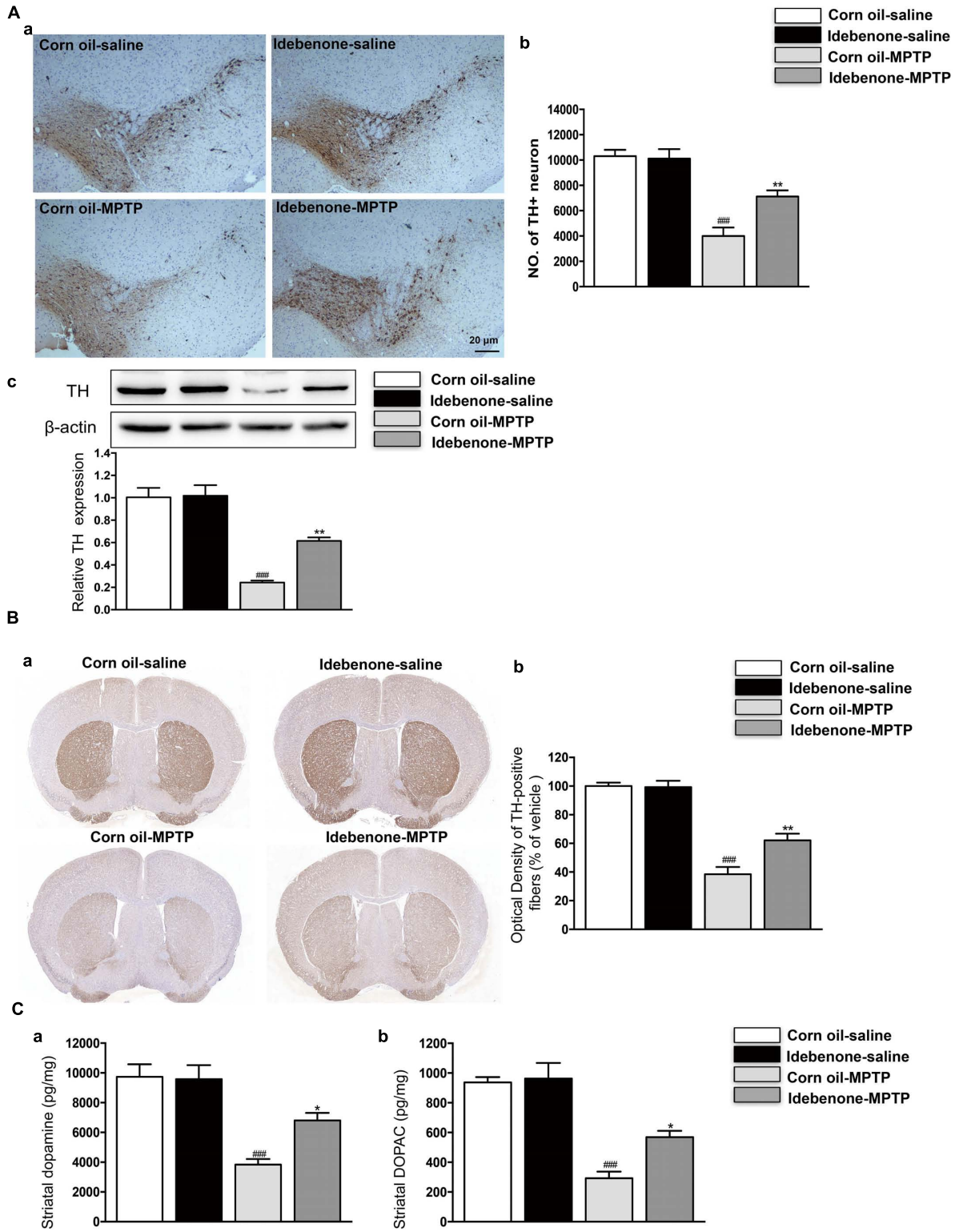

FIGURE 6 | Idebenone treatments reduced MPTP-induced loss of TH and striatal dopamine and its metabolites, DOPAC. **(Aa)** Dopaminergic neurons were evaluated by immunohistochemical analysis of TH in the SN. Scale bar = 20 μm. **(b)** Quantification of the TH+ neuron in the SN. **(c)** The expression level of TH was analyzed by western blotting. **(Ba)** Optical density analysis for TH-positive fibers in the striatum. **(b)** Quantification of the TH in the striatum. **(C)** Striatal dopamine and its metabolites levels measured by HPLC (**a**: dopamine; **b**: DOPAC). Values are presented as the mean ± SEM. $^{**}p < 0.01$: idebenone-MPTP vs. corn oil-MPTP; $^{###}p < 0.001$: corn oil-MPTP vs. corn oil-saline.

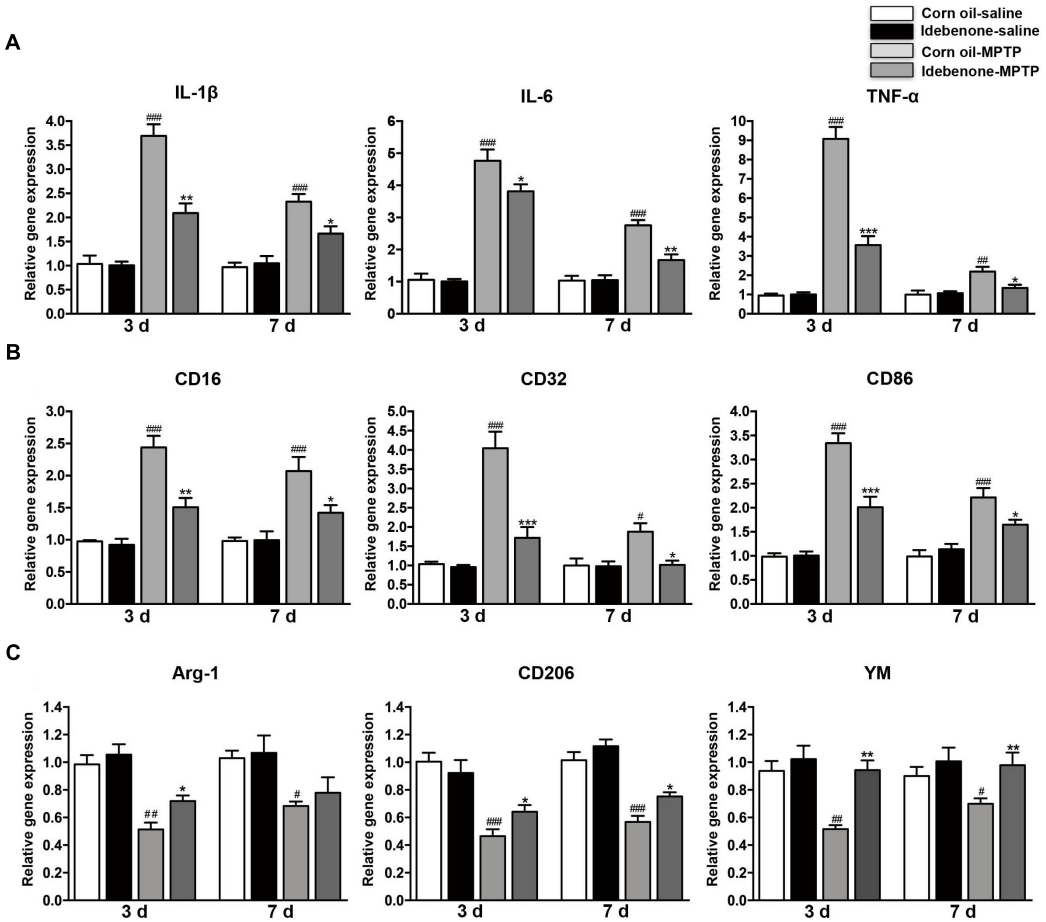

FIGURE 7 | Idebenone treatments inhibited expression of proinflammatory cytokines and M1 markers and promoted M2 markers in the SN of PD mice. **(A)** The expression of proinflammatory factors (IL-1β, IL-6, and TNF-α) in the SN as determined by RT-qPCR. **(B)** The expression of M1 markers (CD16, CD32, and CD86) in the SN as determined by RT-qPCR. **(C)** The expression of M2 microglial markers (Arg-1, CD206, and YM) in the SN as determined by RT-qPCR. Values are presented as the mean ± SEM. $^{*}p < 0.05$, $^{**}p < 0.01$, $^{***}p < 0.001$: idebenone-MPTP vs. corn oil-MPTP; $^{\#}p < 0.05$, $^{\#\#}p < 0.01$, $^{\#\#\#}p < 0.001$: corn oil-MPTP vs. corn oil-saline.

In accordance with the previous reports (Zhu et al., 2018; Chen et al., 2019), MPTP-induced PD model decreased the TH-positive fibers and neurotransmitters, such as dopamine and its metabolites DOPAC in the striatum ($p < 0.001$; **Figures 6B,C**). Compared with corn oil-MPTP group, idebenone prevented TH positive fibers loss ($p < 0.01$; **Figure 6B**) and increased the dopamine and DOPAC levels ($p < 0.05$; **Figure 6C**). These results suggest a neuroprotective effect of idebenone against MPTP toxicity.

Idebenone Treatment Inhibited the Inflammatory Response and Modulated Microglial Polarization in MPTP-Treated Mice

To determine whether the protective effect of idebenone was related to anti-inflammatory effects and microglial phenotypic shift, we used RT-qPCR to detect proinflammatory cytokines and microglial phenotypic markers in the SN and in the striatum of mice sacrificed at 3 and 7 days after the last MPTP injection. The result indicated that the expression of proinflammatory cytokines (IL-1β, IL-6, and TNF-α) was significantly higher in the corn oil-MPTP treated mice than the corn oil-saline treated mice at 3 and 7 days after the last MPTP administration ($p < 0.01$; **Figures 7A**, **8A**). In the idebenone-MPTP treated mice, idebenone inhibited the expression of IL-1β, IL-6, and TNF-α compared with the corn oil-MPTP treated mice ($p < 0.05$; **Figures 7A**, **8A**).

To determine whether the anti-inflammatory effect of idebenone resulted from the regulation of microglial polarization in the SN and in the striatum of PD mice, we detected the expression of M1 and M2 markers by RT-qPCR. Increased mRNA expression of M1 markers (CD16, CD32, and CD86) and decreased mRNA expression of M2 markers (Arg-1, CD206, and YM-1) were observed at 3 and 7 days after the last MPTP administration ($p < 0.05$; **Figures 7B,C**, **8B,C**). In animals pretreated with idebenone, M1 marker levels were decreased, and M2 markers increased gradually at 3 and 7 days

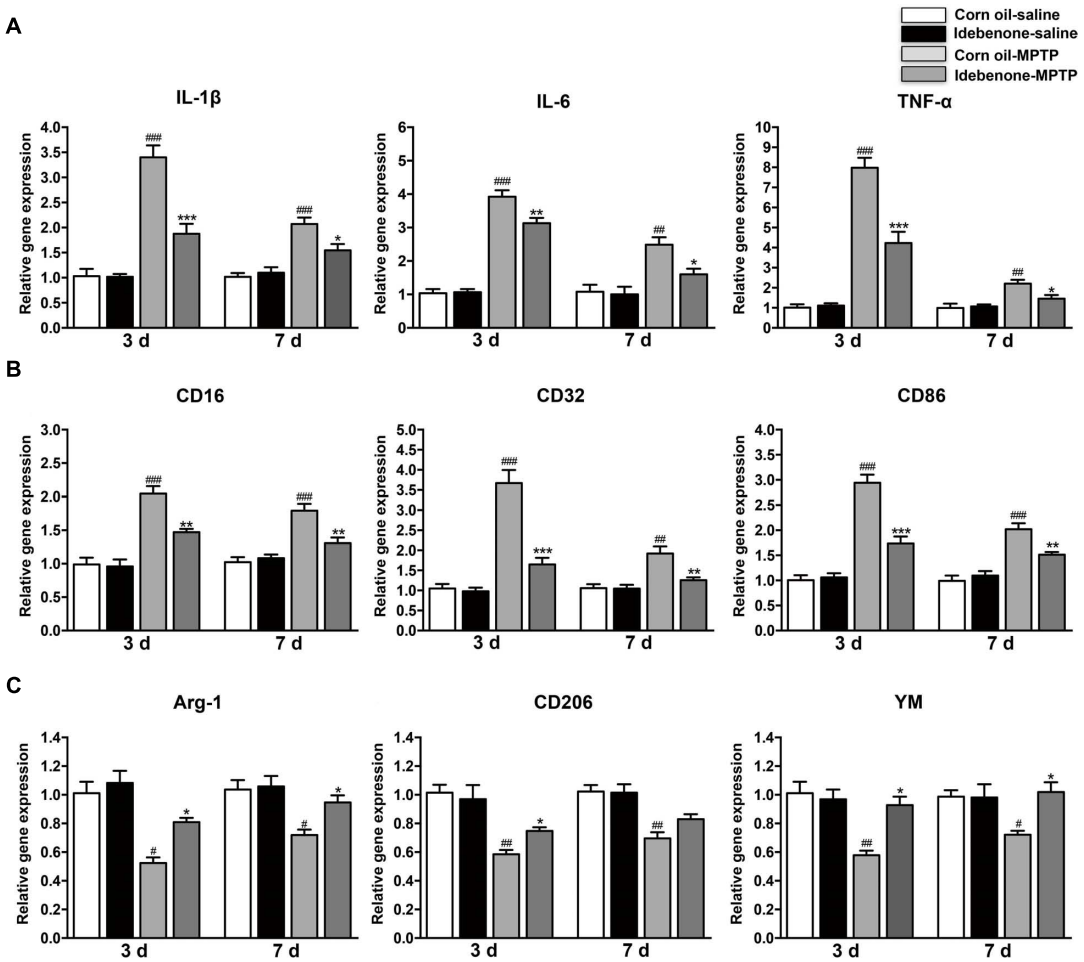

FIGURE 8 | Idebenone treatments inhibited expression of proinflammatory cytokines and M1 markers and promoted M2 markers in the striatum of PD mice. **(A)** The expression of proinflammatory factors (IL-1β, IL-6, and TNF-α) in the striatum as determined by RT-qPCR. **(B)** The expression of M1 markers (CD16, CD32, and CD86) in the striatum as determined by RT-qPCR. **(C)** The expression of M2 microglial markers (Arg-1, CD206, and YM) in the striatum as determined by RT-qPCR. Values are presented as the mean ± SEM. $^{*}p < 0.05$, $^{**}p < 0.01$, $^{***}p < 0.001$: idebenone-MPTP vs. corn oil-MPTP; $^{\#}p < 0.05$, $^{\#\#}p < 0.01$, $^{\#\#\#}p < 0.001$: corn oil-MPTP vs. corn oil-saline.

after the last MPTP administration ($p < 0.05$; **Figures 7B,C**, **8B,C**).

The M1 and M2 signature genes are expressed not only in microglia but also in other central nervous system cells. The results of RT-qPCR reflected the changes of these genes in mixed cell types. To specifically evaluate the polarization state of microglia after MPTP injection, M1 marker (CD16) or M2 marker (Arg-1) were analyzed by double immunofluorescent staining with the microglia marker (Iba-1) in the SN and in the striatum. Consistent with the RT-qPCR results, expression of the M1 marker CD16 was lower in Iba-1+ microglia cells in idebenone-MPTP treated group compared with the corn oil-MPTP treated group at 3 days after MPTP injection ($p < 0.01$; **Figures 9A,D**, **10A,D**). Expression of the M2 marker Arg-1 was higher in Iba-1+ microglia in idebenone-MPTP treated group compared with the corn oil-MPTP treated group ($p < 0.01$; **Figures 9B,E**, **10B,E**).

We also evaluated the effect of idebenone on the numbers of microglia in the SN and in the striatum of MPTP mice. The percentage of Iba-1+ microglia in idebenone-MPTP treated group was obviously lower than that in corn oil-MPTP treated group ($p < 0.01$; **Figures 9A–C**, **10A–C**). Our results suggested that idebenone could inhibit proliferation of the microglia in the SN and in the striatum.

Idebenone Treatment Inhibited MPTP-Induced Activation of MAPK and NF-κB in the SN of PD Mice

To confirm whether idebenone treatment suppressed activation of MAPK and NF-κB in the SN of PD mice, we tested the phosphorylation of MAPK/NF-κB in the mice. Our result showed that MPTP injection could induce the phosphorylation of p38, ERK, JNK, and NF-κB in the SN at 7 days after the last MPTP administration ($p < 0.01$, **Figures 11A,B**). Treatment of

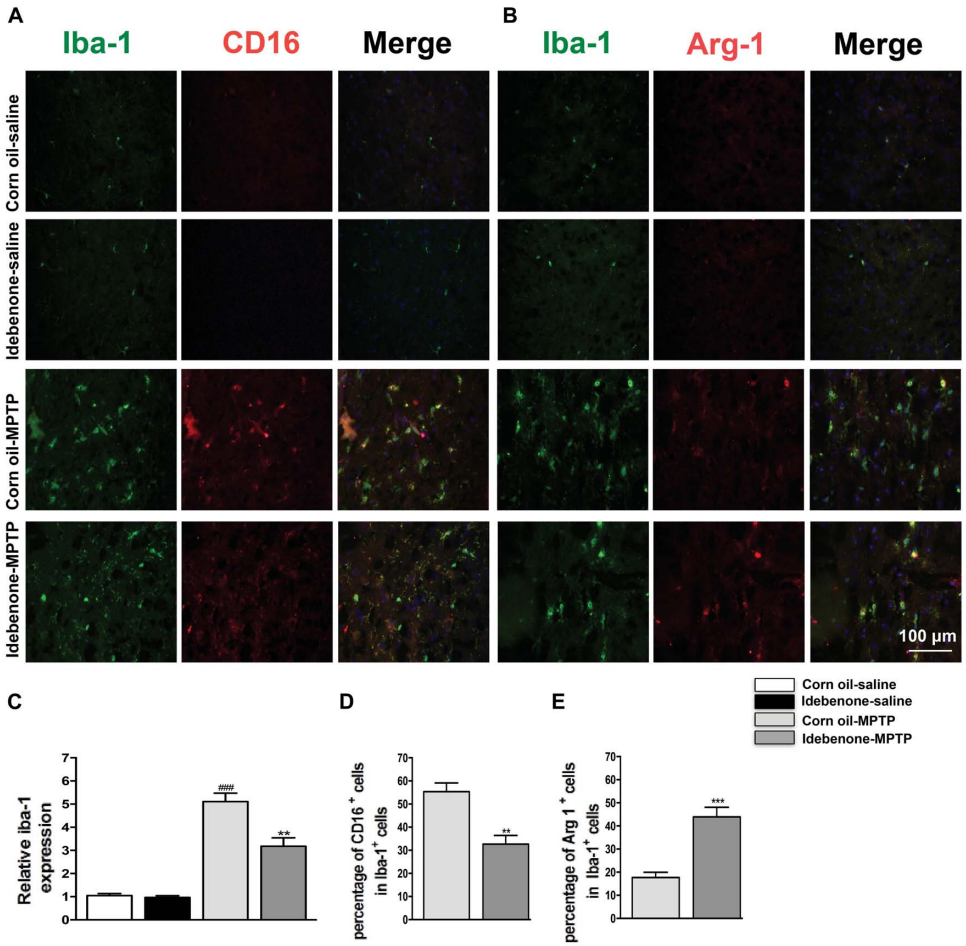

FIGURE 9 | Idebenone reduces M1 phenotype and increased M2 phenotype in the SN of PD mice. **(A,B)** Immunofluorescence double staining for Iba-1 (green) with CD16 (red) or Arg-1 (red) in the SN at 3 days following MPTP injection. **(C)** The quantity of microglia in the SN is quantified by the intensity of Iba-1+ immunofluorescence. **(D,E)** Quantification of the percentage of CD16+/Iba-1+ and Arg-1+/Iba-1+ cells. Scale bar = 100 μm. Values are presented as the mean ± SEM. $^{**}p < 0.01$, $^{***}p < 0.001$: idebenone-MPTP vs. corn oil-MPTP; $^{###}p < 0.001$: corn oil-MPTP vs. corn oil-saline.

idebenone could inhibit the phosphorylation of ERK, p38, JNK, and NF-κB in the SN compared with the corn oil-MPTP mice ($p < 0.05$, **Figures 11A,B**).

DISCUSSION

Idebenone is a synthetic analog of the coenzyme Q10 (CoQ10), and its therapeutic potential has been reported in many diseases, including cerebrovascular disorders and neurodegenerative disorders (Nagaoka et al., 1989a,b). A growing number of studies suggest that idebenone protects against PD, and in agreement, we report that idebenone treatment not only ameliorated neurological dysfunction but also decreased the inflammatory response and modulated M1/M2 microglial polarization in LPS-activated BV2 microglial cells and MPTP-treated PD mice.

Accumulating evidence from human and animal studies suggests that the microglia-mediated neuroinflammatory response is a hallmark shared by PD (Xu et al., 2016). Microglia activation states are classified as the classically activated M1 state or the alternatively activated M2 state (Colton, 2009). LPS, an inducer of the M1 state, induces the release of several proinflammatory cytokines (Yang et al., 2017). These cytokines induce the expression of M1 markers (CD16, CD86) and elicit the progressive death of neurons in the SN (Tian et al., 2006). By contrast, CD206 and arg-1, which are markers of the M2 microglia, block the expression of proinflammatory cytokines and promote neuroprotection (Liu et al., 2013). The switch between the M1 state and M2 state has been regarded as a novel therapeutic strategy for neurodegenerative diseases (Yang et al., 2017).

Previously, some studies showed that idebenone had anti-inflammatory abilities. Lauro et al. (2016) reported that when complexed with HP-β-cyclodextrins, idebenone exerted a potent anti-inflammatory efficacy. Another observation of previous studies was that idebenone behaved similar to

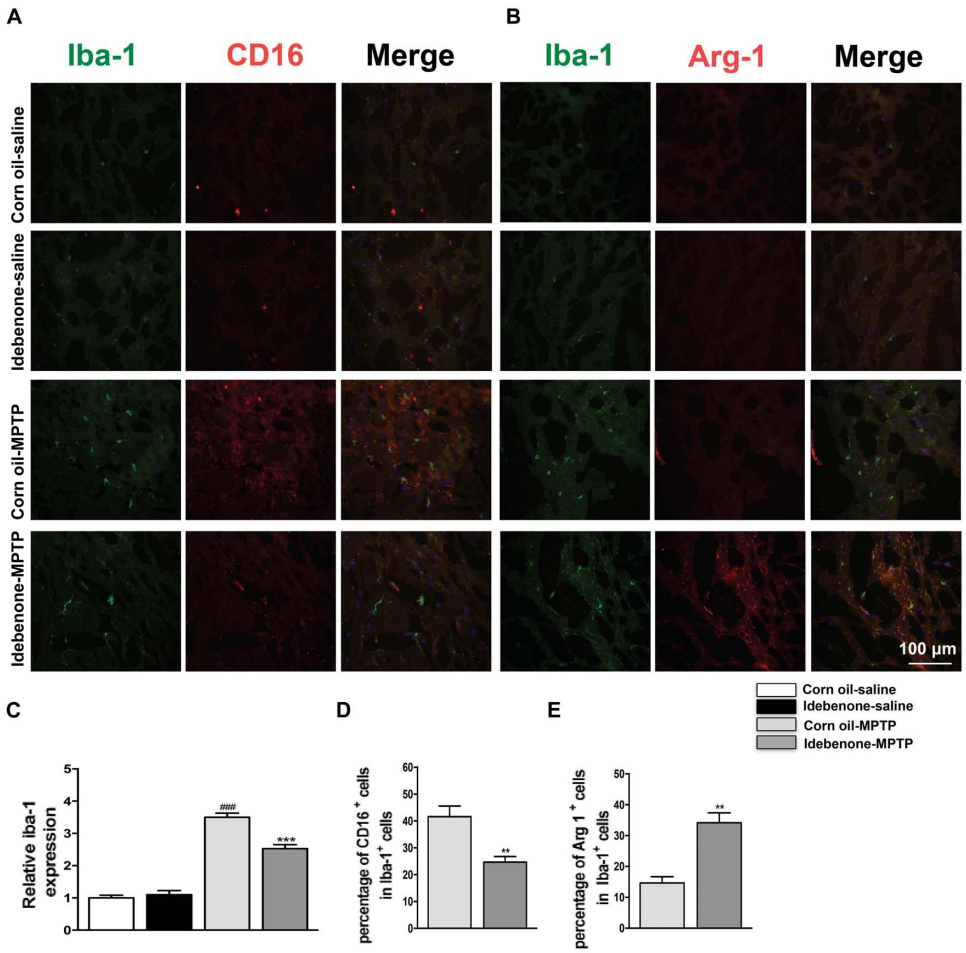

FIGURE 10 | Idebenone reduces M1 phenotype and increased M2 phenotype in the striatum of PD mice. **(A,B)** Immunofluorescence double staining for Iba-1 (green) with CD16 (red) or Arg-1 (red) in the striatum at 3 d following MPTP injection. **(C)** The quantity of microglia in the striatum is quantified by the intensity of Iba-1+ immunofluorescence. **(D,E)** Quantification of the percentage of CD16+/Iba-1+ and Arg-1+/Iba-1+ cells. Scale bar = 100 μm. Values are presented as the mean ± SEM. $^{**}p < 0.01$, $^{***}p < 0.001$: idebenone-MPTP vs. corn oil-MPTP; $^{###}p < 0.001$: corn oil-MPTP vs. corn oil-saline.

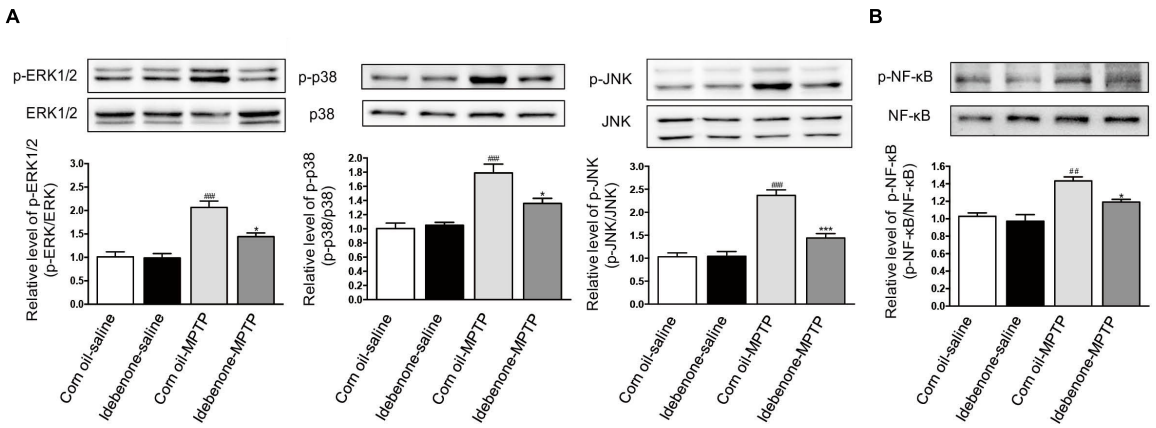

FIGURE 11 | Idebenone inhibited the MPTP-induced activation of MAPKs and NF-κB in the SN of PD mice. **(A)** Expression levels of p-ERK, ERK, p-p38, p38, p-JNK, and JNK in the SN were analyzed by western blotting. **(B)** Expression levels of p-NF-κB and NF-κB in the SN were analyzed by western blotting. Values are presented as the mean ± standard error. $^{*}p < 0.05$, $^{***}p < 0.001$: idebenone-MPTP vs. corn oil-MPTP; $^{##}p < 0.01$, $^{###}p < 0.001$: corn oil-MPTP vs. corn oil-saline.

indomethacin and piroxicam—two typical anti-inflammatory agents (Civenni et al., 1999). In our study, we evaluated the anti-inflammatory effect of idebenone in LPS-activated BV2 microglial cells. Our results indicated that idebenone significantly attenuated the LPS-induced production of proinflammatory factors. Another finding from our research was that idebenone could inhibit LPS-stimulated M1 microglia activation and promote M2 microglia polarization *in vitro*. Furthermore, conditioned medium from the LPS-stimulated BV2 cells decreased SH-SY5Y cell viability, while pretreatment with idebenone significantly attenuated the effect of LPS. Our experiments indicated that LPS could induce proinflammatory cytokines released in BV2 cells, which may explain the reduction in SH-SY5Y cell survival in conditioned medium from activated BV2 cells.

To further investigate the potential mechanisms of inhibition of inflammatory factors release and modulation of microglia phenotypes by idebenone, different signal pathways activated by LPS were evaluated. NF-κB and MAPKs signaling pathways are significant regulators of LPS-induced expression of proinflammatory cytokines in microglia (Boje, 2004). Inhibition of these signaling pathways reduced the release of proinflammatory cytokines in LPS-activated BV2 cells (Yu et al., 2015). In our experiments, the phosphorylation of ERK, p38, JNK, and NF-κB were observed to occur within 30 min of LPS treatment and can be reduced by idebenone. These results demonstrated that idebenone inhibited LPS-induced activation of BV2 microglial cells by suppressing MAPKs and NF-κB activation.

For *in vivo* experiments, idebenone was treated at a dose of 100 mg/kg body weight. In previous studies, 100 mg/kg of idebenone improved neurological deficits and energy metabolism in animal with cerebral ischemia (Nagaoka et al., 1989a,b) and was shown to reduce age related neurodegeneration (Scavini et al., 1996). 100 mg/kg of idebenone was sufficient to attenuate neurological dysfunction following cerebral hypoxia in rats (Abdel Baky et al., 2010). Thus, in view of these research reporting administration of idebenone in mice, we considered 100 mg/kg idebenone to be a reasonable dose to test. Consistent with *in vitro* studies implicating the protective role of idebenone, we found that idebenone protected against MPTP-induced motor dysfunction and reduced the neuronal death in the SN and in the striatum. Idebenone also lessened the decline of dopamine levels and its metabolites in the striatum of MPTP-induced PD mice. As the dopamine level is a marker of dopaminergic synaptic function, these results indicate that idebenone exerts neuroprotective effects on MPTP-induced PD mice. This effect may be related to the inhibition of proinflammatory cytokines release, as evidenced by the decreased expression of IL-6, IL-1β, and TNF-α in the SN and in the striatum of MPTP-treated animals.

Conversion of M1 state to M2 state prevented death of TH+ neurons in the MPTP induced PD model (Zhao et al., 2015). Fasudil, a Rho kinase inhibitor, decreased the expression of M1 markers and increased the expression of M2 markers. Thus, fasudil promoted recovery of motor function and was neuroprotective (Zhao et al., 2015). In our study, idebenone suppressed the "proinflammatory" M1 phenotype, while enhancing the "anti-inflammatory" M2 microglia phenotype in the SN and striatum after MPTP administration. Our findings revealed that the anti-inflammatory effects and modulation of M1/M2 polarization by idebenone contributed to the survival of TH+ neurons in the MPTP-induced PD model. We attempted to identify the underlying mechanism that inhibits M1 polarization and promotes M2 polarization *in vivo*. Consistent with *in vitro* study, idebenone suppressed the phosphorylation of ERK, p38, JNK, and NF-κB in the SN of MPTP-treated animals. These data suggested that idebenone could inhibit M1 polarization and promotes M2 polarization by modulating the MAPKs and NF-κB signaling pathway *in vivo*.

Our work reveals a new insight into idebenone neuroprotection. Idebenone could attenuate the proinflammatory cytokines expression, and promote the phenotypic shift of microglia from the M1 to M2 phenotype in LPS-activated BV2 cells and the MPTP induced PD model. Mechanistically, these effects of idebenone may be mediated by inhibition of the MAPK and NK-κB pathway. Taken together, the present data suggested that the preventive potential of idebenone as a novel anti-inflammatory and microglia-modulating drug for neurodegenerative diseases associated with neuroinflammation, such as PD.

AUTHOR CONTRIBUTIONS

ZgL and AY designed the experiments. AY, ZhL, LS, XW, YZ, NW, JL, and YL performed the experiments. AY and ZhL analyzed the results. AY wrote the manuscript with contributions from ZgL. All authors read and approved the final manuscript.

FUNDING

This study was supported by the National Key R&D Program of China (2017YFC1310300 and 2016YFC1306600), National Natural Science Foundation of China (81471148, 81671273, 81771211, and 81703852), Projects of the Shanghai Committee of Science and Technology (17401901000), and SHSMU-ION Research Center for Brain Disorders (2015NKX007).

SUPPLEMENTARY MATERIAL

The Supplementary Material for this article can be found online at: https://www.frontiersin.org/articles/10.3389/fncel.2018.00529/full#supplementary-material

FIGURE S1 | Idebenone, LPS, idebenone plus LPS treatment did not induce cytotoxicity in SH-SY5Y cells. Idebenone, LPS, idebenone plus LPS were directly added to SH-SY5Y cells that had been seeded in 96-well plates for 24 h. CCK-8 assay kit was used to assess the changes in SH-SY5Y cells viability.

REFERENCES

Abdel Baky, N. A., Zaidi, Z. F., Fatani, A. J., Sayed-Ahmed, M. M., and Yaqub, H. (2010). Nitric oxide pros and cons: the role of L-arginine, a nitric oxide precursor, and idebenone, a coenzyme-Q analogue in ameliorating cerebral hypoxia in rat. *Brain Res. Bull.* 83, 49–56. doi: 10.1016/j.brainresbull.2010.07.004

Boje, K. M. (2004). Nitric oxide neurotoxicity in neurodegenerative diseases. *Front. Biosci.* 9, 763–776. doi: 10.2741/1268

Brochard, V., Combadiere, B., Prigent, A., Laouar, Y., Perrin, A., Beray-Berthat, V., et al. (2009). Infiltration of CD4 + lymphocytes into the brain contributes to neurodegeneration in a mouse model of Parkinson disease. *J. Clin. Invest.* 119, 182–192. doi: 10.1172/JCI36470

Cai, G., Yan, A., Fu, N., and Fu, Y. (2018). Thromboxane A2 receptor antagonist SQ29548 attenuates SHSY5Y neuroblastoma cell impairments induced by oxidative stress. *Int. J. Mol. Med.* 42, 479–488. doi: 10.3892/ijmm.2018.3589

Chen, L., Xue, L., Zheng, J., Tian, X., Zhang, Y., and Tong, Q. (2019). PPARss/delta agonist alleviates NLRP3 inflammasome-mediated neuroinflammation in the MPTP mouse model of Parkinson's disease. *Behav. Brain Res.* 356, 483–489. doi: 10.1016/j.bbr.2018.06.005

Civenni, G., Bezzi, P., Trotti, D., Volterra, A., and Racagni, G. (1999). Inhibitory effect of the neuroprotective agent idebenone on arachidonic acid metabolism in astrocytes. *Eur. J. Pharmacol.* 370, 161–167. doi: 10.1016/S0014-2999(99)00127-2

Colton, C., and Wilcock, D. M. (2010). Assessing activation states in microglia. *CNS Neurol. Disord. Drug Targets* 9, 174–191. doi: 10.2174/187152710791012053

Colton, C. A. (2009). Heterogeneity of microglial activation in the innate immune response in the brain. *J. Neuroimmune Pharmacol.* 4, 399–418. doi: 10.1007/s11481-009-9164-4

Czlonkowska, A., Kurkowska-Jastrzebska, I., Czlonkowski, A., Peter, D., and Stefano, G. B. (2002). Immune processes in the pathogenesis of Parkinson's disease - a potential role for microglia and nitric oxide. *Med. Sci. Monit.* 8, RA165–RA177.

Dauer, W., and Przedborski, S. (2003). Parkinson's disease: mechanisms and models. *Neuron* 39, 889–909. doi: 10.1016/S0896-6273(03)00568-3

Fenn, A. M., Henry, C. J., Huang, Y., Dugan, A., and Godbout, J. P. (2012). Lipopolysaccharide-induced interleukin (IL)-4 receptor-alpha expression and corresponding sensitivity to the M2 promoting effects of IL-4 are impaired in microglia of aged mice. *Brain Behav. Immun.* 26, 766–777. doi: 10.1016/j.bbi.2011.10.003

Fiebiger, S. M., Bros, H., Grobosch, T., Janssen, A., Chanvillard, C., Paul, F., et al. (2013). The antioxidant idebenone fails to prevent or attenuate chronic experimental autoimmune encephalomyelitis in the mouse. *J. Neuroimmunol.* 262, 66–71. doi: 10.1016/j.jneuroim.2013.07.002

Giaume, C., Kirchhoff, F., Matute, C., Reichenbach, A., and Verkhratsky, A. (2007). Glia: the fulcrum of brain diseases. *Cell Death Differ.* 14, 1324–1335. doi: 10.1038/sj.cdd.4402144

Han, Z., Zhao, H., Tao, Z., Wang, R., Fan, Z., Luo, Y., et al. (2018). TOPK promotes microglia/macrophage polarization towards M2 phenotype via inhibition of HDAC1 and HDAC2 activity after transient cerebral ischemia. *Aging Dis.* 9, 235–248. doi: 10.14336/AD.2017.0328

Horvath, T. L., Diano, S., Leranth, C., Garcia-Segura, L. M., Cowley, M. A., Shanabrough, M., et al. (2003). Coenzyme Q induces nigral mitochondrial uncoupling and prevents dopamine cell loss in a primate model of Parkinson's disease. *Endocrinology* 144, 2757–2760. doi: 10.1210/en.2003-0163

Hunot, S., Vila, M., Teismann, P., Davis, R. J., Hirsch, E. C., Przedborski, S., et al. (2004). JNK-mediated induction of cyclooxygenase 2 is required for neurodegeneration in a mouse model of Parkinson's disease. *Proc. Natl. Acad. Sci. U.S.A.* 101, 665–670. doi: 10.1073/pnas.0307453101

Jaber, S., and Polster, B. M. (2015). Idebenone and neuroprotection: antioxidant, pro-oxidant, or electron carrier? *J. Bioenerg. Biomembr.* 47, 111–118. doi: 10.1007/s10863-014-9571-y

Lauro, F., Ilari, S., Giancotti, L. A., Ventura, C. A., Morabito, C., Gliozzi, M., et al. (2016). Pharmacological effect of a new idebenone formulation in a model of carrageenan-induced inflammatory pain. *Pharmacol. Res.* 111, 767–773. doi: 10.1016/j.phrs.2016.07.043

Liu, C., Li, Y., Yu, J., Feng, L., Hou, S., Liu, Y., et al. (2013). Targeting the shift from M1 to M2 macrophages in experimental autoimmune encephalomyelitis mice treated with fasudil. *PLoS One* 8:e54841. doi: 10.1371/journal.pone.0054841

Liu, Y., Hao, W., Letiembre, M., Walter, S., Kulanga, M., Neumann, H., et al. (2006). Suppression of microglial inflammatory activity by myelin phagocytosis: role of p47-PHOX-mediated generation of reactive oxygen species. *J. Neurosci.* 26, 12904–12913. doi: 10.1523/JNEUROSCI.2531-06.2006

Lu, J., Duan, X., Zhao, W., Wang, J., Wang, H., Zhou, K., et al. (2018). Aged mice are more resistant to influenza virus infection due to reduced inflammation and lung pathology. *Aging Dis.* 9, 358–373. doi: 10.14336/AD.2017.0701

Luster, A. D., Alon, R., and von Andrian, U. H. (2005). Immune cell migration in inflammation: present and future therapeutic targets. *Nat. Immunol.* 6, 1182–1190. doi: 10.1038/ni1275

Min, S., More, S. V., Park, J. Y., Jeon, S. B., Park, S. Y., Park, E. J., et al. (2014). EOP, a newly synthesized ethyl pyruvate derivative, attenuates the production of inflammatory mediators via p38, ERK and NF-kappaB pathways in lipopolysaccharide-activated BV-2 microglial cells. *Molecules* 19, 19361–19375. doi: 10.3390/molecules191219361

Muscoli, C., Fresta, M., Cardile, V., Palumbo, M., Renis, M., Puglisi, G., et al. (2002). Ethanol-induced injury in rat primary cortical astrocytes involves oxidative stress: effect of idebenone. *Neurosci. Lett.* 329, 21–24. doi: 10.1016/S0304-3940(02)00567-0

Nagaoka, A., Kakihana, M., and Fujiwara, K. (1989a). Effects of idebenone on neurological deficits following cerebrovascular lesions in stroke-prone spontaneously hypertensive rats. *Arch. Gerontol. Geriatr.* 8, 203–212. doi: 10.1016/0167-4943(89)90003-4

Nagaoka, A., Suno, M., Shibota, M., and Kakihana, M. (1989b). Effects of idebenone on neurological deficits, local cerebral blood flow, and energy metabolism in rats with experimental cerebral ischemia. *Arch. Gerontol. Geriatr.* 8, 193–202. doi: 10.1016/0167-4943(89)90002-2

Parkinson, M. H., Schulz, J. B., and Giunti, P. (2013). Co-enzyme Q10 and idebenone use in Friedreich's ataxia. *J. Neurochem.* 126(Suppl. 1), 125–141. doi: 10.1111/jnc.12322

Saijo, K., and Glass, C. K. (2011). Microglial cell origin and phenotypes in health and disease. *Nat. Rev. Immunol.* 11, 775–787. doi: 10.1038/nri3086

Saijo, K., Winner, B., Carson, C. T., Collier, J. G., Boyer, L., Rosenfeld, M. G., et al. (2009). A Nurr1/CoREST pathway in microglia and astrocytes protects dopaminergic neurons from inflammation-induced death. *Cell* 137, 47–59. doi: 10.1016/j.cell.2009.01.038

Scavini, C., Rozza, A., Lanza, E., Favalli, L., Racagni, G., and Brunello, N. (1996). Effect of idebenone on in vivo serotonin release and serotonergic receptors in young and aged rats. *Eur. Neuropsychopharmacol.* 6, 95–102. doi: 10.1016/0924-977X(95)00067-Y

Shao, J., Liu, T., Xie, Q. R., Zhang, T., Yu, H., Wang, B., et al. (2013). Adjudin attenuates lipopolysaccharide (LPS)- and ischemia-induced microglial activation. *J. Neuroimmunol.* 254, 83–90. doi: 10.1016/j.jneuroim.2012.09.012

Song, G. J., and Suk, K. (2017). Pharmacological modulation of functional phenotypes of microglia in neurodegenerative diseases. *Front. Aging Neurosci.* 9:139. doi: 10.3389/fnagi.2017.00139

Tian, Y. Y., An, L. J., Jiang, L., Duan, Y. L., Chen, J., and Jiang, B. (2006). Catalpol protects dopaminergic neurons from LPS-induced neurotoxicity in mesencephalic neuron-glia cultures. *Life Sci.* 80, 193–199. doi: 10.1016/j.lfs.2006.09.010

Voronkova, K. V., and Meleshkov, M. N. (2009). Use of Noben (idebenone) in the treatment of dementia and memory impairments without dementia. *Neurosci. Behav. Physiol.* 39, 501–506. doi: 10.1007/s11055-009-9148-0

Weyer, G., Babej-Dolle, R. M., Hadler, D., Hofmann, S., and Herrmann, W. M. (1997). A controlled study of 2 doses of idebenone in the treatment of Alzheimer's disease. *Neuropsychobiology* 36, 73–82. doi: 10.1159/000119366

Whitton, P. S. (2007). Inflammation as a causative factor in the aetiology of Parkinson's disease. *Br. J. Pharmacol.* 150, 963–976. doi: 10.1038/sj.bjp.0707167

Wu, D. D., Huang, L., Zhang, L., Wu, L. Y., Li, Y. C., and Feng, L. (2012). LLDT-67 attenuates MPTP-induced neurotoxicity in mice by up-regulating NGF expression. *Acta Pharmacol. Sin.* 33, 1187–1194. doi: 10.1038/aps.2012.88

Xu, L., He, D., and Bai, Y. (2016). Microglia-mediated inflammation and neurodegenerative disease. *Mol. Neurobiol.* 53, 6709–6715. doi: 10.1007/s12035-015-9593-4

Yan, A., Cai, G., Xia, W., and Fu, Y. (2017). Thromboxane A2 receptor antagonist SQ29548 suppresses the LPSinduced release of inflammatory cytokines in BV2 microglia cells via suppressing MAPK and NFkappaB signaling pathways. *Mol. Med. Rep.* 16, 2491–2496. doi: 10.3892/mmr.2017.6884

Yan, A., Zhang, T., Yang, X., Shao, J., Fu, N., Shen, F., et al. (2016). Thromboxane A2 receptor antagonist SQ29548 reduces ischemic stroke-induced microglia/macrophages activation and enrichment, and ameliorates brain injury. *Sci. Rep.* 6:35885. doi: 10.1038/srep35885

Yan, A., Zhang, Y., Lin, J., Song, L., Wang, X., and Liu, Z. (2018). Partial depletion of peripheral M1 macrophages reverses motor deficits in MPTP-treated mouse by suppressing neuroinflammation and dopaminergic neurodegeneration. *Front. Aging Neurosci.* 10:160. doi: 10.3389/fnagi.2018.00160

Yang, W., Yan, A., Zhang, T., Shao, J., Liu, T., Yang, X., et al. (2016). Thromboxane A2 receptor stimulation enhances microglial interleukin-1beta and NO biosynthesis mediated by the activation of ERK pathway. *Front. Aging Neurosci.* 8:8. doi: 10.3389/fnagi.2016.00008

Yang, X., Xu, S., Qian, Y., and Xiao, Q. (2017). Resveratrol regulates microglia M1/M2 polarization via PGC-1alpha in conditions of neuroinflammatory injury. *Brain Behav. Immun.* 64, 162–172. doi: 10.1016/j.bbi.2017.03.003

Yu, L., Wang, X., Chen, H., Yan, Z., Wang, M., and Li, Y. (2017). Neurochemical and behavior deficits in rats with iron and rotenone co-treatment: role of redox imbalance and neuroprotection by biochanin A. *Front. Neurosci.* 11:657. doi: 10.3389/fnins.2017.00657

Yu, Z., Tang, L., Chen, L., Li, J., Wu, W., and Hu, C. (2015). Capillarisin suppresses lipopolysaccharide-induced inflammatory mediators in BV2 microglial cells by suppressing TLR4-mediated NF-kappaB and MAPKs signaling pathway. *Neurochem. Res.* 40, 1095–1101. doi: 10.1007/s11064-015-1567-4

Zhao, Y., Zhang, Q., Xi, J., Xiao, B., Li, Y., and Ma, C. (2015). Neuroprotective effect of fasudil on inflammation through PI3K/Akt and Wnt/beta-catenin dependent pathways in a mice model of Parkinson's disease. *Int. J. Clin. Exp. Pathol.* 8, 2354–2364.

Zhu, Y. L., Sun, M. F., Jia, X. B., Zhang, P. H., Xu, Y. D., Zhou, Z. L., et al. (2018). Aucubin alleviates glial cell activation and preserves dopaminergic neurons in 1-methyl-4-phenyl-1,2,3,6-tetrahydropyridine-induced parkinsonian mice. *Neuroreport* 29, 1075–1083. doi: 10.1097/WNR.0000000000001075

Conflict of Interest Statement: The authors declare that the research was conducted in the absence of any commercial or financial relationships that could be construed as a potential conflict of interest.

frontiers in Cellular Neuroscience

MINI REVIEW
published: 27 March 2019
doi: 10.3389/fncel.2019.00116

Emerging Role of Schwann Cells in Neuropathic Pain: Receptors, Glial Mediators and Myelination

Zhongya Wei[1], *Ying Fei*[1], *Wenfeng Su*[1] *and Gang Chen*[1,2]*

[1]*Key Laboratory of Neuroregeneration of Jiangsu and Ministry of Education, Co-innovation Center of Neuroregeneration, Nantong University, Nantong, China,* [2]*Department of Anesthesiology, Affiliated Hospital of Nantong University, Nantong, China*

Neuropathic pain caused by nerve injury or disease remains a major challenge for modern medicine worldwide. Most of the pathogenic mechanisms underlying neuropathic pain are centered on neuronal mechanisms. Accumulating evidence suggests that non-neuronal cells, especially glial cells, also play active roles in the initiation and resolution of pain. The preponderance of evidence has implicated central nervous system (CNS) glial cells, i.e., microglia and astrocytes, in the control of pain. The role of Schwann cells in neuropathic pain remains poorly understood. Schwann cells, which detect nerve injury and provide the first response, play a critical role in the development and maintenance of neuropathic pain. The cells respond to nerve injury by changing their phenotype, proliferating and interacting with nociceptive neurons by releasing glial mediators (growth factors, cytokines, chemokines, and biologically active small molecules). In addition, receptors expressed in active Schwann cells have the potential to regulate different pain conditions. In this review article, we will provide and discuss emerging evidence by integrating recent advances related to Schwann cells and neuropathic pain.

Keywords: Schwann cells, neuropathic pain, receptors, glial mediators, myelination

OPEN ACCESS

Edited by:
Stefania Ceruti,
University of Milan, Italy

Reviewed by:
Livio Luongo,
Second University of Naples, Italy
Valerio Magnaghi,
University of Milan, Italy

***Correspondence:**
Gang Chen
chengang6626@ntu.edu.cn

Received: *31 December 2018*
Accepted: *11 March 2019*
Published: *27 March 2019*

Citation:
Wei Z, Fei Y, Su W and Chen G (2019) Emerging Role of Schwann Cells in Neuropathic Pain: Receptors, Glial Mediators and Myelination. Front. Cell. Neurosci. 13:116. doi: 10.3389/fncel.2019.00116

INTRODUCTION

Neuropathic pain is a typically persistent and intractable type of chronic pain. This condition is not a symptom of a disorder but a pathological state caused by a primary lesion or dysfunction in the nervous system (Backonja, 2003). It is well known that neuropathic pain is an expression of neuroplasticity and arises from both the peripheral nervous system (PNS) and the central nervous system (CNS).

Past research on neuropathic pain has focused mostly on the role of neurons (Ji et al., 2003; Chen et al., 2016, 2017). Following a nerve injury, both peripheral and central sensitization act as important disease mechanisms, including sensitization and hyperexcitability of primary sensory neurons as well as enhanced excitatory synaptic transmission or reduced inhibitory synaptic transmission in the neurons of the CNS (Gold and Gebhart, 2010; Kuner, 2010). In parallel to the changes in the activity of neuronal systems, non-neuronal cells, especially glial cells, are increasingly recognized as important in the development and maintenance of neuropathic pain (Ji et al., 2013, 2016). Regarding the glial cells in the CNS, both astrocytes and microglia have well-documented roles in the regulation of neuropathic pain, primarily in the spinal cord and brain (Ji et al., 2013, 2016; Chen et al., 2014, 2018).

The glial cells of the PNS primarily include Schwann cells and satellite glial cells. The satellite glial cells surrounding the somata of dorsal root ganglion (DRG) neurons are activated

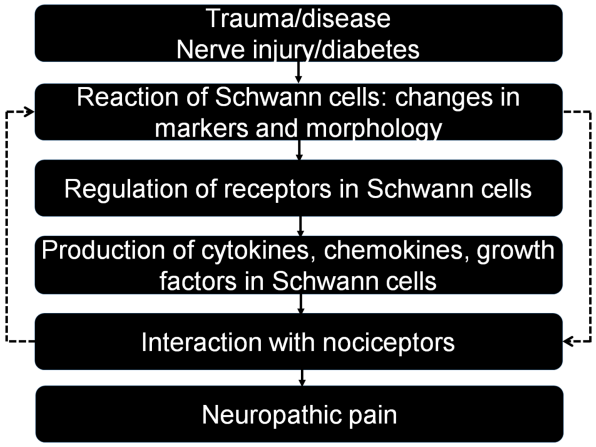

FIGURE 1 | Interactions between Schwann cells and neurons in different pain conditions after trauma and disease. Note that Schwann cells can modulate neuropathic pain in different directions by producing relevant mediators that act on specific receptors. Activated neurons also have a feedback effect on Schwann cells, completing an interaction loop.

prior to central glial cells after nerve injury and play a critical role in the development of neuropathic pain (Jasmin et al., 2010; Ji et al., 2013). Schwann cells not only physically support the long axons but also release a variety of growth factors to nourish and myelinate the large associated axons (Chen et al., 2012; Kidd et al., 2013; Su et al., 2016). After sciatic nerve injury, activated Schwann cells undergo dramatic changes in response, including phenotype modulation, proliferation, migration and release of numerous factors, which eventually promote nerve regeneration (Scheib and Höke, 2013). It is well known that nerve injury is of utmost importance in the generation of neuropathic pain. Thus, Schwann cells play a key role in the study of neuropathic pain, but little is known about how these cells regulate this condition. In this review article, we will discuss and update the current knowledge of how Schwann cells modulate neuropathic pain, and we will provide an improved understanding of the underlying mechanisms (**Figure 1**).

SCHWANN CELLS AND THEIR MULTIPOTENCY

Schwann cells, the most abundant glial cells in the PNS, include two major phenotypes: myelinating Schwann cells and non-myelinating Schwann cells. Both types originate from embryonic Schwann cell precursors derived from the neural crest. Initially, these cells surround the external margins of the axon bundles (Kidd et al., 2013). Schwann cells support axonal outgrowth during this stage by producing a variety of growth factors, such as nerve growth factor (NGF), glial cell line-derived neurotrophic factor (GDNF), and brain-derived neurotrophic factor (BDNF; Kidd et al., 2013). While maturing and interacting with axons, myelinating Schwann cells wrap larger axons at a one-to-one ratio to produce a myelin sheath, while nonmyelinating Schwann cells embed smaller axons, forming a Remak bundle (Kidd et al., 2013).

After nerve injury, the former myelinating cells degrade their myelin and become a class of nonmyelinating cells, repair Schwann cells, which regain their developmental potential, including the capacity for proliferation, growth factor production, sorting, or sprouting and myelination if they receive the suitable neuronal signals (Griffin and Thompson, 2008; Scheib and Höke, 2013). Importantly, signaling systems that are crucial for the development of the Schwann cell lineage, but they have no or little role in the generation of repair Schwann cells and nerve regeneration (Jessen and Arthur-Farraj, 2019). This encourages the view that the different phenotype of Schwann cells and their transitions are likely to play a different role in regulating neuropathic pain, but it still awaits the selective tools to control the particular cells and reveal their specific role in the process of neuropathic pain. Notably, multiple receptors, channels and active molecules are altered or activated in different neuropathic pain conditions. Glial mediators, including cytokines, chemokines and growth factors are produced and secreted from activated Schwann cells.

RECEPTORS, CHANNELS AND ACTIVE MOLECULES OF SCHWANN CELLS MEDIATE NEUROPATHIC PAIN

As shown in **Table 1**, multiple receptors and channels are expressed in Schwann cells and regulated in different pain conditions. Although these molecules are not released, they activate intracellular signaling to release growth factors, cytokines, and chemokines that regulate pain states (**Table 2**).

Adenosine triphosphate (ATP) is an important molecule in the process of pain information transmission (Kuan and Shyu, 2016). This substance modulates glial activation primarily *via* activating the P2X ion channel receptor and the G-protein-coupled receptor (GPCR)-coupled receptor P2Y (Lecca et al., 2012). Although both P2X and P2Y receptors are expressed in Schwann cells, accumulating evidence shows that P2X receptors play a critical role in the regulation of neuropathic pain (Mayer et al., 1998). mRNAs for all P2X receptor subtypes are detectable in Schwann cells, with P2X4–7 receptors being highly expressed (Su et al., 2019). *In vivo* and *in vitro* experiments have revealed that the expression of the P2X4 receptor is markedly upregulated in Schwann cells of injured nerves. Blocking the P2X4 receptor in microglia can reverse established pain hypersensitivity after nerve injury, and the development of pain hypersensitivity after nerve injury is prevented in P2X4 receptor knockout mice (Tsuda et al., 2003; Ulmann et al., 2008). However, we did not observe increased pain hypersensitivity in mice with specific overexpression of the P2X4 receptor in Schwann cells compared with the control group (Su et al., 2019). While the expression of P2X7 receptor in Schwann cells and Schwann cell-like adipose-derived stem cells has been found to contribute to ATP-induced cell death (Faroni et al., 2013). Notably, the study from P2X7 knockout mice has revealed that P2X7 knockout nerves possess more unmyelinated axons containing a higher number of Remak bundle, which increase nociception (Faroni et al., 2014b). Another report regarding Schwann cells involved in regulating neuropathic pain shows

TABLE 1 | Regulation of receptors and active molecules in Schwann cells in neuropathic pain.

Molecule	Classification	Change after nerve injury	References
P2X4R	Receptor	↑	Su et al. (2019)
P2X2/3R	Receptor	↑	Zhang et al. (2018)
P2X7R	Receptor	—	Faroni et al. (2014b)
TLR2	Receptor	↑	Boivin et al. (2007) and Lee et al. (2013)
LRP1	Receptor	↓	Campana et al. (2006a) and Orita et al. (2013)
TRPA1	Channel	↑	De Logu et al. (2017)
LPA1 R	Receptor	↑	Inoue et al. (2004)
HCAR2	Receptor	↑	Boccella et al. (2019)
GABA-B	Receptor	—	Faroni et al. (2014a) and Magnaghi et al. (2014)
MHC-II	Antigen	↑	Hartlehnert et al. (2017)
ErbB	Receptor	—	Chen et al. (2006)
gp120	Glycoprotein	—	Keswani et al. (2006)

Purinergic receptors: P2X4R, P2X2/3R, P2X7R; TLR2, Toll-like receptor 2; LRP1, LDL receptor-related protein 1; TRPA1, Transient receptor potential Ankyrin 1; LPA1 R, Lysophosphatidic acid 1 receptor; HCAR2, Hydroxyl carboxylic acid receptor type 2; GABA-B, γ-aminobutyric acid type B receptor; MHC-II, Class II major histocompatibility complex; ErbB, Epidermal growth factor receptor; gp120, HIV-1 envelope glycoprotein. Symbols: ↑ denotes upregulation or activation; ↓ denotes downregulation or inactivation; —denotes data unavailable.

TABLE 2 | Regulation of cytokines, chemokines, and growth factors in Schwann cells in neuropathic pain.

Mediator	Classification	Change after nerve injury	References
TNF-α	Proinflammatory cytokine	↑	Scholz and Woolf (2007) and Sacerdote et al. (2008)
IL-1	Proinflammatory cytokine	↑	Martucci et al. (2008)
IL-6	Proinflammatory cytokine	↑	Martucci et al. (2008)
IL-10	Anti-inflammatory cytokine	↓	Franchi et al. (2012) and Wang et al. (2012)
Epo	Anti-inflammatory cytokine	↑	Keswani et al. (2004) and Campana et al. (2006b)
COX2	Chemokine	↑	Takahashi et al. (2004)
MCP-1	Chemokine	↑	Toews et al. (1998) and De Logu et al. (2017)
BDNF	Growth factor	↑	Yajima et al. (2005) and Su et al. (2019)
ATP	Messenger molecule	↑	Martucci et al. (2008)

TNF-α, Tumor necrosis factor-α; IL-1, IL-6, IL-10, Interleukin related cytokine; Epo, Erythropoietin; COX-2, Cyclooxygenase-2; MCP-1, Monocyte chemoattractant protein-1; BDNF, Brain derived neurotrophic factor; ATP, Adenosine triphosphate. Symbols:↑denotes upregulation or activation; ↓denotes downregulation or inactivation.

that the transplantation of microencapsulated Schwann cells can alleviate neuropathic pain by inhibiting P2X2/3 receptor overexpression in sciatic nerve injury (Zhang et al., 2018). The underlying mechanism of upregulation of P2X receptors in nerve injury is centered on the enhancement of BDNF release (Ulmann et al., 2008; Su et al., 2019), while the other mechanisms are still unclear.

Toll-like receptors (TLRs) are known to regulate innate immunity and have been strongly linked to the activation of glial cells (Nicotra et al., 2012). TLR2, 3 and 4 are highly expressed in Schwann cells at both the mRNA and protein levels (Lee et al., 2013). Lee et al. (2013) found that necrotic sensory neurons induced the release of proinflammatory mediators such as tumor necrosis factor-α (TNF-α) and iNOS by cultured rat Schwann cells from wild-type mice but not those from TLR2 knockout mice, suggesting that Schwann cells are activated through TLR2 recognition of damage-associated molecular patterns (DAMPs) during nerve injury. Notably, an *in vivo* study by Boivin et al. (2007) demonstrated that the Wallerian degeneration and expression of proinflammatory molecules induced by nerve injury were severely impaired in TLR2-knockout mice. Strikingly, the male specificity of the involvement of spinal TLR4 in neuropathic pain suggests a sex difference in TLR4 and microglial signaling (Sorge et al., 2011). Despite the lack of evidence that Schwann cells are involved in the sex difference in TLR signaling in neuropathic pain, any research to develop a TLR-antagonist analgesic or characterize a *Tlr* mutation must take the effect of sex differences into account if such information is available.

The endocytic transmembrane receptor known as LDL receptor-related protein 1 (LRP1) is a potent regulator of Schwann cells that orchestrates many of the physiological changes and the activation of Schwann cells after injury (Campana et al., 2006a; Mantuano et al., 2011). When Schwann cells lose LRP1 function through a cell-type-specific deletion in scLRP1$^{-/-}$ mice or through an antagonist of the receptor-associated protein, both the survival and the function of those cells are compromised (Campana et al., 2006a; Orita et al., 2013). Prior to nerve injury, *LRP1* gene deletion in Schwann cells resulted in the activation of regeneration-associated genes in DRG neurons and the potential to cause chronic pain. Although the presence of abnormal Schwann cells in scLRP1$^{-/-}$ mice primed injured DRG neurons to develop neuropathic pain, nerve repair in scLRP1$^{-/-}$ mice was associated with abnormalities in ultrastructure and primarily in Remak bundles (Orita et al., 2013; Boivin et al., 2007).

It is well known that transient receptor potential ankyrin 1 (TRPA1) channels are highly expressed by a subpopulation of primary sensory neurons (Story et al., 2003). TRPA1 has been shown to mediate mechanical hypersensitivity in different

types of neuropathic pain, including those induced by peripheral nerve injury (Eid et al., 2008). In 2017, TRPA1 was found to be expressed in Schwann cells both in cultures and in the sciatic nerve trunk (De Logu et al., 2017). The same study found that TRPA1 silencing in nociceptors attenuated mechanical allodynia without affecting macrophage infiltration, whereas TRPA1 silencing in Schwann cells reduced both mechanical allodynia and neuroinflammation. Activation of Schwann cell TRPA1 induces and maintains macrophage infiltration to the injured nerve and sends paracrine signals to activate TRPA1 in ensheathed nociceptors to sustain mechanical allodynia (De Logu et al., 2017).

Lysophosphatidic acid (LPA) is a bioactive lipid that interacts with specific GPCRs (Ishii et al., 2004). At least three specific LPA receptors are expressed in Schwann cells, and this cell type is known to primarily express the LPA1 receptor (Weiner et al., 2001). The LPA1 receptor is upregulated following sciatic nerve injury, and Schwann cells cultured from *LPA1*-null mice exhibit greatly diminished morphological responses to LPA (Weiner et al., 2001). Intrathecal injection of LPA induced morphological, biochemical and behavioral changes similar to those observed after nerve injury. However, mice lacking the LPA1 receptor do not develop signs of neuropathic pain after peripheral nerve injury, suggesting that receptor-mediated LPA signaling is crucial in the initiation of neuropathic pain (Inoue et al., 2004). Although there is no direct, accurate evidence characterizing the role of Schwann cell LPA1 receptors in neuropathic pain, the LPA1 receptor is a critical factor in the mediation of neuropathic pain by Schwann cells.

Hydroxyl carboxylic acid receptor type 2 (HCAR2), another class of GPCR is primarily expressed on adipocytes, peripheral immune cells and brain microglia, and involved in lipogenesis, inflammatory processes (Offermanns, 2017). Recently, the HCAR2 expression has been highlighted in the sciatic nerve, primarily in cells positive for S100 specifically marked by Schwann cells. An up-regulation of HCAR2 in the sciatic nerve and the DRG is present in neuropathic mice. Moreover, the HCAR2 endogenous ligand β-hydroxybutyrate can reduce the tactile allodynia in neuropathic pain models in female but not male mice. But the effect only occurs in wild-type mice but not in the HCAR2-null mice (Boccella et al., 2019). Although HCAR2 is not specifically expressed in Schwann cells, and do not have the evidence to investigate its role in conditional knockout mouse models, HCAR2 may be a new receptor for the regulation of neuropathic pain.

γ-aminobutyric acid type B (GABA-B) receptor, is one of the native targets of GABA, and mediates the inhibitory transmission in the CNS. Emerging evidence of GABA-B receptor functions in the PNS suggest its contribution in regulating maturation and plasticity of Schwann cells (Magnaghi et al., 2006). Both GABA-B1 and GABA-B2 receptors are present in neurons, and also in Schwann cells (Magnaghi et al., 2004). The conditional mice with specific deletion of GABA-B receptors in Schwann cells are hyperalgesic and allodynia, which associated with a morphological phenotype characterized by a peculiar increase in the number of small unmyelinated fibers and Remak bundles, including nociceptive C-fibers (Procacci et al., 2012; Faroni et al., 2014a). Meanwhile, GABA-B receptor activation following GABA-B ligands treatments with baclofen and CGP56433, promotes nerve regeneration and ameliorates neuropathic pain (Magnaghi et al., 2014). These findings support the importance of GABA-B receptors in the peripheral myelination process, and in modulating the nociceptive fiber activity.

The class II major histocompatibility complex (MHC-II) is presented on the surfaces of antigen presenting cells (APCs) for recognition by T cells. The main professional APCs are dendritic cells, macrophages and B cells (Neefjes et al., 2011). However, under traumatic and inflammatory conditions, Schwann cells have the potential to express MHC-II and present antigens (Meyer zu Hörste et al., 2010a,b). Notably, Schwann cells upregulate MHC-II under traumatic conditions in female but not male rats (Liu et al., 2012). MHC-II on Schwann cells activates T helper cells and promotes posttraumatic axon loss and subsequent neuropathic pain. Meanwhile, deletion of MHC-II in myelinating Schwann cells can diminish mechanical allodynia and thermal hyperalgesia in a chronic constriction injury (CCI) model in female mice (Hartlehnert et al., 2017).

Other interesting examples suggest that Schwann cells directly control the development of neuropathic pain. Deficiency of the Neuregulin/ErbB cell signaling pathway induces an enhanced response to mechanical allodynia but no changes in thermal hyperalgesia (Chen et al., 2006). In addition, mice expressing the HIV-1 envelope glycoprotein gp120 in nonmyelinating Schwann cells and treated with didanosine, an antiretroviral drug, had changes in sensory function (thermal allodynia; Keswani et al., 2006). Another candidate target is the acetylcholine system. *Botulinum* neurotoxins, an inhibitor of acetylcholine neurotransmitter release, exerting their action by cleaving soluble NSF attachment proteins, SNARE proteins, is well established in the treatment of neuropathic pain (Oh and Chung, 2015). *In vitro* experiments showed that *Botulinum* neurotoxins was able to interact with the proliferative state of Schwann cells, and facilitate Schwann cell proliferation (Marinelli et al., 2012). Moreover, acetylcholine receptors are present on Schwann cell membrane, and the activation of acetylcholine receptors can induce myelin structure reorganization (Verdiyan et al., 2016). Although there is no direct evidence to strongly characterize the role of Schwann cell acetylcholine system in neuropathic pain, these studies indicate that *Botulinum* neurotoxins may regulate the function of Schwann cells by the acetylcholine system to reduce neuropathic pain.

REGULATION OF GROWTH FACTORS, CYTOKINES, AND CHEMOKINES IN SCHWANN CELLS IN NEUROPATHIC PAIN

In response to nerve injury, glial mediators produced or released by activated Schwann cells or recruited immune cells are also a key issue in the control of neuropathic pain by Schwann cells. As shown in **Table 2**, Schwann cells produce both large molecules, such as growth factors, cytokines and chemokines,

and small molecules, including ATP. These mediators from Schwann cells play a critical role in neuronal and synaptic activity as well as pain.

Proinflammatory cytokines such as TNF-α, IL-1, and IL-6 are well-studied glial mediators. The expression levels of these molecules are upregulated in the sciatic nerve, spinal cord and DRG of animals after CCI (Martucci et al., 2008). Activated Schwann cells and infiltrating macrophages release these mediators, which contribute to axonal damage and enhance nociceptor activity (Campana, 2007; Sacerdote et al., 2008). TNF, the most prominent proinflammatory cytokine, is detectable as early as 6 h after sciatic nerve injury but has no significant difference from the control group within 7 days after nerve injury (Scholz and Woolf, 2007). Activated resident Schwann cells and macrophages are thought to be the sources for TNF production in the early stage of sciatic nerve injury (Campana, 2007; Sacerdote et al., 2008). IL-1 and IL-6 are also produced at the onset of injury but have a sustained effect on neuropathic pain. In CCI models, the mRNA levels of these cytokines increase at 1 day after injury, and the levels remain high for up to 21 days after surgery. In addition to the proinflammatory cytokines, anti-inflammatory mediators are also critical to the regulation of neuropathic pain (Martucci et al., 2008). The accumulating reports show that IL-10, the predominant anti-inflammatory mediator, is detected in the sciatic nerve after a lesion develops (Austin and Moalem-Taylor, 2010; Franchi et al., 2012). Meanwhile, several strategies aimed at enhancing the level of endogenous IL-10 have succeeded in preventing and relieving pain hypersensitivity in several neuropathic pain models (Franchi et al., 2012; Wang et al., 2012).

Erythropoietin (Epo), another anti-inflammatory cytokine, is upregulated along with its receptor EpoR after nerve injury, and the primary cellular source of EPO is activated Schwann cells (Li et al., 2005). In the early stage of nerve injury, Epo is able to reduce the production of TNF-α and facilitate recovery from chronic pain states (Keswani et al., 2004; Campana et al., 2006b). Therefore, the balance of inflammatory and anti-inflammatory mediators may be a future target for therapeutic intervention.

Chemokines, as another pain modulator, are expressed in neurons as well as in glial cells (Ji et al., 2013, 2016). In Schwann cells, cyclooxygenase-2 (COX-2) and monocyte chemoattractant protein-1 (MCP-1) are expressed after nerve injury (Toews et al., 1998; Takahashi et al., 2004). However, the cellular sources of these molecules differ between the early and late stages of nerve injury. The first increase in the number of positive cells occurred approximately 1 day after nerve injury in Schwann cells coexpressing S-100. The second increase was noted after 7–14 days and these cells were macrophages coexpressing ED-1 (Toews et al., 1998; Takahashi et al., 2004). Notably, a distinct CCL2 and TRPA1/oxidative stress pathway induced macrophage accumulation in Schwann cells (De Logu et al., 2017). Oxidative stress has been thought to exert a chemoattractant effect by macrophage infiltration. NADPH oxidase-1 (NOX1) is noticeably expressed in Schwann cells. TRPA1 in Schwann cells activates a NOX1-mediated intracellular signaling pathway to produce sustained oxidative stress, and it also maintains macrophage infiltration into lesion sites, which induces allodynia by activating TRPA1 on the nociceptors (De Logu et al., 2017).

Growth factors are known to play important roles in neuronal survival, myelination and synaptic plasticity (Park and Poo, 2013). In response to sciatic nerve injury, Schwann cells secrete multiple growth factors, such as NGF, BDNF, and neurotrophin-3 and 4 (Scheib and Höke, 2013). Among these factors, we found that TNF-α-induced BDNF release beyond the basal level in Schwann cells depends on P2X4R (Su et al., 2019). However, P2X4R-knockout mice do not show pain hypersensitivity after nerve injury, which has an ill effect on the release of intracellular signaling factors, including BDNF (Tsuda et al., 2003). On the other hand, as BDNF is a key mediator of neuropathic pain, BDNF-knockout mice display reduced pain hypersensitivity after nerve lesion compared with wild-type mice (Yajima et al., 2005). However, overexpression of P2X4R in Schwann cells did not result in increased pain hypersensitivity. In addition, intraplantar injection of BDNF induced mechanical allodynia only in naïve mice and not in mice with crush injuries of the sciatic nerve (Su et al., 2019).

ATP is an important intracellular messenger molecule that interacts with purinoceptors, playing a crucial role in the formation and regulation of neuropathic pain (Burnstock, 2006). Several subtypes of P2X receptors are highly expressed in Schwann cells (Su et al., 2019). ATP is released from Schwann cells under physiological conditions, and after nerve injury, increasing levels of ATP play an important role in both peripheral and central sensitization (Martucci et al., 2008; Tsuda et al., 2010). Released ATP activates neurons and Schwann cells to release certain mediators, including proinflammatory cytokines and chemokines (Inoue, 2006). Notably, when the broad-spectrum P2 receptor antagonist pyridoxal phosphate-6-azophenyl-2′,4′-disulfonic acid (PPADS) was administered after nerve injury, it significantly reduced the levels of IL-1 and IL-6, decreased tactile allodynia and thermal hyperalgesia, and continued to exert an effect for 2–3 weeks after administration (Martucci et al., 2008).

RELATIONSHIP OF DEMYELINATION AND REMYELINATION WITH NEUROPATHIC PAIN

It is well established that demyelination contributes to the development of neuropathic pain by disrupting the precise molecular and structural features of nerve fibers. For example, in females specifically, algesic MBP fragments released from the intact myelin sheath after nerve injury *via* MT1-MMP proteolysis control mechanical allodynia (Hong et al., 2017). The alteration of ErbB signaling in myelination Schwann cells leads to demyelination and induces mechanical hypersensitivity (Tao et al., 2013).

However, a direct relationship between remyelination and pain relief has not been investigated. Several studies have shown

an indirect association between them. For example, Gabapentin alleviates mechanical and thermal allodynia and improves nerve remyelination after chronic constriction of the sciatic nerve (Camara et al., 2015). Focal lysolecithin-induced demyelination of peripheral afferents results in neuropathic pain behaviors, which are reversible by cannabinoids after nerve remyelination nearly 3 weeks after treatment (Wallace et al., 2003). Our work reveals that the P2X4-LV group is related to improve remyelination and has the potential to reduce the mechanical allodynia induced by sciatic nerve injury (Su et al., 2019). Thus, the accurate relationship of remyelination with neuropathic pain will require further study.

CONCLUSIONS

Peripheral neuropathic pain is a disorder caused by nerve trauma or disease. In this review article, we mainly discuss the role of Schwann cells in the development and relief of neuropathic pain directly induced by nerve injury. In fact, diabetes may induce several types of neuropathies, resulting in spontaneous pain and eventual loss of pain sensation (Mizisin, 2014; Gonçalves et al., 2017). The state of Schwann cells and their communication with axons might be disturbed, ultimately leading to fiber loss and pain. However, the mechanistic understanding of the Schwann cell response to diabetes is unclear. In addition to the importance of glial receptors and mediators, Schwann cell autophagy represents a powerful approach to prevent the onset and chronification of neuropathic pain (Marinelli et al., 2014). Notably, caloric restriction promotes Schwann cell autophagy *via* AMP-activated protein kinase and facilitates remyelination in nerve injury, which provides new evidence for Schwann cell autophagy as a therapeutic approach against neuropathic pain (Coccurello et al., 2018). Overall, accumulating evidence has revealed the key role of Schwann cells in the regulation of neuropathic pain. An improved and extended comprehension of the underlying neurobiological mechanisms of neuropathic pain would allow the development of successful targeted pain therapy.

FUTURE PROSPECTS

Increased mechanistic study of the response of Schwann cells to nerve injury could reveal the underlying molecular mechanisms specific to neuropathic pain. The first pertinent approach would be to expand the recent development of conditional knockin/knockout mouse models to study the specific roles of target genes expressed in Schwann cells following nerve injury. Second, nonmyelinating Remak Schwann cells are characterized by a lack of myelin, but they also characteristically express cell surface receptors and cell adhesion molecules that are downregulated on myelinating Schwann cells. The difference between the two types of Schwann cells is a factor that merits additional study in the future. Third, neuropathic pain can result from different types of nerve injury or disease but has a higher prevalence in females than in males. How sex differences influence neuropathic pain must also be elucidated in future studies. Finally, drug targeting or transplantation of Schwann cells will be of great interest in the search for therapeutic strategies against neuropathic pain.

AUTHOR CONTRIBUTIONS

GC and ZW contributed to the conception and design of the review and wrote the first draft of the manuscript. ZW, GC, WS and YF wrote sections of the manuscript. All authors contributed to manuscript revision, read and approved the submitted version.

FUNDING

This work was supported by the National Key Research and Development Program of China (2017YFA0104704), the National Natural Science Foundation of China (31872773), the Basic Research Program of the Education Department of Jiangsu Province (17KJA180009), the Jiangsu Province Natural Science Foundation of China (BK20181460), and the Postgraduate Research & Practice Innovation Program of Jiangsu Province (KYCX17-1906).

REFERENCES

Austin, P. J., and Moalem-Taylor, G. (2010). The neuro-immune balance in neuropathic pain: involvement of inflammatory immune cells, immune-like glial cells and cytokines. *J. Neuroimmunol.* 229, 26–50. doi: 10.1016/j.jneuroim.2010.08.013

Backonja, M. M. (2003). Defining neuropathic pain. *Anesth. Analg.* 97, 785–790. doi: 10.1213/01.ane.0000062826.70846.8d

Boccella, S., Guida, F., De Logu, F., De Gregorio, D., Mazzitelli, M., Belardo, C., et al. (2019). Ketones and pain: unexplored role of hydroxyl carboxylic acid receptor type 2 in the pathophysiology of neuropathic pain. *FASEB J.* 33, 1062–1073. doi: 10.1096/fj.201801033r

Boivin, A., Pineau, I., Barrette, B., Filali, M., Vallieres, N., Rivest, S., et al. (2007). Toll-like receptor signaling is critical for Wallerian degeneration and functional recovery after peripheral nerve injury. *J. Neurosci.* 27, 12565–12576. doi: 10.1523/JNEUROSCI.3027-07.2007

Burnstock, G. (2006). Purinergic P2 receptors as targets for novel analgesics. *Pharmacol. Ther.* 110, 433–454. doi: 10.1016/j.pharmthera.2005.08.013

Camara, C. C., Araujo, C. V., de Sousa, K. K. O., Brito, G. A. C., Vale, M. L., Raposo, R. D. S., et al. (2015). Gabapentin attenuates neuropathic pain and improves nerve myelination after chronic sciatic constriction in rats. *Neurosci. Lett.* 607, 52–58. doi: 10.1016/j.neulet.2015.09.021

Campana, W. M. (2007). Schwann cells: activated peripheral glia and their role in neuropathic pain. *Brain Behav. Immun.* 21, 522–527. doi: 10.1016/j.bbi.2006.12.008

Campana, W. M., Li, X., Dragojlovic, N., Janes, J., Gaultier, A., and Gonias, S. L. (2006a). The low-density lipoprotein receptor-related protein is a pro-survival receptor in Schwann cells: possible implications in peripheral nerve injury. *J. Neurosci.* 26, 11197–11207. doi: 10.1523/JNEUROSCI.2709-06.2006

Campana, W. M., Li, X., Shubayev, V. I., Angert, M., Cai, K., and Myers, R. R. (2006b). Erythropoietin reduces Schwann cell TNF-α, Wallerian degeneration and pain-related behaviors after peripheral nerve injury. *Eur. J. Neurosci.* 23, 617–626. doi: 10.1111/j.1460-9568.2006.04606.x

Chen, G., Kim, Y. H., Li, H., Luo, H., Liu, D. L., Zhang, Z. J., et al. (2017). PD-L1 inhibits acute and chronic pain by suppressing nociceptive neuron activity via PD-1. *Nat. Neurosci.* 20, 917–926. doi: 10.1038/nn.4571

Chen, G., Luo, X., Qadri, M. Y., Berta, T., and Ji, R. R. (2018). Sex-dependent glial signaling in pathological pain: distinct roles of spinal microglia and astrocytes. *Neurosci. Bull.* 34, 98–108. doi: 10.1007/s12264-017-0145-y

Chen, G., Park, C. K., Xie, R. G., Berta, T., Nedergaard, M., and Ji, R. R. (2014). Connexin-43 induces chemokine release from spinal cord astrocytes to maintain late-phase neuropathic pain in mice. *Brain* 137, 2193–2209. doi: 10.1093/brain/awu140

Chen, S., Velardez, M. O., Warot, X., Yu, Z. X., Miller, S. J., Cros, D., et al. (2006). Neuregulin 1-erbB signaling is necessary for normal myelination and sensory function. *J. Neurosci.* 26, 3079–3086. doi: 10.1523/JNEUROSCI.3785-05.2006

Chen, G., Xie, R. G., Gao, Y. J., Xu, Z. Z., Zhao, L. X., Bang, S., et al. (2016). β-arrestin-2 regulates NMDA receptor function in spinal lamina II neurons and duration of persistent pain. *Nat. Commun.* 7:12531. doi: 10.1038/ncomms12531

Chen, G., Zhang, Z., Wei, Z., Cheng, Q., Li, X., Li, W., et al. (2012). Lysosomal exocytosis in Schwann cells contributes to axon remyelination. *Glia* 60, 295–305. doi: 10.1002/glia.21263

Coccurello, R., Nazio, F., Rossi, C., De Angelis, F., Vacca, V., Giacovazzo, G., et al. (2018). Effects of caloric restriction on neuropathic pain, peripheral nerve degeneration and inflammation in normometabolic and autophagy defective prediabetic Ambra1 mice. *PLoS One* 13:e0208596. doi: 10.1371/journal.pone.0208596

De Logu, F., Nassini, R., Materazzi, S., Carvalho Gonçalves, M., Nosi, D., Rossi Degl'Innocenti, D., et al. (2017). Schwann cell TRPA1 mediates neuroinflammation that sustains macrophage-dependent neuropathic pain in mice. *Nat. Commun.* 8:1887. doi: 10.1038/s41467-017-01739-2

Eid, S. R., Crown, E. D., Moore, E. L., Liang, H. A., Choong, K. C., Dima, S., et al. (2008). HC-030031, a TRPA1 selective antagonist, attenuates inflammatory- and neuropathy-induced mechanical hypersensitivity. *Mol. Pain* 4:48. doi: 10.1186/1744-8069-4-48

Faroni, A., Castelnovo, L. F., Procacci, P., Caffino, L., Fumagalli, F., Melfi, S., et al. (2014a). Deletion of GABA-B receptor in Schwann cells regulates remak bundles and small nociceptive C-fibers. *Glia* 62, 548–565. doi: 10.1002/glia.22625

Faroni, A., Smith, R. J., Procacci, P., Castelnovo, L. F., Puccianti, E., Reid, A. J., et al. (2014b). Purinergic signaling mediated by P2X7 receptors controls myelination in sciatic nerves. *J. Neurosci. Res.* 92, 1259–1269. doi: 10.1002/jnr.23417

Faroni, A., Rothwell, S. W., Grolla, A. A., Terenghi, G., Magnaghi, V., and Verkhratsky, A. (2013). Differentiation of adipose-derived stem cells into Schwann cell phenotype induces expression of P2X receptors that control cell death. *Cell Death Dis.* 4:e743. doi: 10.1038/cddis.2013.268

Franchi, S., Valsecchi, A. E., Borsani, E., Procacci, P., Ferrari, D., Zalfa, C., et al. (2012). Intravenous neural stem cells abolish nociceptive hypersensitivity and trigger nerve regeneration in experimental neuropathy. *Pain* 153, 850–861. doi: 10.1016/j.pain.2012.01.008

Gold, M. S., and Gebhart, G. F. (2010). Nociceptor sensitization in pain pathogenesis. *Nat. Med.* 16, 1248–1257. doi: 10.1038/nm.2235

Gonçalves, N. P., Vægter, C. B., Andersen, H., Østergaard, L., Calcutt, N. A., and Jensen, T. S. (2017). Schwann cell interactions with axons and microvessels in diabetic neuropathy. *Nat. Rev. Neurol.* 13, 135–147. doi: 10.1038/nrneurol.2016.201

Griffin, J. W., and Thompson, W. J. (2008). Biology and pathology of nonmyelinating Schwann cells. *Glia* 56, 1518–1531. doi: 10.1002/glia.20778

Hartlehnert, M., Derksen, A., Hagenacker, T., Kindermann, D., Schäfers, M., Pawlak, M., et al. (2017). Schwann cells promote post-traumatic nerve inflammation and neuropathic pain through MHC class II. *Sci. Rep.* 7:12518. doi: 10.1038/s41598-017-12744-2

Hong, S., Remacle, A. G., Shiryaev, S. A., Choi, W., Hullugundi, S. K., Dolkas, J., et al. (2017). Reciprocal relationship between membrane type 1 matrix metalloproteinase and the algesic peptides of myelin basic protein contributes to chronic neuropathic pain. *Brain Behav. Immun.* 60, 282–292. doi: 10.1016/j.bbi.2016.11.003

Inoue, K. (2006). The function of microglia through purinergic receptors: neuropathic pain and cytokine release. *Pharmacol. Ther.* 109, 210–226. doi: 10.1016/j.pharmthera.2005.07.001

Inoue, M., Rashid, M. H., Fujita, R., Contos, J. J., Chun, J., and Ueda, H. (2004). Initiation of neuropathic pain requires lysophosphatidic acid receptor signaling. *Nat. Med.* 10, 712–718. doi: 10.1038/nm1060

Ishii, I., Fukushima, N., Ye, X., and Chun, J. (2004). Lysophospholipid receptors: signaling and biology. *Annu. Rev. Biochem.* 73, 321–354. doi: 10.1146/annurev.biochem.73.011303.073731

Jasmin, L., Vit, J. P., Bhargava, A., and Ohara, P. T. (2010). Can satellite glial cells be therapeutic targets for pain control? *Neuron Glia Biol.* 6, 63–71. doi: 10.1017/s1740925x10000098

Jessen, K. R., and Arthur-Farraj, P. (2019). Repair Schwann cell update: adaptive reprogramming, EMT, and stemness in regenerating nerves. *Glia* 67, 421–437. doi: 10.1002/glia.23532

Ji, R. R., Berta, T., and Nedergaard, M. (2013). Glia and pain: is chronic pain a gliopathy? *Pain* 154, S10–S28. doi: 10.1016/j.pain.2013.06.022

Ji, R. R., Chamessian, A., and Zhang, Y. Q. (2016). Pain regulation by non-neuronal cells and inflammation. *Science* 354, 572–577. doi: 10.1126/science.aaf8924

Ji, R. R., Kohno, T., Moore, K. A., and Woolf, C. J. (2003). Central sensitization and LTP: do pain and memory share similar mechanisms? *Trends Neurosci.* 26, 696–705. doi: 10.1016/j.tins.2003.09.017

Keswani, S. C., Buldanlioglu, U., Fischer, A., Reed, N., Polley, M., Liang, H., et al. (2004). A novel endogenous erythropoietin mediated pathway prevents axonal degeneration. *Ann. Neurol.* 56, 815–826. doi: 10.1002/ana.20285

Keswani, S. C., Jack, C., Zhou, C., and Höke, A. (2006). Establishment of a rodent model of HIV-associated sensory neuropathy. *J. Neurosci.* 26, 10299–10304. doi: 10.1523/JNEUROSCI.3135-06.2006

Kidd, G. J., Ohno, N., and Trapp, B. D. (2013). Biology of Schwann cells. *Handb. Clin. Neurol.* 115, 55–79. doi: 10.1016/B978-0-444-52902-2.00005-9

Kuan, Y. H., and Shyu, B. C. (2016). Nociceptive transmission and modulation via P2X receptors in central pain syndrome. *Mol. Brain* 9:58. doi: 10.1186/s13041-016-0240-4

Kuner, R. (2010). Central mechanisms of pathological pain. *Nat. Med.* 16, 1258–1266. doi: 10.1038/nm.2231

Lecca, D., Ceruti, S., Fumagalli, M., and Abbracchio, M. P. (2012). Purinergic trophic signalling in glial cells: functional effects and modulation of cell proliferation, differentiation, and death. *Purinergic Signal.* 8, 539–557. doi: 10.1007/s11302-012-9310-y

Lee, H., Lee, S., Cho, I. H., and Lee, S. J. (2013). Toll-like receptors: sensor molecules for detecting damage to the nervous system. *Curr. Protein Pept. Sci.* 14, 33–42. doi: 10.2174/1389203711314010006

Li, X., Gonias, S. L., and Campana, W. M. (2005). Schwann cells express erythropoietin receptor and represent a major target for Epo in peripheral nerve injury. *Glia* 51, 254–265. doi: 10.1002/glia.20202

Liu, H., Shiryaev, S. A., Chernov, A. V., Kim, Y., Shubayev, I., Remacle, A. G., et al. (2012). Immunodominant fragments of myelin basic protein initiate T cell-dependent pain. *J. Neuroinflammation* 9:119. doi: 10.1186/1742-2094-9-119

Magnaghi, V., Ballabio, M., Cavarretta, I. T., Froestl, W., Lambert, J. J., Zucchi, I., et al. (2004). $GABA_B$ receptors in Schwann cells influence proliferation and myelin protein expression. *Eur. J. Neurosci.* 19, 2641–2649. doi: 10.1111/j.0953-816x.2004.03368.x

Magnaghi, V., Ballabio, M., Consoli, A., Lambert, J. J., Roglio, I., and Melcangi, R. C. (2006). GABA receptor-mediated effects in the peripheral nervous system: a cross-interaction with neuroactive steroids. *J. Mol. Neurosci.* 28, 89–102. doi: 10.1385/jmn:28:1:89

Magnaghi, V., Castelnovo, L. F., Faroni, A., Cavalli, E., Caffino, L., Colciago, A., et al. (2014). Nerve regenerative effects of GABA-B ligands in a model of neuropathic pain. *Biomed. Res. Int.* 2014:368678. doi: 10.1155/2014/368678

Mantuano, E., Henry, K., Yamauchi, T., Hiramatsu, N., Yamauchi, K., Orita, S., et al. (2011). The unfolded protein response is a major mechanism by which LRP1 regulates Schwann cell survival after injury. *J. Neurosci.* 31, 13376–13385. doi: 10.1523/JNEUROSCI.2850-11.2011

Marinelli, S., Nazio, F., Tinari, A., Ciarlo, L., D'Amelio, M., Pieroni, L., et al. (2014). Schwann cell autophagy counteracts the onset and chronification of neuropathic pain. *Pain* 155, 93–107. doi: 10.1016/j.pain.2013.09.013

Marinelli, S., Vacca, V., Ricordy, R., Uggenti, C., Tata, A. M., Luvisetto, S., et al. (2012). The analgesic effect on neuropathic pain of retrogradely transported botulinum neurotoxin A involves Schwann cells and astrocytes. *PLoS One* 7:e47977. doi: 10.1371/journal.pone.0047977

Martucci, C., Trovato, A. E., Costa, B., Borsani, E., Franchi, S., Magnaghi, V., et al. (2008). The purinergic antagonist PPADS reduces pain related behaviours and interleukin-1 β, interleukin-6, iNOS and nNOS overproduction in central and peripheral nervous system after peripheral neuropathy in mice. *Pain* 137, 81–95. doi: 10.1016/j.pain.2007.08.017

Mayer, C., Quasthoff, S., and Grafe, P. (1998). Differences in the sensitivity to purinergic stimulation of myelinating and non-myelinating Schwann cells in peripheral human and rat nerve. *Glia* 23, 374–382. doi: 10.1002/(sici)1098-1136(199808)23:4<374::aid-glia9 >3.0.co;2-2

Meyer zu Hörste, G., Heidenreich, H., Lehmann, H. C., Ferrone, S., Hartung, H. P., Wiendl, H., et al. (2010a). Expression of antigen processing and presenting molecules by Schwann cells in inflammatory neuropathies. *Glia* 58, 80–92. doi: 10.1002/glia.20903

Meyer zu Hörste, G., Heidenreich, H., Mausberg, A. K., Lehmann, H. C., ten Asbroek, A. L., Saavedra, J. T., et al. (2010b). Mouse Schwann cells activate MHC class I and II restricted T-cell responses, but require external peptide processing for MHC class II presentation. *Neurobiol. Dis.* 37, 483–490. doi: 10.1016/j.nbd.2009.11.006

Mizisin, A. P. (2014). Mechanisms of diabetic neuropathy: schwann cells. *Handb. Clin. Neurol.* 126, 401–428. doi: 10.1016/B978-0-444-53480-4.00029-1

Neefjes, J., Jongsma, M. L., Paul, P., and Bakke, O. (2011). Towards a systems understanding of MHC class I and MHC class II antigen presentation. *Nat. Rev. Immunol.* 11, 823–836. doi: 10.1038/nri3084

Nicotra, L., Loram, L. C., Watkins, L. R., and Hutchinson, M. R. (2012). Toll-like receptors in chronic pain. *Exp. Neurol.* 234, 316–329. doi: 10.1016/j.expneurol.2011.09.038

Offermanns, S. (2017). Hydroxy-carboxylic acid receptor actions in metabolism. *Trends Endocrinol. Metab.* 28, 227–236. doi: 10.1016/j.tem.2016.11.007

Oh, H. M., and Chung, M. E. (2015). Botulinum toxin for neuropathic pain: a review of the literature. *Toxins* 7, 3127–3154. doi: 10.3390/toxins7083127

Orita, S., Henry, K., Mantuano, E., Yamauchi, K., De Corato, A., Ishikawa, T., et al. (2013). Schwann cell LRP1 regulates remak bundle ultrastructure and axonal interactions to prevent neuropathic pain. *J. Neurosci.* 33, 5590–5602. doi: 10.1523/JNEUROSCI.3342-12.2013

Park, H., and Poo, M. M. (2013). Neurotrophin regulation of neural circuit development and function. *Nat. Rev. Neurosci.* 14, 7–23. doi: 10.1038/nrn3379

Procacci, P., Ballabio, M., Castelnovo, L. F., Mantovani, C., and Magnaghi, V. (2012). GABA-B receptors in the PNS have a role in Schwann cells differentiation? *Front. Cell. Neurosci.* 6:68. doi: 10.3389/fncel.2012.00068

Sacerdote, P., Franchi, S., Trovato, A. E., Valsecchi, A. E., Panerai, A. E., and Colleoni, M. (2008). Transient early expression of TNF-α in sciatic nerve and dorsal root ganglia in a mouse model of painful peripheral neuropathy. *Neurosci. Lett.* 436, 210–213. doi: 10.1016/j.neulet.2008.03.023

Scheib, J., and Höke, A. (2013). Advances in peripheral nerve regeneration. *Nat. Rev. Neurol.* 9, 668–676. doi: 10.1038/nrneurol.2013.227

Scholz, J., and Woolf, C. J. (2007). The neuropathic pain triad: neurons, immune cells and glia. *Nat. Neurosci.* 10, 1361–1368. doi: 10.1038/nn1992

Sorge, R. E., LaCroix-Fralish, M. L., Tuttle, A. H., Sotocinal, S. G., Austin, J. S., Ritchie, J., et al. (2011). Spinal cord Toll-like receptor 4 mediates inflammatory and neuropathic hypersensitivity in male but not female mice. *J. Neurosci.* 31, 15450–15454. doi: 10.1523/JNEUROSCI.3859-11.2011

Story, G. M., Peier, A. M., Reeve, A. J., Eid, S. R., Mosbacher, J., Hricik, T. R., et al. (2003). ANKTM1, a TRP-like channel expressed in nociceptive neurons, is activated by cold temperatures. *Cell* 112, 819–829. doi: 10.1016/s0092-8674(03)00158-2

Su, W. F., Gu, Y., Wei, Z. Y., Shen, Y. T., Jin, Z. H., Yuan, Y., et al. (2016). Rab27a/Slp2-a complex is involved in Schwann cell myelination. *Neural Regen. Res.* 11, 1830–1838. doi: 10.4103/1673-5374.194755

Su, W. F., Wu, F., Jin, Z. H., Gu, Y., Chen, Y. T., Fei, Y., et al. (2019). Overexpression of P2X4 receptor in Schwann cells promotes motor and sensory functional recovery and remyelination via BDNF secretion after nerve injury. *Glia* 67, 78–90. doi: 10.1002/glia.23527

Takahashi, M., Kawaguchi, M., Shimada, K., Konishi, N., Furuya, H., and Nakashima, T. (2004). Cyclooxygenase-2 expression in Schwann cells and macrophages in the sciatic nerve after single spinal nerve injury in rats. *Neurosci. Lett.* 363, 203–206. doi: 10.1016/j.neulet.2004.03.040

Tao, F., Li, Q., Liu, S., Wu, H., Skinner, J., Hurtado, A., et al. (2013). Role of neuregulin-1/ErbB signaling in stem cell therapy for spinal cord injury-induced chronic neuropathic pain. *Stem Cells* 31, 83–91. doi: 10.1002/stem.1258

Toews, A. D., Barrett, C., and Morell, P. (1998). Monocyte chemoattractant protein 1 is responsible for macrophage recruitment following injury to sciatic nerve. *J. Neurosci. Res.* 53, 260–267. doi: 10.1002/(sici)1097-4547(19980715)53:2<260::aid-jnr15 >3.0.co;2-a

Tsuda, M., Shigemoto-Mogami, Y., Koizumi, S., Mizokoshi, A., Kohsaka, S., Salter, M. W., et al. (2003). P2X4 receptors induced in spinal microglia gate tactile allodynia after nerve injury. *Nature* 424, 778–783. doi: 10.1038/nature01786

Tsuda, M., Tozaki-Saitoh, H., and Inoue, K. (2010). Pain and purinergic signaling. *Brain Res. Rev.* 63, 222–232. doi: 10.1016/j.brainresrev.2009.11.003

Ulmann, L., Hatcher, J. P., Hughes, J. P., Chaumont, S., Green, P. J., Conquet, F., et al. (2008). Up-regulation of P2X4 receptors in spinal microglia after peripheral nerve injury mediates BDNF release and neuropathic pain. *J. Neurosci.* 28, 11263–11268. doi: 10.1523/JNEUROSCI.2308-08.2008

Verdiyan, E. E., Allakhverdiev, E. S., and Maksimov, G. V. (2016). Study of the peripheral nerve fibers myelin structure changes during activation of schwann cell acetylcholine receptors. *PLoS One* 11:e0158083. doi: 10.1371/journal.pone.0158083

Wallace, V. C., Cottrell, D. F., Brophy, P. J., and Fleetwood-Walker, S. M. (2003). Focal lysolecithin-induced demyelination of peripheral afferents results in neuropathic pain behavior that is attenuated by cannabinoids. *J. Neurosci.* 23, 3221–3233. doi: 10.1523/JNEUROSCI.23-08-03221.2003

Wang, Z. H., Zeng, X. Y., Han, S. P., Fan, G. X., and Wang, J. Y. (2012). Interleukin-10 of red nucleus plays anti-allodynia effect in neuropathic pain rats with spared nerve injury. *Neurochem. Res.* 37, 1811–1819. doi: 10.1007/s11064-012-0795-0

Weiner, J. A., Fukushima, N., Contos, J. J., Scherer, S. S., and Chun, J. (2001). Regulation of Schwann cell morphology and adhesion by receptor-mediated lysophosphatidic acid signaling. *J. Neurosci.* 21, 7069–7078. doi: 10.1523/JNEUROSCI.21-18-07069.2001

Yajima, Y., Narita, M., Usui, A., Kaneko, C., Miyatake, M., Narita, M., et al. (2005). Direct evidence for the involvement of brain-derived neurotrophic factor in the development of a neuropathic pain-like state in mice. *J. Neurochem.* 93, 584–594. doi: 10.1111/j.1471-4159.2005.03045.x

Zhang, Y. L., Liu, Y. G., Chen, D. J., Yang, B. L., Liu, T. T., Li, J. J., et al. (2018). Microencapsulated Schwann cell transplantation inhibits P2X2/3 receptors overexpression in a sciatic nerve injury rat model with neuropathic pain. *Neurosci. Lett.* 676, 51–57. doi: 10.1016/j.neulet.2018.03.063

Conflict of Interest Statement: The authors declare that the research was conducted in the absence of any commercial or financial relationships that could be construed as a potential conflict of interest.

frontiers in Cellular Neuroscience

ORIGINAL RESEARCH
published: 24 May 2019
doi: 10.3389/fncel.2019.00237

Early Pro-inflammatory Microglia Activation After Inflammation-Sensitized Hypoxic-Ischemic Brain Injury in Neonatal Rats

*Meray Serdar[1], Karina Kempe[1], Mandana Rizazad[1], Josephine Herz[1], Ivo Bendix[1], Ursula Felderhoff-Müser[1] and Hemmen Sabir[1,2,3]**

[1] Department of Pediatrics I, Neonatology and Experimental Perinatal Neuroscience, University Hospital Essen, University Duisburg-Essen, Essen, Germany, [2] Department of General Pediatrics, Neonatology and Pediatric Cardiology, University Children's Hospital Düsseldorf, Medical Faculty, Heinrich Heine University, Düsseldorf, Germany, [3] Department of Neonatology and Pediatric Intensive Care, Children's Hospital, University of Bonn, Bonn, Germany

Background: Perinatal asphyxia, leading to neonatal encephalopathy, is one of the leading causes for child mortality and long-term morbidities. Neonatal encephalopathy rates are significantly increased in newborns with perinatal infection. Therapeutic hypothermia is only neuroprotective in 50% of cooled asphyxiated newborns. As shown experimentally, cooling has failed to be neuroprotective after inflammation-sensitized hypoxic ischemic (HI) brain injury. Microglia are thought to be key players after inflammation-sensitized HI brain injury. We performed this study investigating early microglia phenotype polarization in our newborn animal model of inflammation-sensitized HI brain injury, better understanding the underlying pathophysiological processes.

Methods: Seven days old Wistar rat pups were injected with either vehicle (NaCl 0.9%) or E. coli lipopolysaccharide (LPS), followed by left carotid ligation combined with global hypoxia inducing a mild unilateral hypoxic-ischemic injury. Pups were randomized to (1) Sham group (n = 41), (2) LPS only group (n = 37), (3) Veh/HI group (n = 56), and (4) LPS/HI group (n = 79). On postnatal days 8 and 14 gene-expression analysis or immunohistochemistry was performed describing early microglia polarization in our model.

Results: We confirmed that LPS pre-sensitization significantly increases brain area loss and induced microglia activation and neuronal injury after mild hypoxia-ischemia. Additionally, we show that microglia upregulate pro-inflammatory genes involving *NLRP-3* inflammasome gene expression 24 h after inflammation-sensitized hypoxic-ischemic brain injury.

Conclusion: These results demonstrate that microglia are early key mediators of the inflammatory response following inflammation-sensitized HI brain injury and that they polarize into a predominant pro-inflammatory phenotype 24 h post HI. This may lead to new treatment options altering microglia phenotype polarization early after HI brain injury.

Keywords: newborn, HIE, brain, infection, inflammation, microglia

OPEN ACCESS

Edited by:
Stefania Ceruti, University of Milan, Italy

Reviewed by:
Catherine Gorrie, University of Technology Sydney, Australia
Marianne Thoresen, University of Oslo, Norway

***Correspondence:**
Hemmen Sabir
hemmen.sabir@uk-essen.de

Specialty section:
This article was submitted to Non-Neuronal Cells, a section of the journal Frontiers in Cellular Neuroscience

Received: *26 February 2019*
Accepted: *09 May 2019*
Published: *24 May 2019*

Citation:
Serdar M, Kempe K, Rizazad M, Herz J, Bendix I, Felderhoff-Müser U and Sabir H (2019) Early Pro-inflammatory Microglia Activation After Inflammation-Sensitized Hypoxic-Ischemic Brain Injury in Neonatal Rats. Front. Cell. Neurosci. 13:237. doi: 10.3389/fncel.2019.00237

INTRODUCTION

Perinatal asphyxia is one of the leading causes of neonatal mortality and long-term mental and motor disabilities, including cerebral palsy (Jacobs et al., 2013). Between 2 and 4 of 1000 term newborns in the western world suffer from birth asphyxia, whereas globally the incidence is described to be much higher (Jacobs et al., 2013; United Nations Report, 2015). Perinatal asphyxia may lead to neonatal encephalopathy (NE), most likely due to hypoxia-ischemia (HI). Currently therapeutic hypothermia (TH) is the standard treatment for hypoxic-ischemic encephalopathy (HIE), however, only 50% of cooled asphyxiated newborns benefit from cooling treatment (Jacobs et al., 2013). Early identification of "non-responders" to cooling therapy is not feasible yet, as specific and robust biomarkers are lacking and early identification of non-responders is yet not possible. In low- and middle-income countries, where NE rates are significantly higher, the introduction of TH was unsuccessful, increasing mortality (Robertson et al., 2011). Perinatal infection is a well-recognized risk factor for cerebral palsy, long-term disability and mortality in term newborns (Grether and Nelson, 1997). Recently, it has been shown that neonatal infection rates in asphyxiated newborns are significantly higher, compared to the general population (Tann et al., 2017). Whether TH is neuroprotective in these newborns remains unknown. We have previously shown that TH is not neuroprotective in our established animal model of inflammation-sensitized hypoxic-ischemic brain injury (Osredkar et al., 2013, 2015). However, the underlying mechanisms remained unclear.

Microglia, the tissue-resident macrophages of the central nervous system (CNS), are responsible for combating infection, clearing cellular debris, and maintaining tissue homeostasis (Pierre et al., 2017; Lenz and Nelson, 2018). Within minutes following an injurious insult, such as hypoxia, ischemia, infection and trauma, microglia become activated, changing their gene expression profile (Ohsawa and Kohsaka, 2011; Lenz and Nelson, 2018). We have previously shown that microglia cells are significantly upregulated in our inflammation-sensitized model of HI brain injury (Osredkar et al., 2015; Falck et al., 2018). However, we have not further investigated microglial polarization yet. Activated microglia are capable to polarize into different phenotypic categories (Lenz and Nelson, 2018). The M1 microglia, or classical activated microglia phenotype is associated with an increased production of pro-inflammatory cytokines and chemokines (Chhor et al., 2013; Cunha et al., 2016). The alternative anti-inflammatory M2 phenotype is less aggressive to the neuronal tissue, promoting tissue repair, phagocytosis of protein aggregates and cell debris (Wang et al., 2014).

The *nucleotide-binding domain, leucine-rich repeat protein (NLRP)-3* inflammasome is highly involved in neonatal brain injury either due to LPS or hypoxia-ischemia (Hedtjarn et al., 2002; Gustin et al., 2015). Regarding our inflammation-sensitized HI model, no data are available on *NLRP3* activity yet. *NLRP3* is responsible for the cleavage of *interleukin IL-18* and *IL-1beta* from its preforms. As shown the vulnerability of the neonatal brain to LPS or hypoxia-ischemia is *IL-18* and *IL-1beta* dependent predominantly leading to microglia activation (Gustin et al., 2015).

The mechanisms responsible for microglia phenotype regulation in the newborn CNS are poorly understood. The interaction of M1/M2 microglia does not seem to follow strict differentiation, but to be a complex time dependent continuum, which may be altered due to its actual needs (Wang et al., 2014; Mallard et al., 2018). Following neonatal HI brain injury, it has been shown that M1/M2 specific genes are upregulated in a time dependent manner, with early M1 response and delayed M2 response possibly regulating the pro-inflammatory, neurotoxic cascade (Hellstrom Erkenstam et al., 2016). Furthermore, it has been successfully shown that shifting the microglia phenotype toward an M2 phenotype, using TH, is neuroprotective in an adult traumatic brain injury animal model (Truettner et al., 2016). In our neonatal model of inflammation-sensitized HI the time dependent microglial phenotype expression pattern has yet not been investigated. As TH is not neuroprotective in our experimental setup, understanding microglia phenotype polarization might help to develop new additional treatment options. Therefore, we examined early M1/M2 marker gene expression in different brain regions (hippocampus and cortex) and in *ex vivo* isolated microglia cells in our newborn animal model of inflammation-sensitized HI brain injury.

MATERIALS AND METHODS

Animals and Experimental Procedure

All animal experiments were performed in accordance to the Animal Research: Reporting of *in vivo* Experiments (ARRIVE) guidelines with government approval by the State Agency for Nature, Environment and Consumer Protection North Rhine-Westphalia, Germany. We used 7-day old (P7) Wistar rat pups of both genders in all our experiments. All pups were kept at the central animal laboratory of the University Hospital Essen, Germany with a 12:12 h dark:light cycle at an environmental temperature of 21°C with food and water *ad libitum*. As previously described, all animals were randomized across litter, sex, and weight before the experiments commenced and all following experiments and analysis were performed by observers blinded to the different treatments (Osredkar et al., 2013, 2015).

A total of 223 P7 rat pups (n = 108 female; n = 115 male) from 21 litters were used in this study. Temperature during handling and experimental procedures was monitored in "sentinel" rat pups (n = 10) not further allocated to the different treatment groups. All rat pups were kept on a servo-controlled mat (CritiCool, MTRE, Yavne, Israel) during separation from their dams, controlled by the sentinel pup via a rectal temperature probe (IT-21, Physitemp Instruments, Clifton, NJ, United States), continuously maintaining nesting temperature of P7 rat pups (Wood et al., 2016) or treatment temperatures during experiments (see below). Forty-one rats underwent sham surgery (Sham group) and 37 rats received a single i.p. injection of lipopolysaccharide (LPS) solution (*Escherichia coli* O55:B5, Sigma; 0.1 mg/kg) followed by sham

surgery (LPS group). The remaining animals (n = 135) were exposed to our inflammation-sensitized model of hypoxic-ischemic brain injury as previously described (Osredkar et al., 2013, 2015). In brief, at the start of every experiment, animals were injected according to randomization with either a single intraperitoneal (i.p.) injection of vehicle solution (0.9% NaCl; Veh/HI group, n = 56) or LPS solution (Escherichia coli O55:B5, Sigma; 0.1 mg/kg; LPS/HI group, n = 79). After a 4 h delay, whilst animals were kept with their dams, animals were exposed to HI as described. Under general isoflurane anesthesia, the left common carotid artery was ligated and cut. Within 3 h the pups were subjected to 8% O_2 for 50 min at a rectal temperature (T_{rectal}) of 36°C, resulting in mild HI injury (Osredkar et al., 2013, 2015). Immediately after the HI insult, pups were kept at T_{rectal} of 37.0°C for 5 h, representing the normothermia treatment group in our previous experiments (Sabir et al., 2012; Osredkar et al., 2013, 2015). After the treatment period, pups were immediately returned to their dam.

For histological analysis and determination of brain area loss pups were sacrificed at P14. Rats were transcardially perfused with phosphate-buffered saline (PBS) followed by 4% paraformaldehyde (Sigma-Aldrich). Brains were post-fixed in 4% paraformaldehyde overnight at 4°C and embedded in paraffin. For mRNA and microglia analyses pups were transcardially perfused with PBS. For mRNA analysis, different brain regions (hippocampus and cortex) were prepared, using a standard matrix for uniformity (ASI instruments Inc., Warren, MI, United States) and immediately snap-frozen in liquid nitrogen.

Area Measurement

In total 52 rat pups were used for area loss analysis [n = 13 in group (1), n = 10 in group (2), n = 17 in group (3), n = 12 in group (4)]. The embedded brains were cut in 10 μm coronal sections. Sections were stained with cresyl-violet. Brain area loss was determined by measurement of intact areas in ipsilateral and contralateral hemispheres of two sections, from two neighboring blocks (−3.72 ± 0.7 mm from Bregma) at a distance of 50 μm using ImageJ software (ImageJ, version 1.46r, National Institutes of Health, Bethesda, MD, United States). Tissue loss was determined by comparison with contralateral areas according to the following equation: 1- (area ratio (left vs. right)) × 100 (Sabir et al., 2012) and mean values of the two analyzed sections were calculated.

Immunohistochemistry

Immunohistochemistry was performed as previously described (Serdar et al., 2016). After deparaffinization, 10 μm coronal sections (−3.72 ± 0.7 mm from Bregma) were rehydrated. Antigen retrieval was performed in a pre-heated 10 mM sodium-citrate buffer (pH 6.0) for 30 min. After blocking with 1% bovine serum albumin and 0.3% cold fish skin gelatine in 0.1% Tween-20 TBS (all Sigma–Aldrich, Germany), slides were incubated with primary antibodies overnight at 4°C followed by appropriate secondary antibody incubation for 1h at room temperature. Sections were counterstained with 4,6-diamidino-2-phenylindole (DAPI) (1 μg/ml, Invitrogen, Germany). Microglia activation was detected by Iba1 (1:1000, rabbit polyclonal anti-Iba1, Wako, Germany) staining on sections of P14 rat pups. At the same time point neurons were evaluated using the marker NeuN (1:200, polyclonal rabbit anti-NeuN, Millipore, Germany). Two regions of interest (ROI, each 45,500 μm^2) in the hippocampus (CA1 and CA2 region) and cortex of contra- and ipsilateral brain hemispheres were visualized by fluorescence microscopy (Axioplan; Zeiss, Germany) connected to a CCD camera (Axioplan, Zeiss, Germany). The area of positive staining of the ipsilateral side was determined by using Image J software and was normalized to the contralateral side (Reinboth et al., 2016). There were no differences in staining of the contralateral side.

Magnetic Activated Cell Sorting (MACS) of CD11 b/c Positive Microglia

To analyze the different alterations in phenotype polarization of microglia, we specifically isolated CD11 b/c positive microglia *ex vivo* from rat brains 24 h after hypoxia. In total 32 rat pups were used [n = 8 in group (1), n = 8 in group (2), n = 8 in group (3), n = 8 in group (4)]. At first, pups were perfused with PBS. In groups (1) and (2) full brains (ipsi-/contralateral hemispheres) were used for analysis, while in group (3) and (4) ipsilateral hemispheres were pooled to get a workable concentration of microglia. A Neural tissue dissociation kit (Miltenyi Biotech) was used for mechanical and enzymatic dissociation of brain tissues. Myelin-removal was performed following distributors instructions before MACS. For MACS the obtained cell mixtures were washed with MACS buffer (PBS containing 0.5% BSA) and incubated with anti-CD11b/c coupled microbeads (Miltenyi Biotech) followed by magnetic separation on MS columns of the MiniMACS magnetic separation kit (Miltenyi Biotech, Germany). The cell mixture was then passed through the column placed in MiniMACS magnets followed by a series of three washes (500 μl each). The total effluent was collected as the negative fraction. After removal of the column CD11 b/c positive microglia were eluted in a volume of 1 ml MACS buffer. To investigate the purity of the magnetically separated cells, the positive eluate was analyzed via immunocytochemistry through Iba1 staining (data not shown).

Real-Time PCR

RNA was generated from ipsilateral regions through the classic phase extraction method, using TRIzol and Chloroform. First strand complementary DNA was synthesized using 1 or 4 μg of total RNA and TaqMan reverse transcription reagents (Applied Biosystems/Thermo Fisher Scientific, United States). PCR amplification was performed in 96 well optical reaction plates for 40 cycles with each cycle at 94°C for 15 s and 60°C for 1 min using the StepOnePlus Real Time PCR system (Applied Biosystems/Thermo Fisher Scientific, United States). Analysis was performed 24 h post HI using the hippocampus and cortex of the ipsilateral hemispheres in our 4 pre-defined groups [n = 7 in group (1), n = 7 in group (2), n = 12 in group (3), n = 12 in group (4)]. The PCR products of pro- and anti-inflammatory cytokines,

associated with classical or alternative microglial activation, were quantified by fluorogenic reporter oligonucleotide probes. Pro-inflammatory markers used in this study are: *Interleukin IL-1beta* (Rn00580432_m1; life technologies, Germany), *IL-6* (Rn01410330_m1; Life Technologies, Germany), *inducible nitric oxide synthase (iNOS)* (Rn00561646_m1; Life Technologies, Germany) and *IL12* (Rn00584538_m1; Life Technologies, Germany). Anti-inflammatory markers used in this study are *transforming growth factor (TGF)-beta* (Rn00572010_m1; Life Technologies, Germany), *Arginase-1* (Rn00691090_m1; Life Technologies, Germany) and *cluster of differentiation (CD)-206* (Rn01487342_m1; Life Technologies, Germany). Additionally, we analyzed gene expression of the inflammasome *cryopyrin (Nlrp3)* (Rn04244620_m1; Life Technologies, Germany). *Beta-2-microtubulin (B2M)* was used as housekeeping gene (Rn00560865_m1; Life Technologies, Germany). Results were normalized to the ipsilateral hemispheres of the sham group.

To further analyze microglia polarization in this model, the same pro- and anti-inflammatory marker gene expression was analyzed in the previous described CD11 b/c positive microglia cells.

Generally, RealTime PCR and detection were performed in duplicates; measurements were repeated two times for each sample. Target gene expression was quantified according to the $2^{\Delta\Delta CT}$ method (Livak and Schmittgen, 2001).

Statistical Analysis

Graphical data are presented as median values with 95% confidence intervals or boxplots including the 25% and the 75% percentile. Data were analyzed using GraphPad Prism 6 (GraphPad Software, United States). Non-parametric statistics were applied. The Kruskal–Wallis test was used for comparisons across multiple treatment groups, and the Bonferroni *post hoc* test was used for 2-group comparisons. *p*-values less than 0.05 were considered as statistically significant.

RESULTS

In total 10 experiments were performed using a 4-group design: (1) Sham group, (2) LPS group, (3) Veh/HI group and (4) LPS/HI group. Out of the 213 animals used in our 4-group design, mortality was highest in the LPS/HI group. In total 40 animals died during HI [three animals from group (2), two animals from group (3), 35 animals from group (4)], leaving 173 rat pups for further analysis. The high mortality in the LPS/HI group has been expected and reported by us before (Osredkar et al., 2013, 2015) and we accounted this during group randomization.

LPS Pre-sensitization Increases Brain Area Loss and Induces Microglia Activation and Neuronal Injury After Mild Hypoxia-Ischemia

As shown in **Figure 1**, pre-sensitization with LPS 4 h prior to a mild HI insult, increases brain area loss compared to a mild HI insult alone at P14. Median area loss was 1.1% (0.5 – 2.3) in group (1), 0.5% (0 – 2.2) in group (2), 5.9% (1.4 – 10.5) in group (3) and 19.3% (7.5 – 31.2) in group (4), respectively. The low area loss in group (3) indicates the mild nature of our hypoxic-ischemic insult, following 50 min of hypoxia at T_{rectal} of 36°C. This mild insult was intended, as LPS pre-sensitization combined with a moderate to severe insult would result in almost 100% mortality in the LPS/HI group, as previously shown by ourselves and others before (Eklind et al., 2001; Osredkar et al., 2013, 2015).

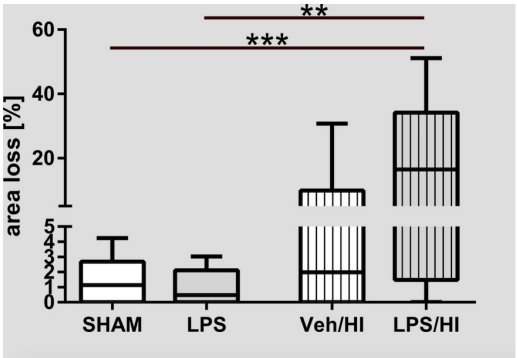

FIGURE 1 | Brain area loss 1 week after inflammation-sensitized hypoxic-ischemic brain injury. We found increased brain area loss of ipsilateral brain hemispheres in the LPS/HI group compared to the other treatment groups. In the Veh/HI group injury was mild, representing the mild character of our hypoxic-ischemic insult. Group sizes: Sham $n = 13$, LPS $n = 10$, Veh/HI $n = 17$, LPS/HI $n = 12$; $^{**}p < 0.01$, $^{***}p < 0.001$.

Immunohistochemistry showed that Iba1 staining was significantly increased in the hippocampus and cortex of animals from the LPS/HI group compared to the sham (hippocampus: $p = 0.0012$; cortex: $p = 0.0390$) and LPS group (hippocampus: $p = 0.0103$) (**Figures 2A,B**). In addition, we found that neuronal density was significantly decreased in the hippocampus and cortex of animals from the LPS/HI group compared to the sham (hippocampus: $p = 0.0086$; cortex: $p = 0.0068$) and LPS group (cortex: $p = 0.0373$) (**Figures 2C,D**). These findings demonstrate that pre-sensitization with a non-injurious dose of LPS significantly increases brain damage in a mild HI brain injury model and underlie the important role of microglia in our established inflammation-sensitized hypoxic-ischemic brain injury model, leading to further analyses.

Early Pro-inflammatory Gene Expression Following Inflammation-Sensitized Hypoxic-Ischemic Brain Injury

To further determine early inflammatory responses in our model, we assessed gene expression profiles associated with M1/M2 microglial polarization in total brain lysates of the hippocampus and the cortex. We determined a significantly upregulated gene expression of pro-inflammatory molecules, e.g., *iNOS* ($p = 0.0483$), *IL-1beta* ($p = 0.049$), and *IL-6* ($p = 0.0492$) in the hippocampus of the LPS/HI group compared to sham controls (**Figure 3A**). Animals from the Veh/HI group only presented with mild upregulation of pro-inflammatory genes [*IL-6* in hippocampus ($p = 0.0024$,

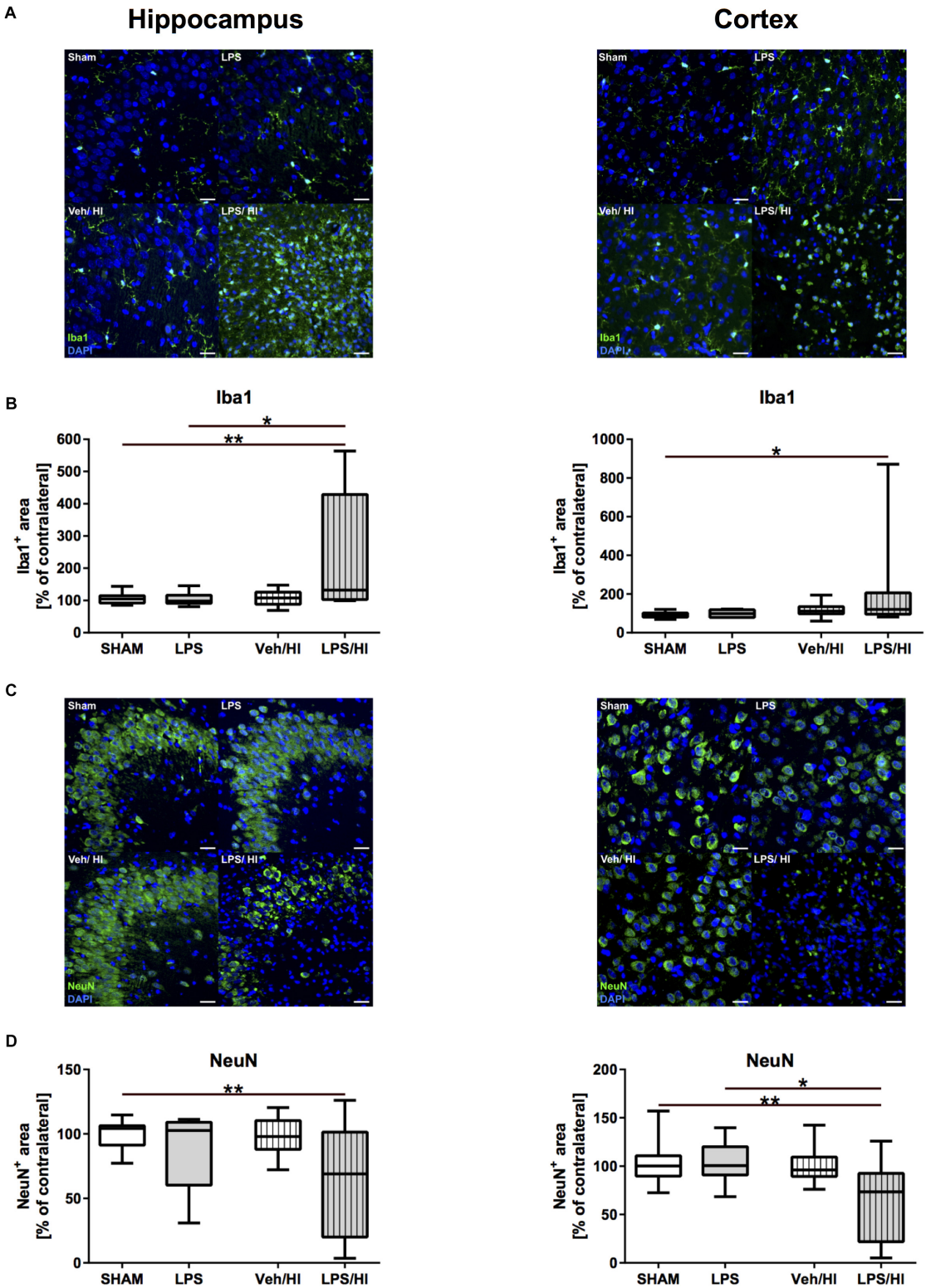

FIGURE 2 | Microglia and neuronal density 1 week after inflammation-sensitized hypoxic-ischemic brain injury. **(A)** Representative Iba1 staining images from the hippocampus and cortex. **(B)** There was a significantly increased Iba 1 staining in the hippocampus and cortex of rat pups of the LPS/HI group compared to the sham (hippocampus and cortex) and LPS group (cortex). **(C)** Representative NeuN staining images of the hippocampus and cortex. **(D)** Neuronal staining was significantly reduced in the hippocampus and cortex of the LPS/HI group compared to sham-operated rats (hippocampus and cortex) and LPS-treated animals (cortex). Group sizes: Sham $n = 13$, LPS $n = 9$, Veh/HI $n = 17$, LPS/HI $n = 12$; $^{*}p < 0.05$, $^{**}p < 0.01$.

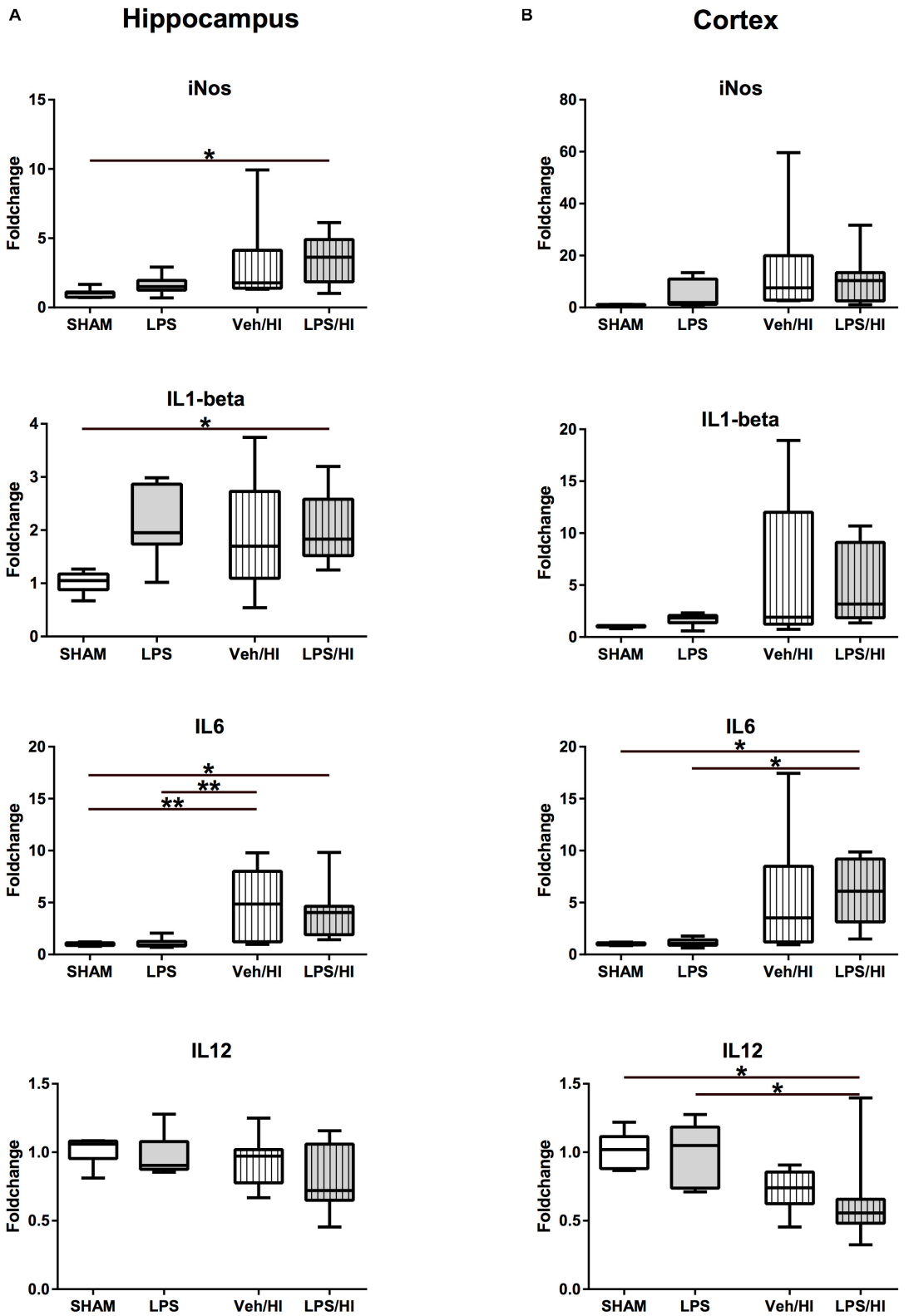

FIGURE 3 | Pro-inflammatory cytokine expression 24 h after inflammation-sensitized hypoxic-ischemic brain injury. **(A)** In the hippocampus pro-inflammatory genes of *iNOS, IL-1beta* and *IL-6* were significantly upregulated in animals pre-sensitized with LPS undergoing a mild HI injury. **(B)** In the cortex, *IL-6* was significantly upregulated, whilst *IL-12* was downregulated after inflammation-sensitized hypoxic-ischemic brain injury. Group sizes: Sham $n = 7$, LPS $n = 7$, Veh/HI $n = 12$, LPS/HI $n = 12$; $^{*}p < 0.05$, $^{**}p < 0.01$.

Figure 3A)], mainly due to the aimed mild injury in this group. Additionally, *IL-6* was significantly upregulated ($p = 0.0191$), while *IL-12* was significantly downregulated ($p = 0.0490$) (**Figure 3B**) in the cortex of animals from the LPS/HI group.

Besides a significant increase in *TGF-beta* expression in the cortex of the VEH/HI and LPS/HI group compared to the Sham and LPS group ($p < 0.05$, **Figure 4B**), M2 associated anti-inflammatory gene expression was not significantly modulated by the different treatments at the analyzed time point (**Figure 4**).

Overall, these results show an early significant M1 associated pro-inflammatory gene expression in the hippocampus and cortex predominately in rats of the LPS/HI group compared to the Sham- and LPS/Veh group.

Microglia Reveal Early Pro-inflammatory Gene Expression Following Inflammation-Sensitized Hypoxic-Ischemic Brain Injury

After we found that pro-inflammatory gene expression was upregulated in total brain lysates of the LPS/HI group, we specifically wanted to analyze the role of CD11b/c microglia, as microglia are supposed to be a major source of pro-inflammatory gene expression (Hellstrom Erkenstam et al., 2016). Therefore, we sorted CD11b/c positive microglia via magnetic activated cell sorting 24 h post HI. Similarly, as in total brain lysates, we observed a significant increase in M1 associated pro-inflammatory gene expression for *iNOS* ($p < 0.0001$) and *IL-1beta* ($p = 0.0029$) in microglia of the LPS/HI group compared to the LPS and Sham group (**Figure 5**). *iNOS* was also significantly upregulated in the Veh/HI group, compared to the sham group ($p = 0.0015$). In addition, a significant upregulation of *CD206* ($p = 0.031$) was detected in microglia of the LPS/HI group, compared to the LPS group (**Figure 5**).

These results underlie the role of pro-inflammatory M1 microglia polarization in animals pre-sensitized with LPS prior to hypoxia-ischemia, compared to animals from the Veh/HI and other groups in this specific combined animal model.

NLRP3 Inflammasome Activation After Inflammation-Sensitized Hypoxic-Ischemic Brain Injury

As *NLRP3* is responsible for the cleavage of *interleukin IL-18* and *IL-1beta* from its preforms, leading to microglia activation, we last analyzed *NLRP3* gene expression in our model. We found that 24 h post HI, *NLRP3* gene expression is significantly upregulated in the hippocampus ($p = 0.0060$) and cortex ($p = 0.0081$) of rats from the LPS/HI group compared to the Sham group (**Figure 6**).

DISCUSSION

The present study confirms that pre-exposure with a non-injurious dose of LPS followed by mild hypoxic-ischemic brain injury exacerbates brain injury in 7 days old rats. The mechanism is not fully understood. We now show that microglia gene expression is polarized into a M1, pro-inflammatory phenotype 24 h following inflammation-sensitized hypoxic-ischemic brain injury. Additionally, we highlight the involvement of the *NLRP3* inflammasome in the inflammatory process, probably activating *IL-1beta* in rats pre-exposed with LPS and undergoing our HI brain injury model. These results demonstrate that microglia are early key mediators of the inflammatory response following inflammation-sensitized HI brain injury, polarizing into a predominant pro-inflammatory (M1) phenotype 24 h post HI.

We have previously described the combined animal model of inflammation and HI brain injury by modification of the classical Rice-Vannucci rat model of HI brain injury followed by post-insult normothermia or hypothermia (Osredkar et al., 2013, 2015; Falck et al., 2018). The Rice-Vannucci HI rat model has been used for over three decades to describe and assess newborn brain injury, leading to translational clinical trials and the establishment of therapeutic hypothermia (TH) to reduce mortality and morbidities following perinatal asphyxia (Rice et al., 1981). However, clinically ∼50% of all cooled newborns from these large randomized controlled trials did not benefit from cooling therapy (Jacobs et al., 2013). Early identification of these non-responders is yet not possible.

Recently, it has been shown that neonatal infection rates in asphyxiated newborns are much higher, compared to the general population and that perinatal infection contributes to perinatal asphyxia (Tann et al., 2016, 2017). Whether TH is neuroprotective in these newborns remains unknown. A single-center study reported that TH was not neuroprotective in asphyxiated newborns with proven bacterial chorioamnionitis, despite antibiotic treatment (Wintermark et al., 2010). Recently, a retrospective analysis from the Netherlands and Belgium reported that outcome in newborns with perinatal asphyxia and proven culture-positive sepsis did not significantly differ from outcome of infants with perinatal asphyxia without sepsis (Hakobyan et al., 2018). However, the number of infants with culture-positive sepsis involved in both studies was very low.

We have previously shown that TH is not beneficial in our animal model of inflammation-sensitized HI brain injury and that microglia cells are activated in our injury model (positive Iba1 staining) (Osredkar et al., 2013, 2015). Before new treatment interventions can be explored and tested, we need to understand the underlying pathophysiology, leading to the failure of the established neuroprotective treatment (therapeutic hypothermia). In the current study, we aimed to specifically investigate the underlying early pathophysiological processes in our model of LPS-sensitized HI brain injury, focusing on the early polarization of microglia and to describe their role in sensitizing the brain to a higher degree of injury.

M1 microglia produce a large number of pro-inflammatory cytokines (e.g., *IL-6, IL-1beta, IL-12*), chemokines, reactive oxygen species and *iNOS* (Cunha et al., 2016; Hellstrom Erkenstam et al., 2016). These could potentially be used as early reliable biomarkers after HI or LPS exposition, discriminating between HI or infection-sensitized HI. Activated microglia have been found in the gray and white matter following HI. However, this has so far not been analyzed in a combined neonatal model of inflammation and hypoxia-ischemia. We show here

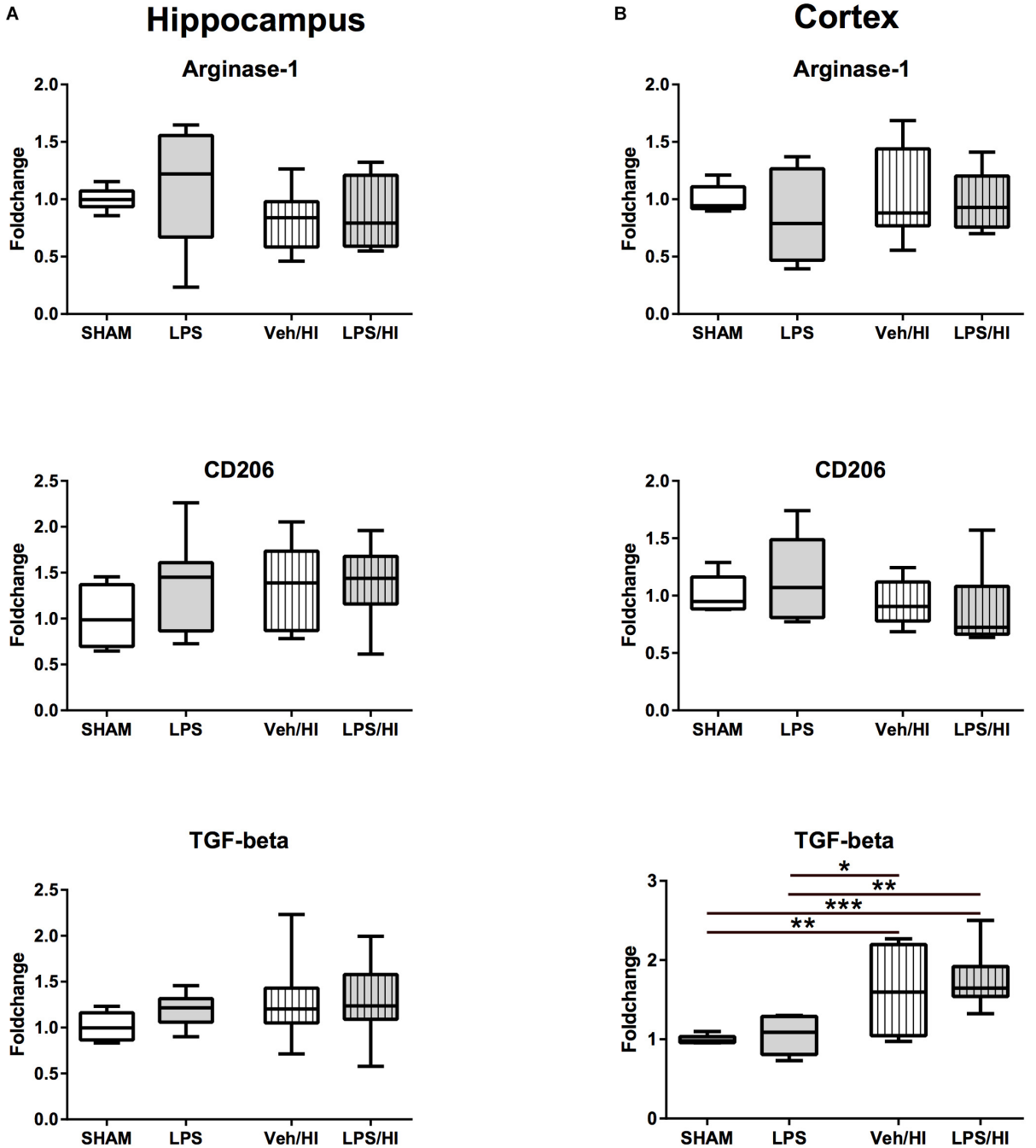

FIGURE 4 | Anti-inflammatory cytokine expression 24 h after inflammation-sensitized hypoxic-ischemic brain injury. **(A)** There was no significant difference for the further analyzed cytokines in the hippocampus 24 h after our experiments. **(B)** There was a significant upregulation of *TGF-beta* in the cortex of animals from the Veh/HI and LPS/HI groups compared to the Sham and LPS groups. Group sizes: Sham $n = 7$, LPS $n = 7$, Veh/HI $n = 12$, LPS/HI $n = 12$; $^{*}p < 0.05$, $^{**}p < 0.01$, $^{***}p < 0.001$.

that rats sensitized with LPS prior to HI brain injury reveal most pronounced changes/increases in the amount of activated microglia, assessed by total Iba-1 expression in the hippocampus and cortex following LPS/HI. This was accompanied by a significantly increased expression of pro-inflammatory cytokines and *iNOS*.

As the determined increased pro-inflammatory gene expression might also be due to reactive astrogliosis, we specifically sorted microglia cells, proving their specific role in our model. We confirmed that microglia associated genes are significantly upregulated in rats following LPS pre-exposure before HI brain injury compared to the other treatment groups

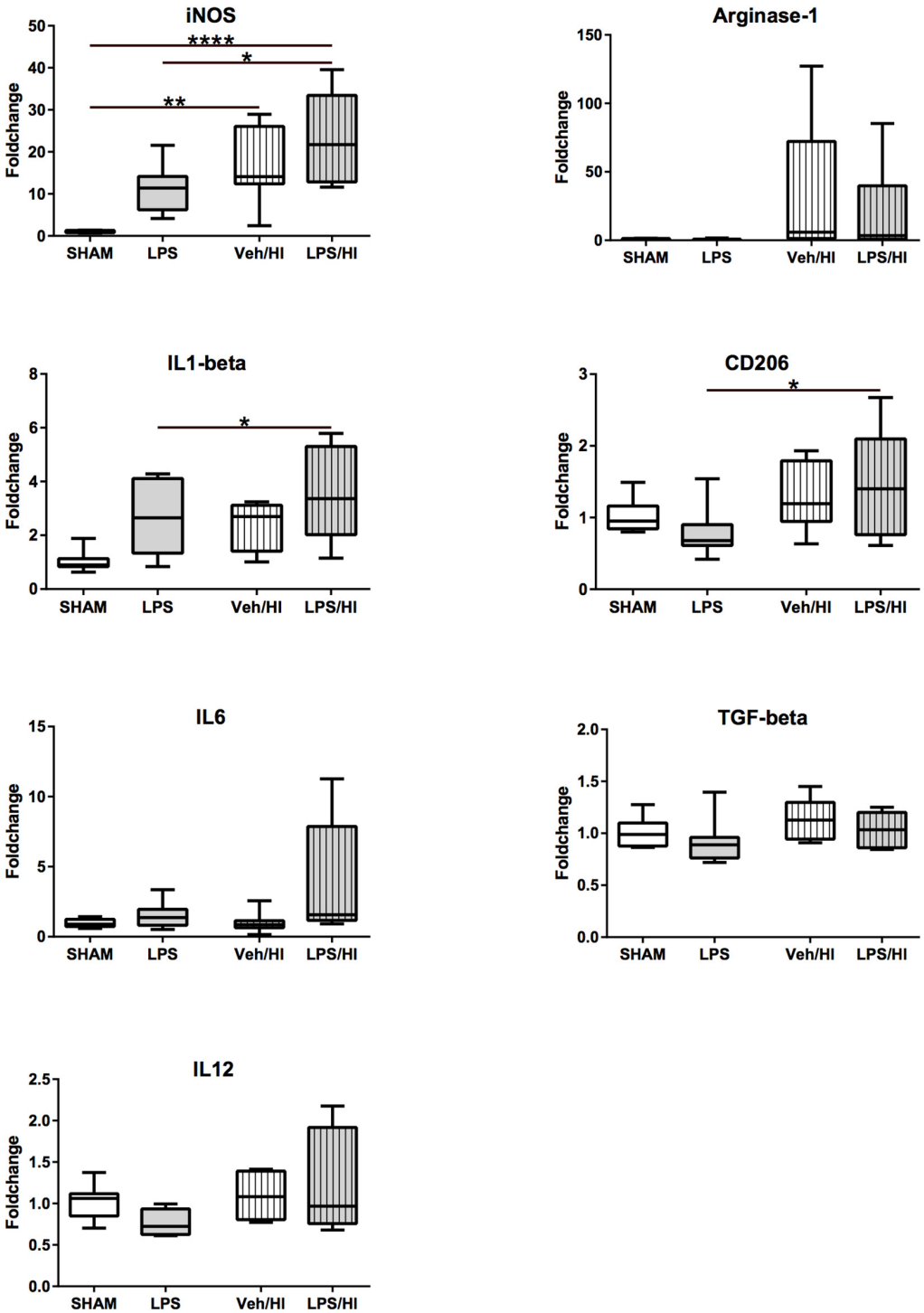

FIGURE 5 | Gene-expression of CD11b/c microglia 24 h after inflammation-sensitized hypoxic-ischemic brain injury. Gene expression of pro-inflammatory genes for *iNOS* and *IL-1beta* was significantly upregulated in microglia from the LPS/HI group compared to Sham. Additionally, gene expression of the anti-inflammatory gene for *CD206* was significantly upregulated in microglia from the LPS/HI group. Group sizes: Sham $n = 8$, LPS $n = 8$, Veh/HI $n = 8$, LPS/HI $n = 8$; $^{*}p < 0.05$, $^{**}p < 0.01$, $^{****}p < 0.0001$.

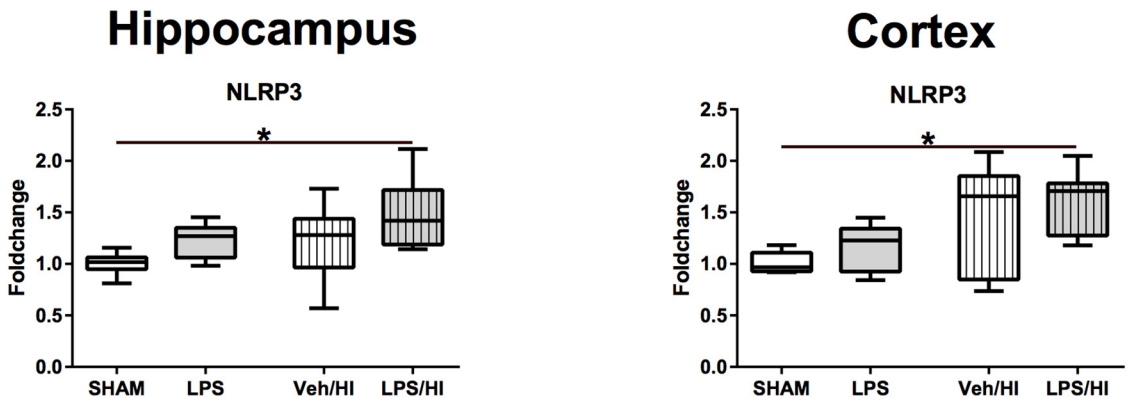

FIGURE 6 | Gene expression of *NLRP3* 24 h after inflammation-sensitized hypoxic-ischemic brain injury. Gene expression of *NLRP3* was highest in the LPS/HI group in both analyzed brain regions and significantly increased compared to the Sham group in the hippocampus and cortex. Group sizes: Sham $n = 7$, LPS $n = 7$, Veh/HI $n = 12$, LPS/HI $n = 12$; $^*p < 0.05$.

and that microglia early polarize into a pro-inflammatory phenotype, leading to brain injury and neuronal loss at P14. As previously described, the interaction of M1/M2 microglia is a time dependent process (Hellstrom Erkenstam et al., 2016), which may be altered due to its actual needs, potentially leading to novel treatment options. This has successfully been shown in an experimental adult traumatic brain injury model, where M1/M2 phenotype polarization could be externally altered by cooling therapy, stimulating the polarization into the anti-inflammatory M2 phenotype resulting in neuroprotection (Truettner et al., 2016). As we have only analyzed one specific time point yet, further analyzing different time points is crucial. This will help us to describe the time-dependent shift of the M1 microglia, into the anti-inflammatory M2 microglia in our specific injury model. Most importantly, we have to identify the regulators of the presumed M1/M2 activation in our model. Despite hypoxia-ischemia, LPS exposure to the neonatal brain directly activates microglia (Mallard et al., 2018). Toll-like receptors (TLRs) are tightly linked to the innate immune response in microglia (Nair-Gupta et al., 2014). Microglia express a large repertoire of TLRs, allowing them to react to different pathogens. LPS primarily binds to TLR-4 (Feezor et al., 2003). Stimulation of TLR-4 triggers the translocation of *nuclear factor kappa B (NF-kappaB)* into the nucleus, expressing proinflammatory genes in microglia, involving the activation of the inflammasome (O'Callaghan et al., 2014; Cunha et al., 2016). The inflammasome is a *caspase-1* activating multiprotein that results from oligomerization of inactive monomeric proteins from the *NLRP* family. The most intensively studied inflammasome is *NLRP3*. *NLRP3* has been shown to be involved in many neurological diseases in adults, such as multiple sclerosis, Alzheimer's and Parkinson's disease (Strowig et al., 2012). After being activated by *NLRP3, IL-18* and *IL-1beta* are activated from their preforms. As shown here, the vulnerability of the neonatal brain to LPS and HI is also attributed to *IL-1beta*. We also show that *NLRP3* gene expression is highest and significantly upregulated in rats being exposed to LPS before undergoing our mild HI insult. This might be one involved regulatory pathway, explaining how LPS pre-exposure significantly increases the vulnerability of the newborn brain to a mild hypoxic-ischemic event.

In our study, we observed an upregulation of the anti-inflammatory cytokine *TGF-beta* in animals from the LPS/HI group. At first sight, these results seem controversial. However, it has been shown that *TGF-beta* is a pleiotropic cytokine, with potent regulatory and inflammatory activity (Sanjabi et al., 2009). In the presence of *IL-6, TGF-beta* induces the differentiation of specific T-cells (TH17), promoting an inflammatory response (Qin et al., 2009). Transferred to our findings, it might be possible that the observed upregulation of *IL-6* in the hippocampus induces an overexpression of the cytokine *TGF-beta* triggering the inflammatory process through the differentiation of TH17 cells, which migrated into the brain after the acute brain injury in our model. To verify this hypothesis, there is an urgent need to analyze the activation, migration and differentiation of leukocytes in our model. On the other hand, it has been shown that peripheral T-cell depletion exacerbates brain injury in a neonatal rodent model of HI brain injury (Herz et al., 2018). These findings underlie the importance of further investigating the role of different T cells subsets in newborn brain injury models, as there is a clear gap in knowledge about T-cell differentiation and -function in newborn brain injury models.

Furthermore, we observed a significant upregulation of *CD206* gene expression in microglia of the LPS/HI group. Conversely, *CD206* is thought to be associated with the M2, anti-inflammatory microglia phenotype. As described in detail by Hellstrom Erkenstam et al. (2016) this may underlie the complexity of the inflammatory responses and cascades using *in vivo* injury models and stresses the question whether using a simple M1/M2 phenotype theory is inadequate to describe the complex concept of distinct inflammatory cell phenotypes in the brain.

There are limitations to our study. First, we have analyzed gene-expression patterns and not protein levels. As gene-expression levels do not always fully represent the protein expression, this will need to be confirmed in further studies.

However, we have previously shown in our model that pro-apoptotic proteins (cleaved caspase-3) are upregulated, leading to brain area loss at P14 (Osredkar et al., 2015). As we find a comparable level of brain area loss in our current study, we believe that pro-inflammatory and pro-apoptotic proteins will be involved, potentially activated by our pro-inflammatory gene-expression profiles. Second, we have only investigated early pro-inflammatory responses after 24 h yet. As M1/M2 phenotype expressions will change over time, we will need to analyze later time points. From a clinical perspective, new treatment interventions may only be applicable after understanding the complex time-dependent changes of inflammatory responses, as they might lead to early treatment interventions. This will be tested by us in the future and may lead to translational treatment options in newborns presenting with NE. Third, compared to our previous publications of this model (Osredkar et al., 2013, 2015), we did not find a significant increase of brain injury between the LPS/HI and Veh/HI groups. Pre-sensitization with LPS increased brain injury, compared to Veh/HI, without reaching the 5% significance level, most likely due to the mild HI injury in the current study compared to our previous publications. However, the pre-sensitization effect of LPS is clearly demonstrated by our results.

In summary, our results highlight that microglia are early key mediators of the inflammatory response following inflammation-sensitized HI brain injury, polarizing into a predominant pro-inflammatory phenotype 24 h post HI. Additionally, we demonstrate the involvement of the *NLRP3* inflammasome, possibly highlighting one potential regulatory pathway in our model. These findings will help us to better understand the complex pathophysiological changes in our model and in the future, this may give us the possibility to early intervene and offer new treatment options, helping to further improve outcome in asphyxiated newborns, especially in countries with high perinatal infection and perinatal asphyxia rates.

DATA AVAILABILITY

All datasets generated for this study are included in the manuscript and/or the supplementary files.

ETHICS STATEMENT

This study was carried out in accordance with the recommendations of the State Agency for Nature, Environment and Consumer Protection North Rhine-Westphalia, Germany. The protocol was approved by the State Agency for Nature, Environment and Consumer Protection North Rhine-Westphalia, Germany.

AUTHOR CONTRIBUTIONS

MS and HS planned and designed the study. MS and HS performed the animal experiments. MS, KK, MR, JH, IB, and HS performed tissue analysis. MS and HS analyzed the data. MS, JH, IB, and UF-M wrote and corrected the manuscript.

FUNDING

This study was supported by the European Society of Pediatric Research (ESPR), the Elterninitiative Kinderkrebsklinik Düsseldorf e.V. and the Foundation "Stiftung Helfen aus Dank."

ACKNOWLEDGMENTS

We would like to thank Christian Köster and Ralf Herrmann for technical support and data interpretation during the analysis.

REFERENCES

Chhor, V., Le Charpentier, T., Lebon, S., Ore, M. V., Celador, I. L., Josserand, J., et al. (2013). Characterization of phenotype markers and neuronotoxic potential of polarised primary microglia in vitro. *Brain Behav. Immun.* 32, 70–85. doi: 10.1016/j.bbi.2013.02.005

Cunha, C., Gomes, C., Vaz, A. R., and Brites, D. (2016). Exploring new inflammatory biomarkers and pathways during LPS-induced M1 polarization. *Mediators Inflamm.* 2016:6986175. doi: 10.1155/2016/6986175

Eklind, S., Mallard, C., Leverin, A. L., Gilland, E., Blomgren, K., Mattsby-Baltzer, I., et al. (2001). Bacterial endotoxin sensitizes the immature brain to hypoxic–ischaemic injury. *Eur. J. Neurosci.* 13, 1101–1106. doi: 10.1046/j.0953-816x.2001.01474.x

Falck, M., Osredkar, D., Wood, T. R., Maes, E., Flatebo, T., Sabir, H., et al. (2018). Neonatal systemic inflammation induces inflammatory reactions and brain apoptosis in a pathogen-specific manner. *Neonatology* 113, 212–220. doi: 10.1159/000481980

Feezor, R. J., Oberholzer, C., Baker, H. V., Novick, D., Rubinstein, M., Moldawer, L. L., et al. (2003). Molecular characterization of the acute inflammatory response to infections with gram-negative versus gram-positive bacteria. *Infect. Immun.* 71, 5803–5813. doi: 10.1128/iai.71.10.5803-5813.2003

Grether, J. K., and Nelson, K. B. (1997). Maternal infection and cerebral palsy in infants of normal birth weight. *JAMA* 278, 207–211. doi: 10.1001/jama.278.3.207

Gustin, A., Kirchmeyer, M., Koncina, E., Felten, P., Losciuto, S., Heurtaux, T., et al. (2015). NLRP3 inflammasome is expressed and functional in mouse brain microglia but not in astrocytes. *PLoS One* 10:e0130624. doi: 10.1371/journal.pone.0130624

Hakobyan, M., Dijkman, K. P., Laroche, S., Naulaers, G., Rijken, M., Steiner, K., et al. (2018). Outcome of infants with therapeutic hypothermia after perinatal asphyxia and early-onset sepsis. *Neonatology* 115, 127–133. doi: 10.1159/000493358

Hedtjarn, M., Leverin, A. L., Eriksson, K., Blomgren, K., Mallard, C., and Hagberg, H. (2002). Interleukin-18 involvement in hypoxic-ischemic brain injury. *Neuroscience* 22, 5910–5919. doi: 10.1523/jneurosci.22-14-05910.2002

Hellstrom Erkenstam, N., Smith, P. L., Fleiss, B., Nair, S., Svedin, P., Wang, W., et al. (2016). Temporal characterization of microglia/macrophage phenotypes in a mouse model of neonatal hypoxic-ischemic brain injury. *Front. Cell. Neurosci.* 10:286. doi: 10.3389/fncel.2016.00286

Herz, J., Koster, C., Crasmoller, M., Abberger, H., Hansen, W., Felderhoff-Muser, U., et al. (2018). Peripheral T cell depletion by FTY720 exacerbates hypoxic-ischemic brain injury in neonatal mice. *Front. Immunol.* 9:1696. doi: 10.3389/fimmu.2018.01696

Jacobs, S. E., Berg, M., Hunt, R., Tarnow-Mordi, W. O., Inder, T. E., and Davis, P. G. (2013). Cooling for newborns with hypoxic ischaemic encephalopathy. *Cochrane Database Syst. Rev.* 1:CD003311.

Lenz, K. M., and Nelson, L. H. (2018). Microglia and beyond: innate immune cells as regulators of brain development and behavioral function. *Front. Immunol.* 9:698. doi: 10.3389/fimmu.2018.00698

Livak, K. J., and Schmittgen, T. D. (2001). Analysis of relative gene expression data using real-time quantitative PCR and the 2(-Delta Delta C(T)) method. *Methods* 25, 402–408. doi: 10.1006/meth.2001.1262

Mallard, C., Tremblay, M. E., and Vexler, Z. S. (2018). Microglia and neonatal brain injury. *Neuroscience* 405, 68–76. doi: 10.1016/j.neuroscience.2018.01.023

Nair-Gupta, P., Baccarini, A., Tung, N., Seyffer, F., Florey, O., Huang, Y., et al. (2014). TLR signals induce phagosomal MHC-I delivery from the endosomal recycling compartment to allow cross-presentation. *Cell* 158, 506–521. doi: 10.1016/j.cell.2014.04.054

O'Callaghan, J. P., Kelly, K. A., VanGilder, R. L., Sofroniew, M. V., and Miller, D. B. (2014). Early activation of STAT3 regulates reactive astrogliosis induced by diverse forms of neurotoxicity. *PLoS One* 9:e102003. doi: 10.1371/journal.pone.0102003

Ohsawa, K., and Kohsaka, S. (2011). Dynamic motility of microglia: purinergic modulation of microglial movement in the normal and pathological brain. *Glia* 59, 1793–1799. doi: 10.1002/glia.21238

Osredkar, D., Sabir, H., Falck, M., Wood, T., Maes, E., Flatebo, T., et al. (2015). Hypothermia does not reverse cellular responses caused by lipopolysaccharide in neonatal hypoxic-ischaemic brain injury. *Dev. Neurosci.* 37, 390–397. doi: 10.1159/000430860

Osredkar, D., Thoresen, M., Maes, E., Flatebo, T., Elstad, M., and Sabir, H. (2013). Hypothermia is not neuroprotective after infection-sensitized neonatal hypoxic-ischemic brain injury. *Resuscitation* 85, 567–572. doi: 10.1016/j.resuscitation.2013.12.006

Pierre, W. C., Smith, P. L., Londono, I., Chemtob, S., Mallard, C., and Lodygensky, G. A. (2017). Neonatal microglia: the cornerstone of brain fate. *Brain Behav. Immun.* 59, 333–345. doi: 10.1016/j.bbi.2016.08.018

Qin, H., Wang, L., Feng, T., Elson, C. O., Niyongere, S. A., Lee, S. J., et al. (2009). TGF-beta promotes Th17 cell development through inhibition of SOCS3. *J. Immunol.* 183, 97–105. doi: 10.4049/jimmunol.0801986

Reinboth, B. S., Koster, C., Abberger, H., Prager, S., Bendix, I., Felderhoff-Muser, U., et al. (2016). Endogenous hypothermic response to hypoxia reduces brain injury: implications for modeling hypoxic-ischemic encephalopathy and therapeutic hypothermia in neonatal mice. *Exp. Neurol.* 283(Pt A), 264–275. doi: 10.1016/j.expneurol.2016.06.024

Rice, J. E. III, Vannucci, R. C., and Brierley, J. B. (1981). The influence of immaturity on hypoxic-ischemic brain damage in the rat. *Ann. Neurol.* 9, 131–141. doi: 10.1002/ana.410090206

Robertson, N. J., Hagmann, C. F., Acolet, D., Allen, E., Nyombi, N., Elbourne, D., et al. (2011). Pilot randomized trial of therapeutic hypothermia with serial cranial ultrasound and 18-22 month follow-up for neonatal encephalopathy in a low resource hospital setting in uganda: study protocol. *Trials* 12:138. doi: 10.1186/1745-6215-12-138

Sabir, H., Scull-Brown, E., Liu, X., and Thoresen, M. (2012). Immediate hypothermia is not neuroprotective after severe hypoxia-ischemia and is deleterious when delayed by 12 hours in neonatal rats. *Stroke* 43, 3364–3370. doi: 10.1161/strokeaha.112.674481

Sanjabi, S., Zenewicz, L. A., Kamanaka, M., and Flavell, R. A. (2009). Anti-inflammatory and pro-inflammatory roles of TGF-beta, IL-10, and IL-22 in immunity and autoimmunity. *Curr. Opin. Pharmacol.* 9, 447–453. doi: 10.1016/j.coph.2009.04.008

Serdar, M., Herz, J., Kempe, K., Lumpe, K., Reinboth, B. S., Sizonenko, S. V., et al. (2016). Fingolimod protects against neonatal white matter damage and long-term cognitive deficits caused by hyperoxia. *Brain Behav. Immun.* 52, 106–119. doi: 10.1016/j.bbi.2015.10.004

Strowig, T., Henao-Mejia, J., Elinav, E., and Flavell, R. (2012). Inflammasomes in health and disease. *Nature* 481, 278–286. doi: 10.1038/nature10759

Tann, C. J., Nakakeeto, M., Hagmann, C., Webb, E. L., Nyombi, N., Namiiro, F., et al. (2016). Early cranial ultrasound findings among infants with neonatal encephalopathy in uganda: an observational study. *Pediatr. Res.* 80, 190–196. doi: 10.1038/pr.2016.77

Tann, C. J., Nakakeeto, M., Willey, B. A., Sewegaba, M., Webb, E. L., Oke, I., et al. (2017). Perinatal risk factors for neonatal encephalopathy: an unmatched case-control study. *Arch. Dis. Child Fetal Neonatal Ed.* 103, F250–F256. doi: 10.1136/archdischild-2017-312744

Truettner, J. S., Bramlett, H. M., and Dietrich, W. D. (2016). Posttraumatic therapeutic hypothermia alters microglial and macrophage polarization toward a beneficial phenotype. *J. Cereb. Blood Flow Metab.* 37, 2952–2962. doi: 10.1177/0271678X16680003

United Nations Report (2015). *LEVELS and Trends in Child Mortality. Report 2015. Estimates Developed by the UN Inter-agency Group for Child Mortality Estimation*. New York, NY: United Nations Children's Fund.

Wang, N., Liang, H., and Zen, K. (2014). Molecular mechanisms that influence the macrophage m1-m2 polarization balance. *Front. Immunol.* 5:614. doi: 10.3389/fimmu.2014.00614

Wintermark, P., Boyd, T., Gregas, M. C., Labrecque, M., and Hansen, A. (2010). Placental pathology in asphyxiated newborns meeting the criteria for therapeutic hypothermia. *Am. J. Obstet. Gynecol.* 203, 579.e1–579.e19.

Wood, T., Osredkar, D., Puchades, M., Maes, E., Falck, M., Flatebo, T., et al. (2016). Treatment temperature and insult severity influence the neuroprotective effects of therapeutic hypothermia. *Sci. Rep.* 6:23430. doi: 10.1038/srep23430

Conflict of Interest Statement: The authors declare that the research was conducted in the absence of any commercial or financial relationships that could be construed as a potential conflict of interest.

The reviewer MT declared a past co-authorship with one of the authors HS to the handling Editor.

frontiers in Cellular Neuroscience

ORIGINAL RESEARCH
published: 06 June 2019
doi: 10.3389/fncel.2019.00230

A Novel Transwell Blood Brain Barrier Model Using Primary Human Cells

Nicole L. Stone, Timothy J. England and Saoirse E. O'Sullivan*

Division of Medical Sciences and Graduate Entry Medicine, School of Medicine, University of Nottingham, Nottingham, United Kingdom

Structural alterations and breakdown of the blood brain barrier (BBB) is often a primary or secondary consequence of disease, resulting in brain oedema and the transport of unwanted substances into the brain. It is critical that effective *in vitro* models are developed to model the *in vivo* environment to aid in clinically relevant research, especially regarding drug screening and permeability studies. Our novel model uses only primary human cells and includes four of the key cells of the BBB: astrocytes, pericytes, brain microvascular endothelial cells (HBMEC) and neurons. We show that using a larger membrane pore size (3.0 μM) there is an improved connection between the endothelial cells, astrocytes and pericytes. Compared to a two and three cell model, we show that when neurons are added to HBMECs, astrocytes and pericytes, BBB integrity was more sensitive to oxygen-glucose deprivation evidenced by increased permeability and markers of cell damage. Our data also show that a four cell model responds faster to the barrier tightening effects of glucocorticoid dexamethasone, when compared to a two cell and three cell model. These data highlight the important role that neurons play in response to ischaemia, particularly how they contribute to BBB maintenance and breakdown. We consider that this model is more representative of the interactions at the neurovascular unit than other transwell models and is a useful method to study BBB physiology.

Keywords: blood-brain barrier, transwell, *in vitro*, BBB model, BBB permeability, primary human cells, stroke

OPEN ACCESS

Edited by:
Stefania Ceruti, University of Milan, Italy

Reviewed by:
Förster Carola, Universitätsklinikum Würzburg, Germany
Babette Weksler, Cornell University, United States

****Correspondence:***
Nicole L. Stone
mzxns2@nottingham.ac.uk;
nicole.stone@nottingham.ac.uk

Specialty section:
This article was submitted to Non-Neuronal Cells, a section of the journal Frontiers in Cellular Neuroscience

Received: *21 February 2019*
Accepted: *08 May 2019*
Published: *06 June 2019*

Citation:
Stone NL, England TJ and O'Sullivan SE (2019) A Novel Transwell Blood Brain Barrier Model Using Primary Human Cells. Front. Cell. Neurosci. 13:230. doi: 10.3389/fncel.2019.00230

INTRODUCTION

The blood brain barrier (BBB) is a unique interface that separates the peripheral blood supply and neuronal tissue. Structurally, the BBB is comprised of specialized brain microvascular endothelial cells (HBMECs), perivascular cells (pericytes) and astrocytes (Abbott et al., 2006, 2010). Neurons and microglia also contribute to the maintenance of the BBB and form what is known as the neurovascular unit (NVU) (Abbott et al., 2006). Pericytes contribute 22–32% of the cerebral vasculature and together with vascular smooth muscle cells and endothelial cells they maintain vascular function (Martini and Bartholomew, 2017). In the CNS, pericytes are present at a higher ratio to HBMECs in the brain compared to the periphery and recent studies have shown the extensive role of pericytes in BBB development and maintenance (Kacem et al., 1998; Armulik et al., 2011; Sweeney et al., 2016). As well as offering mechanical support, they also regulate vessel contractility, endothelial proliferation, blood flow and angiogenesis (Bergers and Song, 2005;

Dore-Duffy, 2008). Pericytes have also been shown to secrete angiogenic factors such as vascular endothelial growth factor (VEGF), that support endothelial cell survival and proliferation (Darland et al., 2003). In pathologies such as ischaemic stroke, large gaps can develop between adjacent pericytes, increasing barrier permeability and vessel leakage. These alterations in pericyte morphology, coupled with an upregulation in the expression of adhesion molecules and leukocyte integrin ligands, contribute to the extravasation of peripheral leukocytes into the brain following ischaemic insult (Pieper et al., 2013). Thus, pericytes play a large role in cerebral vascular function under normal physiological conditions as well as vascular dysfunction in hypoxia.

Several studies have also highlighted the roles of neurons and glia in BBB development and maintenance. Neural progenitor cells present in the ventricular neuroepithelium have been shown to aid endothelial cell recruitment during early BBB development, which is largely governed by the Wnt signaling pathway (Risau et al., 1986). Specifically, Wnt signaling in early CNS development is responsible for vascular stabilization and angiogenesis (Liebner et al., 2008). Further to this, early neuronal signaling has been shown to be essential for the maturation of the BBB, specifically, tight junction (TJ) organization. A study carried out using rat microvascular endothelial cells and neuronal progenitor cells, showed that in the presence of neural progenitor cells, endothelial cells established regular TJ formation including: claudin 5, zonula occludens (ZO-1) and occludin (Weidenfeller et al., 2007). After maturation, maintenance of the BBB and preservation of brain homeostasis is largely dependent on adequate perfusion to neuronal tissue and neuronal signaling to cerebral vessels, a process known as hyperaemia (Attwell et al., 2010). Studies have shown that neuronal-astrocyte crosstalk is important for appropriate vessel contractility and blood flow, depending on metabolic demand (Zonta et al., 2003; Attwell et al., 2010; Macvicar and Newman, 2015). In cerebral ischaemia, astrocytes sense elevations in Ca^{2+} ions and increases in extracellular glutamate released by neurons and respond accordingly, secreting a range of vasoactive substances to help mitigate the effects of the blood vessel occlusion (Macvicar and Newman, 2015). Altogether, interactions between both neural and vascular cells within the NVU is considered to be paramount in BBB functionality because together they induce and strengthen barrier properties; helping to maintain its key features including low paracellular permeability and functional tightness (Abbott et al., 2010). Breakdown of the BBB in conditions such as ischaemic stroke can lead to severe consequences to brain homeostasis, therefore, modeling these interactions is necessary to understand the complex signaling networks between these cell types and how they are influenced in disease states.

To date, a number of BBB models have been developed ranging from HBMEC monolayers to more sophisticated spheroid and chip style models, see **Table 1**. After the successful isolation of brain endothelial cells, the first, most simplistic BBB models were developed utilizing HBMECs as a single monolayer in the abluminal side of transwell inserts, see **Table 1** (Borges et al., 1994; Hartz et al., 2010). Later addition of other BBB cell types (namely astrocytes and pericytes), led to the development of co-culture transwell systems which exhibited greater barrier strength, exhibited by higher transepithelial resistance (TEER) and lower permeability than single HBMEC models, see **Figure 1**. More recent transwell systems typically use three cell types originating from either bovine, porcine or rodent origin, see **Table 1** (Gaillard et al., 2000; Nakagawa et al., 2009; Thomsen et al., 2015).

Whilst modeling using non-human cells is cheaper and easier to obtain, they are not comparable to human cells, with many studies showing key differences in morphology and function, particularly their sensitivity to glutamate and expression of efflux transporter proteins (Oberheim et al., 2009; Warren et al., 2009; Zhang et al., 2016). More complex BBB models are also available, such as spheroid or microfluidic models and offer a closer representation of the *in vivo* environment. However, these set ups are difficult and expensive to assemble (Ruck et al., 2015). Therefore, there is a need to develop a multicellular transwell model that incorporates multiple NVU cell types to study their interactions, particularly the role of neurons and their influence on barrier strength in both physiological and disease states. Transwell systems still offer a distinct advantage in that they are relatively easy to setup and control, as well as offering a range of endpoints to study. Measuring TEER in these types of models is commonplace as it provides a reliable, non-invasive quantitative measure of barrier integrity, enabling repeated measurements to be taken over the desired time period with minimal damage to cells (Srinivasan et al., 2015). Further to this, transwell models enable access to both the apical and basolateral (basal) compartments for drug application and medium sampling as well as being able to visualize cells over the course of the experiment.

Our aim was therefore to create a novel four cell human BBB model to study changes in permeability post oxygen-glucose deprivation (OGD) and for use in *in vitro* pharmacology. We initially focused on model development, refining a protocol first outlined by Hind (2014) by optimizing the inserts themselves, insert coating, cell seeding densities and cell culture timelines. Finally, we incorporated a method of seeding neurons on plastic coverslips which were placed on the bottom of 12 well cell culture plates. Thus, our model maintains the ease of the transwell setup but utilizes four primary human cells, making it a closer representation of the human *in vivo* environment.

MATERIALS AND METHODS

Primary cells (astrocytes, pericytes, HBMECs, and neurons) and specialized cell culture medium (astrocyte medium, pericyte medium, endothelial cell medium, and neuronal medium) were obtained from ScienCell, United States supplied by Caltag Medsystems, United Kingdom. Poly-L-lysine and porcine fibronectin were also obtained from ScienCell, United States supplied by Caltag Medsystems, United Kingdom. Collagen coated inserts, 3.0 μm, 12 mm were obtained from Corning, United Kingdom. Plastic coverslips (Thermanox® 13 mm diameter), Accutase dissociation reagent and glucose free RPMI medium were obtained from Thermo Fisher Scientific, United Kingdom.

TABLE 1 | Different models of the blood brain barrier; their features, advantages, and disadvantages.

Model type	Typical components	Advantages	Limitations	Representative of BBB phenotype	References
Single-cell transwell systems (non-co-culture)	A monolayer of HBMECs cultured in the apical compartment of the transwell insert.	Very easy to set up. Minimal cost. Low labor intensity. Useful if wanting to study endothelial cells alone.	TEER is typically low.	Cobblestone appearance of HBMECs, barrier formation. Little information on the impact of additional cell types.	Borges et al., 1994; Hartz et al., 2010
Co-culture /multicellular transwell systems	HBMECs cultured on the apical side of the transwell insert and astrocytes and/or pericytes cultured on the underside of the transwell insert.	Time and cost effective. Higher TEER. Greater barrier stability.	Some models are not fully in contact.	Closer representation of the BBB with the addition of important cell types. Able to study interactions between cell types and how they influence BBB phenotype.	Hind, 2014; Wang et al., 2015; Appelt-Menzel et al., 2017
Spheroid	3D organization of cells typically using matrigel. Typically consists of HBMECs and astrocytes and/or pericytes with some models containing neuronal cell types.	3D Cell model. No scaffold. Reduced de-differentiation.	Cannot measure permeability with this model. Expensive and greater skill required.	Microvessels wrap around endothelial cells and provide structural support. Helps to induce tight junction proteins. Closely represents the *in vivo* set up with cells in direct contact with each other. Applications include: cancer drug and neurotoxicity screening.	Cho et al., 2017; Nzou et al., 2018
Microfluidic systems/3D chip-style models	3D organization of cells with the added benefit of a "flow" system to mimic cerebral blood flow. Typically consists of HBMECs and astrocytes and/or pericytes with some models containing neuronal cell types.	Advantage of mimicking sheer stress which is essential for HBMECs optimum phenotype.	Difficult to set up and maintain adequate flow unless linked to a computer system.	Useful to assess the impact of blood flow on cell development and optimum phenotype. Also useful in studying cell migration and metastatic progression.	Yeon et al., 2012; Wang et al., 2017

HBMECs = human brain microvascular endothelial cells, TGFβ = transforming growth factor beta, TEER = transepithelial resistance, BBB = blood brain barrier.

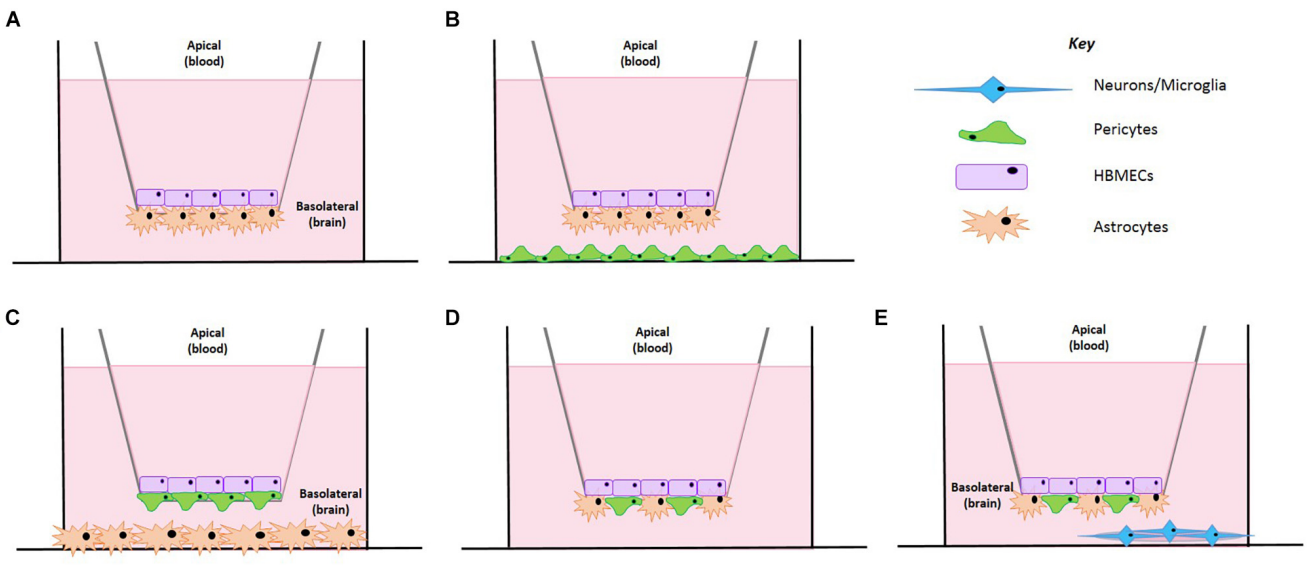

FIGURE 1 | Schematic representation of the BBB model development. **(A)** A co-culture cell model containing HBMECs and astrocytes. **(B)** HBMECs seeded on the apical side, astrocytes seeded on the underside of the insert and pericytes seeded on the plate bottom. **(C)** HBMECs seeded on the apical side of the insert, pericytes seeded on the underside of the insert and astrocytes seeded on the plate bottom. **(D)** HBMECs seeded on the apical side of the insert with mixed culture of astrocytes and pericytes on the underside of the insert. **(E)** HBMECs seeded on the apical side of the insert with mixed culture of astrocytes and pericytes on the underside of the insert and neurons seeded on a poly-L-lysine coated coverslip on the plate bottom.

Cells were maintained in a humidified incubator (37°C, 5% CO_2). Astrocytes and pericytes were cultured and used between passages 4 and 6. Human brain microvascular endothelial cells (HBMECs) were used between passages 3 and 5 and neurons were used at passage 1. During subculture, flasks containing HBMECs were coated with 2 $\mu g \cdot cm^2$ of fibronectin before reviving or splitting cells as per manufacturers recommendations. Cells were passaged at 80–90% confluency. Inserts contained 1.2 mL of medium in the basolateral compartment and 800 µL in the apical compartment.

STX-3 probes and Ohms meter were obtained from World Precision Instruments, United Kingdom. Dexamethasone was obtained from Sigma, United Kingdom and dissolved in DMSO at a stock concentration of 10 mM and subsequently diluted in cell culture medium. GasPak^{TM} EZ anaerobe container systems were obtained from BD, United Kingdom.

Model Validation

Our model was based on an initial co-culture set up established by Hind (2014) and previous models by Allen and Bayraktutan (2009). Our model was modified and developed in a number of preliminary experiments including comparison of insert pore sizes, insert coating, cell organization and addition of multiple cell types.

Pore Size, Insert Size and Coating

Initially, pore sizes of Corning, United Kingdom inserts were compared (0.4 µm vs. 3.0 µm) as well as cell culture plates (12 well vs. 24 well). This was to determine the best initial setup that provided the highest and most stable barrier resistance, as well as giving the best cell contact. During protocol development, we found addition of pericytes in the smaller 24 well plates yielded poor results and insufficient TEER, suggesting inadequate barrier formation. Possibly as a result of inadequate cellular growth in such a small surface area and environment. Therefore, 24 well plates were switched back to 12 well plates, which resulted in substantially higher TEER readings. Following work carried out by Niego and Medcalf (2013), we also found that inserts with a 3.0 µm pore size had higher TEER values than 0.4 µm inserts, suggesting that increased contact between the cells in the apical and basolateral sides of the insert resulted in greater barrier strength, see **Figure 2A**.

Addition of Multiple Cell Types and Cell Positioning

Despite these improvements on the co-culture model, the need for additional cell types was critical to create a closer representation of the *in vivo* BBB. We established three different set ups as shown in **Figure 1**. In one, astrocytes were seeded on the basolateral side of the inserts and pericytes on the bottom of the culture dish (**Figure 1B**), in another pericytes were seeded on the basolateral of the inserts whilst astrocytes were seeded on the bottom of the culture dish (**Figure 1C**) and finally the last set up involved a mixed culture of astrocytes and pericytes seeded on the basolateral side of the insert (**Figure 1D**). In all models tested, HBMECs were seeded in the apical side of the transwell insert.

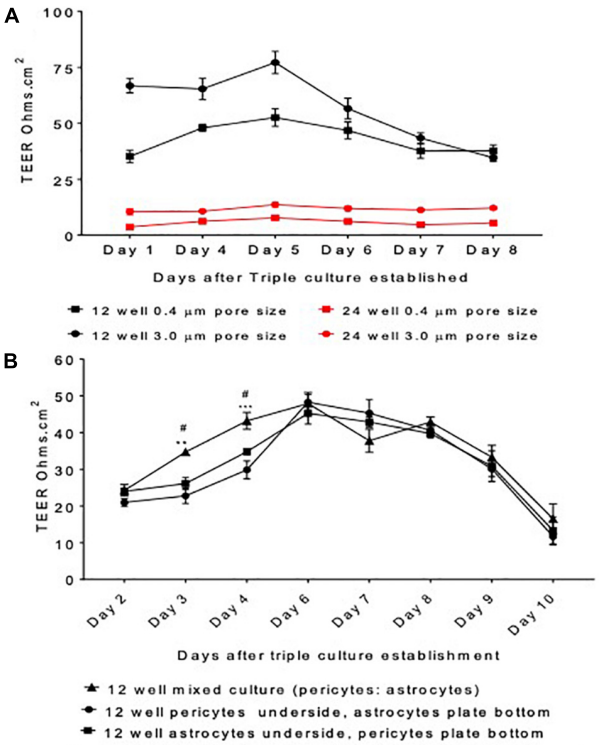

FIGURE 2 | Model protocol development **(A)** measured transepithelial resistance (TEER) as a marker of barrier tightness comparing a 12 well plate transwell set up vs. a 24 well plate transwell set up and insert pore size 3.0 µm vs. 0.4 µm. HBMECs seeded on the apical side of the insert, astrocytes underneath and pericytes on the plate bottom. **(B)** The organization of cells was optimized by comparing the TEER generated by a mixed culture of astrocytes and pericytes, pericytes or astrocytes alone on the underside of transwell inserts and astrocytes or pericytes on the cell culture plate bottom. HBMECs were seeded on the apical side of the insert. Data given as mean ± SEM, n = 4–6 from two experimental repeats. Statistical analysis conducted using 2-way ANOVA with Turkey's multiple comparisons test, $^{**}P < 0.01$ and $^{***}P < 0.001$ mixed culture astrocytes and pericytes vs. pericytes underside the insert and astrocytes on plate bottom. $^{\#}P < 0.05$ mixed culture astrocytes and pericytes vs. astrocytes underside the insert and pericytes on plate bottom.

The final set up offered a closer replication of the organization held at the *in vivo* BBB, as cells would be in direct contact allowing them to exchange vital growth factors required for cellular growth and development. We found that mixed culture of pericytes and astrocytes exhibited significantly higher TEER values when compared to the set-up with pericytes seeded on the plate bottom and astrocytes underneath the insert or astrocytes on the plate bottom and pericytes underneath the insert on days 3 and 4, $P < 0.05$ and $P < 0.01$, respectively (**Figure 2B**). Furthermore, this set up was also considered the most stable, as shown by steadier TEER readings and was altogether more physiologically relevant. This set up was therefore taken forward in subsequent four cell protocol development.

To test the viability of adding neurons to the model, we originally seeded neurons on the bottom of the 12 well plate in which the inserts were hung. This, however, was

not feasible as the TEER probes touched the bottom of the plate causing unwanted damage to the cells. Therefore, we decided to utilize coverslips that could be positioned on the plate bottom, but not take up the entirety of the well, allowing the probe to sit where the cells were not present. After testing both poly-L-lysine coated glass and plastic coverslips, we found that plastic coverslips coated were the most effective in neuronal adhesion and this method was used in the final model.

Four Cell Method Overview

After optimization, our four cell BBB model consisted of four major NVU cell types arranged in a transwell permeability set-up (see **Figure 1E**). The assembly of this involves seeding different cell types at different times on the apical and basolateral sides of the transwell insert. During this time, neurons are seeded on plastic coverslips placed on the bottom of a separate 12 well plate to develop neurite before putting both parts of the model together on the final day of model establishment. Cell culture medium in both compartments was replaced every other day and the final set up was left to equilibrate for 2 days before commencing experiments. Greater than 85% of inserts are feasible for use in experiments and the model remained viable for up to 5 days.

Insert Coating and Astrocyte Seeding

On day one, the basolateral side of transwell inserts were coated with poly-L-Lysine and astrocytes were seeded on the basolateral side of the inserts, see **Figure 3**. Briefly, 3.0 μm, 12 mm collagen coated inserts (Corning, United Kingdom) were carefully removed from outer packaging and placed into 12 well cell culture plates using sterile forceps. A solution of poly-L-Lysine (2 $\mu g/cm^2$) was prepared in sterile water, homogenously mixed and carefully pipetted using a Pasteur pipette to just cover the basolateral of the insert, see **Figures 4A,i**. Plates containing inserts were then returned to the incubator, 37°C, 5% CO_2 for 1 h as per supplier recommendations. After 1 h, plates were removed from the incubator and washed twice with sterile water to remove any residual poly-L-lysine. All remaining liquid was removed by careful aspiration. Transwell inserts were then flipped inside the plate and the lid removed (**Figure 4B**). On the newly coated inserts, 100 μL of astrocyte cell suspension in astrocyte medium (3.13×10^5 cells) was pipetted quickly onto the basolateral side of the transwell and the lid carefully replaced (see **Figures 4C,ii**). Plates were returned to the cell culture incubator for 2–3 h for the cells to adhere. After this time, transwell inserts were reverted and any excess medium was removed by aspiration. Medium was topped up in the apical and basolateral compartments, see **Figure 4iii**. Again, plates were returned to the incubator.

Pericyte Seeding

On day 2, plates were removed from the incubator and the astrocyte medium was removed with care so as to not disturb the layer of cells on the basolateral side of the insert. Inserts were then inverted again and 100 μL of 6.25×10^4 pericyte cell suspension was added to the astrocyte cell layer on the basolateral side of the transwell inserts, giving an approximate ratio of 5:1 astrocytes to pericytes (Pardridge, 1999). Plate lids were quickly replaced and returned to the incubator for 2–3 h. After this time, transwell inserts were reverted and any excess medium was removed by aspiration and a mixture of astrocyte and pericyte medium (1:1) was added to the apical and basolateral compartments.

HBMEC Seeding

Once astrocytes and pericytes reached 90% confluency (approximately day 4 from model initiation, see **Figure 3**), the astrocyte:pericyte (1:1) medium in the apical compartment was removed and 100 μL of HBMEC cell suspension (7.5×10^4) in HBMEC medium was added to the apical compartment of transwell inserts and cells were left to adhere for a minimum of 5 h, then medium was topped up to 700 μL with endothelial cell medium and plates returned to the incubator.

Neuronal Seeding

On the same day as HBMEC seeding, plastic coverslips (13 mm diameter) were coated with poly-L-lysine and placed in the cell culture incubator for a minimum of 1 h, as per supplier recommendations. Plates containing coverslips were carefully removed from the incubator and coverslips were washed twice with sterile water and left to air dry in the cell culture hood. Following this, cryopreserved neurons were revived into 3 mL of neuronal medium (to give a total cell suspension of 4 mL) and 100 μL of cell suspension was added to each coverslip (thus seeded at a density of approximately 2.5×10^4 cells per cm^2 within the optimum range according to the manufacturer's

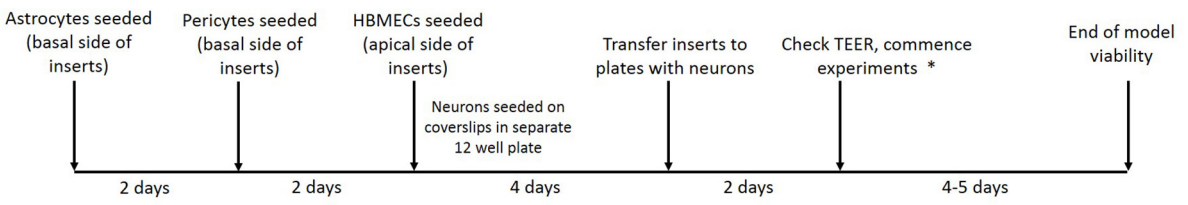

FIGURE 3 | Timeline showing stages of model establishment. On day 1, inserts were coated and astrocyte seeded on the basolateral side of transwell inserts and on day 3 pericytes were seeded on the basolateral side of inserts to form a mixed culture. On day 6 HBMECs were seeded on the apical side of inserts and neurons were seeded on coated plastic coverslips in a separate 12 well plate. On day 10/11, inserts are carefully lifted out of their current plate and placed into the second 12 well plate containing the neurons seeded on coverslips. After 2 days, TEER measurements are taken to ensure adequate barrier formation. *In our lab OGD experiments were commenced at this point and were viable for 4–5 days.

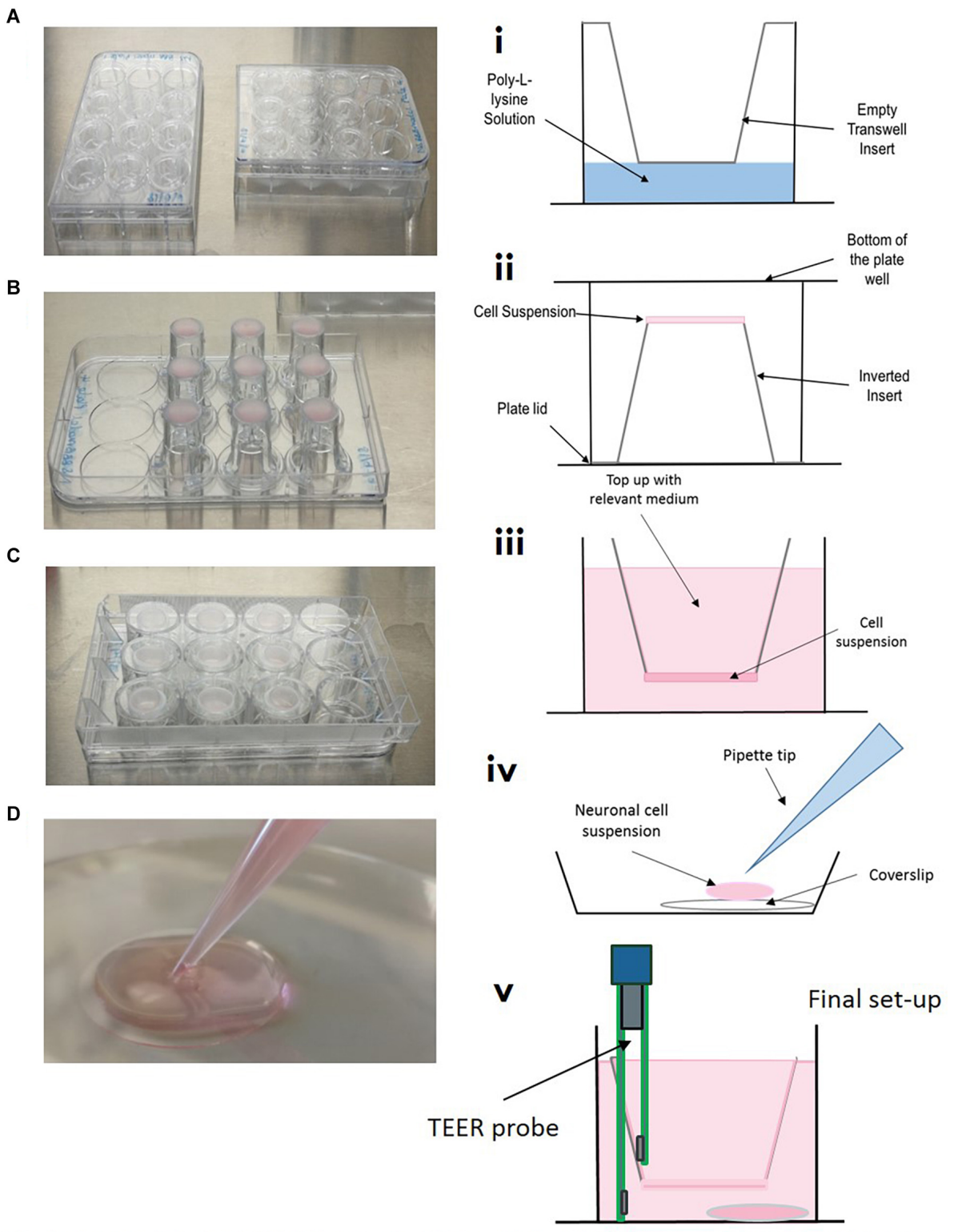

FIGURE 4 | Model setup **(A–D)** and **(i–v)**. **(A/i)** Inserts are placed into 12 well plate, coated with poly-L-lysine and washed, ensuring all of the liquid is removed. **(B/ii)** Inserts are carefully flipped inside the plate and the plate removed. 100 μL of relevant cell suspension is carefully placed on the underside of the insert. **(C/ii)** The bottom of the cell culture plate acts as a "lid" and is replaced as quickly as possible, plates are then returned to the incubator for the cells to adhere for 3–4 h. **(iv)** In a separate 12 well plate, coverslips are placed in the bottom of the culture dish, coated with poly-L-lysine and seeded with neuronal cell suspension. **(v)** Once all cells have been seeded on transwells, inserts are carefully transferred to plates containing neurons on coverslips.

recommendations) (**Figures 4D,iv**). Medium was topped up after 2 h and half of the medium replaced every 2–3 days. After light microscope observation, neurons began showing extensive neurite growth at approximately day 5. At this point HBMECs will have almost formed a confluent monolayer above the astrocytes and pericytes. Transwells were then carefully lifted out of their current 12 well plate using sterile forceps and placed into the 12 well plate containing the neuronal coverslips. Fresh HBMEC medium was applied to the apical compartment and a mix of pericyte, astrocyte and neuronal medium (1:1:2, respectively) was added to the basolateral compartment. This was to maintain a low concentration of fetal bovine serum optimum for neuronal maintenance, whilst also preserving growth of astrocytes and pericytes. As all cells were confluent and the barrier was adequately formed, conditions were able to be maintained in the different compartments.

Oxygen-Glucose Deprivation (OGD) Protocol

An oxygen-glucose deprivation (OGD) protocol was used to increase barrier permeability, simulating the effects of ischaemic stroke *in vitro* (Hind et al., 2015, 2016). Normal cell culture medium was removed from transwell inserts and replaced with glucose free RPMI medium (Thermo Fisher Scientific, United Kingdom) and placed in a 0% O_2 environment (GasPak^{TM} anaerobe pouch Beckton Dickinson, Oxford, United Kingdom) for 20 min to ensure anaerobic conditions for a further 4 h. There was no initial pre-conditioning period. Reperfusion was initiated by removing plates from the anaerobe pouch and returning cells to their normal medium (HBMEC medium in the apical compartment and in the basolateral compartment a mix of pericyte, astrocyte and neuronal medium, 1:1:2, respectively). TEER was measured at baseline (0 h), immediately post OGD (4 h), 24, 48, and 72 h.

Evaluation of Barrier Integrity

Transepithelial resistance (TEER) was measured prior to commencing OGD experiments to ensure model barrier integrity; inserts should exhibit a TEER value of $\geq$45 Ω/cm^2 (**Figure 4v**). Light microscope observation was also carried out to ensure cell confluency and successful neurite formation. To ensure consistency, TEER measures should always be read at least 24 h after a medium change. Briefly, STX3 electrodes were sterilized by placing the tips of the probe in 70% ethanol, and then equilibrated for 15 min in endothelial cell culture medium at room temperature. The STX probe was then connected to an EVOM^2 meter (Both World Precision Instruments, United Kingdom) and inserted into the transwell insert. The electrode has two parts that are uneven in length, the longer part of the electrode was placed so it gently touched the bottom of the cell culture plate, whilst the shorter electrode rested slightly above the insert dish, not quite making contact the HBMEC cell layer. Care should be taken to avoid disrupting the neurons on the bottom of the cell plate, see technical comments and limitations. As TEER values are very susceptible to change, it is important to keep the electrode upright and avoid tilting as this can cause fluctuation in the TEER values. A background reading for an insert with just cell culture medium was taken and subtracted from each reading (readings were repeated twice to ensure reproducibility), this was then multiplied by 1.12 to address the cell culture insert area (cm^2) (Hind, 2014).

Dexamethasone Protocol

Dexamethasone is a synthetic glucocorticoid and several groups have shown that is able to artificially improve barrier strength (Shi and Zheng, 2005; Pyrgos et al., 2010; Hind, 2014). Therefore, we used dexamethasone as a positive control to investigate any potential difference in the response of the three versus four cell model to a drug application. Baseline TEER readings were recorded and medium replaced, then dexamethasone was added to the apical compartment of the transwell insert, giving a final concentration of 1 μM. TEER was measured at 2, 4, and 24 h.

Data Analysis

Data analysis was carried out using GraphPad prism software (La Jolla, CA, United States). Data are presented as mean ± SEM and analyzed using two-way ANOVA, followed by Sidak's or Turkey's multiple comparisons test. $^*P < 0.05$ was considered significant.

Technical Comments and Limitations

A critical step for setting up the four cellular model is timing and the revival and seeding of human neurons. Addition of the cells at incorrect timings will result in the model not working as effectively and TEER values will be lower than anticipated. We have therefore outlined a timeline for setting the model up (**Figure 2**), steps 4 and 5 can vary depending on the time taken for barrier formation to take place and for neurons to form neurite. Improper technique when seeding neurons on the coverslips will result in a lack of uniformity and inadequate neurite formation. Ensure coverslips are adequately air dried and neuronal cell suspension is carefully but adequately mixed during the revival and seeding process. Avoid removing neurons from the incubator for long periods.

When taking TEER values, ensure that the larger part of the STX probe does not touch the neurons cultured on the coverslip. This is especially important if multiple readings are being made (recommended). Utilization of neurons after primary experiments have been completed is also possible. Staining can be done on the coverslips using a variety of techniques including propidium iodide (PI) and DAPI staining, neurons can be lysed and intracellular assays can be performed.

RESULTS

Protocol Development

During BBB model development various set ups were compared including; insert pore size, plate size, and cell organization. **Figure 2** highlights stages in protocol development and their respective TEER values, prior to the addition of neurons into the model. **Figure 2A** shows that a larger pore size (3.0 μm) exhibited greater barrier integrity (as shown by greater TEER readings) than the smaller pore size (0.4 μm). Furthermore, the

12 well inserts displayed considerably greater TEER readings than the 24 well inserts. Continuing model development using 12 3.0 μm inserts, **Figure 2B** compares three different cell culture set-ups days after model establishment. On days three and four, the inserts containing a mixed culture of astrocytes and pericytes displayed significantly higher TEER readings than set-ups containing astrocytes or pericytes seeded on the underside of the inserts or the cell culture plate bottom, $P < 0.05$ and $P < 0.01$, respectively.

OGD Model Simulation

To assess the effect of having different cells present, changes in TEER from models D and E shown in **Figure 1**, were compared following an OGD protocol. **Figure 5A** highlights the different responses of a three cell and four cell model in response to a 4 h OGD protocol, followed by a reperfusion period. The three-cell mode exhibited approximately a 30% drop in TEER from baseline after 4 h OGD. This contrasts to the four-cell model which exhibited a 50% drop in TEER post OGD and was significantly different to the three-cell model $P < 0.05$. After OGD, when reperfusion was initiated, TEER was able to return to baseline in the three-cell model, however, BBB permeability only marginally recovered by 20% in the four-cell model. This was significantly different at 24 h ($P < 0.01$) but not 48 or 72 h. Images 5B and C show light microscope images of neurons in the four-cell model before and immediately after the OGD protocol, respectively. In **Figure 5C** neuronal clumping is clearly visible along with apparent neurite fragmentation compared to **Figure 5B** showing healthy neurons prior to OGD.

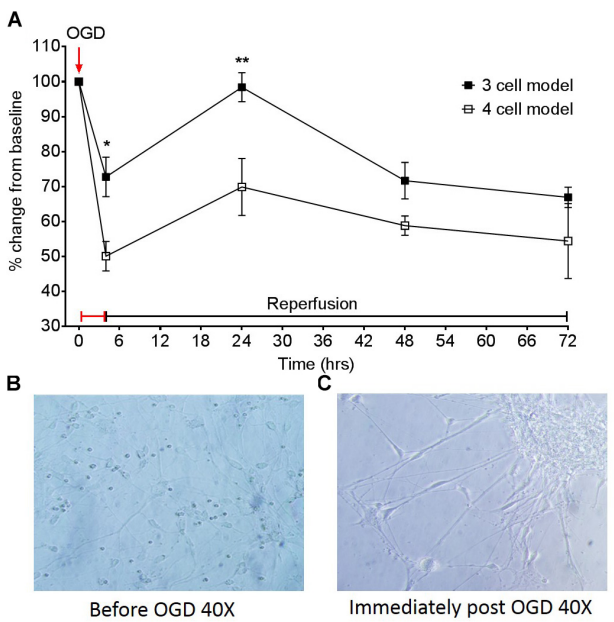

FIGURE 5 | (A) Effect of a 4 h oxygen-glucose deprivation (OGD) protocol on transepithelial resistance (TEER) as a marker of barrier tightness in a three cell model (HBMECs, astrocytes, and pericytes) and a four cell model (HBMECs, astrocytes, pericytes, and neurons). Neuronal images taken from the four cell model **(B)** before OGD 40× and **(C)** neuronal images immediately post OGD 40×. Data given as mean ± SEM, n = 3–6 from two experimental repeats, calculated as a % change from baseline TEER readings. Statistical analysis was conducted using 2-way ANOVA with Sidak's multiple comparisons test, $^{*}P < 0.05$ and $^{**}P < 0.01$ was considered significant.

Dexamethasone Application

Dexamethasone increased barrier tightness in all three models, as shown by increases in TEER and exhibiting overall significance as a result of drug interaction in the three cell and four cell model, $P < 0.05$. The two-cell model was the most unstable out of the three models, as shown by greater fluctuations and variability in TEER measurements (**Figure 6A**). The three-cell model was considerably more stable but differences in TEER between dexamethasone treated and control were only observed after 2 h (**Figure 6B**). The four-cell model was the fastest to exhibit an increase in barrier tightness (i.e., increased TEER) as a result of dexamethasone application (**Figure 6C**) and this reached significance compared to the vehicle control at 2 and 24 h ($P < 0.05$).

DISCUSSION

The BBB can be compromised in a range of different conditions, including but not limited to ischaemic stroke, Alzheimer's disease, cancer, and multiple sclerosis (MS). Research into these disorders that affect the BBB is plagued by translational difficulty, resulting in many potential compounds and/or therapies failing to surpass phase I/II clinical trials. This is at least partly due to a lack of suitable *in vitro* models that can predict drug effectiveness pre-clinically. Most, if not all, current BBB models exhibit "pitfalls" whether that be cost, time or resources. Models that offer the closest representation of the BBB are often complex and expensive to replicate, adding to the cost of the drug screening process. To help improve the translatability of *in vitro* data, we developed a transwell style model that incorporates four primary human cell types, representing the NVU more than other BBB models currently available. We found that our novel four-cell model was superior in modeling ischaemic stroke and drug application *in vitro* compared to a three-cell and a two-cell model as shown through changes in TEER as a measure of barrier integrity and dexamethasone application.

Implications for Drug Testing

The effect of dexamethasone was assessed in three transwell models; a two cell, three cell and four cell model. Greater instability in barrier strength and a slower response was exhibited by the two-cell model after dexamethasone application. This could also suggest that models containing just two cell types, in this case astrocytes and HBMECs, would also react differently to other drug applications and are therefore are not sufficient to truly model drug interactions at the BBB. Whilst the three-cell model shared the same trend in increasing barrier strength, it exhibited more stable TEER values compared to the two-cell model and dexamethasone

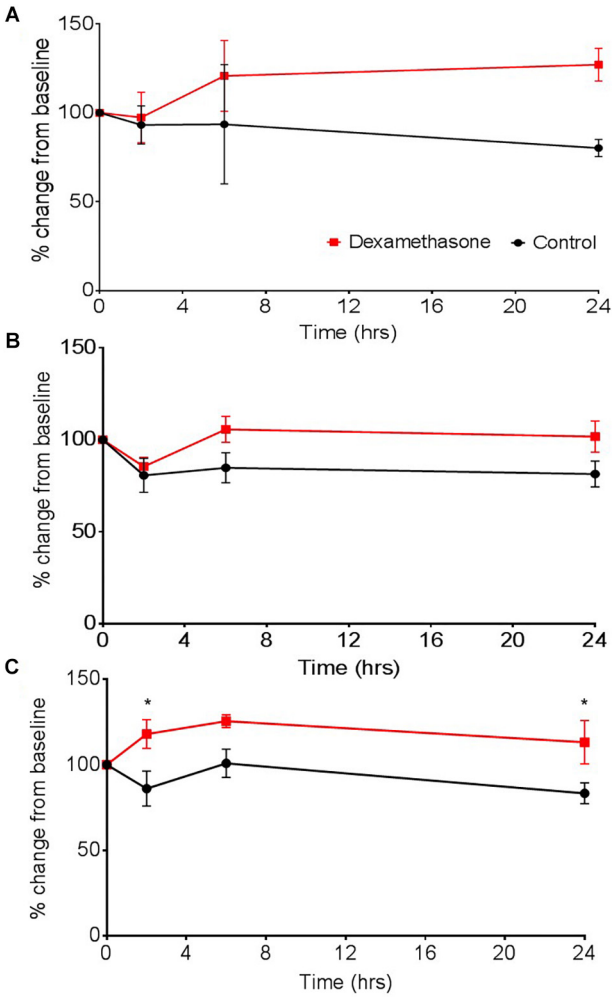

FIGURE 6 | The effect of dexamethasone on transepithelial resistance (TEER) as a measure of barrier tightness in **(A)** a two cell (astrocytes and HBMECs), **(B)** three cell (astrocytes, HBMECs, and pericytes), and **(C)** four cell model (astrocytes, HBMECs, pericytes, and neurons). Dexamethasone (1 μM) was added to the luminal side and used as positive control that is known to decrease permeability, thus increase TEER. Data represented as mean ± SEM, $n = 4$ from two experimental repeats. Statistical analysis was conducted using 2-way ANOVA with Sidak's multiple comparisons test, $^*P < 0.05$ was considered significant.

treated wells were overall significantly different to the vehicle control. Also, by introducing pericytes (generating a three cell model) there was a large increase in baseline TEER from 30 to 40 Ω, again highlighting the role of pericytes in strengthening vascular stability at the BBB and the need for their presence in BBB models (Bergers and Song, 2005; Dohgu et al., 2005; Nakagawa et al., 2007; Ferland-McCollough et al., 2017) Interestingly, the four-cell model exhibited a significant increase in barrier tightness (as shown by an increase in TEER) compared to the vehicle control at just 2 h after dexamethasone application. Although neurons in this model do not directly interact with the BBB, neurons have been shown to secrete a number of vasoactive substances, including VEGF, which influence barrier forming properties and early angiogenesis (Engelhardt, 2003; Eichmann and Thomas, 2013). These comparison data highlight the variations in data obtained from models containing different cell types and the impact this can have on drug screening. This stresses the importance of having a more representative BBB model containing additional cells present at the NVU.

Implications for Protocol Testing

Currently there are a wide range of *in vitro* BBB models available, but despite promising developments in modeling the BBB, there are still gaps in model design, primarily the inability to include all cell types present in the NVU. Whilst most transwell systems incorporate astrocytes and HBMECs, only more recent studies have introduced pericytes or neurons into these model designs. To gain a better understanding of how these cells contribute to the breakdown of the BBB in ischaemic conditions, we subjected our three cell and four cell models to an OGD protocol and measured TEER overtime to assess changes in barrier integrity. Interestingly, we found that with the presence of neurons our model exhibited a larger decrease in TEER compared to the three-cell model, which only contained astrocytes, pericytes and HBMECs. Similarly, whilst the three-cell model was able to recover 24 h post OGD the four-cell model only marginally recovered by approximately 20%, highlighting the role of and sensitivity of neurons in the level of damage ensued by the OGD protocol. Altogether, we have shown that with the addition of neurons our model became more vulnerable to damage; exhibiting a greater loss of barrier strength shown by a decrease in TEER, supporting previous work which showed that ischaemic neurons disrupt the endothelial barrier through increasing VEGF secretion (Li et al., 2014). Thus, omitting neurons from a BBB modeling stroke would underestimate the damage caused and contribution of neurons to the breakdown of the BBB post ischaemia.

Limitations and Future Development

Although our model now includes four cell present in the NVU, our model does not incorporate flow which is an important feature to maintain the BBB phenotype *in vitro*. Studies have shown that sheer stress is critical to increase cell longevity and influence cell phenotype, regulate BBB transport, preventing de-differentiation (Desai et al., 2002; Chiu et al., 2005; Partyka et al., 2017). Culturing HBMECs under physiological shear stress, is particularly important in a ischaemic stroke setting because there is an interruption in blood flow. Microfluidic systems that mimic physiological flow have the advantage in that they can simulate continuous flow improving translation to the environment (Partyka et al., 2017; Wang et al., 2017).

Equally, there is increasing evidence of the role of microglial cells in BBB breakdown. These resident brain immune cells have been shown to release pro-inflammatory mediators that increase barrier permeability and reduce levels of certain TJs, thus playing a key role in BBB breakdown in pathological states

(da Fonseca et al., 2014; Shigemoto-Mogami et al., 2018) Therefore, future work should assess whether additional cells and shear stress can be incorporated into transwell style models.

CONCLUSION

The overall function of the NVU is the perfusion of brain tissue to supply neurons with essential nutrients and the ability of neurons to regulate this blood flow. Glia, namely astrocytes, act as mediators between the vascular and neural compartments (Lo et al., 2015). Pericytes provide an extra level of communication between the endothelia and astrocytes as well as serving a prominent immune function (Darland et al., 2003; Armulik et al., 2011; Kovac et al., 2011). During cerebral ischaemia, these complex interactions are disrupted, and homeostasis is lost as a consequence of functional, morphological and metabolic changes within the NVU (Lo et al., 2015). It is important to model how these cells interact in both normoxic and ischaemic conditions to study the pathophysiology of ischaemic stroke. Finally, transwell systems offer noticeable advantages over the more complex models as they maintain the ease simpler cell culture set up and often use minimal resources. We believe our model offers a closer representation of the BBB, whilst maintaining the ease of a transwell setup.

DATA AVAILABILITY

The datasets generated for this study are available on request to the corresponding author.

AUTHOR CONTRIBUTIONS

NS performed the research. TE and SO'S designed the research study. NS and SO'S analyzed the data. NS, TE, and SO'S wrote the manuscript.

FUNDING

This work was supported by the Biotechnology and Biological Sciences Research Council (Grant No. BB/M008770/1).

REFERENCES

Abbott, N. J., Patabendige, A. A. K., Dolman, D. E. M., Yusof, S. R., and Begley, D. J. (2010). Structure and function of the blood-brain barrier. *Neurobiol. Dis.* 37, 13–25. doi: 10.1016/j.nbd.2009.07.030

Abbott, N. J., Rönnbäck, L., and Hansson, E. (2006). Astrocyte–endothelial interactions at the blood–brain barrier. *Nat. Rev. Neurosci.* 7, 41–53. doi: 10.1038/nrn1824

Allen, C. L., and Bayraktutan, U. (2009). Antioxidants attenuate hyperglycaemia-mediated brain endothelial cell dysfunction and blood-brain barrier hyperpermeability. *Diabetes Obes. Metab.* 11, 480–490. doi: 10.1111/j.1463-1326.2008.00987.x

Appelt-Menzel, A., Cubukova, A., Günther, K., Edenhofer, F., Piontek, J., Krause, G., et al. (2017). Establishment of a human blood-brain barrier co-culture model mimicking the neurovascular unit using induced pluri- and multipotent stem cells. *Stem Cell Rep.* 8, 894–906. doi: 10.1016/j.stemcr.2017.02.021

Armulik, A., Genové, G., and Betsholtz, C. (2011). Pericytes: developmental, physiological, and pathological perspectives, problems, and promises. *Dev. Cell* 21, 193–215. doi: 10.1016/j.devcel.2011.07.001

Attwell, D., Buchan, A. M., Charpak, S., Lauritzen, M., MacVicar, B. A., and Newman, E. A. (2010). Glial and neuronal control of brain blood flow. *Nature* 468, 232–243. doi: 10.1038/nature09613

Bergers, G., and Song, S. (2005). The role of pericytes in blood-vessel formation and maintenance. *Neuro. Oncol.* 7, 452–464. doi: 10.1215/S1152851705000232

Borges, N., Shi, F., Azevedo, I., and Audus, K. L. (1994). Changes in brain microvessel endothelial cell monolayer permeability induced by adrenergic drugs. *Eur. J. Pharmacol. Mol. Pharmacol.* 269, 243–248. doi: 10.1016/0922-4106(94)90092-2

Chiu, J. J., Chen, L. J., Chang, S. F., Lee, P. L., Lee, C. I., Tsai, M. C., et al. (2005). Shear stress inhibits smooth muscle cell-induced inflammatory gene expression in endothelial cells: Role of NF-κB. *Arterioscler. Thromb. Vasc. Biol.* 25, 963–969. doi: 10.1161/01.ATV.0000159703.43374.19

Cho, C. F., Wolfe, J. M., Fadzen, C. M., Calligaris, D., Hornburg, K., Chiocca, E. A., et al. (2017). Blood-brain-barrier spheroids as an in vitro screening platform for brain-penetrating agents. *Nat. Commun.* 8:15623. doi: 10.1038/ncomms15623

da Fonseca, A. C. C., Matias, D., Garcia, C., Amaral, R., Geraldo, L. H., Freitas, C., et al. (2014). The impact of microglial activation on blood-brain barrier in brain diseases. *Front. Cell. Neurosci.* 8:362. doi: 10.3389/fncel.2014.00362

Darland, D. C., Massingham, L. J., Smith, S. R., Piek, E., Saint-Geniez, M., and D'Amore, P. A. (2003). Pericyte production of cell-associated VEGF is differentiation-dependent and is associated with endothelial survival. *Dev. Biol.* 264, 275–288. doi: 10.1016/j.ydbio.2003.08.015

Desai, S. Y., Marroni, M., Cucullo, L., Krizanac-Bengez, L., Mayberg, M. R., Hossain, M. T., et al. (2002). Mechanisms of endothelial survival under shear stress. *Endothel. J. Endothel. Cell Res.* 9, 89–102. doi: 10.1080/10623320212004

Dohgu, S., Takata, F., Yamauchi, A., Nakagawa, S., Egawa, T., Naito, M., et al. (2005). Brain pericytes contribute to the induction and up-regulation of blood-brain barrier functions through transforming growth factor-β production. *Brain Res.* 1038, 208–215. doi: 10.1016/j.brainres.2005.01.027

Dore-Duffy, P. (2008). Pericytes: pluripotent cells of the blood brain barrier. *Curr. Pharm. Des.* 14, 1581–1593. doi: 10.2174/138161208784705469

Eichmann, A., and Thomas, J. L. (2013). Molecular parallels between neural and vascular development. *Cold Spring Harb. Perspect. Med.* 3:a006551. doi: 10.1101/cshperspect.a006551

Engelhardt, B. (2003). Development of the blood-brain barrier. *Cell Tissue Res.* 314, 119–129. doi: 10.1007/s00441-003-0751-z

Ferland-McCollough, D., Slater, S., Richard, J., Reni, C., and Mangialardi, G. (2017). Pericytes, an overlooked player in vascular pathobiology. *Pharmacol. Ther.* 171, 30–42. doi: 10.1016/j.pharmthera.2016.11.008

Gaillard, P. J., Voorwinden, L. H., Nielsen, J. L., Ivanov, A., Atsumi, R., Engman, H., et al. (2000). Establishment and functional characterization of an in vitro model of the blood-brain barrier, comprising a co-culture of brain capillary endothelial cells and astrocytes. *Eur. J. Pharm. Sci.* 12, 215–222. doi: 10.1016/S0928-0987(00)00123-8

Hartz, A. M. S., Miller, D. S., and Bauer, B. (2010). Restoring blood-brain barrier P-glycoprotein reduces brain amyloid- in a mouse model of alzheimer's disease. *Mol. Pharmacol.* 77, 715–723. doi: 10.1124/mol.109.061754

Hind, W. H. (2014). *The Effects of Cannabinoids on Blood-Brain Barrier Permeability in vitro*. Ph.D. thesis, University of Nottingham, Nottingham.

Hind, W. H., England, T. J., and O'Sullivan, S. E. (2016). Cannabidiol protects an in vitro model of the blood-brain barrier from oxygen-glucose deprivation via PPARγ and 5-HT1A receptors. *Br. J. Pharmacol.* 173, 815–825. doi: 10.1111/bph.13368

Hind, W. H., Tufarelli, C., Neophytou, M., Anderson, S. I., England, T. J., and O'Sullivan, S. E. (2015). Endocannabinoids modulate human blood-brain barrier permeability in vitro. *Br. J. Pharmacol.* 172, 3015–3027. doi: 10.1111/bph.13106

Kacem, K., Lacombe, P., Seylaz, J., and Bonvento, G. (1998). Structural organization of the perivascular astrocyte endfeet and their relationship with the endothelial glucose transporter: a confocal microscopy study. *Glia* 23, 1–10.

Kovac, A., Erickson, M. A., Banks, W. A., Neuwelt, E., Abbott, N., Abrey, L., et al. (2011). Brain microvascular pericytes are immunoactive in culture: cytokine, chemokine, nitric oxide, and LRP-1 expression in response to lipopolysaccharide. *J. Neuroinflam.* 8:139. doi: 10.1186/1742-2094-8-139

Li, Y. N., Pan, R., Qin, X. J., Yang, W. L., Qi, Z., Liu, W., et al. (2014). Ischemic neurons activate astrocytes to disrupt endothelial barrier via increasing VEGF expression. *J. Neurochem.* 129, 120–129. doi: 10.1111/jnc.12611

Liebner, S., Corada, M., Bangsow, T., Babbage, J., Taddei, A., Czupalla, C. J., et al. (2008). Wnt/β-catenin signaling controls development of the blood–brain barrier. *J. Cell. Biol.* 183, 409–417. doi: 10.1083/jcb.200806024

Lo, E., Mendelow, A., Sacco, R., and Wong, L. (2015). "7. The neurovascular unit and responses to ischaemia," in *Stroke*, eds J. Grotta, G. Albers, J. Broderickm, S. Kasner, E. Lo, R. Sacco, et al. (Amsterdam: Elsevier).

Macvicar, B. A., and Newman, E. A. (2015). Astrocyte regulation of blood flow in the brain. *Cold Spring Harb. Perspect. Biol.* 7, 1–15. doi: 10.1101/cshperspect.a020388

Martini, F., and Bartholomew, E. F. (2017). *Essentials of Anatomy & Physiology*. Amsterdam: Elsevier.

Nakagawa, S., Deli, M. A., Kawaguchi, H., Shimizudani, T., Shimono, T., Kittel, Á, et al. (2009). A new blood-brain barrier model using primary rat brain endothelial cells, pericytes and astrocytes. *Neurochem. Int.* 54, 253–263. doi: 10.1016/j.neuint.2008.12.002

Nakagawa, S., Deli, M. A., Nakao, S., Honda, M., Hayashi, K., Nakaoke, R., et al. (2007). Pericytes from brain microvessels strengthen the barrier integrity in primary cultures of rat brain endothelial cells. *Cell. Mol. Neurobiol.* 27:687. doi: 10.1007/s10571-007-9195-4

Niego, B., and Medcalf, R. L. (2013). Improved method for the preparation of a human cell-based, contact model of the blood-brain barrier*. *J. Vis. Exp.* 81:e50934. doi: 10.3791/50934

Nzou, G., Wicks, R. T., Wicks, E. E., Seale, S. A., Sane, C. H., Chen, A., et al. (2018). Human cortex spheroid with a functional blood brain barrier for high-throughput neurotoxicity screening and disease modeling. *Sci. Rep.* 8:7413. doi: 10.1038/s41598-018-25603-5

Oberheim, N. A., Takano, T., Han, X., He, W., Lin, J. H. C., Wang, F., et al. (2009). Uniquely hominid features of adult human astrocytes. *J. Neurosci.* 29, 3276–3287. doi: 10.1523/JNEUROSCI.4707-08.2009

Pardridge, W. M. (1999). Blood-brain barrier biology and methodology. *J. Neurovirol.* 5, 556–569. doi: 10.3109/13550289909021285

Partyka, P. P., Godsey, G. A., Galie, J. R., Kosciuk, M. C., Acharya, N. K., Nagele, R. G., et al. (2017). Mechanical stress regulates transport in a compliant 3D model of the blood-brain barrier. *Biomaterials* 115, 30–39. doi: 10.1016/j.biomaterials.2016.11.012

Pieper, C., Pieloch, P., and Galla, H. J. (2013). Pericytes support neutrophil transmigration via interleukin-8 across a porcine co-culture model of the blood-brain barrier. *Brain Res.* 1524, 1–11. doi: 10.1016/j.brainres.2013.05.047

Pyrgos, V., Mickiene, D., Sein, T., Cotton, M., Fransesconi, A., Mizrahi, I., et al. (2010). Effects of immunomodulatory and organism-associated molecules on the permeability of an in vitro blood-brain barrier model to amphotericin B and fluconazole. *Antimicrob. Agents Chemother.* 54, 1305–1310. doi: 10.1128/AAC.01263-09

Risau, W., Hallmann, R., and Albrecht, U. (1986). Differentiation-dependent expression of proteins in brain endothelium during development of the blood-brain barrier. *Dev. Biol.* 117, 537–545. doi: 10.1016/0012-1606(86)90321-0

Ruck, T., Bittner, S., and Meuth, S. G. (2015). Blood-brain barrier modeling: challenges and perspectives. *Neural Regen. Res.* 10, 889–891. doi: 10.4103/1673-5374.158342

Shi, L. Z., and Zheng, W. (2005). Establishment of an in vitro brain barrier epithelial transport system for pharmacological and toxicological study. *Brain Res.* 1057, 37–48. doi: 10.1016/j.brainres.2005.07.046

Shigemoto-Mogami, Y., Hoshikawa, K., and Sato, K. (2018). Activated microglia disrupt the blood-brain barrier and induce chemokines and cytokines in a rat in vitro model. *Front. Cell. Neurosci.* 12:494. doi: 10.3389/fncel.2018.00494

Srinivasan, B., Kolli, A. R., Esch, M. B., Abaci, H. E., Shuler, M. L., and Hickman, J. J. (2015). TEER measurement techniques for in vitro barrier model systems. *J. Lab. Autom.* 20, 107–126. doi: 10.1177/2211068214561025

Sweeney, M. D., Ayyadurai, S., and Zlokovic, B. V. (2016). Pericytes of the neurovascular unit: key functions and signaling pathways. *Nat. Neurosci.* 19, 771–783. doi: 10.1038/nn.4288

Thomsen, L. B., Burkhart, A., and Moos, T. (2015). A triple culture model of the blood-brain barrier using porcine brain endothelial cells, astrocytes and pericytes. *PLoS One* 10:e0134765. doi: 10.1371/journal.pone.0134765

Wang, Y., Wang, N., Cai, B., Wang, G. Y., Li, J., and Piao, X. X. (2015). In vitro model of the blood-brain barrier established by co-culture of primary cerebral microvascular endothelial and astrocyte cells. *Neural Regen. Res.* 10, 2011–2017. doi: 10.4103/1673-5374.172320

Wang, Y. I., Abaci, H. E., and Shuler, M. L. (2017). Microfluidic blood–brain barrier model provides in vivo-like barrier properties for drug permeability screening. *Biotechnol. Bioeng.* 114, 184–194. doi: 10.1002/bit.26045

Warren, M. S., Zerangue, N., Woodford, K., Roberts, L. M., Tate, E. H., Feng, B., et al. (2009). Comparative gene expression profiles of ABC transporters in brain microvessel endothelial cells and brain in five species including human. *Pharmacol. Res.* 59, 404–413. doi: 10.1016/j.phrs.2009.02.007

Weidenfeller, C., Svendsen, C. N., and Shusta, E. V. (2007). Differentiating embryonic neural progenitor cells induce blood-brain barrier properties. *J. Neurochem.* 101, 555–565. doi: 10.1111/j.1471-4159.2006.04394.x

Yeon, J. H., Na, D., Choi, K., Ryu, S. W., Choi, C., and Park, J. K. (2012). Reliable permeability assay system in a microfluidic device mimicking cerebral vasculatures. *Biomed. Microdevices.* 14, 1141–1148. doi: 10.1007/s10544-012-9680-5

Zhang, Y., Sloan, S. A., Clarke, L. E., Caneda, C., Plaza, C. A., Blumenthal, P. D., et al. (2016). Purification and characterization of progenitor and mature human astrocytes reveals transcriptional and functional differences with mouse. *Neuron* 89, 37–53. doi: 10.1016/j.neuron.2015.11.013

Zonta, M., Angulo, M. C., Gobbo, S., Rosengarten, B., Hossmann, K. A., Pozzan, T., et al. (2003). Neuron-to-astrocyte signaling is central to the dynamic control of brain microcirculation. *Nat. Neurosci.* 6, 43–50. doi: 10.1038/nn980

Conflict of Interest Statement: The authors declare that the research was conducted in the absence of any commercial or financial relationships that could be construed as a potential conflict of interest.

frontiers in Cellular Neuroscience

ORIGINAL RESEARCH
published: 03 July 2019
doi: 10.3389/fncel.2019.00299

Heterogeneity of Human Mast Cells With Respect to MRGPRX2 Receptor Expression and Function

Gilda Varricchi[1,2,3], Antonio Pecoraro[1†], Stefania Loffredo[1,2,3‡], Remo Poto[1§], Felice Rivellese[4‖], Arturo Genovese[1,2,3¶], Gianni Marone[1,2,3,5]* and Giuseppe Spadaro[1,2,3#]*

[1] Department of Translational Medical Sciences, University of Naples Federico II, Naples, Italy, [2] Center for Basic and Clinical Immunology Research (CISI), University of Naples Federico II, Naples, Italy, [3] World Allergy Organization Center of Excellence, University of Naples Federico II, Naples, Italy, [4] Center for Experimental Medicine and Rheumatology, William Harvey Research Institute, Barts and The London School of Medicine and Dentistry, Queen Mary University of London, London, United Kingdom, [5] Institute of Experimental Endocrinology and Oncology "Gaetano Salvatore", National Research Council (CNR), Naples, Italy

OPEN ACCESS

Edited by:
Rashid Giniatullin,
University of Eastern Finland, Finland

Reviewed by:
Elsa Fabbretti,
University of Trieste, Italy
Lorenzo Di Cesare Mannelli,
University of Florence, Italy

***Correspondence:**
Gilda Varricchi
gildanet@gmail.com
orcid.org/0000-0002-9285-4657
Gianni Marone
marone@unina.it
orcid.org/0000-0002-9849-4701
†orcid.org/0000-0003-3617-2819
‡orcid.org/0000-0002-5871-1898
§ orcid.org/0000-0002-4723-0167
‖orcid.org/0000-0002-6759-7521
¶ orcid.org/0000-0002-7821-2957
#orcid.org/0000-0001-7889-425

Specialty section:
This article was submitted to Non-Neuronal Cells, a section of the journal Frontiers in Cellular Neuroscience

Received: 12 March 2019
Accepted: 18 June 2019
Published: 03 July 2019

Citation:
Varricchi G, Pecoraro A, Loffredo S, Poto R, Rivellese F, Genovese A, Marone G and Spadaro G (2019) Heterogeneity of Human Mast Cells With Respect to MRGPRX2 Receptor Expression and Function. Front. Cell. Neurosci. 13:299. doi: 10.3389/fncel.2019.00299

Mast cells and their mediators play a role in the control of homeostasis and in the pathogenesis of several disorders. The concept of rodent mast cell heterogeneity, initially established in the mid-1960s has been extended in humans. Human mast cells isolated and purified from different anatomic sites can be activated *via* aggregation of cell surface high affinity IgE receptors (FcεRI) by antigens, superantigens, anti-IgE, and anti-FcεRI. MAS-related G protein-coupled receptor-X2 (MRGPRX2) is expressed at high level in human skin mast cells (MCs) (HSMCs), synovial MCs (HSyMCs), but not in lung MCs (HLMCs). MRGPX2 can be activated by neuropeptide substance P, several opioids, cationic drugs, and 48/80. Substance P (5×10^{-7} M – 5×10^{-6} M) induced histamine and tryptase release from HSMCs and to a lesser extent from HSyMCs, but not from HLMCs and human cardiac MCs (HHMCs). Morphine (10^{-5} M – 3×10^{-4} M) selectively induced histamine and tryptase release from HSMCs, but not from HLMCs and HHMCs. SP and morphine were incomplete secretagogues because they did not induce the *de novo* synthesis of arachidonic acid metabolites from human mast cells. In the same experiments anti-IgE (3 μg/ml) induced the release of histamine and tryptase and the *de novo* synthesis of prostaglandin D_2 (PGD_2) from HLMCs, HHMCs, HSyMCs, and HSMCs. By contrast, anti-IgE induced the production of leukotriene C_4 (LTC_4) from HLMCs, HHMCs, HSyMCs, but not from HSMCs. These results are compatible with the heterogeneous expression and function of MRGPRX2 receptor on primary human mast cells isolated from different anatomic sites.

Keywords: heart, histamine, leukotriene C_4, mast cells, MRGPRX2, prostaglandin D_2, substance P and tryptase

INTRODUCTION

Mast cells arise from stem cell-derived human mast cell progenitors in the bone marrow, circulate and complete their maturation in all vascularized tissues (Galli, 2016; Olivera et al., 2018). Mast cell differentiation, phenotypes and functions in tissues are largely determined by the microenvironment (e.g., cytokines, activating and inhibitory stimuli, chemokines)

(Mukai et al., 2018). Mast cells are canonically implicated in allergic disorders (Liccardi et al., 2003; Fujisawa et al., 2014; Bradding and Arthur, 2016; Canonica et al., 2016; Subramanian et al., 2016; Mukai et al., 2018), but also in several non allergic conditions including autoimmune disorders (de Paulis et al., 1996; Brown and Weinberg, 2018; Rivellese et al., 2018; Yu et al., 2018), cardiovascular diseases (Patella et al., 1996, 1998; Theoharides et al., 2011; Shi et al., 2015; Ngkelo et al., 2016), bacterial (Piliponsky and Romani, 2018) and viral diseases (Haidl and Marshall, 2015), neurological disorders (Skaper et al., 2014; Theoharides et al., 2016; Skaper et al., 2017; Conti et al., 2018), and cancer (Galdiero et al., 2016; Varricchi et al., 2017). Increasing evidence supports the role of mast cells and their mediators in neurogenic inflammation leading to pain and itch (Gupta and Harvima, 2018; Steinhoff et al., 2018; Yosipovitch et al., 2018).

Enerbäck first established the concept of mast cell heterogeneity through detailed morphological and histochemical studies (Enerback, 1966a,b,c). Two distinct subpopulations of rodent mast cells, connective tissue mast cells and mucosal mast cells, differ in their location, staining features, mediator content and responsiveness to activating stimuli (Enerback, 1966a,b,c; Tainsh and Pearce, 1992; Varricchi et al., 2016). Mast cells isolated and purified from several human tissues have led to the recognition of histochemical, functional, and immunological differences among these cells in humans (Church et al., 1982; Schwartz et al., 1987; Casolaro et al., 1989; Stellato et al., 1991; Bischoff and Dahinden, 1992). For example, activation of mast cells isolated from human lung (HLMCs) by antigens, anti-IgE and superantigens leads to arachidonic acid metabolism through both the cyclooxygenase (prostaglandin D_2, PGD_2) and the 5-lipoxygenase pathway (peptide leukotriene C_4, LTC_4) (Schulman et al., 1982; de Paulis et al., 1991; Stellato et al., 1992a), whereas HSMCs only synthesize PGD_2 (Benyon et al., 1987; Stellato et al., 1992b). Based on their protease composition, two types of human mast cells have been proposed: tryptase$^+$ chymase$^+$ cells (M_{TC}), and tryptase$^+$ chymase$^-$ (M_T), being the prototypes (Schwartz et al., 1987). However, this traditional classification is rather simplistic and mast cells show significant plasticity (Galli et al., 2011; Borriello et al., 2014). Indeed, analysis of human mast cell transcriptome demonstrated considerable greater heterogeneity across tissues than previously appreciated (Motakis et al., 2014; Dwyer et al., 2016). Moreover, recent evidence indicates that each of the two mast cell subsets originates from different precursors through several waves of mast cell differentiation, and that they display distinct surface receptors and mediators (Gentek et al., 2018; Li et al., 2018).

Human mast cells can be activated by the engagement of a plethora of receptors (Varricchi et al., 2018). Aggregation of cell surface FcεRI by antigens, anti-IgE or superantigens leads to the degranulation and the generation of newly synthesized lipid mediators, cytokines, angiogenic, and lymphangiogenic factors (Marone et al., 2006; Detoraki et al., 2009; Theoharides et al., 2010; Taracanova et al., 2018). The identification of MRGPRX2 receptor and its mouse orthologue Mrgprb2 has opened a new research avenue in mast cell biology (Tatemoto et al., 2006; Fujisawa et al., 2014; McNeil et al., 2015). MRGPRX2 can be activated by several ligands such as neuropeptides (e.g., substance P, VIP, etc.), opioids (i.e., morphine), cationic drugs (e.g., atracurium, icatibant), and 48/80 (Tatemoto et al., 2006; McNeil et al., 2015; Ali, 2017). A clinical relevance is emerging for MRGPRX2 because this receptor is implicated in drug reactions (McNeil et al., 2015) and is overexpressed in HSMCs of patients with chronic urticaria (Fujisawa et al., 2014). Gaudenzio et al. have elegantly demonstrated that substance P (SP) and IgE cross-linking (i.e., anti-IgE) induce distinct mast cell degranulation strategies in human primary MC cultures and mouse MCs (Gaudenzio et al., 2016). In this study we compared the patterns of responsiveness to anti-IgE and to MRGPRX2 agonists (SP and morphine) and the mediators synthesized by primary human lung (HLMCs), cardiac (HHMCs), skin (HSMCs), and synovial MCs (HSyMCs).

MATERIALS AND METHODS

Reagents

$HClO_4$ (Baker Chemical Co., Deventer, Netherlands), BSA, piperazine-N, N′-bis (2-ethanesulfonic acid), hyaluronidase, chymopapain, elastase type I, morphine, substance P, LTC_4, and PGD_2 (Sigma Chemical Co., St. Louis, MO), collagenase (Worthington Biochemical Co., Freehold, NJ), Hanks' balanced salt solution and fetal calf serum (FCS; GIBCO, Grand Island, NY), deoxyribonuclease I and pronase (Calbiochem, La Jolla, CA), RPMI 1640 with 25 mM HEPES buffer, Eagle's minimum essential medium (Flow Laboratories, Irvine, United Kingdom), Percoll (Pharmacia Fine Chemicals, Uppsala, Sweden), (^{3}H)-LCT_4 and (^{3}H)-PGD_2 (New England Nuclear, Boston, MA) were commercially purchased. CD117 MicroBead kit was purchased from Miltenyi Biotec (Bologna, Italy). Rabbit anti-IgE antibody was kindly donated by Dr. Kimishige Ishizaka (La Jolla Institute for Allergy and Immunology, La Jolla, CA). Rabbit anti-LTC_4 antibody was a gift of Dr. Lawrence M. Lichtenstein (The Johns Hopkins University, Baltimore, MD). Tryptase fluoro-enzyme immune assay (FEIA; Phadia Diagnostic AB, Uppsala, Sweden) was kindly donated by Kabi Pharmacia (Milan, Italy).

Buffers

The Pipes buffer used in these experiments was made by 25 mM Pipes, 110 mM NaCl, 5 mM KCl, pH 7.37 and referred to as P buffer. P2CG contains, in addition to P buffer, 2 mM $CaCl_2$ and 1 g/l dextrose (Patella et al., 1996); pH was titrated to 7.4 with sodium bicarbonate. PGMD contains 1 mM $MgCl_2$, 10 mg/l DNase, and 1 g/l gelatin in addition to P buffer, pH 7.37. The Tyrode's buffer was made by 12 mM $NaHCO_3$, 127 mM NaCl, 5 mM KCl, 0.5 mM NaH_2PO_4, 1 mM $MgCl_2$, 5 mM glucose, and 10 mM HEPES.

Isolation of HLMCs

The study was approved by the Ethics Committee of the University of Naples Federico II (N. 7/9). Macroscopically normal lung tissue obtained from patients undergoing lung resection for lung cancer was dissected free from pleura, bronchi, and blood vessels, minced into 5- to 10-mm fragments and dispersed into

a single cell suspension as previously described (de Paulis et al., 1991; Staiano et al., 2016). Yields with this technique ranged between 0.4×10^5 and 1.5×10^6 mast cells per g of wet tissue and purity between 1 and 8%. Mast cells of enhanced purity (10–65%) were obtained by flotation over discontinuous Percoll gradient. Mast cells were further purified using a CD117 MicroBead kit sorting system according to the manufacturer's instructions. Mast cell purities using this technique ranged from 85 to 98%.

Isolation of HSMCs

Skin obtained from patients undergoing either mastectomy for breast cancer or elective cosmetic surgery was separated from the subcutaneous fat by blunt dissection. The tissue was cut into 1- to 2-mm fragments dispersed into single cell suspension as previously described (de Paulis et al., 1992). Yields with this technique ranged between 0.1 and 0.9×10^6 mast cells/g of wet tissue and purities were between 4 and 8%. Mast cells were further purified using a CD117 MicroBead kit cell sorting system (Miltenyi Biotec, Bologna, Italy) according to the manufacturer's instructions. Mast cell purities using this technique ranged from 84 to 96%.

Isolation of HHMCs

The heart tissue used in this study was obtained from patients undergoing heart transplantation at the Deutsches Herzzentrum, Berlin, mostly for cardiomyopathy (Patella et al., 1998). The explanted heart, immediately immersed in cold (4°C) cardioplegic solution, was processed within 5–18 h of removal. Fat tissue, large vessels, and pericardium were removed. The tissue was finely minced into 2- to 5-mm fragments, suspended in P buffer (10 ml/g of wet tissue), and washed by centrifugation 3 times. After each centrifugation, the heart fragments were filtered through a 150-μm pore Nytex cloth (Tetko, Elmsford, NY). Fragments were incubated (15 min, 37°C) under constant stirring in P buffer containing 10 mg collagenase/g of wet tissue. At the end of the incubation the cell suspension was filtered through a 150-μm pore Nytex cloth and three additional cycles of enzymatic digestion were performed. After the last procedure, the cells were centrifuged (150 g, 22°C, 8 min) and filtered through a 60-μm pore Nytex cloth to remove large particles and large cells (mostly myocytes). Lastly, cells were washed twice in PGMD by centrifugation (150 g, 22°C, 8 min). Cell pellets were resuspended in P buffer containing 2% BSA and centrifuged (25 g, 22°C, 2 min) to remove sedimented myocytes. Myocytes (>100 μm long) were pelleted and discarded; supernatants containing endothelial cells, fibroblasts and mast cells were then collected and centrifuged (150 g, 22°C, 8 min). HHMCs were partially purified by flotation through a discontinuous Percoll gradient (Patella et al., 1998). The purity of these populations ranged from 0.1 to 18%. The enzymatic dispersion tissue yielded $\approx 5 \times 10^4$ mast cells per gram of heart tissue. HHMCs were further purified using a CD117 MicroBead kit sorting system. Mast cell purities using these techniques ranged from 26 to 58%.

Isolation of HSyMCs

The synovial tissue used in this study was obtained from patients with osteorthrites or rheumatoid arthritis undergoing synoviectomy. Resected joint tissue was immersed in P buffer (4°C) and was processed within 2 h of removal (de Paulis et al., 1996). Fat and fibrous tissue were removed and the tissue was finely minced into 2-5-mm fragments, suspended in P buffer (10 ml/g of wet tissue), and washed twice by centrifugation (150 g, 22°C, 8 min). The minced synovium was incubated (45 min at 37°C) with chymopapain (1 mg/ml) and pronase (0.5 mg/ml) in 1 ml Tyrode's buffer/g synovial tissue. Remaining tissue was digested for another 45 min at 37°C with collagenase (1 mg/ml). Cell suspensions were filtered twice through 200 μ pore Nytex cloth, centrifuged (200 g, 22°C, 8 min), and washed twice with P buffer. Yields with this technique ranged from 0.2×10^6 to 1.0×10^6 mast cells/g of wet tissue. HSyMCs were purified by discontinuous Percoll gradient (de Paulis et al., 1996). The purity of these populations ranged from 16 to 35%. Mast cells were further purified using a CD117 MicroBead kit sorting system. HSyMCs purities using these techniques ranged from 71 to 94%.

Histamine Release Assay

Cells ($\approx 3 \times 10^4$ mast cells per tube) were resuspended in P2CG, and 0.3 ml of the cell suspension were placed in 12×75 mm polyethylene tubes and warmed to 37°C; 0.2 ml of each prewarmed releasing stimulus (anti-IgE, substance P or morphine) was added, and incubation was continued at 37°C for 45 min (Patella et al., 1990). Cell were centrifuged (1000 g, 22°C, 2 min), and the supernatants were stored at −70°C for subsequent assay of histamine, tryptase, LTC_4 and PGD_2 content. Experiments with HSMCs were performed at 30°C as previously described (Stellato et al., 1992a). The cell-free supernatants were assayed for histamine with an automated fluorometric technique (Siraganian, 1974). The percent histamine release from mast cells was calculated as previously described (de Paulis et al., 1991; Varricchi et al., 2019). All values are based on means of duplicate determinations which differed by less than 10%.

Immunoassay of Tryptase, PGD_2, and LTC_4

Tryptase was analyzed by FEIA (Phadia Diagnostic AB, Uppsala, Sweden) (Stellato et al., 1992a). PGD_2 and LTC_4 were analyzed by radioimmunoassay (Patella et al., 1990; de Paulis et al., 1991). The anti-PGD_2 and anti-LTC_4 antibodies had less than 1% cross-reactivity to other eicosanoids (Patella et al., 1990; de Paulis et al., 1991). Data were normalized on total cell number.

Statistical Analysis

Values are expressed as means ± SEM. Statistical significance was assessed by using 1-way ANOVA (for data sets with Gaussian distribution) or Kruskal-Wallis test (for data sets without Gaussian distribution), followed by the Dunn multiple correction test. Results were analyzed with GraphPad Prism software (version 7.05: GraphPad Software, La Jolla, CA), and *p*-values of less than 0.05 were considered significant.

RESULTS

Heterogeneous Effects of Anti-IgE on the Activation of HLMCs, HSMCs, HHMCs, and HSyMCs

As previously reported (Peachell et al., 1988; de Paulis et al., 1996; Genovese et al., 2000; Varricchi et al., 2019), exposure of mast cells isolated from different anatomic sites (lung: HLMCs; skin: HSMCs; heart: HHMCs; synovial tissue: HSyMCs) to anti-IgE (10^{-1} to 3 μg/ml) resulted in a dose dependent release of histamine (data not shown). The ability of mast cells isolated from different human tissues to secrete histamine when challenged with anti-IgE indicates that they have IgE bound to FcεRI. **Figure 1** summarizes the release of preformed (histamine and tryptase) and *de novo* synthesized mediators (LTC_4 and PGD_2) from HLMCs, HLSMCs, HHMCs, and HSyMCs when challenged anti-IgE (3 μg/ml). All types of human mast cells examined released the same percent of histamine and tryptase (**Figures 1A,B**). By contrast, striking differences were found among different types of mast cells when we compared the *de novo* synthesis of lipid mediators. HSMCs did not produce LTC_4 compared to HLMCs ($p < 0.01$) and to HHMCs and HSyMCs ($p < 0.01$). Moreover, maximal stimulation of HHMCs and HSyMCs with anti-IgE led to the LTC_4 production of 20.2 ± 3.5 and 22.5 ± 4.4 ng/10^6 mast cells, respectively, which was significantly lower than HLMCs (51.5 ± 8.40 ng/10^6 cells; $p < 0.05$). Interestingly, the anti-IgE-mediated production of PGD_2 from HLMCs (52.3 ± 6.9 ng/10^6 mast cells) and HSMCs (39.0 ± 10.0 ng/10^6 mast cells) did not differ between the two groups. However, only the production of PGD_2 from HLMCs, but not HSMCs, was significantly higher than that produced by HHMCs (19.3 ± 4.5 ng/10^6 mast cells) and HSyMCs (21.3 ± 4.6 ng/10^6 mast cells) ($p < 0.01$). Collectively these results identify striking differences with respect to the release of different types of mediators in response to IgE-mediated stimuli among human mast cells isolated from different anatomic sites.

Heterogeneous Effects of Substance P on the Activation of HLMCs, HSMCs, HHMCs, and HSyMCs

Substance P (SP) has long been established as an inflammatory neuropeptide (O'Connor et al., 2004; Mashaghi et al., 2016) and potent endogenous pruritogen in mice and humans (Azimi et al., 2017; Gupta and Harvima, 2018; Yosipovitch et al., 2018). Although the classical receptor for SP is the neurokinin-1 receptor (NK-1R) (Douglas and Leeman, 2011), recent studies have demonstrated that SP activates MRGPRX2 receptor in addition to NK-1R to induce itch (Azimi et al., 2017). There

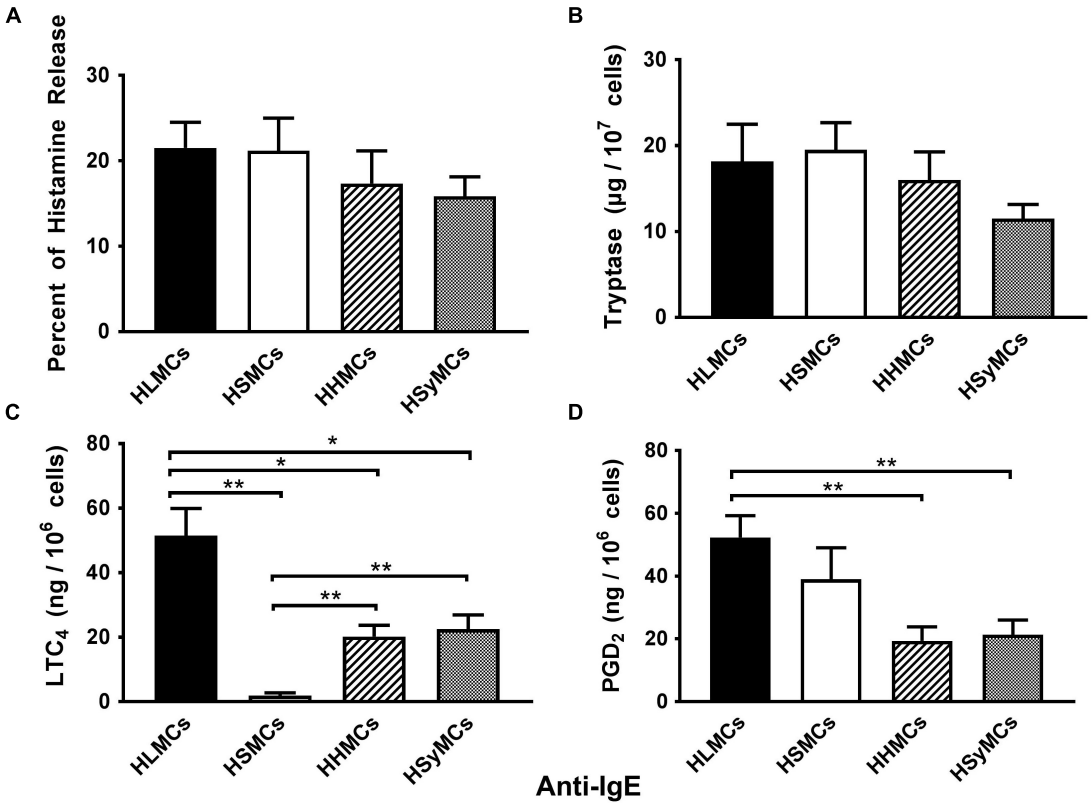

FIGURE 1 | Effects of maximal stimulation of anti-IgE (3 μg/ml) on the release of histamine **(A)**, tryptase **(B)** and the *de novo* synthesis of LTC_4 **(C)**, and PGD_2 **(D)** from HLMCs (black bars), HSMCs (open bars), HHMCs (dashed bars), and HSyMCs (dot bars). Each point represents the mean ± SEM of six experiments in duplicate. Statistical significance was determined by $^*p < 0.05$; $^{**}p < 0.01$.

is also evidence that SP can activate adventitial mast cells (Bot et al., 2010). Moreover, SP can be released into joint tissues from sensory nerve fibers (Pereira da Silva and Carmo-Fonseca, 1990; Gronblad et al., 1991) and its concentrations are increased in synovial fluid from patients with rheumatoid arthritis (Devillier et al., 1986). We therefore compared the effects of increasing concentrations (5×10^{-7} to 5×10^{-6} M) of SP on the activation of HLMCs, HSMCs, HHMCs, and HSyMCs. **Figure 2** shows that SP caused concentration-dependent histamine and tryptase release from HSMCs whereas it had no effect on both HLMCs and HHMCs. SP caused histamine and tryptase release from HSyMCs only at the higher concentrations (10^{-6} M and 5×10^{-6} M) examined. The percent histamine release from HSyMCs caused by the latter concentrations of SP was significantly lower ($p < 0.001$) than that induced from HSMCs. Interestingly, in these experiments SP did not induce the metabolism of arachidonic acid through the 5-lipoxygenase pathway (LTC_4) (**Figure 2C**) and the cyclooxygenase (PGD_2) (**Figure 2D**) in all types of mast cell examined.

Heterogeneous Effects of Morphine on the Activation of HLMCs, HSMCs, HHMCs, and HSyMCs

Opioid compounds bind to multiple receptors also present on several cells of innate and adaptive immunity where they exert immunomodulatory effects (Boland and Pockley, 2018; Plein and Rittner, 2018). Recent evidence indicates that several opioid compounds including morphine can activate the human LAD2 mast cell line through MRGPRX2 (Lansu et al., 2017). **Figure 3** shows the results of several experiments comparing the effects of increasing concentrations (10^{-5} to 3×10^{-4} M) of morphine on mediator release from primary HLMCs, HSMCs, and HHMCs. Morphine selectively induced histamine and tryptase release from HSMCs but not from HLMCs and HHMCs. Interestingly, morphine was an incomplete secretagogue because it did not induce the production of both LTC_4 and PGD_2 from all types of human mast cells.

DISCUSSION

The results of this study extends previous findings demonstrating the functional heterogeneity of human primary mast cells isolated from different anatomic sites with respect to FcεRI-mediated activation (Schwartz et al., 1987; Casolaro et al., 1989; Stellato et al., 1992a; Patella et al., 1998; Galli et al., 2011; Motakis et al., 2014). No differences were found with respect to anti-IgE-mediated release of preformed mediators (histamine and tryptase) from human primary mast cells purified from different anatomic sites. By contrast, striking differences were demonstrated among different types of mast cells with

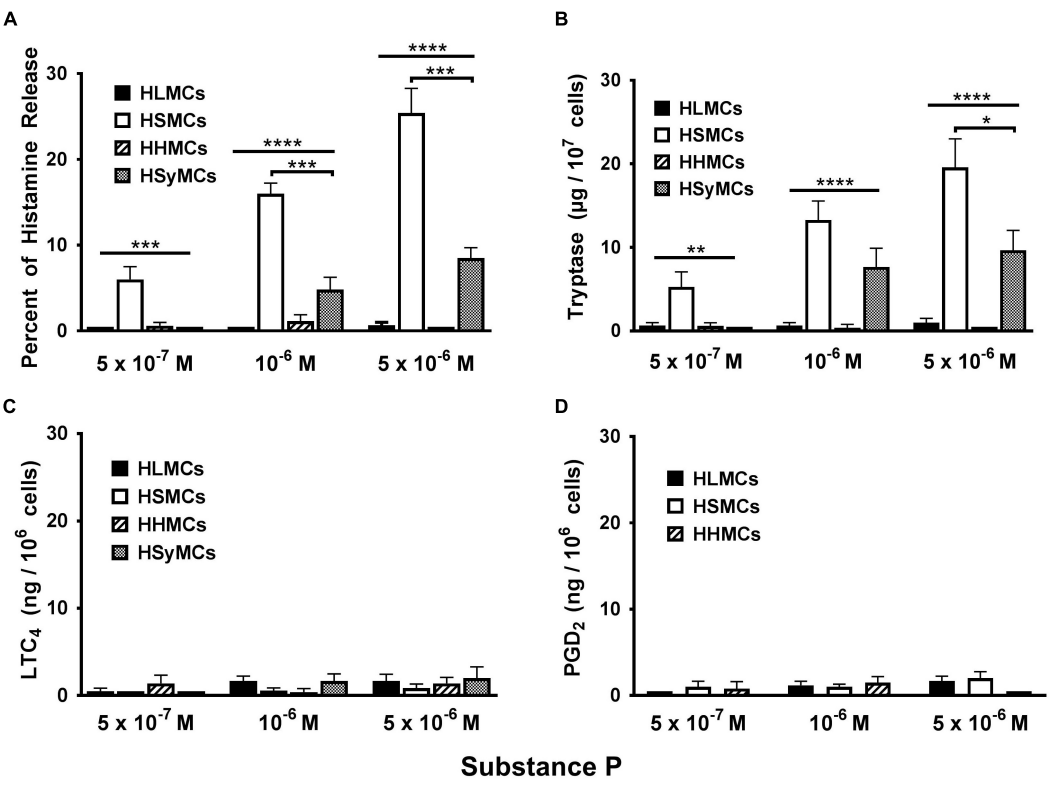

FIGURE 2 | Effects of increasing concentrations of substance P (5×10^{-7} M to 5×10^{-6} M) on the release of histamine **(A)**, tryptase **(B)**, and the *de novo* synthesis of LTC_4 **(C)**, and PGD_2 **(D)** from HLMCs, HSMCs, HHMCs, and HSyMCs. Each point represents the mean ± SEM of six experiments in duplicate. Statistical significance was determined by $^*p < 0.05$; $^{**}p < 0.01$; $^{***}p < 0.001$; $^{****}p < 0.0001$.

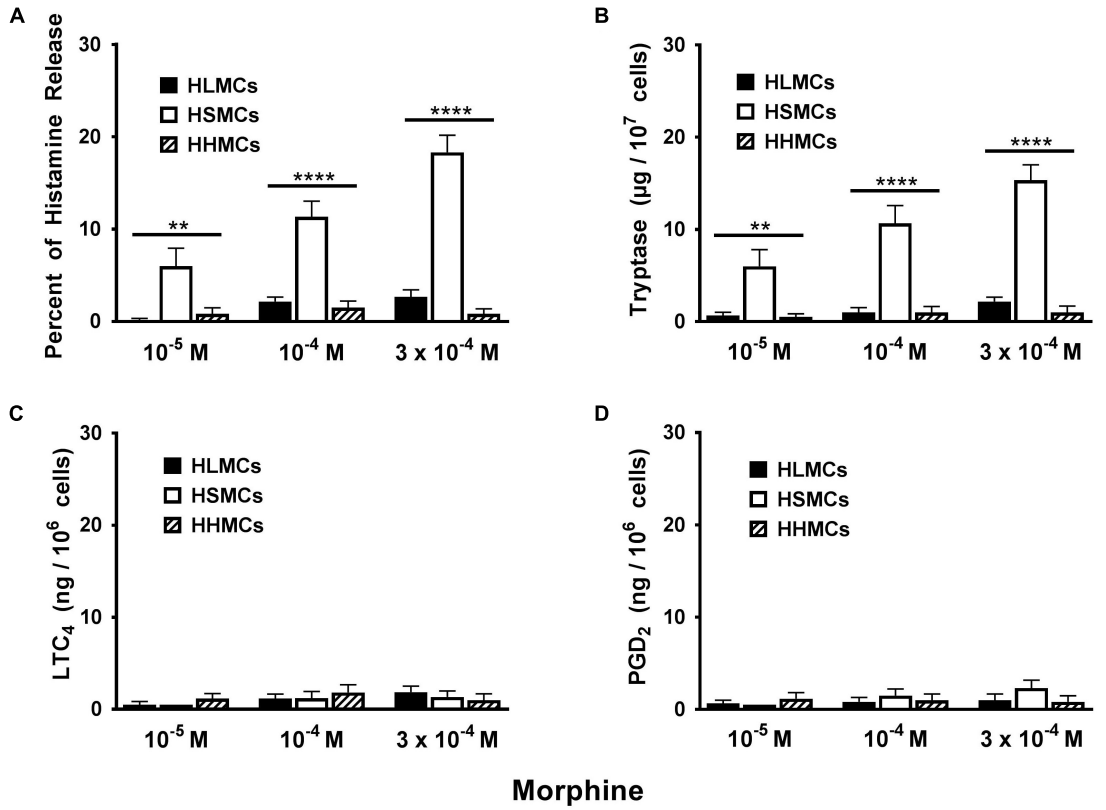

FIGURE 3 | Effects of increasing concentrations of morphine (10^{-5} M to 3×10^{-4} M) on the release of histamine **(A)**, tryptase **(B)** and the *de novo* synthesis of LTC_4 **(C)**, and PGD_2 **(D)** from HLMCs, HSMCs and HHMCs. Each point represents the mean ± SEM of six experiments in duplicate. Statistical significance was determined by $^{**}p < 0.01$; $^{****}p < 0.0001$.

respect to the anti-IgE-induced *de novo* synthesis of LTC_4 and PGD_2. Interestingly, LTC_4 is not produced by anti-IgE-activated HSMCs whereas these cells synthesize PGD_2. Moreover, the IgE-mediated production of both LTC_4 and PGD_2 from HLMCs was higher than that of HHMCs and HSyMCs. Collectively, these results suggest the existence of profound differences between the biochemical mechanisms that regulate the secretion of preformed mediators and the *de novo* production of lipid molecules among different types of human primary mast cells.

Tatemoto and coworkers first demonstrated the presence of MRGPRX2 mRNA in human skin and in human cord blood mast cells (CBMCs) (Tatemoto et al., 2006). They also found that several basic secretagogues, including SP, induced mast cell degranulation. They suggested that MRGPRX2 receptor is highly expressed in MC_{TC} compared to M_T. Since this initial observation several groups have demonstrated that various neuropeptides (e.g., VIP), endogenous and exogenous opioids (e.g., morphine), cationic drugs (e.g., icatibant, atracurium, ciprofloxacin), and 48/80 can activate human mast cells via the MRGPRX2 receptor (McNeil et al., 2015; Gaudenzio et al., 2016; Lansu et al., 2017; Okamura et al., 2017; Alkanfari et al., 2018). Interestingly the group of Theoharides has demonstrated that SP can synergistically potentiate the production of several cytokines (e.g., TNF-α, VEGF, IL-1β) by LAD2 mast cells (Theoharides et al., 2010; Taracanova et al., 2017, 2018).

The activating property of MRGPRX2 agonists has been evaluated in human LAD2 cell line (Guhl et al., 2005; Kulka et al., 2008; Theoharides et al., 2010; McNeil et al., 2015), human peripheral blood-derived cultured mast cells (PBCMCs) (Gaudenzio et al., 2016), and human CBMCs (Tatemoto et al., 2006). In the present study performed using primary mast cell isolated and purified from different human tissues, we found that two MRGPRX2 agonists, SP and morphine, selectively induce the release of preformed mediators (histamine and tryptase) from HSMCs, but not from HLMCs and HHMCs. These findings are consistent with the observation that the MRGPRX2 receptor is expressed in HSMCs but not in lung mast cells (Fujisawa et al., 2014; Babina et al., 2018). We also found that high concentrations of SP caused small but significant release of histamine and tryptase from HSyMCs. This observation could be of some interest because Okamura et al. have demonstrated that SP activates HSyMCs to release histamine and to produce PGD_2 (Lee et al., 2013) through the activation of MRGPRX2 (Okamura et al., 2017). In our study SP caused some release of preformed mediators (i.e., histamine and tryptase) from HSyMCs, but not the *de novo* synthesis of both PGD_2 and LTC_4. Several studies have suggested the involvement of SP

in experimental arthritis (Levine et al., 1984; Ahmed et al., 1995; Seegers et al., 2003) and in rheumatoid arthritis (Hernanz et al., 1993; Menkes et al., 1993; Miller et al., 2000; Grimsholm et al., 2005; Dirmeier et al., 2008). Further studies are needed to clarify the SP-mediated production of proinflammatory and immunomodulatory mediators from HSyMCs.

There is increasing evidence that cardiac mast cells play a role in several myocardial disorders (Patella et al., 1990, 1996, 1998; Theoharides et al., 2011; Shi et al., 2015; Ngkelo et al., 2016; Marino et al., 2017). It has been reported that SP induces adverse myocardial remodeling (Melendez et al., 2011) and intraplaque hemorrhage in atherosclerosis (Bot et al., 2010) *via* the activation of mast cells. Azimi and collaborators have implicated mast cell MRGPRX2 in human and experimental cardiometabolic disorders (Azimi et al., 2017). However, the mechanism(s) of SP-mediated vascular and cardiac mast cell activation remains controversial (Shi et al., 2017). In our study SP and morphine failed to induce the release of preformed and *de novo* synthesized mediators from partially purified HHMCs. Interestingly, we have previously demonstrated by immunoelectron microscopy the presence of both tryptase and chymase in human cardiac mast cells (Patella et al., 1995). Thus, although HHMCs contain both serine proteases, similarly to HSMCs, they differ from the latter in response to MRGPRX2 activators. Several explanations can justify this intriguing observation: first, the possibility of the existence of MRGPRX2 variants expressed in different types of human mast cells (Alkanfari et al., 2018) cannot be excluded; second, the complex enzymatic and mechanical procedure to purify HHMCs might alter the expression and function of MRGPRX2 both at the plasma membrane and intracellular sites (Fujisawa et al., 2014). We are presently investigating the surface and intracellular localization of MRGPRX2 in HHMCs to explain the apparent lack of functional effects of SP and morphine on these cells.

Increasing evidence supports the role of mast cells in neurogenic inflammation (Skaper et al., 2014; Skaper et al., 2017) leading to itch and pain (Vincent et al., 2013; Gupta and Harvima, 2018; Yosipovitch et al., 2018). Nerve fibers release proinflammatory and vasoactive neuropeptides such as SP (Rosa and Fantozzi, 2013; Skaper et al., 2017), which can activate mast cells. These cells release algogenic and pruritogenic mediators such as tryptase and histamine (Yosipovitch et al., 2018), which activate specific nociceptors on sensory nerve fibers (Vergnolle et al., 2001; Rosa and Fantozzi, 2013). There is increasing evidence that SP is linked to itch and pain through activation of MRGPRX2 on mast cells and sensory neurons (Azimi et al., 2016, 2017). We found that SP is a potent activator of the release of both histamine and tryptase from HSMCs that highly express MRGPRX2 (Fujisawa et al., 2014). The role of tryptase is particularly relevant because this protease activates the PAR2 receptor on nerve endings (Vergnolle et al., 2001; Zhang et al., 2012) stimulating the release of SP and other neuropeptides (Steinhoff et al., 2000) that activate nociceptors on nerve terminals as well as mast cells in a paracrine manner. Moreover, *in vivo* administration of morphine can induce histamine release (Baldo and Pham, 2012; Kumar and Singh, 2013) and itching in humans presumably *via* MRGPRX2-mediated HSMC activation.

Our study has some limitations which have to be pointed out. It was performed using primary mast cells isolated from several tissues (i.e., lung, heart, synovial, skin) obtained from different patients. Moreover, these mast cells might have different characteristics from cells obtained from healthy donors. Finally, the mechanical and enzymatic procedures to isolate mast cells from different anatomic sites are quite different. We cannot exclude the possibility that the techniques used to isolate and purify mast cells from different tissues might explain, at least in part, their different response to MRGPRX2 activation.

In conclusion, the results of this study demonstrate that there is greater functional heterogeneity of primary human mast cells across tissues than previously appreciated. First, we extend previous findings demonstrating heterogeneity when different types of human mast cells are activated *via* aggregation of FcεRI by anti-IgE. Second, there is heterogeneity of *de novo* synthesized mediators produced by different human mast cells activated by IgE-cross-linking. Third, there is heterogeneity of human mast cells with respect to MRGPRX2 activation. Additional studies are needed to examine the intracellular and membrane expression of MRGPRX2 in different types of primary human mast cells.

DATA AVAILABILITY

The datasets for this study will not be made publicly available because Some of the data are part of a patent.

AUTHOR CONTRIBUTIONS

GV, AG, SL, RP, GM, and GS have conceived and designed the study. GV, AP, SL, RP, FR, and GM performed the experiments. AP performed the statistical analysis of the results. AP and GM elaborated the figures. All the authors contributed intellectually and to the writing of the final version of the manuscript.

FUNDING

This work was supported partly by grants from the Regione Campania CISI-Lab Project, CRèME Project and TIMING Project.

ACKNOWLEDGMENTS

GM would like to thank Dr. Lawrence M. Lichtenstein for illuminating advice in the initial studies on human skin and synovial mast cells. Special thanks to Dr. Gjada Criscuolo for critical reading of the manuscript and to the administrative staff (Dr. Roberto Bifulco and Dr. Anna Ferraro), without whom we could not function as an integrated team.

REFERENCES

Ahmed, M., Bjurholm, A., Schultzberg, M., Theodorsson, E., and Kreicbergs, A. (1995). Increased levels of substance P and calcitonin gene-related peptide in rat adjuvant arthritis. A combined immunohistochemical and radioimmunoassay analysis. *Arthritis Rheum.* 38, 699–709. doi: 10.1002/art.1780380519

Ali, H. (2017). Emerging roles for MAS-related G protein-coupled receptor-X2 in host defense peptide, opioid, and neuropeptide-mediated inflammatory reactions. *Adv. Immunol.* 136, 123–162. doi: 10.1016/bs.ai.2017.06.002

Alkanfari, I., Gupta, K., Jahan, T., and Ali, H. (2018). Naturally occurring missense MRGPRX2 variants display loss of function phenotype for mast cell degranulation in response to substance P, Hemokinin-1, Human beta-Defensin-3, and Icatibant. *J. Immunol.* 201, 343–349. doi: 10.4049/jimmunol.1701793

Azimi, E., Reddy, V. B., Pereira, P. J. S., Talbot, S., Woolf, C. J., and Lerner, E. A. (2017). Substance P activates Mas-related G protein-coupled receptors to induce itch. *J. Allergy Clin. Immunol.* 140, 447.e3–453.e3. doi: 10.1016/j.jaci.2016.12.980

Azimi, E., Reddy, V. B., Shade, K. C., Anthony, R. M., Talbot, S., Pereira, P. J., et al. (2016). Dual action of neurokinin-1 antagonists on Mas-related GPCRs. *JCI Insight* 1:e89362. doi: 10.1172/jci.insight.89362

Babina, M., Guhl, S., Artuc, M., and Zuberbier, T. (2018). Allergic FcepsilonRI- and pseudo-allergic MRGPRX2-triggered mast cell activation routes are independent and inversely regulated by SCF. *Allergy* 73, 256–260. doi: 10.1111/all.13301

Baldo, B. A., and Pham, N. H. (2012). Histamine-releasing and allergenic properties of opioid analgesic drugs: resolving the two. *Anaesth. Intensive Care* 40, 216–235. doi: 10.1177/0310057x1204000204

Benyon, R. C., Lowman, M. A., and Church, M. K. (1987). Human skin mast cells: their dispersion, purification, and secretory characterization. *J. Immunol.* 138, 861–867.

Bischoff, S. C., and Dahinden, C. A. (1992). c-kit ligand: a unique potentiator of mediator release by human lung mast cells. *J. Exp. Med.* 175, 237–244. doi: 10.1084/jem.175.1.237

Boland, J. W., and Pockley, A. G. (2018). Influence of opioids on immune function in patients with cancer pain: from bench to bedside. *Br. J. Pharmacol.* 175, 2726–2736. doi: 10.1111/bph.13903

Borriello, F., Granata, F., Varricchi, G., Genovese, A., Triggiani, M., and Marone, G. (2014). Immunopharmacological modulation of mast cells. *Curr. Opin. Pharmacol.* 17, 45–57. doi: 10.1016/j.coph.2014.07.002

Bot, I., de Jager, S. C., Bot, M., van Heiningen, S. H., de Groot, P., Veldhuizen, R. W., et al. (2010). The neuropeptide substance P mediates adventitial mast cell activation and induces intraplaque hemorrhage in advanced atherosclerosis. *Circ. Res.* 106, 89–92. doi: 10.1161/CIRCRESAHA.109.204875

Bradding, P., and Arthur, G. (2016). Mast cells in asthma–state of the art. *Clin. Exp. Allergy* 46, 194–263. doi: 10.1111/cea.12675

Brown, M. A., and Weinberg, R. B. (2018). Mast cells and innate lymphoid cells: underappreciated players in CNS autoimmune demyelinating disease. *Front. Immunol.* 9:514. doi: 10.3389/fimmu.2018.00514

Canonica, G. W., Senna, G., Mitchell, P. D., O'Byrne, P. M., Passalacqua, G., and Varricchi, G. (2016). Therapeutic interventions in severe asthma. *World Allergy Organ J.* 9:40. doi: 10.1186/s40413-016-0130-3

Casolaro, V., Galeone, D., Giacummo, A., Sanduzzi, A., Melillo, G., and Marone, G. (1989). Human basophil/mast cell releasability. V. Functional comparisons of cells obtained from peripheral blood, lung parenchyma, and bronchoalveolar lavage in asthmatics. *Am. Rev. Respir. Dis.* 139, 1375–1382. doi: 10.1164/ajrccm/139.6.1375

Church, M. K., Pao, G. J., and Holgate, S. T. (1982). Characterization of histamine secretion from mechanically dispersed human lung mast cells: effects of anti-IgE, calcium ionophore A23187, compound 48/80, and basic polypeptides. *J. Immunol.* 129, 2116–2121.

Conti, P., Caraffa, A., Ronconi, G., Conti, C. M., Kritas, S. K., Mastrangelo, F., et al. (2018). Impact of mast cells in depression disorder: inhibitory effect of IL-37 (new frontiers). *Immunol. Res.* 66, 323–331. doi: 10.1007/s12026-018-9004-9

de Paulis, A., Cirillo, R., Ciccarelli, A., de Crescenzo, G., Oriente, A., and Marone, G. (1991). Characterization of the anti-inflammatory effect of FK-506 on human mast cells. *J. Immunol.* 147, 4278–4285.

de Paulis, A., Marino, I., Ciccarelli, A., de Crescenzo, G., Concardi, M., Verga, L., et al. (1996). Human synovial mast cells. I. Ultrastructural in situ and in vitro immunologic characterization. *Arthritis Rheum.* 39, 1222–1233. doi: 10.1002/art.1780390723

de Paulis, A., Stellato, C., Cirillo, R., Ciccarelli, A., Oriente, A., and Marone, G. (1992). Anti-inflammatory effect of FK-506 on human skin mast cells. *J. Invest. Dermatol.* 99, 723–728.

Detoraki, A., Staiano, R. I., Granata, F., Giannattasio, G., Prevete, N., de Paulis, A., et al. (2009). Vascular endothelial growth factors synthesized by human lung mast cells exert angiogenic effects. *J. Allergy Clin. Immunol.* 123, 1142–1149. doi: 10.1016/j.jaci.2009.01.044

Devillier, P., Regoli, D., Asseraf, A., Descours, B., Marsac, J., and Renoux, M. (1986). Histamine release and local responses of rat and human skin to substance P and other mammalian tachykinins. *Pharmacology* 32, 340–347. doi: 10.1159/000138190

Dirmeier, M., Capellino, S., Schubert, T., Angele, P., Anders, S., and Straub, R. H. (2008). Lower density of synovial nerve fibres positive for calcitonin gene-related peptide relative to substance P in rheumatoid arthritis but not in osteoarthritis. *Rheumatology* 47, 36–40. doi: 10.1093/rheumatology/kem301

Douglas, S. D., and Leeman, S. E. (2011). Neurokinin-1 receptor: functional significance in the immune system in reference to selected infections and inflammation. *Ann. N. Y. Acad. Sci.* 1217, 83–95. doi: 10.1111/j.1749-6632.2010.05826.x

Dwyer, D. F., Barrett, N. A., and Austen, K. F. (2016). Expression profiling of constitutive mast cells reveals a unique identity within the immune system. *Nat. Immunol.* 17, 878–887. doi: 10.1038/ni.3445

Enerback, L. (1966a). Mast cells in rat gastrointestinal mucosa. 1. Effects of fixation. *Acta Pathol. Microbiol. Scand.* 66, 289–302. doi: 10.1111/apm.1966.66.3.289

Enerback, L. (1966b). Mast cells in rat gastrointestinal mucosa. 2. Dye-binding and metachromatic properties. *Acta Pathol. Microbiol. Scand.* 66, 303–312. doi: 10.1111/apm.1966.66.3.303

Enerback, L. (1966c). Mast cells in rat gastrointestinal mucosa. 3. Reactivity towards compound 48/80. *Acta Pathol. Microbiol. Scand.* 66, 313–322. doi: 10.1111/apm.1966.66.3.313

Fujisawa, D., Kashiwakura, J., Kita, H., Kikukawa, Y., Fujitani, Y., Sasaki-Sakamoto, T., et al. (2014). Expression of Mas-related gene X2 on mast cells is upregulated in the skin of patients with severe chronic urticaria. *J. Allergy Clin. Immunol.* 134, 622.e9–633.e9. doi: 10.1016/j.jaci.2014.05.004

Galdiero, M. R., Varricchi, G., and Marone, G. (2016). The immune network in thyroid cancer. *Oncoimmunology* 5:e1168556. doi: 10.1080/2162402X.2016.1168556

Galli, S. J. (2016). The mast cell-IgE paradox: from homeostasis to anaphylaxis. *Am. J. Pathol.* 186, 212–224. doi: 10.1016/j.ajpath.2015.07.025

Galli, S. J., Borregaard, N., and Wynn, T. A. (2011). Phenotypic and functional plasticity of cells of innate immunity: macrophages, mast cells and neutrophils. *Nat. Immunol.* 12, 1035–1044. doi: 10.1038/ni.2109

Gaudenzio, N., Sibilano, R., Marichal, T., Starkl, P., Reber, L. L., Cenac, N., et al. (2016). Different activation signals induce distinct mast cell degranulation strategies. *J. Clin. Invest.* 126, 3981–3998. doi: 10.1172/JCI85538

Genovese, A., Bouvet, J. P., Florio, G., Lamparter-Schummert, B., Björck, L., and Marone, G. (2000). Bacterial immunoglobulin superantigen proteins A and L activate human heart mast cells by interacting with immunoglobulin E. *Infect. Immun.* 68, 5517–5524. doi: 10.1128/iai.68.10.5517-5524.2000

Gentek, R., Ghigo, C., Hoeffel, G., Bulle, M. J., Msallam, R., Gautier, G., et al. (2018). Hemogenic endothelial fate mapping reveals dual developmental origin of mast cells. *Immunity* 48, 1160.e–1171.e. doi: 10.1016/j.immuni.2018.04.025

Grimsholm, O., Rantapaa-Dahlqvist, S., and Forsgren, S. (2005). Levels of gastrin-releasing peptide and substance P in synovial fluid and serum correlate with levels of cytokines in rheumatoid arthritis. *Arthritis Res. Ther.* 7, R416–R426. doi: 10.1186/ar1503

Gronblad, M., Korkala, O., Konttinen, Y. T., Nederstrom, A., Hukkanen, M., Tolvanen, E., et al. (1991). Silver impregnation and immunohistochemical study of nerves in lumbar facet joint plical tissue. *Spine* 16, 34–38. doi: 10.1097/00007632-199101000-00006

Guhl, S., Lee, H. H., Babina, M., Henz, B. M., and Zuberbier, T. (2005). Evidence for a restricted rather than generalized stimulatory response of skin-derived human mast cells to substance P. *J. Neuroimmunol.* 163, 92–101. doi: 10.1016/j.jneuroim.2005.02.015

Gupta, K., and Harvima, I. T. (2018). Mast cell-neural interactions contribute to pain and itch. *Immunol. Rev.* 282, 168–187. doi: 10.1111/imr.12622

Haidl, I. D., and Marshall, J. S. (2015). Human mast cell activation with viruses and pathogen products. *Methods Mol. Biol.* 1220, 179–201. doi: 10.1007/978-1-4939-1568-2_12

Hernanz, A., De Miguel, E., Romera, N., Perez-Ayala, C., Gijon, J., and Arnalich, F. (1993). Calcitonin gene-related peptide II, substance P and vasoactive intestinal peptide in plasma and synovial fluid from patients with inflammatory joint disease. *Br. J. Rheumatol.* 32, 31–35. doi: 10.1093/rheumatology/32.1.31

Kulka, M., Sheen, C. H., Tancowny, B. P., Grammer, L. C., and Schleimer, R. P. (2008). Neuropeptides activate human mast cell degranulation and chemokine production. *Immunology.* 123, 398–410. doi: 10.1111/j.1365-2567.2007.02705.x

Kumar, K., and Singh, S. I. (2013). Neuraxial opioid-induced pruritus: an update. *J. Anaesthesiol. Clin. Pharmacol.* 29, 303–307. doi: 10.4103/0970-9185.117045

Lansu, K., Karpiak, J., Liu, J., Huang, X. P., McCorvy, J. D., Kroeze, W. K., et al. (2017). In silico design of novel probes for the atypical opioid receptor MRGPRX2. *Nat. Chem. Biol.* 13, 529–536. doi: 10.1038/nchembio.2334

Lee, H., Kashiwakura, J., Matsuda, A., Watanabe, Y., Sakamoto-Sasaki, T., Matsumoto, K., et al. (2013). Activation of human synovial mast cells from rheumatoid arthritis or osteoarthritis patients in response to aggregated IgG through Fcgamma receptor I and Fcgamma receptor II. *Arthritis Rheum.* 65, 109–119. doi: 10.1002/art.37741

Levine, J. D., Clark, R., Devor, M., Helms, C., Moskowitz, M. A., and Basbaum, A. I. (1984). Intraneuronal substance P contributes to the severity of experimental arthritis. *Science* 226, 547–549. doi: 10.1126/science.6208609

Li, Z., Liu, S., Xu, J., Zhang, X., Han, D., Liu, J., et al. (2018). Adult connective tissue-resident mast cells originate from late erythro-myeloid progenitors. *Immunity* 49, 640–653. doi: 10.1016/j.immuni.2018.09.023

Liccardi, G., Salzillo, A., Spadaro, G., Senna, G., Canonica, W. G., D'Amato, G., et al. (2003). Anaphylaxis caused by skin prick testing with aeroallergens: case report and evaluation of the risk in Italian allergy services. *J. Allergy Clin. Immunol.* 111, 1410–1412. doi: 10.1067/mai.2003.1521

Marino, A., Sakamoto, T., Robador, P. A., Tomita, K., and Levi, R. (2017). S1P receptor 1-mediated anti-renin-angiotensin system cardioprotection: pivotal role of mast cell aldehyde dehydrogenase type 2. *J. Pharmacol. Exp. Ther.* 362, 230–242. doi: 10.1124/jpet.117.241976

Marone, G., Spadaro, G., Liccardo, B., Rossi, F. W., D'Orio, C., and Detoraki, A. (2006). Superallergens: a new mechanism of immunologic activation of human basophils and mast cells. *Inflamm. Res.* 55(Suppl. 1), S25–S27. doi: 10.1007/s00011-005-0025-1

Mashaghi, A., Marmalidou, A., Tehrani, M., Grace, P. M., Pothoulakis, C., and Dana, R. (2016). Neuropeptide substance P and the immune response. *Cell Mol. Life Sci.* 73, 4249–4264. doi: 10.1007/s00018-016-2293-z

McNeil, B. D., Pundir, P., Meeker, S., Han, L., Undem, B. J., Kulka, M., et al. (2015). Identification of a mast-cell-specific receptor crucial for pseudo-allergic drug reactions. *Nature* 519, 237–241. doi: 10.1038/nature14022

Melendez, G. C., Li, J., Law, B. A., Janicki, J. S., Supowit, S. C., and Levick, S. P. (2011). Substance P induces adverse myocardial remodelling via a mechanism involving cardiac mast cells. *Cardiovasc. Res.* 92, 420–429. doi: 10.1093/cvr/cvr244

Menkes, C. J., Renoux, M., Laoussadi, S., Mauborgne, A., Bruxelle, J., and Cesselin, F. (1993). Substance P levels in the synovium and synovial fluid from patients with rheumatoid arthritis and osteoarthritis. *J. Rheumatol.* 20, 714–717.

Miller, L. E., Justen, H. P., Scholmerich, J., and Straub, R. H. (2000). The loss of sympathetic nerve fibers in the synovial tissue of patients with rheumatoid arthritis is accompanied by increased norepinephrine release from synovial macrophages. *FASEB J.* 14, 2097–2107. doi: 10.1096/fj.99-1082com

Motakis, E., Guhl, S., Ishizu, Y., Itoh, M., Kawaji, H., de Hoon, M., et al. (2014). Redefinition of the human mast cell transcriptome by deep-CAGE sequencing. *Blood* 123, e58–e67. doi: 10.1182/blood-2013-02-483792

Mukai, K., Tsai, M., Saito, H., and Galli, S. J. (2018). Mast cells as sources of cytokines, chemokines, and growth factors. *Immunol. Rev.* 282, 121–150. doi: 10.1111/imr.12634

Ngkelo, A., Richart, A., Kirk, J. A., Bonnin, P., Vilar, J., Lemitre, M., et al. (2016). Mast cells regulate myofilament calcium sensitization and heart function after myocardial infarction. *J. Exp. Med.* 213, 1353–1374. doi: 10.1084/jem.20160081

O'Connor, T. M., O'Connell, J., O'Brien, D. I., Goode, T., Bredin, C. P., and Shanahan, F. (2004). The role of substance P in inflammatory disease. *J. Cell Physiol.* 201, 167–180. doi: 10.1002/jcp.20061

Okamura, Y., Mishima, S., Kashiwakura, J. I., Sasaki-Sakamoto, T., Toyoshima, S., Kuroda, K., et al. (2017). The dual regulation of substance P-mediated inflammation via human synovial mast cells in rheumatoid arthritis. *Allergol. Int.* 66S, S9–S20. doi: 10.1016/j.alit.2017.03.002

Olivera, A., Beaven, M. A., and Metcalfe, D. D. (2018). Mast cells signal their importance in health and disease. *J. Allergy Clin. Immunol.* 142, 381–393. doi: 10.1016/j.jaci.2018.01.034

Patella, V., Casolaro, V., Bjorck, L., and Marone, G. (1990). Protein L. A bacterial Ig-binding protein that activates human basophils and mast cells. *J. Immunol.* 145, 3054–3061.

Patella, V., de Crescenzo, G., Marino, I., Genovese, A., Adt, M., Gleich, G. J., et al. (1996). Eosinophil granule proteins activate human heart mast cells. *J. Immunol.* 157, 1219–1225.

Patella, V., Marino, I., Arbustini, E., Lamparter-Schummert, B., Verga, L., Adt, M., et al. (1998). Stem cell factor in mast cells and increased mast cell density in idiopathic and ischemic cardiomyopathy. *Circulation* 97, 971–978. doi: 10.1161/01.cir.97.10.971

Patella, V., Marino, I., Lamparter, B., Arbustini, E., Adt, M., and Marone, G. (1995). Human heart mast cells. Isolation, purification, ultrastructure, and immunologic characterization. *J. Immunol.* 154, 2855–2865.

Peachell, P. T., Columbo, M., Kagey-Sobotka, A., Lichtenstein, L. M., and Marone, G. (1988). Adenosine potentiates mediator release from human lung mast cells. *Am. Rev. Respir. Dis.* 138, 1143–1151. doi: 10.1164/ajrccm/138.5.1143

Pereira da Silva, J. A., and Carmo-Fonseca, M. (1990). Peptide containing nerves in human synovium: immunohistochemical evidence for decreased innervation in rheumatoid arthritis. *J. Rheumatol.* 17, 1592–1599.

Piliponsky, A. M., and Romani, L. (2018). The contribution of mast cells to bacterial and fungal infection immunity. *Immunol. Rev.* 282, 188–197. doi: 10.1111/imr.12623

Plein, L. M., and Rittner, H. L. (2018). Opioids and the immune system - friend or foe. *Br. J. Pharmacol.* 175, 2717–2725. doi: 10.1111/bph.13750

Rivellese, F., Mauro, D., Nerviani, A., Pagani, S., Fossati-Jimack, L., Messemaker, T., et al. (2018). Mast cells in early rheumatoid arthritis associate with disease severity and support B cell autoantibody production. *Ann. Rheum. Dis.* 77, 1773–1781. doi: 10.1136/annrheumdis-2018-213418

Rosa, A. C., and Fantozzi, R. (2013). The role of histamine in neurogenic inflammation. *Br. J. Pharmacol.* 170, 38–45. doi: 10.1111/bph.12266

Schulman, E. S., MacGlashan, D. W. Jr., Peters, S. P., Schleimer, R. P., Newball, H. H., Lichtenstein, L. M., et al. (1982). Human lung mast cells: purification and characterization. *J. Immunol.* 129, 2662–2667.

Schwartz, L. B., Irani, A. M., Roller, K., Castells, M. C., and Schechter, N. M. (1987). Quantitation of histamine, tryptase, and chymase in dispersed human T and TC mast cells. *J. Immunol.* 138, 2611–2615.

Seegers, H. C., Hood, V. C., Kidd, B. L., Cruwys, S. C., and Walsh, D. A. (2003). Enhancement of angiogenesis by endogenous substance P release and neurokinin-1 receptors during neurogenic inflammation. *J. Pharmacol. Exp. Ther.* 306, 8–12. doi: 10.1124/jpet.103.050013

Shi, G. P., Bot, I., and Kovanen, P. T. (2015). Mast cells in human and experimental cardiometabolic diseases. *Nat. Rev. Cardiol.* 12, 643–658. doi: 10.1038/nrcardio.2015.117

Shi, G. P., Bot, I., and Kovanen, P. T. (2017). Reply: the complexity of substance P-mediated mast cell activation. *Nat. Rev. Cardiol.* 14:124. doi: 10.1038/nrcardio.2016.213

Siraganian, R. P. (1974). An automated continuous-flow system for the extraction and fluorometric analysis of histamine. *Anal. Biochem.* 57, 383–394. doi: 10.1016/0003-2697(74)90093-1

Skaper, S. D., Facci, L., and Giusti, P. (2014). Mast cells, glia and neuroinflammation: partners in crime? *Immunology* 141, 314–327. doi: 10.1111/imm.12170

Skaper, S. D., Facci, L., Zusso, M., and Giusti, P. (2017). Neuroinflammation, mast cells, and glia: dangerous liaisons. *Neuroscientist* 23, 478–498. doi: 10.1177/1073858416687249

Staiano, R. I., Loffredo, S., Borriello, F., Iannotti, F. A., Piscitelli, F., Orlando, P., et al. (2016). Human lung-resident macrophages express CB1 and CB2 receptors whose activation inhibits the release of angiogenic and lymphangiogenic factors. *J. Leukoc. Biol.* 99, 531–540. doi: 10.1189/jlb.3HI1214-584R

Steinhoff, M., Buddenkotte, J., and Lerner, E. A. (2018). Role of mast cells and basophils in pruritus. *Immunol. Rev.* 282, 248–264. doi: 10.1111/imr.12635

Steinhoff, M., Vergnolle, N., Young, S. H., Tognetto, M., Amadesi, S., Ennes, H. S., et al. (2000). Agonists of proteinase-activated receptor 2 induce inflammation by a neurogenic mechanism. *Nat. Med.* 6, 151–158. doi: 10.1038/72247

Stellato, C., Cirillo, R., de Paulis, A., Casolaro, V., Patella, V., Mastronardi, P., et al. (1992a). Human basophil/mast cell releasability. IX. Heterogeneity of the effects of opioids on mediator release. *Anesthesiology* 77, 932–940. doi: 10.1097/00000542-199211000-00016

Stellato, C., de Paulis, A., Ciccarelli, A., Cirillo, R., Patella, V., Casolaro, V., et al. (1992b). Anti-inflammatory effect of cyclosporin A on human skin mast cells. *J. Invest. Dermatol.* 98, 800–804.

Stellato, C., de Paulis, A., Cirillo, R., Mastronardi, P., Mazzarella, B., and Marone, G. (1991). Heterogeneity of human mast cells and basophils in response to muscle relaxants. *Anesthesiology* 74, 1078–1086. doi: 10.1097/00000542-199106000-00016

Subramanian, H., Gupta, K., and Ali, H. (2016). Roles of Mas-related G protein-coupled receptor X2 on mast cell-mediated host defense, pseudoallergic drug reactions, and chronic inflammatory diseases. *J. Allergy Clin. Immunol.* 138, 700–710. doi: 10.1016/j.jaci.2016.04.051

Tainsh, K. R., and Pearce, F. L. (1992). Mast cell heterogeneity: evidence that mast cells isolated from various connective tissue locations in the rat display markedly graded phenotypes. *Int. Arch. Allergy Immunol.* 98, 26–34. doi: 10.1159/000236161

Taracanova, A., Alevizos, M., Karagkouni, A., Weng, Z., Norwitz, E., Conti, P., et al. (2017). SP and IL-33 together markedly enhance TNF synthesis and secretion from human mast cells mediated by the interaction of their receptors. *Proc. Natl. Acad. Sci. U.S.A.* 114, E4002–E4009. doi: 10.1073/pnas.1524845114

Taracanova, A., Tsilioni, I., Conti, P., Norwitz, E. R., Leeman, S. E., and Theoharides, T. C. (2018). Substance P and IL-33 administered together stimulate a marked secretion of IL-1beta from human mast cells, inhibited by methoxyluteolin. *Proc. Natl. Acad. Sci. U.S.A.* 115, E9381–E9390. doi: 10.1073/pnas.1810133115

Tatemoto, K., Nozaki, Y., Tsuda, R., Konno, S., Tomura, K., Furuno, M., et al. (2006). Immunoglobulin E-independent activation of mast cell is mediated by Mrg receptors. *Biochem. Biophys. Res. Commun.* 349, 1322–1328. doi: 10.1016/j.bbrc.2006.08.177

Theoharides, T. C., Sismanopoulos, N., Delivanis, D. A., Zhang, B., Hatziagelaki, E. E., and Kalogeromitros, D. (2011). Mast cells squeeze the heart and stretch the gird: their role in atherosclerosis and obesity. *Trends Pharmacol. Sci.* 32, 534–542. doi: 10.1016/j.tips.2011.05.005

Theoharides, T. C., Stewart, J. M., Panagiotidou, S., and Melamed, I. (2016). Mast cells, brain inflammation and autism. *Eur. J. Pharmacol.* 778, 96–102. doi: 10.1016/j.ejphar.2015.03.086

Theoharides, T. C., Zhang, B., Kempuraj, D., Tagen, M., Vasiadi, M., Angelidou, A., et al. (2010). IL-33 augments substance P-induced VEGF secretion from human mast cells and is increased in psoriatic skin. *Proc. Natl. Acad. Sci. U.S.A.* 107, 4448–4453. doi: 10.1073/pnas.1000803107

Varricchi, G., Galdiero, M. R., and Tocchetti, C. G. (2017). Cardiac toxicity of immune checkpoint inhibitors: cardio-oncology meets immunology. *Circulation* 136, 1989–1992. doi: 10.1161/CIRCULATIONAHA.117.029626

Varricchi, G., Harker, J., Borriello, F., Marone, G., Durham, S. R., and Shamji, M. H. (2016). T follicular helper (Tfh) cells in normal immune responses and in allergic disorders. *Allergy* 71, 1086–1094. doi: 10.1111/all.12878

Varricchi, G., Loffredo, S., Borriello, F., Pecoraro, A., Rivellese, F., Genovese, A., et al. (2019). Superantigenic activation of human cardiac mast cells. *Int. J. Mol. Sci.* 20:1828. doi: 10.3390/ijms20081828

Varricchi, G., Raap, U., Rivellese, F., Marone, G., and Gibbs, B. F. (2018). Human mast cells and basophils-How are they similar how are they different? *Immunol. Rev.* 282, 8–34. doi: 10.1111/imr.12627

Vergnolle, N., Bunnett, N. W., Sharkey, K. A., Brussee, V., Compton, S. J., Grady, E. F., et al. (2001). Proteinase-activated receptor-2 and hyperalgesia: a novel pain pathway. *Nat. Med.* 7, 821–826. doi: 10.1038/89945

Vincent, L., Vang, D., Nguyen, J., Gupta, M., Luk, K., Ericson, M. E., et al. (2013). Mast cell activation contributes to sickle cell pathobiology and pain in mice. *Blood* 122, 1853–1862. doi: 10.1182/blood-2013-04-498105

Yosipovitch, G., Rosen, J. D., and Hashimoto, T. (2018). Itch: from mechanism to (novel) therapeutic approaches. *J. Allergy Clin. Immunol.* 142, 1375–1390. doi: 10.1016/j.jaci.2018.09.005

Yu, X., Kasprick, A., Hartmann, K., and Petersen, F. (2018). The role of mast cells in autoimmune bullous dermatoses. *Front. Immunol.* 9:386. doi: 10.3389/fimmu.2018.00386

Zhang, S., Zeng, X., Yang, H., Hu, G., and He, S. (2012). Mast cell tryptase induces microglia activation via protease-activated receptor 2 signaling. *Cell Physiol. Biochem.* 29, 931–940. doi: 10.1159/000171029

Conflict of Interest Statement: The authors declare that the research was conducted in the absence of any commercial or financial relationships that could be construed as a potential conflict of interest.

frontiers in Cellular Neuroscience

ORIGINAL RESEARCH
published: 25 October 2019
doi: 10.3389/fncel.2019.00472

Microglial Morphometric Parameters Correlate With the Expression Level of IL-1β, and Allow Identifying Different Activated Morphotypes

*María del Mar Fernández-Arjona[1], Jesús M. Grondona[1,2], Pedro Fernández-Llebrez[1,2] and María D. López-Ávalos[1,2]**

[1] Departamento de Biología Celular, Genética y Fisiología, Facultad de Ciencias, Universidad de Málaga, Málaga, Spain,
[2] Instituto de Investigación Biomédica de Málaga-IBIMA, Málaga, Spain

Microglia are the resident macrophages in the brain. Traditionally, two forms of microglia have been described: one considered as a resting/surveillant state in which cells have a highly branched morphology, and another considered as an activated state in which they acquire a de-ramified or amoeboid form. However, many studies describe intermediate microglial morphologies which emerge during pathological processes. Since microglial form and function are closely related, it is of interest to correlate microglial morphology with the extent of its activation. To address this issue, we used a rat model of neuroinflammation consisting in a single injection of the enzyme neuraminidase (NA) within the lateral ventricle. Sections from NA-injected animals were co-immunolabeled with the microglial marker IBA1 and the cytokine IL-1β, which highlight features of the cell's shape and inflammatory activation, respectively. Activated (IL-1β positive) microglial cells were sampled from the dorsal hypothalamus nearby the third ventricle. Images of single microglial cells were processed in two different ways to obtain (1) an accurate measure of the level of expression of IL-1β (indicating the degree of activation), and (2) a set of 15 morphological parameters to quantitatively and objectively describe the cell's shape. A simple regression analysis revealed a dependence of most of the morphometric parameters on IL-1β expression, demonstrating that the morphology of microglial cells changes progressively with the degree of activation. Moreover, a hierarchical cluster analysis pointed out four different morphotypes of activated microglia, which are characterized not only by morphological parameters values, but also by specific IL-1β expression levels. Thus, these results demonstrate in an objective manner that the activation of microglial cells is a gradual process, and correlates with their morphological change. Even so, it is still possible to categorize activated cells according to their morphometric parameters, each category presenting a different activation degree. The physiological relevance of those activated morphotypes is an issue worth to be assessed in the future.

Keywords: microglia, morphotypes, interleukin-1β, hierarchical cluster analysis, neuraminidase

OPEN ACCESS

Edited by:
Silvia Sánchez-Ramón, Complutense University of Madrid, Spain

Reviewed by:
Björn Spittau, Rostock University Hospital, Germany
Antonio J. Herrera, University of Seville, Spain

***Correspondence:**
María D. López-Ávalos
lopezavalos@uma.es

Specialty section:
This article was submitted to Non-Neuronal Cells, a section of the journal Frontiers in Cellular Neuroscience

Received: *26 April 2019*
Accepted: *02 October 2019*
Published: *25 October 2019*

Citation:
Fernández-Arjona MM, Grondona JM, Fernández-Llebrez P and López-Ávalos MD (2019) Microglial Morphometric Parameters Correlate With the Expression Level of IL-1β, and Allow Identifying Different Activated Morphotypes. Front. Cell. Neurosci. 13:472. doi: 10.3389/fncel.2019.00472

INTRODUCTION

Microglial cells are the resident macrophages in the central nervous system. Initially they were considered to be "resting" or "quiescent" in normal or healthy conditions, eventually acquiring an activated phenotype in pathological situations (Davis et al., 1994). However, more recent studies have suggested that microglia play several roles both in the healthy and the pathological brain (Biber and Block, 2014). Thus, the main role of microglia in the healthy brain is to survey the nervous tissue environment, so the previously presumed resting state is actually very active, continuously monitoring the surroundings, and acting as main sensors of brain alterations (Nimmerjahn et al., 2005; Nimmerjahn, 2012). Besides, microglial cells carry out diverse maintenance tasks to provide a propitious physiological environment (Gomez-Nicola and Perry, 2015). In addition, under various stimulus (e.g., infection, trauma or stroke) microglia may acquire different activated phenotypes to engage immunological or repair functions (Ransohoff and Perry, 2009). Those activated phenotypes have been defined as classical activation (M1), alternative activation (M2a), type II alternative activation (M2b), and acquired deactivation (M2c). Among them, M1 is considered a pro-inflammatory phenotype, while M2 subtypes are considered anti-inflammatory states. However, this classification is highly controversial, and many authors do not agree with it. In fact, this scenario is more intricate, since microglial cells exhibit a great plasticity within each specialized niche. Microglia phenotype is usually not absolute, but may display features of different states, or even a continuum of various activated states (Olah et al., 2011; Ransohoff, 2016). In addition, microglial cells can play a confusing toxic or protective role in particular neurological pathologies (Biber and Block, 2014), which represents a crucial issue to unravel.

It is widely accepted that the function of microglial cells and their form are closely coupled (Davis et al., 1994). Therefore, the morphological analysis by quantitative and objective methods is considered as a valuable tool to better understand form and function relationships. In addition, because microglial cells are highly dynamic, quantitative analysis could detect subtle changes in cell morphology. Numerous studies have addressed the morphological analysis of microglia, although many of them used qualitative and subjective approaches to classify them. During the last decade the use of quantitative objective methods to study morphology has gained interest. In this way, microglial cells have been analyzed in healthy brains of both humans and rats (Kongsui et al., 2014; Torres-Platas et al., 2014) as well as in different pathological situations such as brain injuries (Soltys et al., 2001; Zanier et al., 2015), under physiological (salt load) or psychological stress (Ayoub and Salm, 2003; Hinwood et al., 2013), and in mouse models of Alzheimer's disease (Baron et al., 2014). Some studies tried to establish different microglial morphotypes based on morphological parameters. Statistical procedures such as principal component analysis revealed the morphological parameters with greater discriminant capacity (Soltys et al., 2005). Hierarchical cluster analysis, which allows grouping objects based on their similarity, was used to suggest new microglia classifications in different experimental models, such as visual learning in monkeys (Santos-Filho et al., 2014), hypoglossal axotomy (Yamada and Jinno, 2013), experimental neuroinflammation (de Sousa et al., 2015), and a mouse model of amyotrophic lateral sclerosis (Ohgomori et al., 2016). These works objectively proposed different morphotypes, which have been associated to a particular physiological/pathological spatiotemporal condition.

The current study has focused on the morphology of hypothalamic microglia undergoing inflammatory activation. To induce the activation of these cells, an acute neuroinflammation was generated by the intracerebroventricular administration of microbial neuraminidase (Grondona et al., 1996; Del Carmen Gómez-Roldán et al., 2008; Granados-Durán et al., 2015). Neuraminidase (NA) is a sialidase enzyme that removes terminal sialic acid from the carbohydrate chains of glycoproteins and glycolipids. When NA is injected into the lateral ventricle of rodents, it is distributed by the flow of cerebrospinal fluid, affecting the ventricular system and periventricular regions, including the hypothalamus. The diffusion of the enzyme from the ventricular cavity toward the hypothalamic parenchyma provokes the inflammatory activation of resident microglia (Granados-Durán et al., 2015; Fernández-Arjona et al., 2017). On the basis of immunostaining for the pro-inflammatory cytokine IL-1β, the level of activation of these hypothalamic microglial cells appears to be heterogeneous, as well as their morphology. Hence, we tried to correlate the level of activation (assessed by IL-1β immunostaining) with different morphometric parameters measured in single microglial cells. Also, we aimed to defining different subgroups of activated microglia based on the objective quantification of morphological parameters. Our results point that most of the morphometric parameters measured show a dependence on the level of expression of IL-1β, and they progressively change as the cell becomes more activated. Even though the morphological change that accompanies activation is gradual, with the aid of statistical methods it is possible to categorize activated microglial cells using specific morphological parameters. The morphology-based classification obtained is in accordance with different IL-1β expression levels, indicating the value of morphological analysis to examine the degree of inflammatory activation of microglial cells.

MATERIALS AND METHODS

Animals

Six male Wistar rats (350 g, about 10 weeks old) were provided by Charles River Laboratories (Barcelona, Spain). Animals were maintained in the animal house at Universidad de Málaga, under a 12 h light/dark cycle, at 23°C and 60% humidity, with food and water available *ad libitum*. Animal care and handling were performed according to the guidelines established by the Spanish legislation (RD 53/2013) and the European Union regulation (2010/63/EU). All procedures performed were approved by the ethics committee of Universidad de Málaga (Comité Ético de Experimentación de la Universidad de Málaga; reference 2012-0013). All efforts were made to minimize the number of animals used and their suffering.

Intracerebroventricular Injection

An acute and sterile neuroinflammatory process was generated in rats by a single injection of the enzyme NA within the right lateral ventricle of the brain (Grondona et al., 1996; Del Carmen Gómez-Roldán et al., 2008; Granados-Durán et al., 2015). Intracerebroventricular (ICV) injection procedure was performed as previously described (Granados-Durán et al., 2015). Briefly, the animals were anesthetized with ketamine/xylazine solution (80 and 12 mg/kg, respectively; Sigma-Aldrich) and positioned in a stereotaxic frame. A scalp incision along the sagittal midline was performed to access the skull and the bone was perforated with a drill in the following coordinates: 0.5 mm posterior, and 1.4 mm lateral from Bregma (Paxinos and Watson, 2007). Neuraminidase from *Clostridium perfringens* (Sigma-Aldrich, N3001) dissolved in 0.9% sterile saline was administered by a single injection 3.5 mm below the dura mater, with the aid of a pump; a dose of 500 mU (in 20 μL) of NA was perfused during 10 min at a rate of 2 μL/min. The animals were sacrificed at 12 h post-injection. Sham (saline-injected) animals were not included, because: (1) from previous studies (Fernández-Arjona et al., 2017) we knew that IL-1β expression in hypothalamic microglial cells was absent, (2) the aim of this study was focused on activated microglial cells, and (3) in case we wanted to sample IL-1β negative cells, it would be possible to find them in regions of the brain parenchyma farther from the ventricular surface.

Brain Sections and Immunohistochemistry

Prior to sacrifice, the animals were anesthetized (as described above) and systemically perfused with 0.9% saline, followed by 4% parafolmaldehyde. Brains were removed and post-fixed overnight in the same fixative solution. Free floating coronal sections of brain tissue were later obtained with a vibratome (40 μm thickness), and the sections were cryoprotected with a sucrose and ethylene glycol solution (30% w/v and 30% v/v respectively, in 0.1 M phosphate buffer). Brain sections including the third ventricle (distance from Bregma about −3.30 mm) were selected for immunohistochemistry.

With the purpose of measuring morphological parameters of microglial cells along with their IL-1β expression level, double immunofluorescence with IBA1 and IL-1β antibodies was performed. Free floating vibratome sections were washed with PBS, and non-specific binding sites were saturated with PBT solution (0.3% bovine serum albumin, 0.3% Triton X-100 in PBS pH 7.3). Primary antibodies (anti-IBA1, host: rabbit, WAKO, 19-19741 and anti-IL-1β, host: goat, R&D Systems, AF501NA) were co-incubated overnight at 4°C. Sections were washed with PBS and then incubated for 1.5 h with the secondary antibodies (anti-rabbit Alexa 488, host: donkey, Molecular Probes, A-21206; and anti-goat Alexa 594, host: donkey, Invitrogen, A-11058). Sections were washed with PBS, mounted onto gelatine-coated slides, cover slipped with the anti-fading agent Mowiol 4-88 (Calbiochem/EMD Chemicals) and stored at 4°C. Negative controls for the immunohistochemistry consisted in omitting the primary antibodies.

Image Acquisition and Processing

Images of activated microglia from immunolabeled sections including the third ventricle were acquired using the inverted microscope LEICA SP5 II equipped with a confocal scan unit. Images were captured with a 63x oil immersion objective, using the following acquisition parameters: for the fluorochrome Alexa 488 (Iba1-green): Argon laser intensity 55%; Gain 641; Offset 0; and Detector PMT aperture: 500–550 nm. For the fluorochrome Alexa 594 (IL1β-red): Helium-Neon laser intensity 67%; Gain 1009; Offset 0; and Detector PMT aperture: PMT 605–656 nm.

Images were taken using the z-stack tool. The distance between planes was established after prior trials, aimed to get cellular profiles of sufficient resolution for the subsequent morphological analysis; such distance was set in 1 μm. For each microscopic field selected, a z-stack was obtained from 20 to 30 planes (1 μm apart) taken along the *z* axis.

From these images, individual microglial cells were selected and cropped according to the following criteria: (i) random selection from the dorsal wall of the third ventricle, starting in the subependyma and moving toward the brain parenchyma up to a depth of about 100 μm; (ii) different intensities in the IL-1β label (as the study was focused on activated microglia, cells with no IL-1β label at all were excluded); (iii) no overlapping with neighboring cells; and (iv) complete nucleus and branches. The images of selected single microglial cells were processed in two different ways. On one hand, the intensity of the IL-1β label was quantified (see Section Quantification of IL-1β Label in Single Microglial Cells; **Figure 1**), and on the other hand an extensive morphological analysis of the same cell was performed (see Section Quantification of Morphological Parameters in Single Microglial Cells; **Figure 2**). For each type of analysis, a series of steps were performed using FIJI free software (freely downloadable from http://fiji.sc/Fiji).

Quantification of IL-1β Label in Single Microglial Cells

To obtain an accurate measure of the IL-1β label in individual cells, the z-stack images (20–30 planes) from a selected cell (**Figure 1B**) were split into the red (**Figure 1C**, corresponding to IL-1 β) and the green (**Figure 1D**, corresponding to IBA1) channels. First, the intensity of IL-1β label was calculated by an arbitrary method. The *Raw Integrated Density* was measured (the sum of the values of intensity of the pixels in all the planes making up the whole cell). Secondly, the counterpart green channel images (**Figure 1D**) were used to estimate the volume of the cell as follows: to obtain the total positive area in μm^2, the number of green-positive pixels of all planes in the z-stack was counted. Knowing that the distance between the z-planes was 1 μm, the volume of the cell was then calculated (in μm^3). Finally, the IL-1β relative intensity of each cell was calculated by dividing its *Raw Integrated Density* between its volume. This approach intended to avoid bias due to changes of cell size occurring during the activation process.

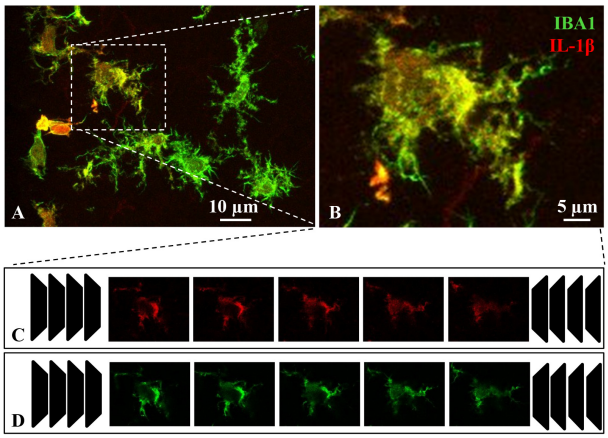

FIGURE 1 | Procedure for the quantification of IL-1β staining in microglial cells. Brain sections containing the hypothalamus were immunostained with IBA1 (green channel) and IL-1β (red channel) antibodies. Activated microglial cells were evidenced by co-staining with both antibodies **(A)**. Activated microglia were randomly picked for image analysis **(B)**. Confocal z-stack images were captured, each containing 20–30 confocal planes **(C,D)**. After splitting the red and green channels, IL-1β intensity for an individual microglial cell was estimated on the red channel images **(C)**. Briefly, the intensity of all red-positive pixels in every plane was measured, and then the counted values of all planes were added up to obtain the total intensity staining per cell. Secondly, the counterpart green channel images **(D)** were used to calculate the cellular volume: the green-positive area was measured for each confocal plane (μm^2), and then the cell volume was calculated knowing the distance between planes ($\approx$ 1 μm). Finally, the ratio red staining intensity to cellular volume yielded the IL-1β expression level of a particular microglial cell, relative to its volume (intensity/μm^3).

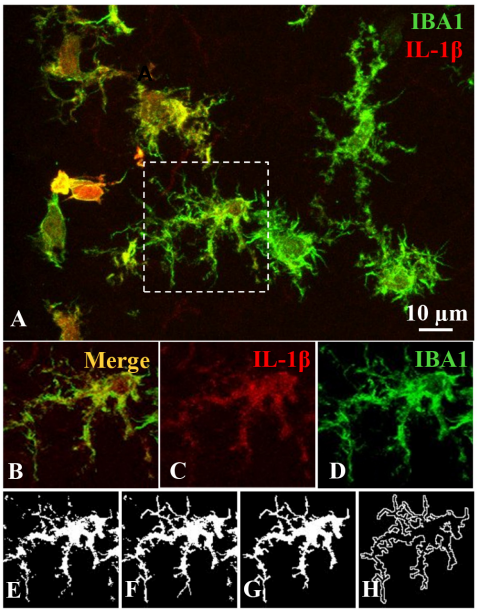

FIGURE 2 | Image processing for an accurate morphometric analysis of individual microglial cells. This procedure was carried out on the same images used for quantifying IL-1β expression level **(A)**. For each single microglial cell, the z-stack planes were projected and grouped, and the resulting image **(B)** was color-splitted to get the cellular profile displayed by IBA1 staining (green channel; **D**) out of IL-1β label (red channel; **C**). The green-channel image **(D)** was transformed to a binary image **(E)** and then edited **(F)** to obtain a single field or area of pixels representing the filled **(G)** and the outlined **(H)** shapes of the cell. These filled and outlined figures were used to measure the morphometric parameters.

Quantification of Morphological Parameters in Single Microglial Cells

Each studied microglial cell was also processed for an accurate morphometric analysis. In this case, two-dimensional projection images were obtained from confocal z-stacks (**Figure 2A**). First, the double-color image (**Figure 2B**) was split to obtain the IBA1 label in the green channel, which quite accurately mirrors the cell profile (**Figure 2D**). This green-channel image was transformed into a binary image (**Figure 2E**), which was then manually edited (**Figure 2F**) to obtain a filled profile (**Figure 2G**) and an outlined shape (**Figure 2H**) of the cell (for more details see Fernández-Arjona et al., 2017). These filled and outlined figures were used to measure the morphologic parameters. For this purpose, the free software plugin FracLac for ImageJ was used (Karperien A., FracLac for ImageJ[1]. 1999–2013; available at the ImageJ website, National Institutes of Health; Karperien et al., 2013). The 15 parameters measured were: *fractal dimension*, *lacunarity*, *cell area*, *cell perimeter*, *cell circularity*, *convex hull area*, *density*, *convex hull perimeter*, *roughness*, *convex hull span ratio*, *convex hull circularity*, *bounding circle diameter*, *maximum span across the convex hull*, *the ratio convex hull radii* and *the mean radius*. All of them are explained in **Supplementary Material**, as well as a step guide for their measurement (**Supplementary Figure S1** and **Supplementary Material** Methods. Fractal analysis; Fernández-Arjona et al., 2017).

[1]http://rsb.info.nih.gov/ij/plugins/fraclac/FLHelp/Introduction.htm

Statistical Analysis

Simple Linear Regression Analysis

To evaluate the correlation between each morphometric parameter and IL-1β label intensity in activated microglial cells, a simple linear regression analysis was performed. Morphological parameters were considered the dependent variables and the relative intensity of IL-1β was the independent one. The relationship between the independent variable and each dependent variable (15 different morphological parameters) was analyzed by pair-wise datasets of each cell, conducting an independent simple linear regression for each parameter. Regression coefficients $[F_{0.05(2),150,150}]$ of each function pointed out the dependence of the dependent variable (morphometric parameters) on the independent variable (IL-1β intensity). Dependence was considered significant when $P < 0.05$. Correlation coefficients $[r_{0.05(2),151}]$ measure the strength of the linear relationship between the two variables.

Hierarchical Cluster Analysis

With the aim of identifying likeness among NA-activated microglial cells and thus obtaining microglial subtypes, a hierarchical cluster analysis (HCA) was performed using

the morphometric parameters previously measured. For this purpose, SPSS Statistics software, version 21.0 (Armonk, NY, United States; IBM Corp.) was used. Similarity appraises were generated by measuring the Euclidean distance (the square root of the sum of the squared differences between values for the items) following the Ward's method (Ward, 1963) for interval data. All data were normalized in order to obtain values in a similar scale. A dendrogram plot based on the Euclidean distance was used to display the number of clusters proposed. To find out the more suitable parameters for separating our population of cells into different groups, the *multimodality index* (*MMI*) of each parameter was calculated (Scheweitzer and Renehan, 1997) using the following formula:

$$MMI = [M3^2 + 1]/[M4 + 3(n-1)^2/(n-2)(n-3)]$$

where n is the sample size (in this case 250 cells), M3 is *asymmetry* (or *skewness*; *A*) and M4 is *kurtosis* (*K*), obtained from dispersion data analysis. The number of appropriate clusters was estimated by the Thorndike procedure (Thorndike, 1953). Briefly, the average within-cluster distance is plotted for different numbers of clusters, resulting in a curve that shows a decrease in the distance as the number of clusters increases. The number of clusters finally selected is revealed by a sudden flattening of the curve in the plot.

Linear Discriminant Analysis

Linear discriminant analysis (LDA) is a statistical method used for pattern recognition, to characterize or separate two or more groups, and also to create a function able to distinguish, as accurately as possible, the pertaining to each group. The evaluation by LDA of 250 NA-activated microglial cells was carried out by SPSS Statistics software. The following equation shows the linear discriminant functions:

$$LD = A1X1 + A2X2 + \ldots AnXn + C$$

where An is a coefficient of each individual morphometric parameter, Xn is each variable (the morphometric parameter value) and C is a constant. The discriminant functions were considered satisfactory when the predictive ability to discriminate exceeded 80%. Wilk's lambda was used to test for significant differences between the groups for each individual predictor variable. The values of standardized coefficients show the net contribution of each variable to the discriminant function. The centroid of each group and the boundaries in the territorial map describes the predicted groups (Fisher, 1936; Yamada and Jinno, 2013; Ohgomori et al., 2016).

Analysis of Variance

Comparisons of data means were carried out using SPSS Statistics software. The Kolmogorov–Smirnov normality test, along with the Levene homoscedasticity test, was used to verify that data could be analyzed by parametric methods. One-way analysis of variance (ANOVA) was used to compare the morphometric parameters means of the different clusters. Pair-wise multiple comparisons were performed by Bonferroni test. Differences were considered statistically significant when the *P* obtained was <0.05.

RESULTS

Diverse Expression Levels of the Pro-inflammatory Cytokine IL-1β Are Observed in Hypothalamic Activated Microglial Cells

The ICV administration of NA results in the activation of microglial cells located nearby the ventricular walls, activation that is evidenced by IL-1β expression. Double immunofluorescence showed a broad co-localization of IL-1β in IBA1 positive cells (which mostly correspond to microglia) located in periventricular areas, particularly of the hypothalamus (**Figure 3**). Control animals injected with saline did not show any IL-1β staining (results not shown). Since NA was injected within the right lateral ventricle and then distributed to other brain areas by the rostro-caudal cerebrospinal fluid flow, the IL-1β positive microglia could be observed in the hypothalamus parenchyma close to the third ventricle. Cytokine positive microglial cells were found up to about 100 μm under the ventricular surface, but not further deep, confirming that non-activated cells were also present in this model. The IL-1β and IBA1 positive cells most probably correspond to microglial cells, rather than infiltrated cells, because (1) 12 h after ICV injection infiltration occurs at the lateral ventricle, but not in the hypothalamus, (2) these cells are extensively ramified, and it is unlikely that a peripheral cell might infiltrate in the lateral ventricle, flow to the hypothalamus, migrate through the ependymal layer, and ramify in just 12 h. On the other hand, IL-1β/IBA1 positive cells remarkably presented variable degrees of IL-1β expression, ranging from quite high (**Figures 3B,C**) and medium (**Figures 3D,E**) to almost none (**Figures 3F,G**). With a naked eye, microglial cells with lower IL-1β expression bore more and longer ramifications (**Figures 3F,G**). Cells with higher IL-1β expression were usually located closer to the ventricle. However, an objective method to assess the activation of microglial cells would be more appropriate. Therefore, we aimed to correlate quantitative morphometric parameters with IL-1β expression level. To do so, microglial cells double-labeled with IBA1 (**Figure 3**, green) and IL-1β (**Figure 3**, red) were randomly picked from the periventricular region of the hypothalamus of rats injected with NA 12 h before.

Morphological Parameters Correlate With the Level of Expression of IL-1β in Hypothalamic Microglia From NA-Injected Rats

We have previously verified significant differences in morphological parameters upon transition of microglial cells to an NA-induced activation state (Fernández-Arjona et al., 2017). Here we pursued to investigate if the broad range of values of the different morphological parameters might correlate to different degrees of IL-1β expression. That is, if the gradual morphological change could be associated to a progressive increase of microglial activation, evidenced by the expression of IL-1β. To demonstrate this, fifteen morphological parameters

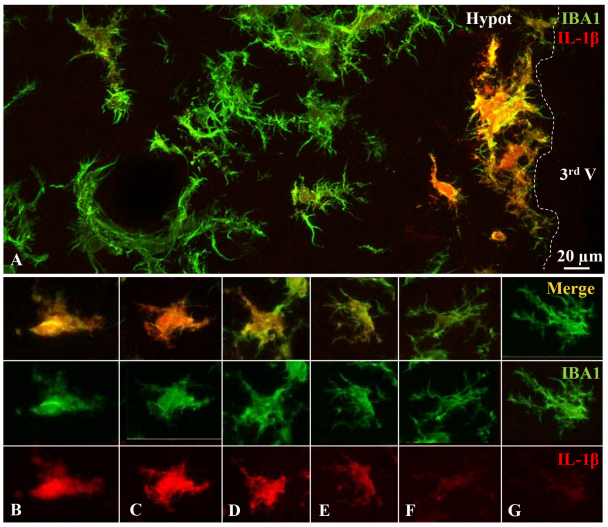

FIGURE 3 | Varied expression level of the inflammatory cytokine IL-1β by hypothalamic microglial cells. Double immunofluorescence staining on brain sections obtained from rats ICV-injected with NA. Twelve hours after NA-injection, a broad co-localization of IL-1β (red) in IBA-1 positive (green) hypothalamic cells can be observed **(A)**. In sub-ependymal and periventricular areas, microglial cells similarly stained with IBA1 displayed diverse IL-1β staining intensities, which ranged from high **(B,C)**, or medium **(D,E)** to low **(F,G)**. Hypot, hypothalamus; 3rd V, third ventricle.

were analyzed in individual microglial cells sampled from the hypothalamus. In those same cells, the level of expression of IL-1β was also measured (IL-1β label, measured as *Raw Integrated Density*, relative to the total cell volume, the later calculated by means of IBA1 labeling). The regression analysis illustrates how the value of a dependent variable varies when the value of an independent variable changes. In this study, the independent variable was the level of IL-1β expression, and the morphological parameters were the dependent variables. Thus, for each morphological parameter, the values of the parameter over the IL-1β relative intensity were analyzed by a simple linear regression of the paired microglial dataset.

Hence, the functional dependence of each variable on IL-1β expression was tested by analysis of variance computing the sum of squares by a linear regression, for a population of 150 microglial cells (**Figure 4** and **Table 1**). The parameters *fractal dimension* (**Figure 4A**), *lacunarity* (**Figure 4B**), *cell area* (**Figure 4C**), *cell perimeter* (**Figure 4D**), *convex hull area* (*CHA*, **Figure 4F**), *convex hull perimeter* (*CHP*, **Figure 4H**), *roughness* (**Figure 4I**), *bounding circle diameter* (*BCD*, **Figure 4L**), *max span across the convex hull* (*MSACH*, **Figure 4N**) and *the mean radius* (**Figure 4O**) showed a negative dependence on IL-1β relative intensity, while the parameter *cell circularity* (**Figure 4E**) and *density* (**Figure 4G**) had a positive dependence on the same independent variable; regression analyses were significant for all these parameters (**Table 1**). However, there was no dependency for the *convex hull span ratio* (*CHSR*, **Figure 4J**), the *convex hull circularity* (*CHC*, **Figure 4K**) and the *ratio convex hull radii* (*RCHR*, **Figure 4M**) versus IL-1β relative intensity. Regression coefficients (*F*) of those functions pointed out a significant dependence of 12 morphometric parameters on IL-1β expression (**Table 1**); three parameters (*the ratio convex hull radii*, *convex hull circularity* and *convex hull span ratio*) did not show any dependence. Correlation coefficients (*r*) were used to calculate the coefficients of determination (r^2) which indicate the strength of the linear relationship between the two variables, and therefore the reliability of the prediction of the dependent variable based on the independent variable. The results showed significant correlations for each linear regression (**Table 1**) except for the three parameters above mentioned (*the ratio convex hull radii*, *convex hull circularity* and *convex hull span ratio*). Regression analysis is widely used to make predictions. Given that most of the morphological parameters used here present a statistically significant dependence on IL-1β relative intensity, it could be inferred that microglial morphological changes are closely related to the extent of the inflammatory activation of the cell. Also, for a population of microglial cells, these parameters might be considered as good predictors of the expression level of this cytokine. However, such prediction would not be reliable in the case of single microglia because, as can be observed in the plots (**Figure 4**), a relatively high dispersion of data exists.

Fractal dimension (*D*) was determined by the box counting method. Previous studies revealed that small changes in *D* values are related to subtle changes in the complexity of branches (Karperien et al., 2013). In our study *D* data ranged from 1.15 to 1.40. High values of *D* corresponded with low cytokine expression. The correlation analysis showed a tendency of *D* to decrease as IL-1β expression increases. This suggests that microglial cells with low NA-activated state (low IL-1β) present phenotypes associated to high values of *D*, like de-ramified, hypertrophied or bushy. When activation escalates (lower values of *D*), microglia profile gradually modifies toward un-ramified. In addition, in our sample the higher value of *D* obtained was 1.45, indicating that highly branched profiles, with small soma and quite fine and long processes, are rare amongst NA-activated hypothalamic microglial cells.

Lacunarity (Λ) assess the heterogeneity of the cell profile. Low Λ values reflect homogeneity and high Λ measures mean heterogeneity (Karperien et al., 2011). In our sample, microglial cells with lower expression of IL-1β presented higher Λ values. Also, the regression analysis pointed out a decrease in Λ in parallel to IL-1β intensity increases. Therefore, microglia with mild NA-activation state present a heterogeneous cellular profile (high Λ values), and as the level of activation increases their shape tends to be more homogeneous (low Λ values).

Cell area and *cell perimeter*, as well as the *area* and the *perimeter* of the *convex hull*, mainly describe the cell size. In the case of NA-activated microglial cells high values of those parameters have been found in cells with low IL-1β expression. The regression analysis showed a decrease in cells size in parallel with increases in the expression of the pro-inflammatory cytokine. These results indicate a progressive reduction of microglial size as the activation state of the cells enhances.

These cell-size changes were complemented with the morphological measures of *density* and *roughness*. On one side, low values of *density* were accompanied with low cytokine

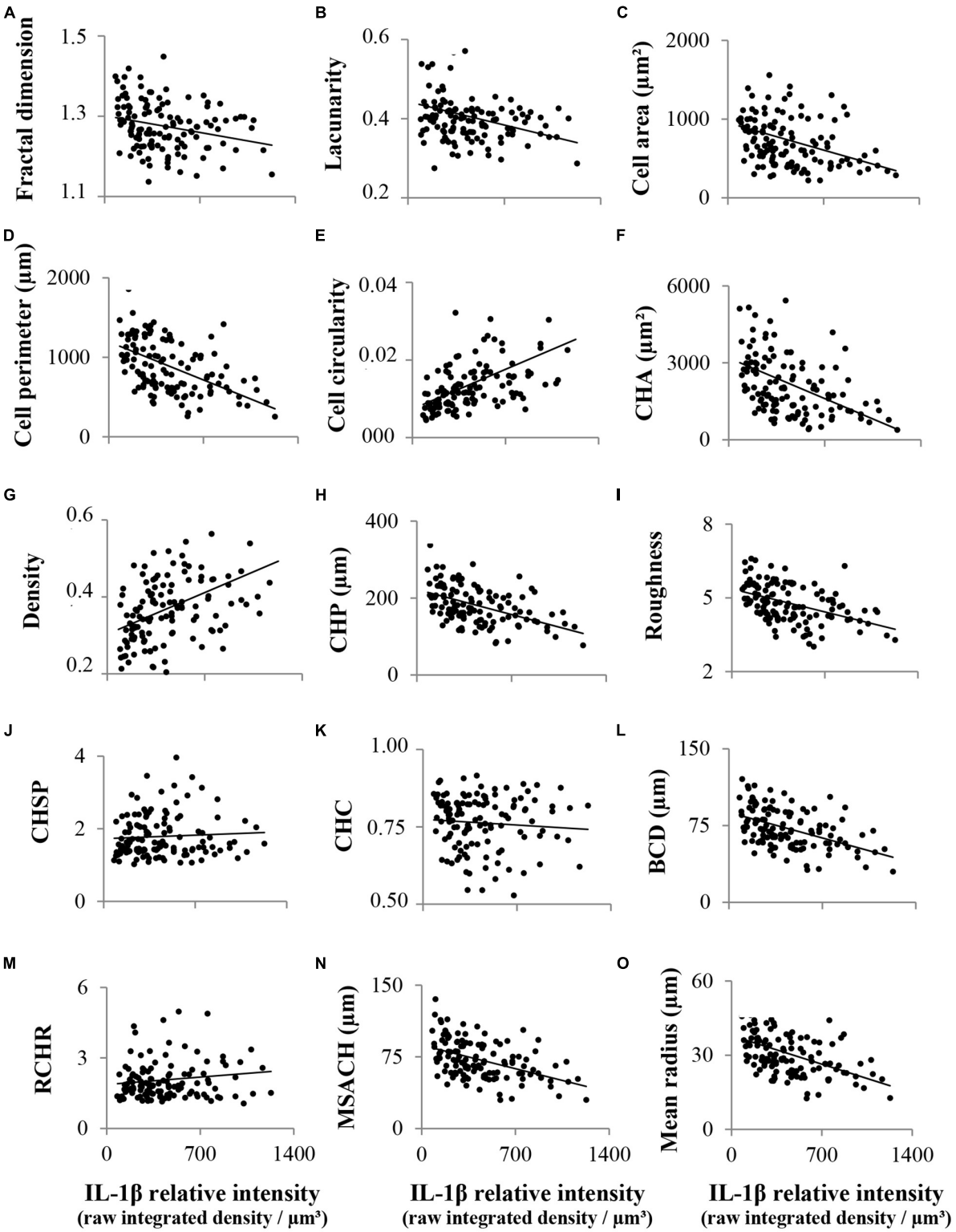

FIGURE 4 | Linear regression analysis between different microglial morphological parameters and IL-1β staining intensity. Fifteen morphological parameters as well as IL-1β relative staining intensity were measured in a total of 150 activated hypothalamic microglial cells. These cells were plotted in scatter graphs, where each morphological parameter was the dependent variable and IL-1β staining intensity (measured as the *Raw Integrated Density* relative to cellular volume) was the independent variable. The parameters *fractal dimension* **(A)**, *lacunarity* **(B)**, *cell area* **(C)**, *cell perimeter* **(D)**, *convex hull area* (*CHA*; **F**), *convex hull perimeter* (*CHP*; **H**), *roughness* **(I)**, *bounding circle diameter* (*BCD*; **L**), *maximum span across the convex hull* (*MSACH*; **N**), and the *mean radius* **(O)**, showed a negative dependence

(Continued)

FIGURE 4 | Continued
on IL-1β expression, while the parameters *cell circularity* **(E)** and *density* **(G)** had a positive dependence on the same independent variable. Regression analyses were significant for all these parameters, and correlation coefficients were significantly strong for the straight-line relationship between each paired variables. On the contrary, there was no dependence for the *ratio convex hull radii* (*RCHR*; **M**), the *convex hull circularity* (*CHC*, **K**), and the *convex hull span ratio* (*CHSR*; **J**).

TABLE 1 | Statistics of simple linear regression analyses performed between different morphological parameters and IL-1β relative intensity of a population of activated microglial cells.

Parameter	*F*	*P* significance	Regression line	r^2
Cell perimeter	40.3	3.7×10^{-9}	$Y = -0.68X + 1195$	0.245***
Cell circularity	37.9	9.5×10^{-9}	$Y = -1 \times 10^{-5}X + 0.007$	0.234***
Mean radius	37.1	1.3×10^{-8}	$Y = -0.017X + 3$	0.231***
Convex hull perimeter	36.1	1.9×10^{-8}	$Y = -0.093X + 222$	0.226***
Bounding circle diameter	34.7	3.5×10^{-8}	$Y = -0.036X + 88$	0.212***
Max span convex hull	32.5	8.4×10^{-8}	$Y = -0.035X + 87$	0.209***
Roughness	32.2	9.3×10^{-8}	$Y = -1.3 \times 10^{-3}X + 5.4$	0.206***
Convex hull area	29.3	3.1×10^{-7}	$Y = -2.26X - 3186$	0.191***
Density	26.7	9.2×10^{-7}	$Y = -2 \times 10^{-4}X + 0.3$	0.177***
Cell area	18.9	2.9×10^{-5}	$Y = -0.48X + 953$	0.132***
Lacunarity	14.3	2.3×10^{-3}	$Y = 8 \times 10^{-5}X + 0.44$	0.104***
Fractal dimension	9.1	0.003	$Y = 6 \times 10^{-5}X+$	0.068**
The ratio convex hull radii	1.7	0.19	$Y = 4 \times 10^{-4}X + 1.87$	0.013
Convex hull circularity	0.7	0.39	$Y = -3 \times 10^{-5}X + 0.77$	0.006
Convex hull span ratio	0.5	0.49	$Y = -1 \times 10^{-4}X + 1.73$	0.004

*Regression dependence by F-test procedure was significant when $P < 0.05$. Coefficient of determination (r^2) was used as a measure of the strength of the straight-linear relationship (***$P < 0.001$; **$P < 0.005$).*

expression; both variables presented a positive correlation. Therefore, the more compact the profile of the cell, the more activated it is. On the other hand, the parameter *roughness* showed the opposite behavior: high *roughness* values relate to low IL-1β intensity, and thus the regression analysis pointed out a negative correlation between both variables. This denotes that microglial cell surface irregularities tend to decrease in parallel with the progressive enhancement of its activation.

These results confirm that, in microglial cells, a correlation exists between different morphological parameters and the degree of inflammatory activation. We next sought to explore the possibility that there are different microglial morphotypes related to various degrees of activation.

Hierarchical Cluster Analysis Allows Identifying Four Types of Activated Microglial Cells Based on Morphological Parameters

The choice of suitable variables is critical for the outcome of HCA. For this reason we initially considered the fifteen parameters above mentioned, and examined their frequency distribution in a histogram (**Supplementary Figure S2**). Each probability distribution was compared with a normal distribution, and *asymmetry* (or *skewness*) together with *kurtosis* were calculated, both of which allowed to estimate the *multimodality index* (*MMI*) of each parameter (see section Materials and Methods). The *MMI* gives an idea of the distribution of the data around one or multiple values. Thus, parameters with $MMI > 0.55$ are multimodal and therefore suitable to perform cluster analysis (Scheweitzer and Renehan, 1997). Based on their *MMIs*, only the following three morphometric parameters were appropriate for the cluster analysis: *lacunarity*, *cell circularity* and *convex hull span ratio* (**Table 2**).

TABLE 2 | Multimodality indexes of morphological parameters.

Parameter	Multimodality index
Lacunarity	0.587*
Cell circularity	0.560*
Convex hull span ratio	0.552*
The ratio convex hull radii	0.522
Convex hull area	0.503
Cell area	0.497
Convex hull circularity	0.456
Density	0.438
Cell perimeter	0.431
Max span convex hull	0.417
Bounding circle diameter	0.414
Mean radius	0.410
Convex hull perimeter	0.402
Fractal dimension	0.385
Roughness	0.372

**Parameters with a MMI > 0.55 presented a multimodal distribution.*

The HCA performed on z-transformed data sets of the three selected parameters yielded a dendrogram based on the Euclidean distance between groups, using the Ward's method (**Figure 5A**). The Thorndike's procedure (Thorndike, 1953) was applied to establish the appropriate number of clusters (**Figure 5B**). This method uses the representation of linkage distance versus linkage steps (or number of clusters); a sudden decrease in linkage distance occurs at a certain number of clusters, which is evidenced by a marked flattening of the curve. In our case, this happens when the number of linkage steps is four (dashed line in **Figure 5B**). Microglial cells were thus classified into four clusters.

Next, we searched for linear discriminant functions which could explain the variance, and that could also suggest the variables that are more relevant for discrimination, i.e., that have the highest predictive capacity. This search resulted in two functions (**Table 3**). The linear discriminant function 1 (LD1), with a correlation of 0.869, which explained 57.4% of variance, and the linear discriminant function 2 (LD2), with a correlation of 0.767, described 26.6% of variance. Thus, both functions together accumulated 84% of variance, remaining unexplained only 16% of it. Moreover, Wilks's lambda and chi-squared pointed out significant differences between the means of the compared groups (Wilks's lambda = 0.054; $\chi^2 = 718.9$; $df = 9$; $P < 0.001$). The discriminant functions include coefficients for each variable, which are listed in **Table 3**. The value of those coefficients indicates the partial contribution of each variable to the function, that is, the importance of each variable as predictor of cell sorting into the four clusters, with a higher absolute value indicating a better predictive variable. LDA revealed that *lacunarity* and *cell circularity* are the critical parameters when sorting microglial cells. The discriminant scores of 252 microglial cells were determined for LD1 and LD2, and plotted in a territorial map using a color code to identify each cluster (**Figure 5C**). This type of graph illustrates how cells within each cluster are grouped around a centroid (the cluster mean).

Once HCA and LDA had yielded four groups of hypothalamic activated microglial cells, we tested if they were actually different morphotypes, comparing their parameters means using one-way ANOVA. The comparison of the four clusters regarding IL-1β relative intensity (**Figure 6A**) showed in an objective manner that they were different in terms of their activation status. Therefore, each cluster or morphotype could be assigned to a particular level of inflammatory activation. Although clusters 1 and 3 were not different regarding IL-1β expression, they were different from clusters 2 and 4, and were also different regarding morphological parameters (*convex hull span ratio* and *cell circularity*; **Figures 6B,D**). Consequently, each morphotype could be assigned a particular level of activation as follows: cluster 2 represents a low activation state, clusters 1 and 3, although morphologically different, fit with intermediate activation states, and cluster 4 appertain to the highest activation level.

Comparisons of each cluster means were also done for all the morphological parameters measured (**Supplementary Figure S3**). One-way ANOVA showed significant differences between clusters in most parameters, what supports that each cluster represents a particular morphotype. To simplify, only the discriminating parameters used to perform HCA and LDA were

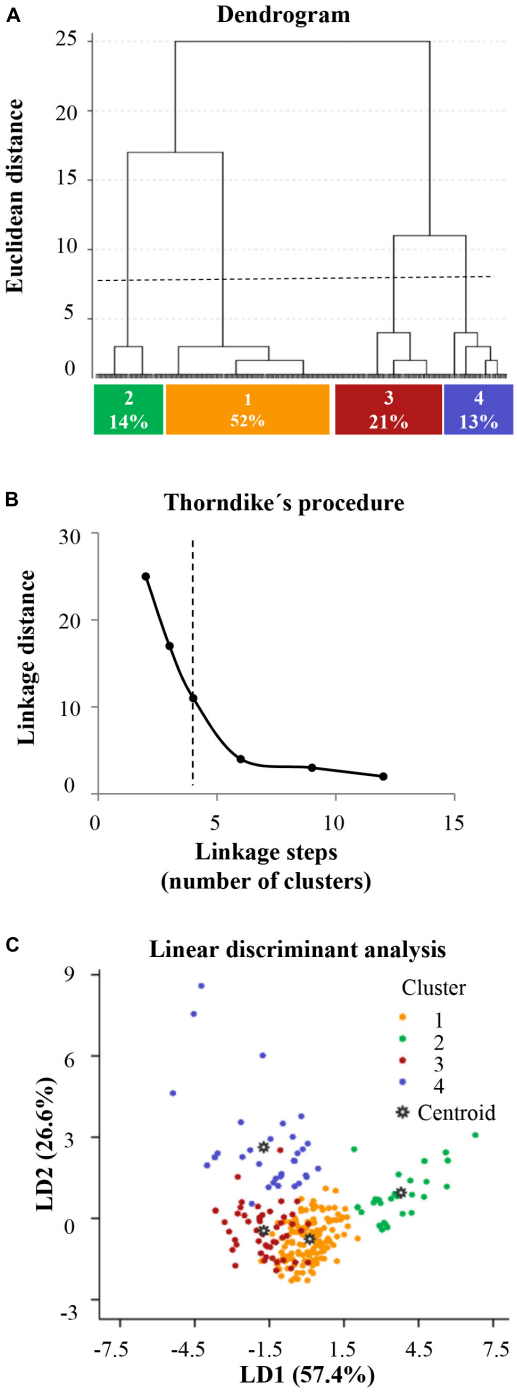

FIGURE 5 | Activated microglia can be classified according to morphological parameters. A hierarchical cluster analysis (HCA) was performed on 250 NA-activated microglial cells sampled from the rat dorsal hypothalamus. This dissimilarity measure was based on three suitable morphological parameters selected according to their multimodality index (*MMI*) value. The clustering results are presented in a dendrogram **(A)**, where the abscissa represents individual microglial cells and the ordinate corresponds to the linkage distance measured as Euclidean distance. The horizontal dashed line denotes the cut off for four clusters, numbered 1 through 4, which are color coded as orange, green, dark red and blue, respectively. The percentage indicates the frequency

(Continued)

FIGURE 5 | Continued
distribution of microglial cells in these clusters. **(B)** A plot of linkage distance vs. linkage steps (or number of clusters) was performed following Thorndike's procedure. The vertical dashed line points out a marked decline in the slope, which indicates that four is an appropriate number of clusters. **(C)** Territorial mapping of microglial cells on the plane explained by the first two linear discriminant functions (LD1 and LD2); the proportion of trace for each LD is shown in parenthesis. The cells are color coded based on their cluster allocation; the centroids represent the mean value of each cluster.

TABLE 3 | Linear discriminant functions.

Parameter	LD1	LD2
Lacunarity	0.85*	0.575
Convex hull span ratio	−0.408	−0.25
Cell circularity	−0.254	1.012*
Proportion of trace (%)	57.4	26.6

The highest absolute values indicate the parameters with greater influence.

presented (**Figures 6B–D**). The cells in cluster 1 do not present any trait that allows distinguishing them from the rest of the cells groups, since their morphometric values are intermediate in comparison to the remaining groups; this is in accordance with their intermediate level of activation, as previously exposed. Cells in cluster 3, although also described as mild activated cells (similarly to cluster 1), showed however an increased *convex hull span ratio* that distinguished them from the remaining groups (**Figure 6B**). The main characteristic of cells in cluster 2 was the high *lacunarity* (**Figure 6C**), while cluster 4 cells exhibited the highest values of *cell circularity* (**Figure 6D**).

Therefore, different morphotypes were associated to each cluster, each of them described by different values of the most discriminant morphometric parameters (**Figure 6E**). According to those parameters, (a) microglial cells in cluster 3 are quite elongated or even rod shaped (red cells in **Figure 6E**); (b) microglial cells in cluster 2 present a heterogeneous or polarized morphology (green cells on **Figure 6E**); (c) cells belonging to cluster 4 are mostly rounded or amoeboid (blue cells on **Figure 6E**); (d) while those included in cluster 1 do not present a characteristic trait appearing quite similar to those in cluster 2 except that they are not elongated (yellow cells on **Figure 6E**). Since each cluster has been previously assigned a certain level of inflammatory activation, a particular microglial cell morphotype (defined by morphometric values) could be assigned to each level of inflammatory activation.

DISCUSSION

In microglial cells, the expression of the cytokine IL-1β reveals its polarization toward a pro-inflammatory phenotype that appears within few hours of exposure to a specific stimulus (Olah et al., 2011; Walker et al., 2014; Orihuela et al., 2016). In our experimental model, the injection of NA into the lateral ventricle generates an acute inflammatory process that involves the activation of microglia, which is evidenced by IL-1β expression (Granados-Durán et al., 2015; Fernández-Arjona et al., 2017). In this study, fluorescence immunohistochemistry showed that microglial cells located nearby the ventricular surfaces specifically express this inflammatory cytokine 12 h after the administration of NA, while in deeper parenchymal areas the IL-1β label was practically absent. In the region selected for this study, the dorsal hypothalamus, activated microglia was found in the nervous parenchyma up to 100–200 μm from the ventricular surface. This fact suggests that the NA spreading from the ventricular cavities toward the nervous parenchyma is responsible for the activation of microglia.

With the aim of identifying features of activated microglial cells, some studies showed that activated cells exhibit morphological changes compared to the typical surveillant morphotype of resting microglia (Boche et al., 2013; Walker et al., 2014). Those studies were accomplished by either subjective (Kloss et al., 2001; Cho et al., 2006; Diz-Chaves et al., 2012; Rodríguez-Arias et al., 2018) or objective (Karperien et al., 2013; York et al., 2018) approaches, the latter employing quantitative morphological analysis. However, the existence of different cellular morphotypes within the population of activated microglial cells has not been previously addressed. In our NA-induced inflammation model it was evident that the IL-1β positive microglial population was heterogeneous both morphologically and regarding cytokine expression. Therefore, we aimed to analyze whether different morphotypes could be defined within the activated microglial population and, moreover, if they could be assigned to different levels of activation. With a naked eye, most of the IL-1β-positive microglial cells selected for this study showed a hypertrophied soma with variety of branching patterns and, apart from rare exceptions, all were far from round or amoeboid. These observations suggested that all microglial cells selected for this analysis were in an inflammatory state of activation, but exhibiting different degrees of activation and a wide range of morphologies.

Traditionally, two forms of microglia have been described: one considered as a resting state in which cells have a highly branched morphology, and another considered as an activated state in which they acquire an amoeboid form (Davis et al., 1994; Sierra et al., 2016). Other studies have described activated microglia as cells with hypertrophied (Ayoub and Salm, 2003) or even cylindrical shape (Wierzba-Bobrowicz et al., 2002; Taylor et al., 2014). Under normal conditions, microglia may display various functional states (Ransohoff and Perry, 2009; Gomez-Nicola and Perry, 2015). Currently, it is widely accepted that highly branched microglia are not in a resting state as initially thought, but are greatly dynamic in their role of monitoring the environment (Nimmerjahn et al., 2005; Nimmerjahn, 2012). This scenario is even more intricate, since it has been observed that in some pathological situations microglial cells show an overall reduction of their processes length (Madore et al., 2013), although in others they preserve the ramifications (Stence et al., 2001; Petersen and Dailey, 2004). On the other hand, it has been observed that, after a traumatic brain injury, microglial prolongations converge toward the site of the lesion without occurring a displacement of the cell body, thus establishing a potential barrier between the healthy and the injured tissues (Davalos et al., 2005). Therefore, microglial cells with intermediate morphotypes, such as those with abundant ramifications in situations of brain damage, have been consistently described. These intermediate

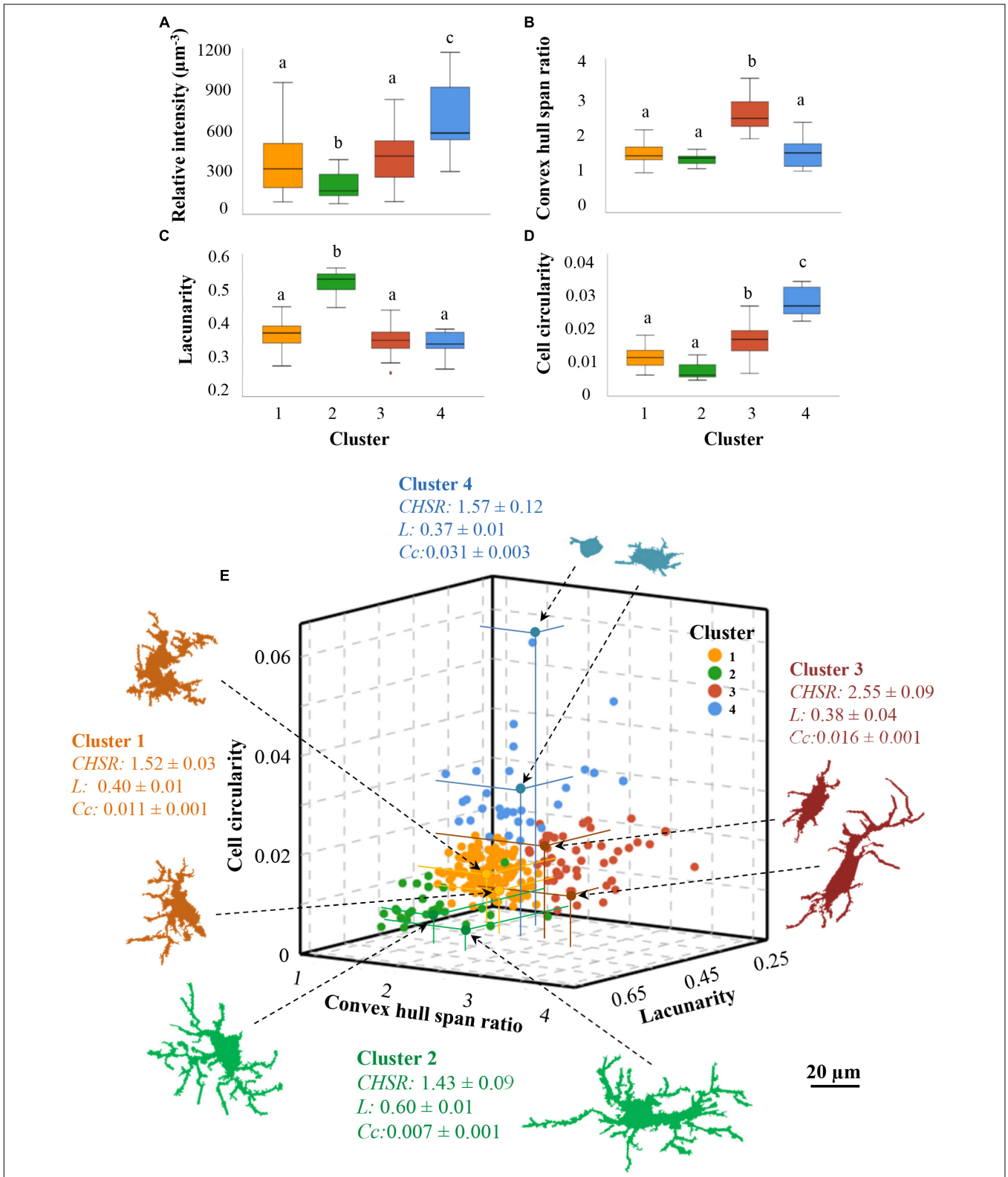

FIGURE 6 | The microglial cells clusters defined by morphological parameters are also different regarding IL-1β expression. The IL-1β relative intensity previously calculated for each microglial cell was represented in a boxes and whiskers plot, showing the mean value (±SD) in each of the morphologically established clusters **(A)**; the average IL-1β relative intensity was lowest in microglia belonging to cluster 2, and highest in those of cluster 4. Mean values of the morphological parameters used for clustering were also different **(B–D)**. Letters on top of each box indicate pair comparisons results: means of boxes with different letters are statistically

(Continued)

FIGURE 6 | Continued
different ($P < 0.05$). **(E)** Data points of a total of 250 activated microglial cells were plotted as a function of the three multimodal variables: *cell circularity* (*Cc*), the *convex hull span ratio* (*CHSR*), and *lacunarity* (*L*), on the y, x and z axes, respectively. A fourth dimension was set by a color code as a function of microglia cluster allocation. This three-dimensional Cartesian coordinate reveals a specific territorial distribution of the cells belonging to each cluster. Exemplary color-coded microglia profiles from each cluster are presented; the arrows point the location of those particular cells in the graph, and the distance to each axis is highlighted with colored lines; next to them, the cluster mean values ± standard deviation of each parameter are also shown.

forms of activated microglia seem to be also the predominant morphotypes in our acute inflammation model. At first sight, the population of hypothalamic microglia activated by NA seems to be branched morphs of the hypertrophied and shrub type. Conversely, there are no surveillant ramified nor hyper-ramified (a morphology found in chronic stress; Hinwood et al., 2013) microglial cells. Likewise, hypothalamic amoeboid microglia are virtually absent in our model.

Morphological Parameters Correlate With the Level of Expression of IL-1β in NA-Activated Hypothalamic Microglia

Fifteen morphometric parameters were measured in single cells sampled from the dorsal hypothalamus, along with the quantification of the level of expression of IL-1β by an image processing method designed to account for minor differences in the immunostaining intensity. To investigate if there was a gradual morphological change that paralleled the activation level in microglial cells, a simple linear regression analysis was performed to search for a correlation between each individual morphometric parameter and the level of expression of IL-1β (as an indicator of pro-inflammatory activation). The regression analysis results showed that, for most morphometric parameters (dependent variable), there is a dependence on the relative intensity of IL-1β (independent variable). That is, upon activation, the increase in the level of expression of IL-1β may predict how the morphology of a population of microglial cells progressively changes. Thus, it seems more accurate to think of a continuum of gradual morphological changes coming about with a gradual increase in activation, more than simply referring to an activated state. The results from this analysis demonstrate, in an objective manner, a long assumed statement: that microglial cells change their shape when they become activated. However, our results support such correlation for a population of microglial cells. Therefore, while morphological parameters could predict the level of activation of a population of cells, such prediction would not be reliable in the case of individual microglial cells, because of the relatively high dispersion of data (paramerters' values) amongst microglia.

The meaning of the gradual changes of individual morphological parameters or, even more, several parameters simultaneously changing, is not easy to unravel. However, in an attempt to visualize and understand the morphological changes, the parameters may be related to the different features of cell's shape. Thus, the variables that significantly change with the level of microglial activation are related to the regularity of the cell's surface (*cell perimeter* and *roughness*), the complexity of ramifications (*fractal dimension*), the heterogeneity of the shape (*lacunarity*), the soma thickness (*cell circularity* and *density*) and the cell's size (*mean radius, convex hull perimeter, bounding circle diameter, max span convex hull, convex hull area,* and *cell area*). No correlation was observed in the parameters related to the cylindrical shape of the cells (*convex hull span ratio* and *the ratio of convex hull radii*), hence this feature is independent of the inflammatory activation degree of microglial cells. Our correlation results indicate, in an objective way, that when microglial cells become increasingly activated the complexity of their ramifications and their heterogeneity decrease, and they become more compact. However, it should be emphasized that the correlation analysis does not allow identifying different morphotypes, nor allows considering several morphological parameters simultaneously. These objectives, which are not the aim of correlation analysis, were therefore approached by HCA.

Hierarchical Cluster Analysis Allows the Identification of Four Types of Activated Microglial Cells Based on Morphological Parameters

After showing microglial morphology dependence on the inflammatory activation level, we proceeded to seek for subgroups of microglial cells sharing similar traits within the population of activated microglia. Among all the morphological variables used in the previous correlation analysis, only *lacunarity*, *cell circularity* and *convex hull span ratio* were suitable to discriminate cellular subtypes. Hence, by using these parameters through HCA and LDA, four different clusters of NA-activated microglia were objectively revealed (**Figure 5**). Each cluster was further identified by particular average values of those three morphological parameters, as well as by a specific value of IL-1β relative intensity (that is, level of activation). Therefore, each cluster may be considered as a particular microglia morphotype within the activated hypothalamic population (**Figure 6**). The classification of activated microglia is relevant because each subgroup could be related to a particular physiological role.

Among the morphological parameters measured here, several of them can be used to discriminate between the arisen clusters (**Supplementary Figure S3**). However, in order to define each group and make these results more comprehensible, we preferred to take into account the most discriminating parameters (*lacunarity*, *cell circularity* and *convex hull span ratio;* **Figure 6**). Consequently, a slightly activated microglial group (cluster 2) is characterized by the greatest heterogeneity (*lacunarity*), and a highly activated microglial group (cluster 4) can be distinguished by the highest *cell circularity*. A third group includes cells with intermediate activation level (cluster 1 and 3), which can be subdivided in two other groups according to morphology (particularly the *convex hull span ratio*): cluster 3 includes rod-shaped cells, and cluster 1 less elongated cells.

Therefore, four groups of microglial cells were defined by their inflammatory activation level and by specific morphological parameters, namely *lacunarity*, *cell circularity* and *convex hull span ratio*. *Lacunarity* indicates the homogeneity (low values) or heterogeneity (high values) of an object (Karperien et al., 2011). If that object happens to be a cell, *lacunarity* defines the polarization of the cell, that is, when their prolongations are oriented toward a specific point. In our sample of hypothalamic activated microglia the morphotype with the highest *lacunarity* shows the lowest activation (cluster 2). This morphotype was also distinguished by the highest values of *fractal dimension* (**Supplementary Figure S3A**) which denotes a high level of complexity in ramifications (Karperien et al., 2013). The analysis of branch complexity has been used to discriminate whether microglial cells are resting or activated. Some researches employed this useful tool in particular situations, such as aged brains (van Olst et al., 2018), ischemic processes (Morrison and Filosa, 2013; Heindl et al., 2018), Alzheimer's models (Baron et al., 2014) or acute pro-inflammatory processes (Verdonk et al., 2016). In those studies ramifications complexity (*fractal dimension*) decrease when microglial cells are activated. In the present study the higher branches intricacy and cell polarization coincides with slightly activated microglia (cluster 2) and, conversely, the morphotypes with intermediate and high activation (clusters 1, 3, and 4) match with decreased processes arborization. Hence, the assessment of branches complexity by *lacunarity* and *fractal dimension* contributes to describe the different morphotypes of activated microglia.

Cell circularity or *roundness* assesses whether microglial cells resemble an amoeboid form, where values closer to 1 indicate a more circular morphology. It is known that microglial dynamic conversion from resting to activated is accompanied by a retraction of the cellular processes into the cell body (Kettenmann et al., 2011). The subjective (Davis et al., 1994; Kloss et al., 2001; Norden et al., 2016) and objective (Kozlowski and Weimer, 2012; Davis et al., 2017; Fang et al., 2018) evaluation of the circularity have shown that *roundness* is directly related to microglial activation. Similarly, in the present study the greater the circularity, the higher the degree of inflammatory activation, a fact that is clearly evidenced in cluster 4.

The *convex hull span ratio* (*CHSR*) is the ratio between the longest and the shortest diameters of the convex hull containing the microglial cell. Therefore, it reflects the degree of elongation (and conversely, circularity) of the cell. This parameter was useful to discriminate a subgroup of microglia known as bipolar or rod microglia, which has a sausage-shaped soma with long thin processes (Taylor et al., 2014). Here, a morphotype of rod-microglial cells (cluster 3) was defined by the highest *CHSR* compared to the other clusters. However, it was indistinguishable from cluster 1 in terms of activation (i.e., both showed intermediate activation based on IL-1β expression). Hence, according to this result, acquiring a more or less pronounced cylindrical profile is not related to the activation level of microglial cells. The physiological function of rod microglia seems to be enigmatic. Plenty rod microglia have been observed in human brains affected by neurological diseases (Wierzba-Bobrowicz et al., 2002), and their abundance has been associated with aging (Bachstetter et al., 2017). Moreover, rod microglial cells arise after brain injury (Morrison et al., 2017), and are distributed in lines, coupled and adjacent to the cytoarchitecture of dendrites and axons (Ziebell et al., 2012). Interestingly, bipolar/rod-shaped microglia happen to be highly proliferative and, in the presence of LPS, quickly convert into amoeboid forms (within 30 min), suggesting that are crucial for repairing the damage (Tam and Ma, 2014). In our work, the elongated shape of cluster 3 microglia could be related to a sub-ependymal location rather than to the degree of activation, since they were always underneath the ependyma monolayer of the ventricular wall. Moreover, a conspicuous layer of sub-ependymal microglia, with relevant roles in periventricular insults, has been described (Carbonell et al., 2005), as well as the movement of IBA1 positive cells across the ependymal layer toward/from the ventricular cavities (Granados-Durán et al., 2015).

CONCLUSION

This work demonstrates in a quantitative and objective way that the inflammatory activation of microglial cells is gradual, and that correlates with a morphological change. Even so, it is still possible to categorize activated cells according to their morphometric parameters, each category presenting a different activation degree. Whether the different activated microglial morphotypes undertake different physiological roles is a matter for future studies.

DATA AVAILABILITY STATEMENT

The raw data supporting the conclusions of this manuscript will be made available by the authors, without undue reservation, to any qualified researcher.

ETHICS STATEMENT

Animal care and handling were performed according to the guidelines established by the Spanish legislation (RD 53/2013) and the European Union regulation (2010/63/EU). All procedures performed were approved by the ethics committee of the Universidad de Málaga (Comité Ético de Experimentación de la Universidad de Málaga; reference 2012-0013). All efforts were made to minimize the number of animals used and their suffering.

AUTHOR CONTRIBUTIONS

ML-Á, PF-L, and MF-A conceived and designed the study. MF-A and JG carried out the experiments, image acquisition,

and image processing. ML-Á and MF-A analyzed the data and wrote the manuscript. All authors read and approved the final manuscript.

FUNDING

This work was carried out with funding from Junta de Andalucía, Consejería de Innovación Ciencia y Empleo (reference P11-CVI-07637), and Ministerio de Economía, Industria y Competitividad (MINECO, reference SAF2017-83645-R). The Leica confocal microscope (SP5 II) was acquired with FEDER funds from the European Union. These results are part of the Ph.D. Thesis of MF-A, who undertook the Ph.D. Program in Advanced Biotechnology, at the University of Málaga.

ACKNOWLEDGMENTS

The authors are grateful to D. Navas-Fernández (Servicios Centrales de Apoyo a la Investigación, Universidad de Málaga) for his help with scanner acquisition of images and confocal microscopy. The authors thank M. Vega-Sánchez and R. Hidalgo-Sánchez (Servicio Central de Informática, Universidad de Málaga) for their support with image analysis and informatics data processing.

SUPPLEMENTARY MATERIAL

The Supplementary Material for this article can be found online at: https://www.frontiersin.org/articles/10.3389/fncel.2019.00472/full#supplementary-material

REFERENCES

Ayoub, A. E., and Salm, A. K. (2003). Increased morphological diversity of microglia in the activated hypothalamic supraoptic nucleus. *J. Neurosci.* 23, 7759–7766. doi: 10.1523/jneurosci.23-21-07759.2003

Bachstetter, A. D., Ighodaro, E. T., Hassoun, Y., Aldeiri, D., Neltner, J. H., Patel, E., et al. (2017). Rod-shaped microglia morphology is associated with aging in 2 human autopsy series. *Neurobiol. Aging* 52, 98–105. doi: 10.1016/j.neurobiolaging.2016.12.028

Baron, R., Babcock, A. A., Nemirovsky, A., Finsen, B., and Monsonego, A. (2014). Accelerated microglial pathology is associated with Aβ plaques in mouse models of Alzheimer's disease. *Aging Cell* 13, 584–595. doi: 10.1111/acel.12210

Biber, K., and Block, M. (2014). "Neuroprotection versus neurotoxicity," in *Microglia in Health and Disease*, eds M.-E. Tremblay, and A. Sierra, (New York, NY: Springer).

Boche, D., Perry, V. H., and Nicoll, J. A. R. (2013). Review?: activation patterns of microglia and their identification in the human brain. *Neuropathol. Appl. Neurobiol.* 39, 3–18. doi: 10.1111/nan.12011

Carbonell, W. S., Murase, S. I., Horwitz, A. F., and Mandell, J. W. (2005). Infiltrative microgliosis: activation and long-distance migration of subependymal microglia following periventricular insults. *J. Neuroinflamm.* 2, 1–9. doi: 10.1186/1742-2094-2-5

Cho, B. P., Song, D. Y., Sugama, S., Shin, D. H., Shimizu, Y., Kim, S. S., et al. (2006). Pathological dynamics of activated microglia following medial forebrain bundle transection. *GLIA* 53, 92–102. doi: 10.1002/glia.20265

Davalos, D., Grutzendler, J., Yang, G., Kim, J. V., Zuo, Y., Jung, S., et al. (2005). ATP mediates rapid microglial response to local brain injury in vivo. *Nat. Neurosci.* 8, 752–758. doi: 10.1038/nn1472

Davis, B. M., Salinas-Navarro, M., Cordeiro, M. F., Moons, L., and De Groef, L. (2017). Characterizing microglia activation: a spatial statistics approach to maximize information extraction. *Sci. Rep.* 7:1576. doi: 10.1038/s41598-017-01747-8

Davis, E. J., Foster, T. D., and Thomas, W. E. (1994). Cellular forms and functions of brain microglia. *Brain Res. Bull.* 34, 73–78. doi: 10.1016/0361-9230(94)90189-9

de Sousa, A. A., dos Reis, R. R., de Lima, C. M., de Oliveira, M. A., Fernandes, T. N., Gomes, G. F., et al. (2015). Three-dimensional morphometric analysis of microglial changes in a mouse model of virus encephalitis: age and environmental influences. *Eur. J. Neurosci.* 42, 2036–2050. doi: 10.1111/ejn.12951

Del Carmen Gómez-Roldán, M., Pérez-Martín, M., Capilla-González, V., Cifuentes, M., Pérez, J., García-Verdugo, J. M., et al. (2008). Neuroblast proliferation on the surface of the adult rat striatal wall after focal ependymal loss by intracerebroventricular injection of neuraminidase. *J. Comp. Neurol.* 507, 1571–1587. doi: 10.1002/cne.21618

Diz-Chaves, Y., Pernía, O., Carrero, P., and Garcia-Segura, L. M. (2012). Prenatal stress causes alterations in the morphology of microglia and the inflammatory response of the hippocampus of adult female mice. *J. Neuroinflamm.* 9:71. doi: 10.1186/1742-2094-9-71

Fang, M., Yamasaki, R., Li, G., Masaki, K., Yamaguchi, H., Fujita, A., et al. (2018). Connexin 30 deficiency attenuates chronic but not acute phases of experimental autoimmune encephalomyelitis through induction of neuroprotective microglia. *Front. Immunol.* 9:2588. doi: 10.3389/fimmu.2018.02588

Fernández-Arjona, M., Grondona, J. M., Granados-Durán, P., Fernández-Llebrez, P., and López-Ávalos, M. D. (2017). Microglia morphological categorization in a rat model of neuroinflammation by hierarchical cluster and principal components analysis. *Front. Cell. Neurosci.* 11:235. doi: 10.3389/fncel.2017.00235

Fisher, R. (1936). The use of multiple measurements in taxonomic problems. *Ann. Eugen.* 7, 179–188. doi: 10.1111/j.1469-1809.1936.tb02137.x

Gomez-Nicola, D., and Perry, V. H. (2015). Microglial dynamics and role in the healthy and diseased brain. *Neuroscientist* 21, 169–184. doi: 10.1177/1073858414530512

Granados-Durán, P., López-Ávalos, M. D., Grondona, J. M., Gómez-Roldán, M. D. C., Cifuentes, M., Pérez-Martín, M., et al. (2015). Neuroinflammation induced by intracerebroventricular injection of microbial neuraminidase. *Front. Med.* 2:14. doi: 10.3389/fmed.2015.00014

Grondona, J. M., Pérez-Martín, M., Cifuentes, M., Pérez, J., Jiménez, A. J., and Pérez-Fígares, J. M. (1996). Ependymal denudation, aqueductal obliteration and hydrocephalus after a single injection of neuraminidase into the lateral ventricle of adult rats. *J. Neuropathol. Exp. Neurol.* 55, 999–1008. doi: 10.1097/00005072-199609000-00007

Heindl, S., Gesierich, B., Benakis, C., Llovera, G., Duering, M., and Liesz, A. (2018). Automated morphological analysis of microglia after stroke. *Front. Cell. Neurosci.* 12:106. doi: 10.3389/fncel.2018.00106

Hinwood, M., Tynan, R. J., Charnley, J. L., Beynon, S. B., Day, T. A., and Walker, F. R. (2013). Chronic stress induced remodeling of the prefrontal cortex: structural re-organization of microglia and the inhibitory effect of minocycline. *Cereb. Cortex* 23, 1784–1797. doi: 10.1093/cercor/bhs151

Karperien, A., Ahammer, H., and Jelinek, H. F. (2013). Quantitating the subtleties of microglial morphology with fractal analysis. *Front. Cell. Neurosci.* 7:3. doi: 10.3389/fncel.2013.00003

Karperien, A., Jelinek, H. F., and Milosevic, N. (2011). "Reviewing lacunarity analysis and classification of microglia in neuroscience," in *Proceedings of the 8th European Conference on Mathematical and Theoretical Biology*, (Cracow: European Society for Mathematical and Theoretical Biology (ESMTB)).

Kettenmann, H., Hanisch, U.-K., Noda, M., and Verkhratsky, A. (2011). Physiology of microglia. *Physiol. Rev.* 91, 461–553. doi: 10.1152/physrev.00011.2010

Kloss, C. U. A., Bohatschek, M., Kreutzberg, G. W., and Raivich, G. (2001). Effect of lipopolysaccharide on the morphology and integrin immunoreactivity of ramified microglia in the mouse brain and in cell culture. *Exp. Neurol.* 168, 32–46. doi: 10.1006/exnr.2000.7575

Kongsui, R., Beynon, S. B., Johnson, S. J., and Walker, F. (2014). Quantitative assessment of microglial morphology and density reveals remarkable consistency in the distribution and morphology of cells within the healthy prefrontal cortex of the rat. *J. Neuroinflamm.* 11:182. doi: 10.1186/s12974-014-0182-7

Kozlowski, C., and Weimer, R. M. (2012). An automated method to quantify microglia morphology and application to monitor activation state longitudinally in vivo. *PLoS One* 7:e31814. doi: 10.1371/journal.pone.0031814

Madore, C., Joffre, C., Delpech, J. C., De Smedt-Peyrusse, V., Aubert, A., Coste, L., et al. (2013). Early morphofunctional plasticity of microglia in response to acute lipopolysaccharide. *Brain Behav. Immun.* 34, 151–158. doi: 10.1016/j.bbi.2013.08.008

Morrison, H., Young, K., Qureshi, M., Rowe, R. K., and Lifshitz, J. (2017). Quantitative microglia analyses reveal diverse morphologic responses in the rat cortex after diffuse brain injury. *Sci. Rep.* 7:13211. doi: 10.1038/s41598-017-13581-z

Morrison, H. W., and Filosa, J. A. (2013). A quantitative spatiotemporal analysis of microglia morphology during ischemic stroke and reperfusion. *J. Neuroinflamm.* 10:4. doi: 10.1186/1742-2094-10-4

Nimmerjahn, A. (2012). Two-photon imaging of microglia in the mouse cortex in Vivo. *Cold Spring Harb. Protoc.* 7, 594–603. doi: 10.1101/pdb.prot069294

Nimmerjahn, A., Kirchhoff, F., and Helmchen, F. (2005). Resting microglial cells are highly dynamic surveillants of brain parenchyma in vivo. *Science* 308, 1314–1318. doi: 10.1126/science.1110647

Norden, D. M., Trojanowski, P. J., Villanueva, E., Navarro, E., and Godbout, J. P. (2016). Sequential activation of microglia and astrocyte cytokine expression precedes increased iba-1 or GFAP immunoreactivity following systemic immune challenge. *GLIA* 64, 300–316. doi: 10.1002/glia.22930

Ohgomori, T., Yamada, J., Takeuchi, H., Kadomatsu, K., and Jinno, S. (2016). Comparative morphometric analysis of microglia in the spinal cord of SOD1 G93A transgenic mouse model of amyotrophic lateral sclerosis. *Eur. J. Neurosci.* 43, 1340–1351. doi: 10.1111/ejn.13227

Olah, M., Biber, K., Vinet, J., and Boddeke, H. W. G. M. (2011). Microglia phenotype diversity. *CNS Neurol. Disord. Drug Targets* 10, 108–118. doi: 10.2174/187152711794488575

Orihuela, R., McPherson, C. A., and Harry, G. J. (2016). Microglial M1/M2 polarization and metabolic states. *Br. J. Pharmacol.* 173, 649–665. doi: 10.1111/bph.13139

Paxinos, G., and Watson, C. (2007). *The Rat Brain in Stereotaxic Coordinates*, 6th Edn. San Diego, CA: Academic Press.

Petersen, M. A., and Dailey, M. E. (2004). Diverse microglial motility behaviors during clearance of dead cells in hippocampal slices. *Glia* 46, 195–206. doi: 10.1002/glia.10362

Ransohoff, R. M. (2016). A polarizing question: do M1 and M2 microglia exist. *Nat. Neurosci.* 19, 987–991. doi: 10.1038/nn.4338

Ransohoff, R. M., and Perry, V. H. (2009). Microglial physiology: unique stimuli, specialized responses. *Annu. Rev. Immunol.* 27, 119–145. doi: 10.1146/annurev.immunol.021908.132528

Rodríguez-Arias, M., Montagud-Romero, S., Carrión, A. M. G., Ferrer-Pérez, C., Pérez-Villalba, A., Marco, E., et al. (2018). Social stress during adolescence activates long-term microglia inflammation insult in reward processing nuclei. *PLoS One* 13:e0206421. doi: 10.1371/journal.pone.0206421

Santos-Filho, C., de Lima, C. M., Fôro, C. A. R., de Oliveira, M. A., Magalhães, N. G. M., Guerreiro-Diniz, C., et al. (2014). Visuospatial learning and memory in the *Cebus apella* and microglial morphology in the molecular layer of the dentate gyrus and CA1 lacunosum molecular layer. *J. Chem. Neuroanat.* 61, 176–188. doi: 10.1016/j.jchemneu.2014.10.001

Scheweitzer, L., and Renehan, W. (1997). The use of cluster analysis for cell typing. *Brain Res. Protoc.* 1, 100–108. doi: 10.1016/s1385-299x(96)00014-1

Sierra, A., de Castro, F., del Río-Hortega, J., Rafael Iglesias-Rozas, J., Garrosa, M., and Kettenmann, H. (2016). The "Big-Bang" for modern glial biology: translation and comments on Pío del Río-Hortega 1919 series of papers on microglia. *Glia* 64, 1801–1840. doi: 10.1002/glia.23046

Soltys, Z., Orzylowska-Sliwinska, O., Zaremba, M., Orlowski, D., Piechota, M., Fiedorowicz, A., et al. (2005). Quantitative morphological study of microglial cells in the ischemic rat brain using principal component analysis. *J. Neurosci. Methods* 146, 50–60. doi: 10.1016/j.jneumeth.2005.01.009

Soltys, Z., Ziaja, M., Pawlinski, R., Setkowicz, Z., and Janeczko, K. (2001). Morphology of reactive microglia in the injured cerebral cortex. *J. Neurosci. Res.* 63, 90–97.

Stence, N., Waite, M., and Dailey, M. E. (2001). Dynamics of microglial activation: a confocal time-lapse analysis in hippocampal slices. *Glia* 33, 256–266.

Tam, W. Y., and Ma, C. H. E. (2014). Bipolar/rod-shaped microglia are proliferating microglia with distinct M1/M2 phenotypes. *Sci. Rep.* 4:7279. doi: 10.1038/srep07279

Taylor, S. E., Morganti-Kossmann, C., Lifshitz, J., and Ziebell, J. M. (2014). Rod microglia: a morphological definition. *PLoS One* 9:e97096. doi: 10.1371/journal.pone.0097096

Thorndike, R. L. (1953). Who belongs in the family? *Psychometrika* 18, 267–276. doi: 10.1007/BF02289263

Torres-Platas, S. G., Comeau, S., Rachalski, A., Bo, G. D., Cruceanu, C., Turecki, G., et al. (2014). Morphometric characterization of microglial phenotypes in human cerebral cortex. *J. Neuroinflamm.* 11:12. doi: 10.1186/1742-2094-11-12

van Olst, L., Bielefeld, P., Fitzsimons, C. P., de Vries, H. E., and Schouten, M. (2018). Glucocorticoid-mediated modulation of morphological changes associated with aging in microglia. *Aging Cell* 17:e12790. doi: 10.1111/acel.12790

Verdonk, F., Roux, P., Flamant, P., Fiette, L., Bozza, F. A., Simard, S., et al. (2016). Phenotypic clustering: a novel method for microglial morphology analysis. *J. Neuroinflamm.* 13:153. doi: 10.1186/s12974-016-0614-7

Walker, F. R., Beynon, S. B., Jones, K. A., Zhao, Z., Kongsui, R., Cairns, M., et al. (2014). Dynamic structural remodelling of microglia in health and disease: a review of the models, the signals and the mechanisms. *Brain Behav. Immun.* 37, 1–14. doi: 10.1016/j.bbi.2013.12.010

Ward, J. H. (1963). Hierarchical grouping to optimize an objective function. *J. Am. Stat. Assoc.* 58, 236–244. doi: 10.1080/01621459.1963.10500845

Wierzba-Bobrowicz, T., Gwiazda, E., Kosno-Kruszewska, E., Lewandowska, E., Lechowicz, W., Bertrand, E., et al. (2002). Morphological analysis of active microglia — rod and ramified microglia in human brains affected by some neurological diseases (SSPE, Alzheimer's disease and Wilson's disease). *Folia Neuropathol.* 40, 125–131.

Yamada, J., and Jinno, S. (2013). Novel objective classification of reactive microglia following hypoglossal axotomy using hierarchical cluster analysis. *J. Comp. Neurol.* 521, 1184–1201. doi: 10.1002/cne.23228

York, E. M., LeDue, J. M., Bernier, L.-P., and MacVicar, B. A. (2018). 3DMorph automatic analysis of microglial morphology in three dimensions from ex vivo and in vivo imaging. *Eneuro* 5:ENEURO.0266-18.2018. doi: 10.1523/ENEURO.0266-18.2018

Zanier, E. R., Fumagalli, S., Perego, C., Pischiutta, F., and De Simoni, M.-G. (2015). Shape descriptors of the "never resting" microglia in three different acute brain injury models in mice. *Intens. Care Med. Exp.* 3:39. doi: 10.1186/s40635-015-0039-0

Ziebell, J. M., Taylor, S. E., Cao, T., Harrison, J. L., and Lifshitz, J. (2012). Rod microglia: elongation, alignment, and coupling to form trains across the somatosensory cortex after experimental diffuse brain injury. *J. Neuroinflamm.* 9:247. doi: 10.1186/1742-2094-9-247

Conflict of Interest: The authors declare that the research was conducted in the absence of any commercial or financial relationships that could be construed as a potential conflict of interest.

frontiers in Cellular Neuroscience

ORIGINAL RESEARCH
published: 10 January 2020
doi: 10.3389/fncel.2019.00581

Cocaine Self-administration and Extinction Inversely Alter Neuron to Glia Exosomal Dynamics in the Nucleus Accumbens

Rachel Jarvis[1], *Alessandra Tamashiro-Orrego*[1], *Vanessa Promes*[1], *Leona Tu*[1], *Jinyuan Shi*[1] *and Yongjie Yang*[1,2]*

[1]*Department of Neuroscience, Tufts University School of Medicine, Boston, MA, United States,* [2]*Graduate School of Biomedical Sciences, Tufts University, Boston, MA, United States*

OPEN ACCESS

Edited by:
Carole Escartin, UMR9199 Laboratory of Neurodegenerative Diseases Mechanisms, Therapies, Imaging, France

Reviewed by:
Ana-Clara Bobadilla, Medical University of South Carolina, United States
Lori A. Knackstedt, University of Florida, United States

***Correspondence:**
Yongjie Yang
yongjie.yang@tufts.edu

Received: *16 September 2019*
Accepted: *19 December 2019*
Published: *10 January 2020*

Citation:
Jarvis R, Tamashiro-Orrego A, Promes V, Tu L, Shi J and Yang Y (2020) Cocaine Self-administration and Extinction Inversely Alter Neuron to Glia Exosomal Dynamics in the Nucleus Accumbens. Front. Cell. Neurosci. 13:581. doi: 10.3389/fncel.2019.00581

Alteration of glutamatergic synaptic plasticity in the Nucleus Accumbens (NAc) has been implicated in cocaine-seeking behaviors. Astroglial mechanisms for maintaining extracellular glutamate homeostasis through cysteine/glutamate exchanger (xCT) and glutamate transporter GLT1 are dysregulated following cocaine exposure and contribute to altered glutamatergic synaptic plasticity. However, how these astroglial proteins become dysregulated in cocaine addiction remains unknown. We recently showed that neuron to astroglial exosome signaling is essential to maintain GLT1 protein expression by transferring neuronal miR-124-3p into astrocytes to suppress GLT1-inhibiting microRNAs (miRs) in astrocytes. In the current study, by selectively labeling neuronal exosomes using CD63-GFP$^{f/+}$ exosome reporter mice, we examined how the self-administration and extinction stages of the mouse cocaine self-administration model alter neuronal exosome signaling to astrocytes and microglia in the NAc. We found that cocaine (but not food) self-administration strongly reduces the internalization of neuronal exosomes, particularly in astrocytes in the NAc (but not in motor cortex), which can be effectively reversed by extinction training. In parallel, cocaine self-administration alone specifically and differentially affects activation of glial cells by decreasing GFAP expression in astrocytes but increasing Iba1 expression in microglia. However, extinction training fully reverses the increased Iba1 expression in microglia but only partially reverses the reduction of GFAP in astrocytes. Taken together, our study reveals altered *in vivo* dynamics of NAc neuronal exosomes in the cocaine addiction model, providing new insights about how altered neuron to glial exosome signaling may contribute to astroglial dysfunction in cocaine addiction.

Keywords: cocaine, exosome, astroglia, GLT1, microglia

INTRODUCTION

Cocaine addiction is a chronic neurological disorder primarily manifested with compulsive drug-seeking behaviors, which are coordinately influenced by multiple neural circuitries in different brain regions, including at least prefrontal cortex, amygdala, nucleus accumbens (NAc), and ventral tegmental area (VTA; Kelley, 2004; Kalivas, 2009). In particular, NAc receives and integrates inputs from both cortical and limbic regions and is considered a central brain structure in developing reward-driven (including drug-seeking) behaviors (Scofield et al., 2016a). Early observations have shown altered dopaminergic neurotransmission as an underlying mechanism for drug-seeking behavior (Berridge and Robinson, 1998). Cocaine-mediated inhibition of dopamine transporter (DAT) leads to elevation of extracellular dopamine levels that enhance dopaminergic synaptic transmission in NAc, resulting in a strengthened rewarding effect of drug-seeking behavior (Nestler, 2005).

Recently, altered glutamate homeostasis and glutamatergic synaptic plasticity in NAc has also been implicated in cocaine addiction behavior (Kalivas, 2009). Cocaine addiction affects both neuronal and astroglial mechanisms for maintaining proper glutamate homeostasis. Cocaine decreases activity and protein expression of the cysteine/glutamate exchanger xCT that is enriched in NAc astrocytes for extracellular transport of glutamate (Baker et al., 2002; Madayag et al., 2007; Knackstedt et al., 2010), leading to reduced activation of pre-synaptic mGluR2/3 receptors and enhanced presynaptic glutamate release (Moussawi and Kalivas, 2010). Cocaine also decreases functional uptake of extracellular glutamate-mediated by the predominant glutamate transporter GLT1 (Knackstedt et al., 2010; Trantham-Davidson et al., 2012), further contributing to increased extracellular glutamate levels. Restoration of xCT or GLT1 expression by N-acetylcysteine (NAC) or the β-lactam antibiotic ceftriaxone, respectively, is sufficient to inhibit cocaine- and cue-induced reinstatement of drug-seeking behavior (Baker et al., 2003; Knackstedt et al., 2010; Reichel et al., 2011). However, how xCT and GLT1 become dysregulated in cocaine addiction remains unknown.

Although GLT1 (human analog EAAT2) is predominantly and abundantly expressed in adult astrocytes across the CNS, the physiological induction of GLT1 in astrocytes is strongly dependent upon neuronal signals (Yang et al., 2009). By employing a VGluT1 KO and generating mGluR5 conditional knock-out mice, we previously showed that glutamatergic neuronal signaling, presumably glutamate itself, plays a role in the developmental induction of GLT1 (Morel et al., 2014). Recently, we also showed that cultured neurons secrete exosomes, a major class of extracellular vesicles (EVs) with a size range of 40–100 nm that originate from endosomes, that contain abundant miR-124 that can be internalized into astrocytes to increase miR-124 levels in astrocytes (Men et al., 2019). MicroRNAs (miRs) are a class of non-coding RNAs with a length of 20–15 nucleotides that actively and significantly modulate development and disease progress in many tissues including the CNS. MiR-124 is one of the most abundant neuronal miRs in the CNS, which is essential for neuronal differentiation during early embryogenesis by antagonizing the anti-neural REST/SCP1 pathway (Conaco et al., 2006). MiR-124 is also an active modulator of synaptic connectivity and plasticity (McNeill and Van Vactor, 2012). Neuronal exosomes and miR-124 are also able to significantly up-regulate GLT1 protein levels by suppressing endogenous GLT1-inhibiting miRs in astrocytes (Men et al., 2019). EVs and exosomes secreted from various CNS cell types have emerged as a novel and important intercellular communication pathway in the CNS that has also been implicated in pathological conditions of the CNS, including neurological injury (Xiong et al., 2017), neurodegenerative diseases (Quek and Hill, 2017), and glioma (Gourlay et al., 2017). Whether exosome signaling between neurons and glia is altered in cocaine addiction has not been explored. In the current study, we examined the *in vivo* dynamics of neuronal exosomes using our recently developed exosome reporter (CD63-GFP$^{f/f}$) mice in the cocaine self-administration model.

MATERIALS AND METHODS

Animals

The CD63-GFP$^{f/f}$ mice have been previously published (Men et al., 2019), and were generated in house with help by Biocytogen (Worcester, MA, USA). CamKIIα-CreERT transgenic mice (strain #012362) were obtained from the Jackson Laboratory. CD63-GFP$^{f/f}$ and CaMKIIα-CreERT mice were bred to generate the experimental CamKIIα-CreERT^{+}CD63-GFP$^{f/+}$ mice. Bac *aldh1l1*-eGFP mice were obtained from the GENSAT project through the Jackson Laboratory. Both male and female mice were used for all experiments. All mice were housed on a 12 h light/dark cycle (lights on at 07:00) with food and water provided *ad libitum*. Care and treatment of the mice during all procedures strictly adhered to the NIH Guide for the Care and Use of Laboratory Animals, the Guidelines for the Use of Animals in Neuroscience Research, and the Tufts University IACUC policies.

Drugs and Tamoxifen Injection

Cocaine HCl (20 mg/ml) was generously provided by the NIDA Drug Supply Program and diluted to working concentration in sterile saline. Tamoxifen (4-OHT, Sigma) was resuspended in 100% ethanol at 20 mg/ml, and then diluted to 2 mg/ml in sunflower oil for injection. CamKIIα-CreERT^{+}CD63-GFP$^{f/+}$ mice were given a single 10 mg/kg dose of tamoxifen by intraperitoneal (i.p.) injection at postnatal day 42 (P42).

Catheter Implantation Surgery

Mice were anesthetized with isoflurane (induction 3–5%, maintenance 1–3%) for surgical implantation of an indwelling jugular vein catheter connected to a head-mounted entry port, as previously described (Griffin et al., 2007). Briefly, the right jugular vein was exposed, and the catheter tubing was inserted and secured to the vein. The catheter was passed under the skin to an incision on the head, and the port was secured to the skull with dental cement anchored by screws. Mice were given buprenorphine (0.1 mg/kg) for

analgesia and allowed to recover for 3–7 days before beginning self-administration. Catheter patency was maintained by daily infusion of 100 μl heparinized saline (100 U/μl) through the catheter. Catheter patency was confirmed by infusion of 20–30 μl Brevital (methohexital, 10 mg/ml) through the catheter the day before self-administration training began, after the last self-administration session, and as needed during self-administration training if mice did not acquire self-administration behavior or if their behavior changed unexpectedly. Mice that did not show signs of sedation within 2–3 s of Brevital infusion were excluded from the study as having non-patent catheters.

Behavior Training

All behavior testing was done in extra wide mouse operant chambers with a modified top (Med Associates, VT, USA). The chambers were fitted with a touchscreen on one side, which was covered with an aperture plate to frame the two presented images. The opposite side of the chamber contained a food pellet receptacle connected to a pellet dispenser, with a stimulus light above the pellet receptacle. The chambers also contained a house light and a tone generator. Cocaine was delivered by a syringe pump located outside the chamber, and the drug delivery tubing was connected to the mice through a swivel and swivel arm (Instech, Plymouth Meeting, PA, USA) mounted on top of the chamber to allow free movement of the animals during self-administration. All aspects of the sessions were controlled and recorded by K-Limbic software (Conclusive Marketing, Limited, UK).

Cocaine Self-administration

Mice were not pre-trained with food to press the touchscreen and were not food-restricted during the study. Self-administration sessions took place once daily during the light cycle for 12 consecutive days. Two images, a circle and an X were presented on the touchscreen (white images on black background, 2 cm × 2 cm). The X was considered the active image and the circle of the inactive image for all mice. The side the active image was presented on was counterbalanced within groups. The availability of cocaine reward was indicated by illumination of the house light and displaying the images on the touchscreen. Touching the active image resulted in a 2 s infusion of cocaine (1 mg/kg in a volume of 12–30 μl, based on weight). Each infusion was paired with a cue (1 s tone and illumination of the stimulus light) followed by a 30 s time-out signaled by turning off the house light and removing the images from the touchscreen. Pressing the inactive image was recorded but had no consequences. Sessions lasted 2 h, or until mice received 30 infusions (30 mg/kg) of cocaine (to prevent overdose). For the first 3 days of self-administration training, a non-contingent dose of cocaine was given through the jugular catheter using the software controls at the start of the session, as well as at intervals throughout the session, to facilitate acquisition of self-administration behavior (no more than eight non-contingent infusions per session, <4 non-contingent infusions/session on average). Sham mice were implanted with a catheter and placed in the operant chambers with identical images and cues, but were not connected to the syringe pump and received no reward for pressing the active image. Sham mice experienced 2–4 non-contingent activations of the paired light and sound cues (as if the active image had been pressed) using the software controls, for the first 3 days of self-administration training. Mice met criteria for acquisition of self-administration when they: (1) self-administered at least 20 infusions in a session; (2) >70% of responses were on the active image; and (3) had no more than 20% variation in number of infusions between sessions.

Cocaine Extinction

Two days following the last self-administration session, extinction training began. Extinction sessions took place 6 days per week. The same active and inactive images (on the same side as during self-administration) were presented on the touchscreen, and the house light was kept turned off. Pressing the touchscreen on either the active or inactive image had no consequences, but all touches were recorded. Mice met criteria for extinction when they: (1) made fewer than eight responses on the active image; and (2) did not distinguish between the active and inactive image (<70% of responses on active image). All mice met extinction criteria within the 18–20 total days of extinction training.

Food Self-administration

Mice in the food self-administration group were not implanted with a jugular catheter and were not food-restricted prior to or during behavior training. Food self-administration took place 5 days per week and was carried out as close to cocaine self-administration procedures as possible. The same active and inactive images were used, but pressing the active image resulted in the delivery of a food pellet (14 mg dustless precision pellets, Bio-Serv) along with the paired light and sound cues. The time-out period was a minimum of 30 s (as in cocaine self-administration), but mice additionally had to retrieve the food pellet (detected by a head entry sensor in the pellet receptacle) before the next trial could start. To facilitate acquisition of food self-administration during the first 1–4 sessions, non-contingent food reward was delivered (once at the start of the session and at intervals during the session, no more than eight non-contingent rewards/session) and trials were manually advanced if the mouse did not retrieve pellet within ∼10 min. Food self-administration sessions ended after 2 h, or when mice received 50 food pellets. Mice in the sham group were placed in the operant chambers under the same conditions, except that no food reward was delivered for pressing the active image. Mice met food self-administration criteria when they: (1) self-administered at least 30 food pellets in a session; (2) >70% of responses were on the active image; and (3) had no more than 20% variation in number of infusions between sessions.

Tissue Processing, Immunohistochemistry, and Imaging

Two hours after the last behavior session, animals were deeply anesthetized with ketamine (100 mg/kg) + xylazine (10 mg/kg) in saline by intraperitoneal (i.p.) injection. Mice were perfused

intracardially with ice-cold 4% paraformaldehyde (PFA) in PBS. Brains were dissected out and post-fixed overnight in 4% PFA at 4°C, then cryoprotected in 30% sucrose for 48 h at 4°C. The brains were embedded and frozen in OCT Compound Tissue-Tek® (Sakura, Tokyo Japan). Twenty micrometer coronal sections were prepared using a Leica HM525 cryostat and mounted on glass SuperFrost+ slides (Thermo Fisher Scientific). For immunohistochemistry, slides were rinsed in PBS then treated with blocking buffer (1% BSA, 5% goat serum, 0.2% Triton in 1× PBS) for 1 h at room temperature. Primary antibodies against GFAP (1:1,000, Dako) and Iba1 (1:500, Wako) were incubated overnight at 4°C in blocking buffer. After washing slides three times in PBS, the secondary antibody (1:2,000, goat anti-rabbit AlexaFluor 633) was added for 2 h at room temperature. The slides were rinsed three times in PBS before mounting with ProLong Gold Antifade Mountant with DAPI (Thermo Fisher Scientific). Representative whole-brain image was taken at 10× magnification using the Keyence BZ-X710 Slide Scanner. Confocal images were taken using the Nikon A1R confocal laser scanning microscope. Representative high magnification images were taken with the 40× (numerical aperture 1.3) objective (15–20 μm *z*-stack with 0.5 μm step). Images for quantification were taken with a 20× (numerical aperture 0.75) objective (13–20 μm *z*-stack with 1.5 μm step). Confocal imaging settings and thresholding parameters were kept consistent within each behavioral group (self-administration, self-administration followed by extinction, and food self-administration).

To quantify the number of CD63-GFP puncta overlapped with astrocytes or microglia, a maximum intensity projection (MIP) image of the GFAP or Iba1 image was first generated. The GFAP or Iba1 labeled glia were then outlined using the freehand tool in ImageJ to create a region of interest (ROI). Next, a MIP image of the CD63-GFP puncta (green channel) was generated, and the image was converted to 8-bit grayscale and then thresholded to remove the background. The glia ROI was then overlaid on the thresholded CD63-GFP image, and the particle analysis function in ImageJ was used to analyze the number of CD63-GFP puncta inside the glia ROI. The area of the ROI was measured, and the number of CD63-GFP puncta was divided by the ROI area to find the number of puncta per μm^2 of glia ROI. GFAP and Iba1 intensity were measured by first generating a MIP image, then converting the image to 8-bit grayscale, and finally using the Measure function in ImageJ to determine the average intensity. Microglia were counted from the MIP of the Iba1 channel. Images from BAC *aldh1l1*-eGFP mice were used to count astrocytes in the NAc, based on the MIP of the GFP channel. DAPI signal was overlaid whenever counting cells to ensure that only bona fide cells were counted.

For immunohistochemistry analyses (puncta count per glia ROI, GFAP/Iba1 intensity, microglia counts), four mice per group were used for cocaine and sham self-administration and cocaine and sham extinction; for food self-administration, three mice were used, and for sham food self-administration, two mice were used. For analysis of CD63-GFP puncta inside of glia, 20 astrocytes or microglia were counted per animal. For counting the number of astrocytes in NAc after cocaine or sham self-administration, three mice per group were used.

Experimental Design and Statistical Analysis

Sample sizes and the statistical approach used for each experiment are described in the figure legends. Previous results were used to estimate reasonable sample sizes. All analyses were performed using GraphPad Prism 7. All values were plotted as column graphs with individual values shown or as a cumulative probability curve. For graphs with error bars, error bars are presented as SEM. No custom code was used in the analysis. For two-group comparison, an unpaired two-tailed student's *t*-test was used. For cumulative probability curves comparison, the Kolmogorov–Smirnov test was used. Behavior data were analyzed using a two-way repeated-measures ANOVA. Statistical significance was tested at a 95% ($P < 0.05$) confidence level, *P*-values are shown in each graph, and *F*-scores (F), *t*-scores (t), and degrees of freedom (*df*) are reported in the text and figure legends. Outlier analysis was done in Prism using the ROUT method ($Q = 1\%$), and individual data points identified as outliers were removed.

RESULTS

We recently generated exosome reporter CD63-GFP$^{f/f}$ mice in which GFP-fused CD63 (membrane marker of exosomes) can be induced following Cre-dependent recombination (Men et al., 2019). To selectively label neuronal exosomes *in vivo*, we bred CD63-GFP$^{f/f}$ mice with CaMKIIα-CreER^{+} mice that specifically express Cre recombinase in neurons under the CaMKIIα promoter, to generate CaMKIIα-CreER^{+}CD63-GFP$^{f/+}$ mice (**Figure 1A**). Following a single injection of 4-OHT (i.p., 10 mg/kg) at P42, clear and robust expression of the CD63-GFP reporter throughout the cortex, hippocampus, and striatum were observed (**Figure 1B**). Adult (P120–140) CaMKIIα-CreER^{+}CD63-GFP$^{f/+}$ mice were implanted with an indwelling jugular catheter, as described previously (Griffin et al., 2007) and split into different groups for the behavior training (**Figure 1C**). One group of mice was used for cocaine self-administration training only ("Self-administration"), while another group went through both cocaine self-administration and extinction training before tissue collection ("Extinction"). Sham mice were also implanted with a catheter and placed in the operant chambers with identical images and cues as the cocaine groups, but were not connected to the syringe pump and received no reward for pressing the active image during either the self-administration or the extinction phase. During the cocaine self-administration training, CaMKIIα-CreER^{+}CD63-GFP$^{f/+}$ mice with access to cocaine clearly favored the active image over the inactive image on the touchscreen [**Figure 1D**; 2-way repeated measures ANOVA showed significant main effect of image ($F_{(1,26)} = 94.44$, $p < 0.0001$) and time ($F_{(11,286)} = 3.064$, $p = 0.007$), as well as significant interaction time × image ($F_{(11,286)} = 14.56$, $p < 0.0001$)], while the sham group (no cocaine access) did not distinguish between the active and inactive images (data not shown). As a result, the CamKIIα-CreER^{+}CD63-GFP$^{f/+}$

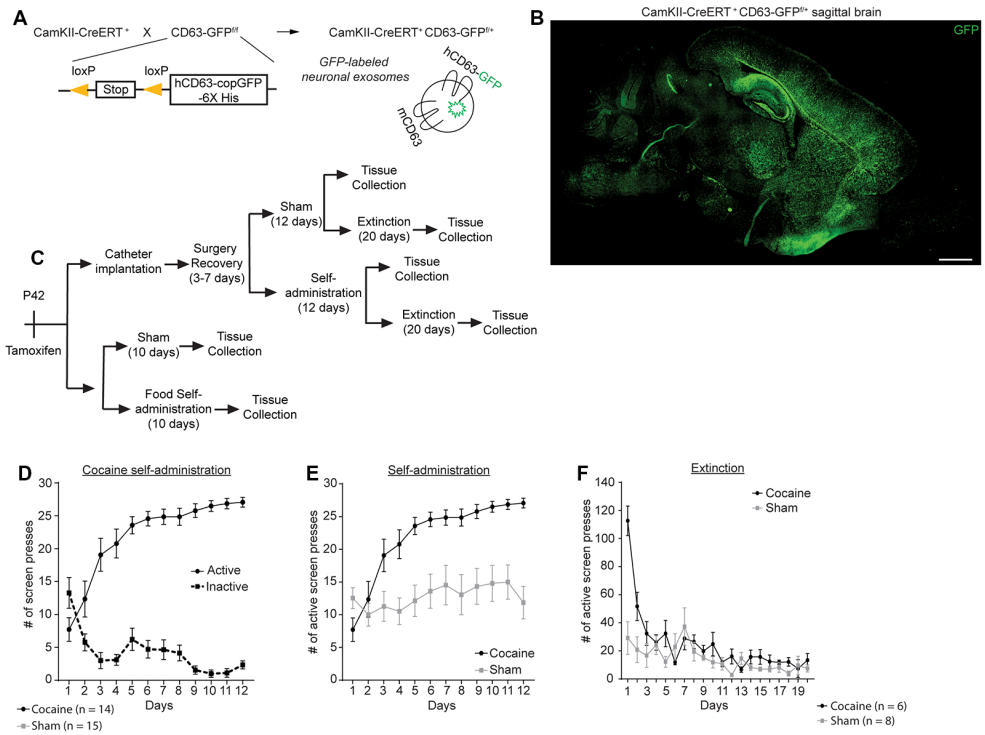

FIGURE 1 | Cocaine self-administration and extinction in CamKIIα-CreER^{+} CD63-GFP$^{f/+}$ mice. **(A)** Schematic diagram of the breeding strategy to generate neuron-specific exosome/intraluminal vesicle (ILV) reporter mice. **(B)** Representative image showing distribution of CD63-GFP puncta in the brain of CamKIIα-CreER^{+}CD63-GFP$^{f/+}$ mice. Scale bar: 2 mm. **(C)** Schematic showing the experimental strategy and behavior testing used in this study. **(D)** Active and inactive image screen presses for cocaine self-administration group; $n = 14$ mice, significant main effect of image ($F_{(1,26)} = 94.44$, $p < 0.0001$) and time ($F_{(11,286)} = 3.064$, $p = 0.007$), as well as significant interaction time × image ($F_{(11,286)} = 14.56$, $p < 0.0001$). **(E)** Cocaine and sham self-administration of mice used in this study; total number of active screen presses are shown; $n = 14$ mice (cocaine group), $n = 16$ mice (sham group), significant main effect of group ($F_{(1,27)} = 16.62$, $p = 0.0004$) and time ($F_{(11,297)} = 12.41$, $p < 0.0001$, as well as a significant interaction time × group ($F_{(11,297)} = 6.605$, $p < 0.0001$). **(F)** Extinction of cocaine and sham mice following self-administration; $n = 6$ (cocaine group), $n = 8$ sham group. Statistics calculated using two-way repeated measures ANOVA.

mice that underwent cocaine self-administration pressed the active image on the touchscreen significantly more than the sham CamKIIα-CreER^{+}CD63-GFP$^{f/+}$ mice (**Figure 1E**; 2-way repeated measures ANOVA showed significant main effect of group ($F_{(1,27)} = 16.62$, $p = 0.0004$) and time [$F_{(11,297)} = 12.41$, $p < 0.0001$, as well as a significant interaction time × group ($F_{(11,297)} = 6.605$, $p < 0.0001$)]. The mice in the cocaine group self-administered, on average, 24–28 mg/kg of cocaine daily during days 5–12 of self-administration training. During extinction training, the mice that had undergone cocaine self-administration exhibited an initial burst of a high number of presses on the active image but quickly decreased to a low level of touches on the active image, while the sham group remained at a baseline low level of active image touches (**Figure 1F**). We observed that the use of a touchscreen for this operant behavior paradigm sometimes resulted in false-positive pressing of the touchscreen in the sham group (25% of mice) but not in the cocaine group, due to mice either laying down or perching next to the touchscreen with their flank or tail in contact with the screen, which can lead to unusually high numbers of screen presses (>100). To minimize the interference of these false-positive presses of the touchscreen, we performed outlier analysis (see "Materials and Methods" section for details) and removed identified outliers (**Figure 1F**, <1% of data points in cocaine group, 7% of data points in sham group).

We have previously shown that neuron-derived CD63-GFP^{+} exosomes can be taken up by astrocytes *in vitro* and *in vivo* (Morel et al., 2013; Men et al., 2019). We have also shown that neuron-derived exosomes carry miRNA cargo that can up-regulate important astrocyte protein expression and functions, such as the glutamate transporter GLT1 and glutamate uptake function (Men et al., 2019). Cocaine self-administration and extinction is known to significantly down-regulate GLT1 expression (Knackstedt et al., 2010; Fischer et al., 2013), which contributes to dysregulation of glutamate homeostasis in the NAc and drug-seeking synaptic plasticity. To determine whether there are alterations in neuron to astrocyte exosomal signaling, we examined whether neuron-derived CD63-GFP^{+} exosomes were differentially taken up by astrocytes following cocaine self-administration training. We focused on NAc, one of the central regions involved in cocaine addiction, and motor cortex, a control region that has not been closely associated with cocaine addiction (Cooper et al., 2017). GFAP immunostaining was performed to identify individual astrocytes in cocaine and sham self-administration CaMKIIα-CreER^{+}CD63-GFP$^{f/+}$ mice. Although GFAP clearly labels individual astrocytes in

the NAc and co-localization of neuronal exosomes (indicated by CD63-GFP) with GFAP immunoreactivity was observed (**Figures 2A,D**), as GFAP immunoreactivity only labels major branches but not fine processes of astrocyte morphology (Morel et al., 2014), we then used the GFAP immunoreactivity as a guide to determine individual astrocyte domains (as shown in the white outline in **Figure 2Aa**) to include the portion of astrocyte morphology that is not labeled by GFAP staining. We subsequently quantified the number of CD63-GFP puncta inside selected astrocyte domains using the ImageJ region of interest (ROI) approach and divided the number of puncta by the area of the astrocyte ROIs. After self-administration training, 90% of astrocytes in NAc of the cocaine group have 0.01 or fewer CD63-GFP puncta per μm^2 inside GFAP-based astrocyte ROIs (a representative image in **Figure 2Ab**), while at least 60% of astrocytes in NAc of the sham group have more than 0.01 CD63-GFP puncta per μm^2 inside the GFAP based ROIs and 20% have more than 0.03 CD63-GFP puncta per μm^2 (**Figure 2B**). In the cortex, however, there is a slightly higher number of puncta per μm^2 of astrocytes after cocaine self-administration compared to the sham group (**Figure 2C**), suggesting a NAc-specific reduction of astroglial internalization of neuronal CD63-GFP$^+$ exosomes. This reduction also appears to be specifically induced by cocaine self-administration, as extinction training completely reversed the reduction of astroglial internalization of neuronal CD63-GFP$^+$ exosomes in the NAc (**Figure 2E**). The distribution of the average number of CD63-GFP puncta per μm^2 inside GFAP-based astrocyte ROIs is very comparable between the sham (NAc: 0.0359 ± 0.0016 puncta/μm^2; ctx: 0.0351 ± 0.0017 puncta/μm^2) and the cocaine extinction (NAc: 0.0347 ± 0.0021 puncta/μm^2; ctx: 0.0348 ± 0.0012 puncta/μm^2) groups in both NAc and cortex (**Figures 2E,F**).

Cocaine self-administration procedures involve both the drug cocaine itself and the learning paradigm. To determine whether the cocaine itself or the learning paradigm contributes to the altered neuronal exosome dynamics in astrocytes, we additionally quantified CD63-GFP puncta inside GFAP-based astrocyte ROIs in food self-administration or sham training groups. This also allowed us to determine whether a natural reward would have the same effect on astroglial internalization of neuronal CD63-GFP$^+$ exosomes as the drug reward, cocaine. We found no difference in the number of CD63-GFP puncta per μm^2 of astrocyte ROIs between the sham and food self-administration groups in the cortex (**Figure 2H**; sham: 0.0138 ± 0.0009 puncta/μm^2; cocaine: 0.0132 ± 0.0010 puncta/μm^2), and in fact saw a slight increase in the number of CD63-GFP puncta per μm^2 of astrocyte ROIs in NAc after food self-administration training (**Figure 2G**; sham: 0.0148 ± 0.0012 puncta/μm^2; food: 0.0221 ± 0.0017 puncta/μm^2). This further suggests that the reduction in astroglial internalization of neuronal CD63-GFP$^+$ exosomes is region (NAc but not cortex) and stimulus (cocaine but not food) specific, and thus is not likely to be due to a general effect of reward-motivated operant learning.

Although several addictive drugs (opioids, methamphetamine) tend to activate astrocytes in the brain (Beitner-Johnson et al., 1993; Friend and Keefe, 2013), evidenced by increased GFAP immunoreactivity, how cocaine specifically affects astrocyte reactivity has not been well documented, especially at different stages of the cocaine self-administration paradigm or in different delivery models. In fact, one study showed that GFAP expression in the NAc is reduced after cocaine self-administration and extinction (Scofield et al., 2016b), while another study, using i.p injection, found increased GFAP immunoreactivity in the dentate gyrus (Fattore et al., 2002). We performed GFAP immunostaining following cocaine self-administration and found that GFAP immunoreactivity was dramatically reduced (**Figures 3Ac,d,B**, $p = 0.0009$, $t = 3.541$, $df = 51$) in the NAc in cocaine self-administration mice compared to sham mice. This GFAP reduction appears to be specific to the NAc, as we found no differences in GFAP immunoreactivity in the cortex (**Figures 3Aa,b,B**; sham: 34.97 ± 4.29, cocaine: 39.17 ± 4.74). To determine whether this reduction in GFAP immunoreactivity represented a decrease in the number of astrocytes, we used BAC-*aldh1l1*-eGFP reporter mice, which express eGFP under the control of the *aldh1l1* promoter, to label astrocytes (Cahoy et al., 2008). We then performed GFAP immunostaining on the NAc sections and quantified eGFP$^+$ astrocytes from BAC-*aldh1l1*-eGFP mice following cocaine or sham self-administration training. As shown in **Figure 3C**, GFAP immunoreactivity that overlapped with eGFP was clearly visualized in individual astrocytes. Despite the reduced GFAP immunoreactivity in the NAc after cocaine self-administration, we found no difference in the number of eGFP$^+$ astrocytes in the NAc between sham and cocaine self-administration mice (**Figure 3D**, $p = 0.111$, $t = 1.631$, $df = 37$; sham: 71.50 ± 3.33, cocaine: 77.67 ± 2.03), supporting the notion that the overall number of astrocytes in the NAc is not affected, while their GFAP immunoreactivity is significantly decreased by cocaine self-administration. To determine whether the extinction process influences GFAP expression in NAc astrocytes, we further examined GFAP immunoreactivity (representative images in **Figure 3E**) after cocaine self-administration and extinction training. Although GFAP immunoreactivity levels in the NAc are still lower in cocaine extinction trained mice compared to sham extinction trained mice (**Figure 3F**, $p = 0.026$, $t = 2.338$, $df = 30$), they are significantly higher than GFAP immunoreactivity levels in mice that have only undergone cocaine self-administration training (**Figure 3G**, $p = 0.0003$, $t = 3.91$, $df = 42$), indicating that extinction training partially reverses the significant cocaine self-administration-induced reduction of GFAP immunoreactivity in NAc astrocytes. On the other hand, GFAP immunoreactivity in the cortex was comparable between the sham (34.56 ± 4.09) and cocaine extinction (40.40 ± 4.09) groups (**Figure 3F**). Interestingly, food self-administration training had no effect on GFAP intensity in either NAc or cortex (**Figure 3H**), suggesting that the reduction in GFAP immunoreactivity in NAc astrocytes is specifically induced by cocaine, and is not a general consequence of reward-based learning.

As the major phagocytic cell type in the CNS, microglia are known to quickly clear debris and foreign pathogens. Recent studies have shown that microglia are able to engulf secreted

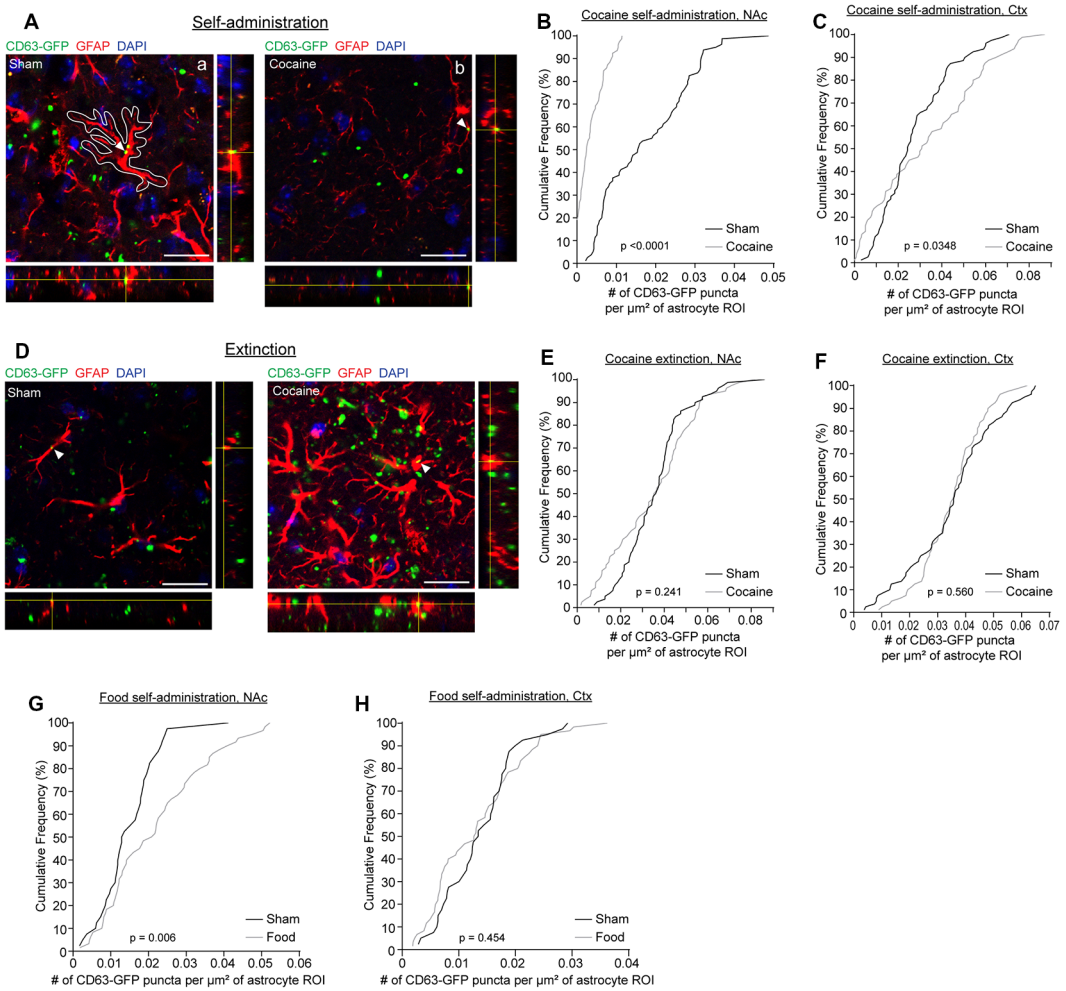

FIGURE 2 | Cocaine self-administration reduces the overlap of CD63-GFP puncta with astrocytes. **(A)** Representative images showing an overlap of CD63-GFP puncta with astrocyte GFAP staining in sham **(a)** and cocaine **(b)** self-administration mice. Each image shows a single slice from a *z*-stack along with the orthogonal view. White outline in the image **(a)** is representative of the ROIs used to measure total CD63-GFP puncta within individual astrocytes. Scale bar: 20 μm. Cumulative frequency curves showing number of GFP puncta per μm^2 of astrocyte ROI after sham or cocaine self-administration in the nucleus accumbens (NAc; **B**, $p < 0.0001$), or the cortex (**C**, $p = 0.0348$); $n = 20$ cells/mouse, four mice/group. **(D)** Representative images showing an overlap of CD63-GFP puncta with astrocyte GFAP staining in sham and cocaine extinction mice. Each image shows a single slice from a *z*-stack along with the orthogonal view. Scale bar: 20 μm. Cumulative frequency curves showing number of GFP puncta per μm^2 of astrocyte ROI after sham or cocaine extinction in the NAc (**E**, $p = 0.241$) or the cortex (**F**, $p = 0.560$); $n = 20$ cells/mouse, four mice/group. Cumulative frequency curves showing number of GFP puncta per μm^2 of astrocyte ROI after sham or food self-administration in the NAc (**G**, $p = 0.006$) or cortex (**H**, $p = 0.454$); $n = 20$ cells/mouse, two mice in the sham group, three mice in food self-administration group. *P*-values determined by the Kolmogorov–Smirnov test.

exosomes and facilitate the spreading of phosphorylated tau and α-synuclein aggregates (Alvarez-Erviti et al., 2011; Asai et al., 2015). To determine whether cocaine induces alterations in neuron to microglial exosome signaling, we examined microglial internalization of neuronal CD63-GFP$^+$ exosomes in the NAc of CaMKIIα-CreER$^+$CD63-GFP$^{f/+}$ mice following cocaine self-administration training alone or followed by extinction training. High magnification confocal images (**Figures 4A,D**) showed co-localization between Iba1 immunostaining signals and CD63-GFP$^+$ puncta in both sham (**Figure 4Aa**) and cocaine (**Figure 4Ab**) self-administration or extinction mice. To quantify the average number of CD63-GFP$^+$ puncta taken up by microglia, we used the Iba1 immunoreactivity as a guide, in the same way as we used the GFAP immunoreactivity for the astrocytes (**Figure 2Aa**), to define individual microglial regions of interest (ROIs, **Figure 4Ab**). We then determined the number of CD63-GFP$^+$ puncta per μm^2 of the microglial ROIs. Cocaine self-administration substantially reduced the number of CD63-GFP$^+$ puncta inside the Iba1-based microglia ROIs in both the NAc (**Figure 4B**, $p = 0.0001$) and the cortex (**Figure 4C**, $p < 0.0001$) when compared to sham mice. In both examined regions, it is also noted that the percentage of microglia that have no co-localized neuronal CD63-GFP$^+$ exosomes increased significantly (from <10 to 45% in the NAc and from 0 to ∼25% in the cortex), suggesting a completely diminished neuronal exosomal signaling in these microglia. Interestingly, extinction

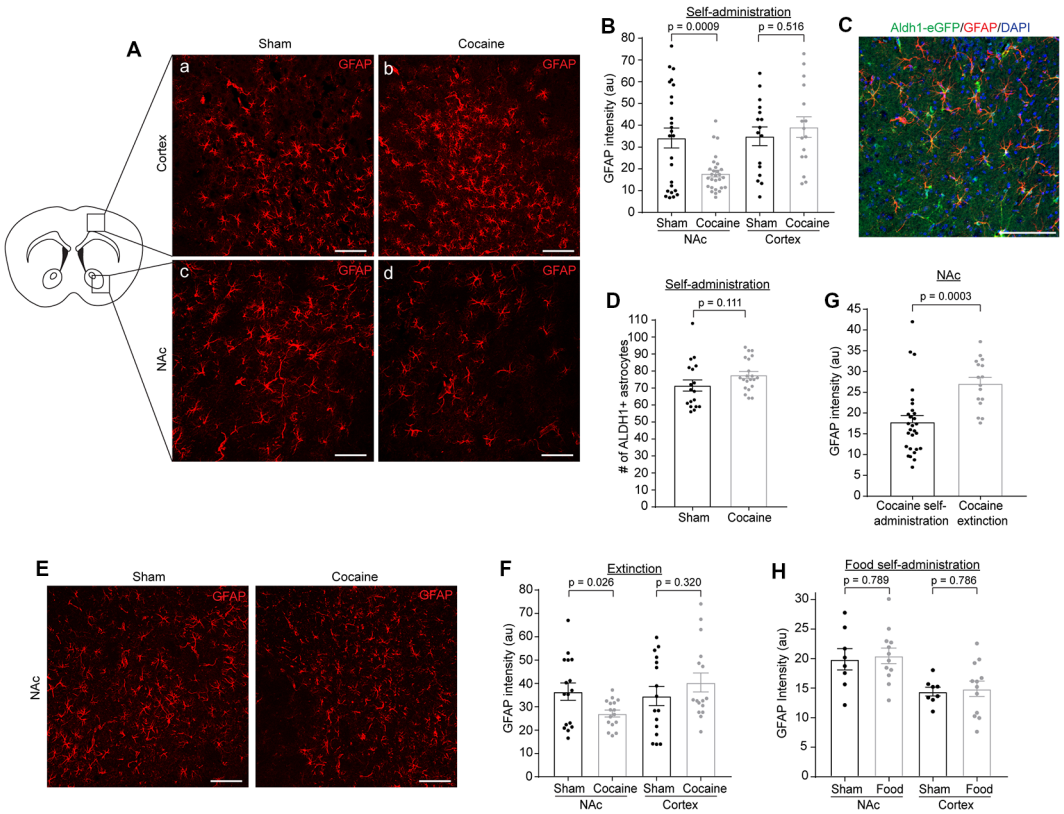

FIGURE 3 | GFAP immunofluorescence is reduced in NAc after cocaine self-administration and is partially rescued after extinction training. **(A)** Representative images showing GFAP immunofluorescence in the cortex **(a,b)** and NAc **(c,d)** after sham or cocaine self-administration. The diagram shows the regions of cortex and NAc that were imaged. Scale bar: 100 μm. **(B)** Quantification of GFAP immunofluorescence intensity in NAc ($p = 0.0009$, $t = 3.541$, $df = 51$) and cortex ($p = 0.516$, $t = 0.657$, $df = 30$) after sham or cocaine self-administration; $n = 4$–12 images/mouse, four mice (total 16–28 images)/group. **(C)** Representative image showing overlap of *aldh1l1*-eGFP astrocyte reporter with GFAP staining. Scale bar: 100 μm. **(D)** Quantification of *aldh1l1*-eGFP^{+} astrocytes in NAc after sham or cocaine self-administration ($p = 0.111$, $t = 1.631$, $df = 37$); $n = 6$–7 images/mouse, three mice/group. **(E)** Representative images showing GFAP immunofluorescence in the NAc after sham or cocaine extinction. Images were taken from same region as the diagram in **(A)**. Scale bar: 100 μm. **(F)** Quantification of GFAP immunofluorescence intensity in NAc ($p = 0.026$, $t = 2.338$, $df = 30$) and cortex ($p = 0.320$, $t = 1.01$, $df = 30$) after sham or cocaine extinction; $n = 4$ images/mouse, four mice/group. **(G)** Comparison of GFAP immunofluorescence intensity in NAc after cocaine self-administration and cocaine extinction ($p = 0.0003$, $t = 3.91$, $df = 42$); $n = 4$–12 images/mouse, four mice (16–28 images)/group. **(H)** Quantification of GFAP immunofluorescence intensity in NAc ($p = 0.789$, $t = 0.278$, $df = 18$) and cortex ($p = 0.786$, $t = 0.275$, $df = 18$) after sham or food self-administration; $p = 4$ images/mouse, two mice in sham group, three mice in food self-administration group. *P*-values, *t* scores, and degrees of freedom determined by two-tailed unpaired *t*-test.

training differentially affects the number of CD63-GFP puncta overlapped with microglia ROIs between the sham and cocaine group in the NAc and in the cortex. While microglia still tend to have a significantly lower number of overlapped CD63-GFP puncta per μm^2 of microglia ROI in the cocaine extinction group compared to the sham extinction group in the NAc (**Figure 4E**, $p = 0.0001$), there was no significant difference in the number of CD63-GFP puncta per μm^2 of microglia ROIs overlapped with microglia ROIs between the sham (0.0335 ± 0.0015 puncta/μm^2) and cocaine (0.0301 ± 0.0014 puncta/μm^2) group in the cortex after extinction training (**Figure 4F**).

Microglia have been shown to be activated in response to cocaine exposure (Lacagnina et al., 2017). We determined Iba1 immunoreactivity as well as the number of microglia through Iba1 immunostaining at each stage of the cocaine or food self-administration behavior paradigm. Representative Iba1 staining confocal images are shown in **Figure 5A**, from which we noticed an increase of Iba1 immunoreactivity after cocaine self-administration. Subsequent quantification confirmed that Iba1 immunoreactivity was increased in both NAc (**Figure 5B**, $p = 0.027$, $t = 2.329$, $df = 30$) and cortex (**Figure 5B**, $p = 0.041$, $t = 2.13$, $df = 30$) after cocaine self-administration, consistent with previous observations that microglia become activated following cocaine exposure. We also examined Iba1 immunoreactivity in the NAc and cortex after extinction training in both the sham and cocaine group (**Figure 5C**). The cocaine self-administration-induced increase in Iba1 immunoreactivity was completely rescued by extinction training in both the NAc and cortex (**Figure 5D**). Despite the increased Iba1 immunoreactivity, there was no difference in the overall number of microglia, quantified based on positive Iba1 staining, in either NAc or cortex after sham or cocaine self-administration, or extinction (**Figures 5E,F**). The increase of Iba1 levels but not the microglial numbers

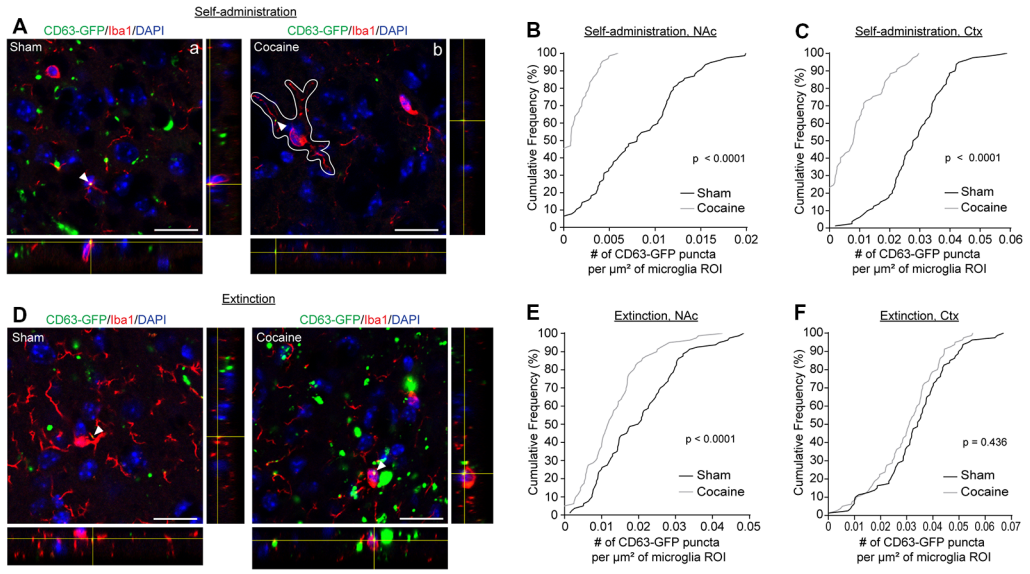

FIGURE 4 | Cocaine self-administration reduces the overlap of CD63-GFP puncta with microglia. **(A)** Representative images showing an overlap of CD63-GFP puncta with microglia Iba1 staining in NAc of sham **(a)** and cocaine **(b)** self-administration mice. Each image shows a single slice from a *z*-stack along with the orthogonal view. White outline in image **(b)** is representative of the ROIs used to measure total CD63-GFP puncta within microglia. Scale bar: 20 μm. Cumulative frequency curves showing number of GFP puncta per μm^2 of microglia ROI after sham or cocaine self-administration in NAc (**B**, $p < 0.0001$) or cortex (**C**, $p < 0.0001$); $n = 20$ cells/mouse, four mice/group. **(D)** Representative images showing an overlap of CD63-GFP puncta with microglia Iba1 staining in NAc of sham and cocaine extinction mice. Scale bar: 20 μm. Cumulative frequency curves showing number of GFP puncta per μm^2 of microglia ROI after sham or cocaine extinction in NAc (**E**, $p = 0.0001$) or cortex (**F**, $p = 0.436$); $n = 20$ cells/mouse, four mice/group. *P*-values determined by the Kolmogorov–Smirnov test.

suggests that cocaine likely induces transient activation of microglia that is reversed once mice become extinguished from responding for cocaine. As a control, we also examined Iba1 immunoreactivity following food self-administration and found no differences in Iba1 immunoreactivity in either NAc (sham—26.79 ± 0.98, food—26.49 ± 1.27) or cortex (sham—11.91 ± 0.57, food—11.95 ± 0.23, **Figure 5G**).

DISCUSSION

In the current study, by selectively labeling neuronal exosomes using CD63-GFP$^{f/+}$ exosome reporter mice, we examined how the self-administration and extinction stages of the mouse cocaine self-administration paradigm alter neuronal exosome signaling to astrocytes and microglia in the NAc. We found that cocaine (but not food) self-administration strongly reduces the internalization of neuronal exosomes in both glial types, which can be effectively reversed by extinction training. Our results also showed that cocaine self-administration itself sufficiently and substantially reduces GFAP expression in the NAc, in contrast to observations that addictive drugs (morphine, methamphetamine, and alcohol) often activate astrocytes by increasing their GFAP expression in the NAc and other brain regions.

Exosomal signaling is emerging as a new mode of intercellular communication in the CNS that has been implicated in development, metastasis of glioblastoma, stroke, and disease spreading of neurodegenerative diseases (Budnik et al., 2016). Although most of the current understanding of exosome signaling is derived from *in vitro* studies, we recently developed the cell-type-specific CD63-GFP$^{f/+}$ exosome reporter mice for examining cell-type-specific exosome signaling changes *in vivo* (Men et al., 2019). Because exosomes are derived from endosomal intraluminal vesicles (ILVs) and released from multivesicular bodies (MVBs; Colombo et al., 2014), CD63-GFP also labels these intracellular organelles, which are typically significantly larger (>250 μm) than exosomes. In our quantification, we specifically quantified CD63-GFP signals within the GFAP or Iba1-based astrocyte or microglia ROI, as these CD63-GFP puncta are initially derived from neurons (with the use of the neuron-specific CaMKIIα-Cre) and are internalized into glial cells, thus representing secreted neuronal exosomes. It is noted that the small exosome size may not be fully resolved with confocal microscopy, which may result in multiple small puncta being quantified as a single particle by this quantification method. However, as all experimental groups were quantified under the same conditions, the results should still be insightful to show how cocaine alters neuronal exosome signaling to glial cells.

There is growing evidence to suggest the involvement of astrocytes and microglia in modulating cocaine addiction behaviors (Lacagnina et al., 2017). In particular, astrocyte-mediated regulation of extracellular glutamate levels through xCT and GLT1 is a key mechanism in modifying synaptic plasticity in the NAc that is related to cocaine-seeking (Kalivas, 2009). Although several studies have observed down-regulation of GLT1 following cocaine exposure (Knackstedt et al., 2010; Fischer-Smith et al., 2012; Fischer et al., 2013), how GLT1 becomes dysregulated remains unknown. Our current study observed a significantly reduced internalization of

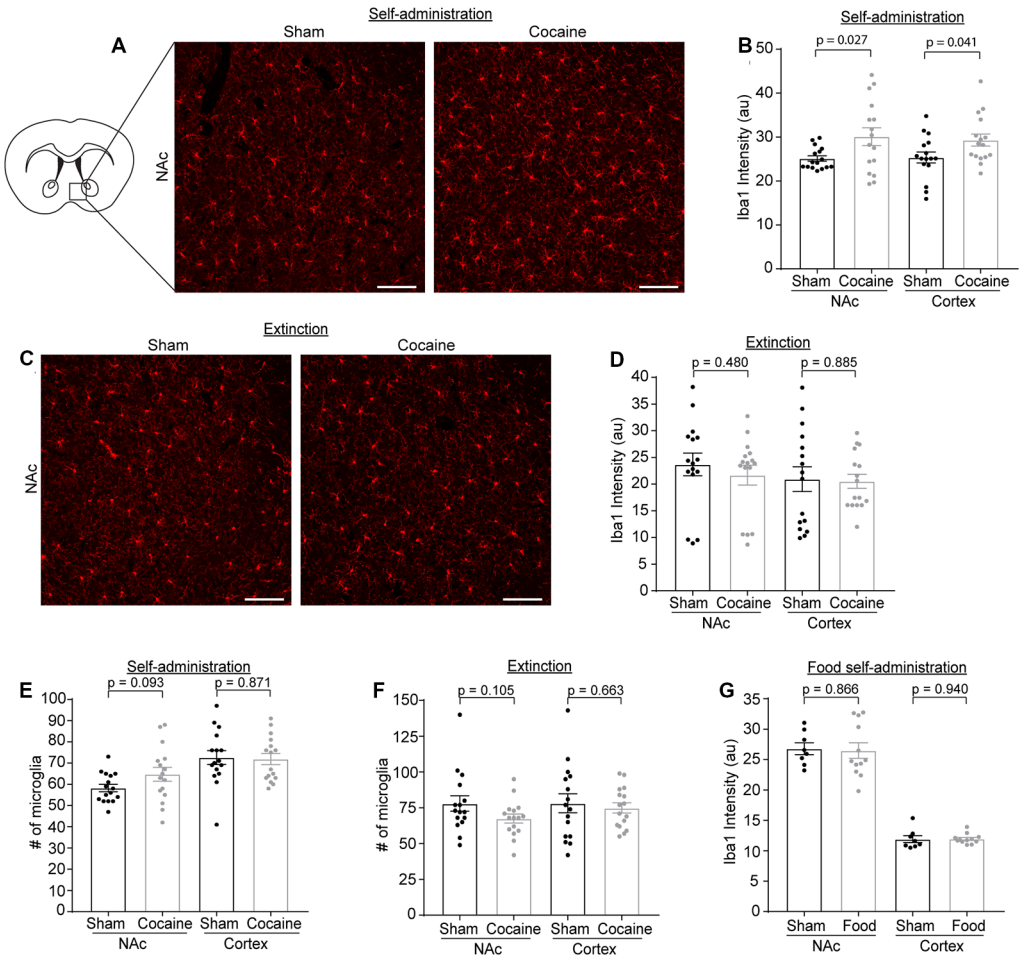

FIGURE 5 | Iba1 immunoreactivity is increased after cocaine self-administration, but not after extinction training or food self-administration. **(A)** Representative images showing Iba1 immunofluorescence in the NAc after sham or cocaine self-administration. The diagram shows the region of NAc that was imaged. Scale bar: 100 μm. **(B)** Quantification of Iba1 immunofluorescence intensity in NAc ($p = 0.027$, $t = 2.329$, $df = 30$) and cortex ($p = 0.041$, $t = 2.13$, $df = 30$) after sham or cocaine self-administration; $n = 4$ images/mouse, four mice/group. **(C)** Representative images showing Iba1 immunofluorescence in the NAc after sham or cocaine extinction. Images were taken from same region as the diagram in **(A)**. Scale bar: 100 μm. **(D)** Quantification of Iba1 immunofluorescence intensity in NAc ($p = 0.480$, $t = 0.715$, $df = 30$) and cortex ($p = 0.885$, $t = 0.145$, $df = 30$) after sham or cocaine extinction; $n = 4$ images/mouse, four mice/group. **(E)** Quantification of the number of Iba1$^+$ microglia in NAc ($p = 0.093$, $t = 1.737$, $df = 30$) and cortex ($p = 0.871$, $t = 0.164$, $df = 30$) after sham or cocaine self-administration; $n = 4$ images/mouse, four mice/group. **(F)** Quantification of the number of Iba1$^+$ microglia in NAc ($p = 0.105$, $t = 1.669$, $df = 30$) and cortex ($p = 0.663$, $t = 0.440$, $df = 30$) after sham or cocaine extinction; $n = 4$ images/mouse, four mice/group. **(G)** Quantification of Iba1 immunofluorescence intensity in NAc ($p = 0.866$, $t = 0.171$, $df = 18$) and cortex ($p = 0.940$, $t = 0.076$, $df = 18$) after sham or food self-administration; $n = 4$ images/mouse, two mice in sham group, three mice in food self-administration group. *P*-values, *t*-scores, and degrees of freedom determined by two-tailed unpaired *t*-test.

neuronal exosomes in NAc astrocytes. We recently showed that a subset of miRNAs are abundantly packed in neuronal exosomes and these miRNAs, especially miR-124-3p, can be transferred into astrocytes to increase protein expression of GLT1 (Men et al., 2019). In particular, *in vivo* inhibition of miR-124-3p or exosome secretion is sufficient to decrease GLT1 protein levels and glutamate uptake (Men et al., 2019). Therefore, cocaine-induced reduction of the internalization of neuronal exosomes into astrocytes could result in less transferred miR-124-3p into astrocytes and consequently decreased GLT1 expression. This process appears to be cocaine and self-administration specific, as food self-administration has no effect on the internalization of neuronal exosomes in astrocytes and cocaine extinction reversed the reduced internalization of neuronal exosomes in astrocytes. In parallel, it has been reported that several neuronal miRs, including miR-124-3p, are down-regulated by cocaine exposure (Cabana-Dominguez et al., 2018). It is thus conceivable that the reduced miR-124 signaling, including reduced transfer from neurons to astrocytes through exosomes, underlies cocaine-induced down-regulation of GLT1 expression.

Although glial cells are often activated following addictive drug exposure, our results found that GFAP expression is significantly decreased. This is an intriguing observation as reduced GLT1 is often associated with reactive astrocytes with highly increased GFAP levels in injury and degenerative conditions. However, reduced GLT1 and GFAP expression

have been associated with several psychiatric disease models, including anxiety, stress, or depression (Banasr et al., 2010; Imbe et al., 2012; Gunn et al., 2013). It is likely that astrocytes undergo different molecular changes in psychiatric conditions vs. injury/degenerative conditions. GFAP alone can be inadequate and limiting to indicate the reactivity change of astrocytes in these conditions. As astrocyte-specific or single cell-based transcriptome techniques become more available (Morel et al., 2017; Zeisel et al., 2018), these approaches are likely to gain more comprehensive insights as to how astrocytes are altered in response to cocaine, which may provide new insights about their involvement in modulating cocaine addiction behaviors.

DATA AVAILABILITY STATEMENT

No large datasets were generated from this study. The data that support the findings of this study are available from the corresponding author upon reasonable request.

ETHICS STATEMENT

The animal study was reviewed and approved by Tufts University Institutional Animal Care and Use Committee (IACUC).

AUTHOR CONTRIBUTIONS

RJ performed catheterization surgeries, behavioral testing, immunostaining, and confocal imaging. AT-O and VP performed behavioral testing, immunostaining, and confocal imaging. LT and JS performed immunostaining and confocal imaging. RJ, AT-O, VP, LT and JS also performed data analysis. RJ co-wrote the manuscript. YY designed the overall study, analyzed the data, and wrote the manuscript.

FUNDING

This work was supported by National Institutes of Health (NIH) grants DA042342, NS087391, AG057882, and AG059610 (YY). Imaging and behavior were carried out with assistance from the Tufts Center for Neuroscience Research.

ACKNOWLEDGMENTS

We thank Dr. Peter Kalivas (Medical University of South Carolina) and his lab for sharing their expertise in surgical procedures and cocaine self-administration behavior testing with us. We thank Drs. Julia Yelick and Haruki Higashimori for initial trials with the catheterization surgery. We thank the present and past members of the Yang lab for helpful discussions and suggestions.

REFERENCES

Alvarez-Erviti, L., Seow, Y., Schapira, A. H., Gardiner, C., Sargent, I. L., Wood, M. J., et al. (2011). Lysosomal dysfunction increases exosome-mediated alpha-synuclein release and transmission. *Neurobiol. Dis.* 42, 360–367. doi: 10.1016/j.nbd.2011.01.029

Asai, H., Ikezu, S., Tsunoda, S., Medalla, M., Luebke, J., Haydar, T., et al. (2015). Depletion of microglia and inhibition of exosome synthesis halt tau propagation. *Nat. Neurosci.* 18, 1584–1593. doi: 10.1038/nn.4132

Baker, D. A., McFarland, K., Lake, R. W., Shen, H., Toda, S., and Kalivas, P. W. (2003). N-acetyl cysteine-induced blockade of cocaine-induced reinstatement. *Ann. N. Y. Acad. Sci.* 1003, 349–351. doi: 10.1196/annals.1300.023

Baker, D. A., Xi, Z. X., Shen, H., Swanson, C. J., and Kalivas, P. W. (2002). The origin and neuronal function of *in vivo* nonsynaptic glutamate. *J. Neurosci.* 22, 9134–9141. doi: 10.1523/jneurosci.22-20-09134.2002

Banasr, M., Chowdhury, G. M., Terwilliger, R., Newton, S. S., Duman, R. S., Behar, K. L., et al. (2010). Glial pathology in an animal model of depression: reversal of stress-induced cellular, metabolic and behavioral deficits by the glutamate-modulating drug riluzole. *Mol. Psychiatry* 15, 501–511. doi: 10.1038/mp.2008.106

Beitner-Johnson, D., Guitart, X., and Nestler, E. J. (1993). Glial fibrillary acidic protein and the mesolimbic dopamine system: regulation by chronic morphine and Lewis-Fischer strain differences in the rat ventral tegmental area. *J. Neurochem.* 61, 1766–1773. doi: 10.1111/j.1471-4159.1993.tb09814.x

Berridge, K. C., and Robinson, T. E. (1998). What is the role of dopamine in reward: hedonic impact, reward learning, or incentive salience? *Brain Res. Brain Res. Rev.* 28, 309–369. doi: 10.1016/s0165-0173(98)00019-8

Budnik, V., Ruiz-Canada, C., and Wendler, F. (2016). Extracellular vesicles round off communication in the nervous system. *Nat. Rev. Neurosci.* 17, 160–172. doi: 10.1038/nrn.2015.29

Cabana-Dominguez, J., Arenas, C., Cormand, B., and Fernandez-Castillo, N. (2018). MiR-9, miR-153 and miR-124 are down-regulated by acute exposure to cocaine in a dopaminergic cell model and may contribute to cocaine dependence. *Transl. Psychiatry* 8:173. doi: 10.1038/s41398-018-0224-5

Cahoy, J. D., Emery, B., Kaushal, A., Foo, L. C., Zamanian, J. L., Christopherson, K. S., et al. (2008). A transcriptome database for astrocytes, neurons and oligodendrocytes: a new resource for understanding brain development and function. *J. Neurosci.* 28, 264–278. doi: 10.1523/JNEUROSCI.4178-07.2008

Colombo, M., Raposo, G., and Thery, C. (2014). Biogenesis, secretion and intercellular interactions of exosomes and other extracellular vesicles. *Annu. Rev. Cell Dev. Biol.* 30, 255–289. doi: 10.1146/annurev-cellbio-101512-122326

Conaco, C., Otto, S., Han, J. J., and Mandel, G. (2006). Reciprocal actions of REST and a microRNA promote neuronal identity. *Proc. Natl. Acad. Sci. U S A* 103, 2422–2427. doi: 10.1073/pnas.0511041103

Cooper, S., Robison, A. J., and Mazei-Robison, M. S. (2017). Reward circuitry in addiction. *Neurotherapeutics* 14, 687–697. doi: 10.1007/s13311-017-0525-z

Fattore, L., Puddu, M. C., Picciau, S., Cappai, A., Fratta, W., Serra, G. P., et al. (2002). Astroglial *in vivo* response to cocaine in mouse dentate gyrus: a quantitative and qualitative analysis by confocal microscopy. *Neuroscience* 110, 1–6. doi: 10.1016/s0306-4522(01)00598-x

Fischer, K. D., Houston, A. C., and Rebec, G. V. (2013). Role of the major glutamate transporter GLT1 in nucleus accumbens core versus shell in cue-induced cocaine-seeking behavior. *J. Neurosci.* 33, 9319–9327. doi: 10.1523/jneurosci.3278-12.2013

Fischer-Smith, K. D., Houston, A. C., and Rebec, G. V. (2012). Differential effects of cocaine access and withdrawal on glutamate type 1 transporter expression in rat nucleus accumbens core and shell. *Neuroscience* 210, 333–339. doi: 10.1016/j.neuroscience.2012.02.049

Friend, D. M., and Keefe, K. A. (2013). Glial reactivity in resistance to methamphetamine-induced neurotoxicity. *J. Neurochem.* 125, 566–574. doi: 10.1111/jnc.12201

Gourlay, J., Morokoff, A. P., Luwor, R. B., Zhu, H. J., Kaye, A. H., and Stylli, S. S. (2017). The emergent role of exosomes in glioma. *J. Clin. Neurosci.* 35, 13–23. doi: 10.1016/j.jocn.2016.09.021

Griffin, W. C. III, Randall, P. K., and Middaugh, L. D. (2007). Intravenous cocaine self-administration: individual differences in male and female C57BL/6J mice. *Pharmacol. Biochem. Behav.* 87, 267–279. doi: 10.1016/j.pbb.2007.04.023

Gunn, B. G., Cunningham, L., Cooper, M. A., Corteen, N. L., Seifi, M., Swinny, J. D., et al. (2013). Dysfunctional astrocytic and synaptic regulation of hypothalamic glutamatergic transmission in a mouse model of early-life adversity: relevance to neurosteroids and programming of the stress response. *J. Neurosci.* 33, 19534–19554. doi: 10.1523/jneurosci.1337-13.2013

Imbe, H., Kimura, A., Donishi, T., and Kaneoke, Y. (2012). Chronic restraint stress decreases glial fibrillary acidic protein and glutamate transporter in the periaqueductal gray matter. *Neuroscience* 223, 209–218. doi: 10.1016/j.neuroscience.2012.08.007

Kalivas, P. W. (2009). The glutamate homeostasis hypothesis of addiction. *Nat. Rev. Neurosci.* 10, 561–572. doi: 10.1038/nrn2515

Kelley, A. E. (2004). Memory and addiction: shared neural circuitry and molecular mechanisms. *Neuron* 44, 161–179. doi: 10.1016/j.neuron.2004.09.016

Knackstedt, L. A., Melendez, R. I., and Kalivas, P. W. (2010). Ceftriaxone restores glutamate homeostasis and prevents relapse to cocaine seeking. *Biol. Psychiatry* 67, 81–84. doi: 10.1016/j.biopsych.2009.07.018

Lacagnina, M. J., Rivera, P. D., and Bilbo, S. D. (2017). Glial and neuroimmune mechanisms as critical modulators of drug use and abuse. *Neuropsychopharmacology* 42, 156–177. doi: 10.1038/npp.2016.121

Madayag, A., Lobner, D., Kau, K. S., Mantsch, J. R., Abdulhameed, O., Hearing, M., et al. (2007). Repeated N-acetylcysteine administration alters plasticity-dependent effects of cocaine. *J. Neurosci.* 27, 13968–13976. doi: 10.1523/jneurosci.2808-07.2007

McNeill, E., and Van Vactor, D. (2012). MicroRNAs shape the neuronal landscape. *Neuron* 75, 363–379. doi: 10.1016/j.neuron.2012.07.005

Men, Y., Yelick, J., Jin, S., Tian, Y., Jarvis, R., Chiang, R., et al. (2019). Exosome reporter mice reveal the involvement of exosomes in mediating neuron to astroglia communication in the CNS. *Nat. Commun.* 10:4136. doi: 10.1038/s41467-019-11534-w

Morel, L., Higashimori, H., Tolman, M., and Yang, Y. (2014). VGluT1+ neuronal glutamatergic signaling regulates postnatal developmental maturation of cortical protoplasmic astroglia. *J. Neurosci.* 34, 10950–10962. doi: 10.1523/jneurosci.1167-14.2014

Morel, L., Regan, M., Higashimori, H., Ng, S. K., Esau, C., Vidensky, S., et al. (2013). Neuronal exosomal miRNA-dependent translational regulation of astroglial glutamate transporter GLT1. *J. Biol. Chem.* 288, 7105–7116. doi: 10.1074/jbc.m112.410944

Morel, L., Chiang, M. S. R., Higashimori, H., Shoneye, T., Iyer, L. K., Yelick, J., et al. (2017). Molecular and functional properties of regional astrocytes in the adult brain. *J. Neurosci.* 37, 8706–8717. doi: 10.1523/jneurosci.3956-16.2017

Moussawi, K., and Kalivas, P. W. (2010). Group II metabotropic glutamate receptors (mGlu2/3) in drug addiction. *Eur. J. Pharmacol.* 639, 115–122. doi: 10.1016/j.ejphar.2010.01.030

Nestler, E. J. (2005). The neurobiology of cocaine addiction. *Sci. Pract. Perspect.* 3, 4–10. doi: 10.1151/spp05314

Quek, C., and Hill, A. F. (2017). The role of extracellular vesicles in neurodegenerative diseases. *Biochem. Biophys. Res. Commun.* 483, 1178–1186. doi: 0.1016/j.bbrc.2016.09.090

Reichel, C. M., Moussawi, K., Do, P. H., Kalivas, P. W., and See, R. E. (2011). Chronic N-acetylcysteine during abstinence or extinction after cocaine self-administration produces enduring reductions in drug seeking. *J. Pharmacol. Exp. Ther.* 337, 487–493. doi: 10.1124/jpet.111.179317

Scofield, M. D., Heinsbroek, J. A., Gipson, C. D., Kupchik, Y. M., Spencer, S., Smith, A. C., et al. (2016a). The nucleus accumbens: mechanisms of addiction across drug classes reflect the importance of glutamate homeostasis. *Pharmacol. Rev.* 68, 816–871. doi: 10.1124/pr.116.012484

Scofield, M. D., Li, H., Siemsen, B. M., Healey, K. L., Tran, P. K., Woronoff, N., et al. (2016b). Cocaine self-administration and extinction leads to reduced glial fibrillary acidic protein expression and morphometric features of astrocytes in the nucleus accumbens core. *Biol. Psychiatry* 80, 207–215. doi: 10.1016/j.biopsych.2015.12.022

Trantham-Davidson, H., LaLumiere, R. T., Reissner, K. J., Kalivas, P. W., and Knackstedt, L. A. (2012). Ceftriaxone normalizes nucleus accumbens synaptic transmission, glutamate transport and export following cocaine self-administration and extinction training. *J. Neurosci.* 32, 12406–12410. doi: 10.1523/jneurosci.1976-12.2012

Xiong, Y., Mahmood, A., and Chopp, M. (2017). Emerging potential of exosomes for treatment of traumatic brain injury. *Neural Regen. Res.* 12, 19–22. doi: 10.4103/1673-5374.198966

Yang, Y., Gozen, O., Watkins, A., Lorenzini, I., Lepore, A., Gao, Y., et al. (2009). Presynaptic regulation of astroglial excitatory neurotransmitter transporter GLT1. *Neuron* 61, 880–894. doi: 10.1016/j.neuron.2009.02.010

Zeisel, A., Hochgerner, H., Lonnerberg, P., Johnsson, A., Memic, F., van der Zwan, J., et al. (2018). Molecular architecture of the mouse nervous system. *Cell* 174, 999.e1022–1014.e1022. doi: 10.1016/j.cell.2018.06.021.

Conflict of Interest: The authors declare that the research was conducted in the absence of any commercial or financial relationships that could be construed as a potential conflict of interest.

frontiers in Cellular Neuroscience

ORIGINAL RESEARCH
published: 10 March 2020
doi: 10.3389/fncel.2020.00043

CD8 T-cell Recruitment Into the Central Nervous System of Cuprizone-Fed Mice: Relevance to Modeling the Etiology of Multiple Sclerosis

Mohammed S. M. Almuslehi[1,2], Monokesh K. Sen[1], Peter J. Shortland[3], David A. Mahns[1] and Jens R. Coorssen[4,5]**

[1]School of Medicine, Western Sydney University, Penrith, NSW, Australia, [2]Department of Physiology, College of Veterinary Medicine, Diyala University, Diyala, Iraq, [3]School of Science, Western Sydney University, Penrith, NSW, Australia, [4]Department of Health Sciences, Faculty of Applied Health Sciences, St. Catharines, ON, Canada, [5]Department of Biological Sciences, Faculty of Mathematics and Science, Brock University, St. Catharines, ON, Canada

OPEN ACCESS

Edited by:
Silvia Sánchez-Ramón, Complutense University of Madrid, Spain

Reviewed by:
Leyre Mestre, Cajal Institute (CSIC), Spain
Stefano Angiari, Trinity College Dublin, Ireland

***Correspondence:**
David A. Mahns
d.mahns@westernsydney.edu.au
Jens R. Coorssen
jcoorssen@brocku.ca

Received: *06 November 2019*
Accepted: *14 February 2020*
Published: *10 March 2020*

Citation:
Almuslehi MSM, Sen MK, Shortland PJ, Mahns DA and Coorssen JR (2020) CD8 T-cell Recruitment Into the Central Nervous System of Cuprizone-Fed Mice: Relevance to Modeling the Etiology of Multiple Sclerosis. Front. Cell. Neurosci. 14:43. doi: 10.3389/fncel.2020.00043

Cuprizone (CPZ)-feeding in mice induces atrophy of peripheral immune organs (thymus and spleen) and suppresses T-cell levels, thereby limiting its use as a model for studying the effects of the immune system in demyelinating diseases such as Multiple Sclerosis (MS). To investigate whether castration (*Cx*) can protect the peripheral immune organs from CPZ-induced atrophy and enable T-cell recruitment into the central nervous system (CNS) following a breach of the blood-brain barrier (BBB), three related studies were carried out. In Study 1, *Cx* prevented the dose-dependent reductions (0.1% < 0.2% CPZ) in thymic and splenic weight, size of the thymic medulla and splenic white pulp, and CD4 and CD8 (CD4/8) levels remained comparable to gonadally intact (*Gi*) control males. Importantly, 0.1% and 0.2% CPZ were equipotent at inducing central demyelination and glial activation. In Study 2, combining *Cx* with 0.1% CPZ-feeding and BBB disruption with pertussis toxin (PT) enhanced $CD8^+$ T-cell recruitment into the CNS. The increased $CD8^+$ T-cell level observed in the parenchyma of the cerebrum, cerebellum, brainstem and spinal cord were confirmed by flow cytometry and western blot analyses of CNS tissue. In Study 3, PT+0.1% CPZ-feeding to *Gi* female mice resulted in similar effects on the peripheral immune organs, CNS demyelination, and gliosis comparable to *Gi* males, indicating that testosterone levels alone were not responsible for the immune response seen in Study 2. The combination of *Cx*+0.1% CPZ-feeding+PT indicates that CPZ-induced demyelination can trigger an *"inside-out"* immune response when the peripheral immune system is spared and may provide a better model to study the initiating events in demyelinating conditions such as MS.

Keywords: castration, gonadally intact, demyelination, gliosis, inside-out, peripheral immune organs, atrophy

INTRODUCTION

Multiple Sclerosis (MS) is a heterogeneous, inflammatory demyelinating disease of the human central nervous system (CNS) for which the early initiating events and thus underlying etiology remain unclear (Stys et al., 2012; Stys, 2013; Partridge et al., 2015). Currently, there are no effective treatments to prevent disease initiation and progression (Sriram and Steiner, 2005; Vargas and Tyor, 2017). Several animal models such as experimental autoimmune encephalomyelitis (EAE; Glatigny and Bettelli, 2018), Theiler's murine encephalomyelitis virus (Carrillo-Salinas et al., 2017), and the diphtheria toxin model (Traka et al., 2016) mimic various clinical and pathological features of the disease but no single model replicates the full complexity of disease initiation and progression. Nonetheless, the cuprizone (CPZ) model possesses many key characteristics of MS including demyelination and gliosis (reviewed in Sen et al., 2019b). According to these pathological features, the CPZ model was selected as the most appropriate tool to test the "inside-out" theory of disease initiation (Caprariello et al., 2018). According to this theory, the initiating event in MS is an early, slow degeneration of myelin, which causes the release of potential myelin antigens (as debris) that then activate microglia and macrophages in the presence of proinflammatory mediators. Consequently, myelin antigen presentation by antigen-presenting cells attracts peripheral T- and B-cells into the CNS, triggering a secondary inflammatory reaction that ultimately leads to the progressive autoimmune response characterized clinically (Stys et al., 2012; Stys, 2013).

While there have been numerous reports of CPZ being used to study demyelination, these have not established the involvement of peripheral T-cells at the sites of CPZ-induced demyelination in the CNS (Remington et al., 2007; Partridge et al., 2016; Traka et al., 2016; Tejedor et al., 2017; Sen et al., 2019a). It was thought that as CPZ does not induce a breach of the blood-brain barrier (BBB), T-cells have no access to the CNS (Remington et al., 2007; Skripuletz et al., 2011; Tejedor et al., 2017). However, even when the BBB was breached using pertussis toxin (PT), CPZ evoked marked CNS demyelination, gliosis and changes in the abundance of proteoforms involved in metabolism, immune and synaptic functions, without detectable T-cell infiltration (Sen et al., 2019a). Studies have indicated that the apparent failure to trigger a T-cell-mediated CNS immune response is due to CPZ-induced atrophy of the thymus (the organ responsible for T-cell maturation and differentiation) and spleen (the organ of T and B lymphocyte production; Solti et al., 2015; Martin et al., 2018; Sui et al., 2019; Sen et al., 2019a). Two additional effects of CPZ on the integrity and function of the peripheral immune system include an increase in the abundance of splenic arginase-I (a protein expressed by myeloid-derived suppressor cells in spleen) and a decreased abundance of protein disulfide isomerize (a protein required for assembly of the major histocompatibility complex-I; Partridge et al., 2016). A change in the abundance of these proteins results in suppressed T-cell function (Kang et al., 2009). Likewise, proteoforms of calcium/calmodulin-dependent protein kinase type II subunit-α and leukocyte elastase inhibitor A, involved in T-cell functions, decreased in abundance following CPZ-feeding (Sen et al., 2019a). Moreover, marked changes in the number of mitochondrial proteoforms are suggested to suppress T-cell function (Sen et al., 2019a). Furthermore, a significant reduction in thymic and splenic T-cell numbers, as well as thymocyte apoptosis, was observed after 1–2 weeks of CPZ-feeding (Solti et al., 2015; Martin et al., 2018). Collectively, these studies indicate that the absence of adaptive immune cell involvement in the CNS of CPZ-fed mice is not only due to the intact BBB but is also due to suppression of the adaptive immune system. However, when the BBB was disrupted by PT and the peripheral immune system "boosted" via injection of Complete Freund's Adjuvant (CFA), an increased pan T-cell marker ($CD3^+$) response was observed in the CNS of CPZ-fed mice (Caprariello et al., 2018).

Circulating T-cell numbers are maintained by the thymus gland through various processes including maturation, selection, differentiation and the release of mature T-cells into the blood. During puberty, in both humans and animals, the thymic become atrophied and inactivated (physiological thymic involution) when circulating androgen concentrations increase (Sutherland et al., 2005; Sheean et al., 2015). Notably, experimental testosterone administration (Oner and Ozan, 2002) or CPZ-feeding produced similar effects to natural androgen-induced physiological thymic involution, including thymic atrophy, with the remaining tissue displaying enlarged and degraded mitochondria, lipid droplets and enlarged lysosomes (Solti et al., 2015). Androgen deprivation following castration (*Cx*) increased T-cell levels, thymic function (maturation and differentiation of T-cells) in young and aged mice (Roden et al., 2004; Sheean et al., 2015), and splenic function (T- and B-cells production) in adult mice (Roden et al., 2004). Likewise, *Cx* increased thymic mass (hypertrophy) and resulted in complete restoration of thymus structure (both lymphocytic and epithelial) and function in the primary peripheral immune organs (thymus and bone marrow), including associated T-cell levels (Sutherland et al., 2005). However, no study has investigated whether *Cx*-induced preservation of the thymic and splenic size and function can surmount the suppressive effects of CPZ on the peripheral immune system (i.e., maintain structure and function). Furthermore, no study has tested whether the effect of BBB disruption during CPZ-feeding in female mice, which have naturally low testosterone levels, can lead to T-cell infiltration into the CNS. This is important as MS is seen ∼2–3 times more frequently in females than males (Ahlgren et al., 2011; Harbo et al., 2013).

The current work tested the hypothesis that *Cx* protects against the negative effects of CPZ-feeding on thymus and spleen and thus enables T-cell recruitment into the CNS following disruption of the BBB by PT. To investigate this hypothesis, three inter-related studies were carried out using CPZ-feeding in male and female mice. In Study 1, surgical *Cx* was used to protect the adaptive immune system against CPZ effects. In Study 2, *Cx* was combined with 0.1% CPZ-feeding and BBB disruption to test whether the CPZ-induced demyelination initiated an "inside-out" T-cell-mediated response in the CNS. In Study 3, gonadally intact (*Gi*) female mice were fed 0.1% CPZ and the BBB disrupted to test whether females could

mount a T-cell response in the CNS, as seen in Study 2. The results suggest a new mouse model for studying the initiating events of MS and further testing the inside-out hypothesis of MS etiology.

MATERIALS AND METHODS

Animals and Monitoring

Weaned (3-week-old) male and/or female C57Bl/6 mice (n = 187) were purchased from the Animal Resources Centre, Murdoch, WA, Australia[1]. Mice were acclimatized for 1 week prior to each study and housed (five animals/ventilated GM500 cage, Tecniplast, Buguggiate, VA, Italy) in a controlled environment (12-h light/dark cycle, 50–60% humidity, and 21–23°C room temperature, RT). Standard rodent powder chow (Gordon's Specialty Stockfeeds, Yanderra, NSW, Australia) and water were available *ad libitum*. Mice were weighed individually at the beginning of the studies, every third day, and prior to sacrifice. Research and animal care procedures were approved by the Western Sydney University animal ethics committee (A11938) in accordance with the Australian Code of Practice for the Care and Use of Animals for Scientific Purposes as laid out by the National Health and Medical Research Council of Australia.

Bilateral Orchiectomy (Castration, *Cx*)

Adolescent (4-week-old) mice (n = 77) were surgically castrated under deep anesthesia using isoflurane (Cenvet, Blacktown, NSW, Australia) 2–3% in 100% oxygen. Mice underwent orchiectomy at this specific age to precede the onset of normal age-related thymic atrophy. The ventral midline of the scrotum was incised (∼1 cm) and the tunica exposed. The vas deferens and spermatic artery of each testis were ligated with absorbable polyglycan sutures and the testicles were excised. Then the incision was closed with silk thread (one stitch) and Michel clips (Fine Science Tools, North Vancouver, BC, Canada). Subcutaneous analgesia (Meloxicam 3 mg/kg, Randdolab, NSW, Australia) was injected twice (at the end of surgery and 12 h later) and mice were kept under a heat lamp (∼37°C) until awake and mobile. All mice (*Cx* and *Gi*) were inspected daily to identify any abnormal changes in gait, movement, posture, and skin; no abnormalities were observed.

Cuprizone Administration

0.1% or 0.2% CPZ {w/w, [Bis(cyclohexanone)oxaldihydrazone], Sigma–Aldrich, St. Louis, MO, USA} was used in Study 1. As 0.1% CPZ-feeding induced comparable demyelination and gliosis (**Figure 4**, Study 1 panel) but less thymic and splenic atrophy than 0.2% CPZ (**Figure 1**, Study 1 panel), 0.1% CPZ was used in studies 2 and 3. CPZ was mixed with powdered chow to induce demyelination as shown previously (Sen et al., 2019a). Animals were fed either 0.1% or 0.2% CPZ for 2 weeks. Chow was prepared daily with and without CPZ.

[1]http://www.arc.wa.gov.au

Pertussis Toxin Injection

In Studies 2 and 3, intraperitoneal injections of PT (Sigma–Aldrich) were used to disrupt the BBB as described previously (Sen et al., 2019a). PT (400 ng/mouse, Sigma–Aldrich) was injected on days 5, 7, and 9 of CPZ-feeding in Studies 2 and 3.

Experimental Groups

In Study 1, male mice were randomly assigned to one of six groups (n = 11/group): controls (Ctrl), 0.1% CPZ and 0.2% CPZ (all *Gi*), *Cx*, *Cx*+0.1% CPZ, and *Cx*+0.2% CPZ. In Study 2, male mice were randomly assigned into one of seven groups: Ctrl, PT, 0.1% CPZ (all *Gi*) and *Cx*, *Cx*+PT, *Cx*+0.1% CPZ and *Cx*+0.1% CPZ+PT (n = 11/group). In Study 3, *Gi* female mice (n = 11/group) were randomly assigned to one of four experimental groups: Ctrl, PT, 0.1% CPZ and 0.1% CPZ+PT. Mice were assigned to each analysis as follows: three animals/group for western blot analysis, three animals/group for paraffin-embedded tissue staining, five animals/group for free-floating tissue staining.

Western Blot

Western blot was carried out as previously described (Sen et al., 2019a). Briefly, mice (n = 3 animals/group) were euthanized and immediately thereafter brains, spinal cords, thymic and spleens were harvested, washed thoroughly with ice-cold 0.01 M phosphate-buffered saline (PBS, Sigma–Aldrich, St. Louis, MO, USA) containing a protease inhibitor cocktail (4 μM staurosporine, 1 mM α-naphthyl phosphate and 1 mM sodium orthovanadate) to prevent protein degradation during sample preparation and then snap-frozen in liquid nitrogen. Frozen samples were pulverized, solubilized (∼1 μl/1 μg tissue) in pre-chilled lysis buffer (25 mM Tris, 1 mM EDTA, 1 mM EGTA, 150 mM NaCl and 1% Triton x-100) and centrifuged at 125,000 *g*, 4°C, for 1 h. Total protein in the supernatant was quantified in each sample using the EZQ protein quantitation kit (Life Technologies, Eugene, OR, USA) with bovine serum albumin (Amresco, Solon, OH, USA) as a calibration standard (Butt and Coorssen, 2005; Churchward et al., 2005). Thymus, spleen, brain, spinal cord and standard purified CD4/8 recombinant proteins (Sino Biological, Wayne, PA, USA) were resolved by 10% sodium dodecyl sulfate-polyacrylamide gel electrophoresis (SDS-PAGE; 100 V for 2 h at 4°C) and then transferred onto polyvinylidene difluoride membrane (PVDF, 0.22 μM pore size, Bio-Rad, Hercules, CA, USA) for 2 h at 4°C; transfer efficiency, determined as previously described (Sen et al., 2019a), was 95.6 ± 1.7% (**Supplementary Figures S1A,B**). The PVDF blots were incubated at RT in blocking solution 5% skimmed milk (Coles, Hawthorn East, VIC, Australia), in 0.05% Tris-buffered saline-Tween-20, TBST (Amresco) and 1% polyvinylpyrrolidone (Sigma–Aldrich, St. Louis, MO, USA). Membranes were then probed with primary antibodies (Abs) to detect the signal of T-cell subtypes according to their cluster of differentiation (CD)—either anti-CD4 (1:500, Abcam, Cambridge, UK) or anti-CD8—(1:75, Santa-Cruz Biotechnology, Dallas, TX, USA) for 1 h at RT. In the next step, each blot was incubated with a horseradish peroxidase-conjugated (HRP) compatible secondary

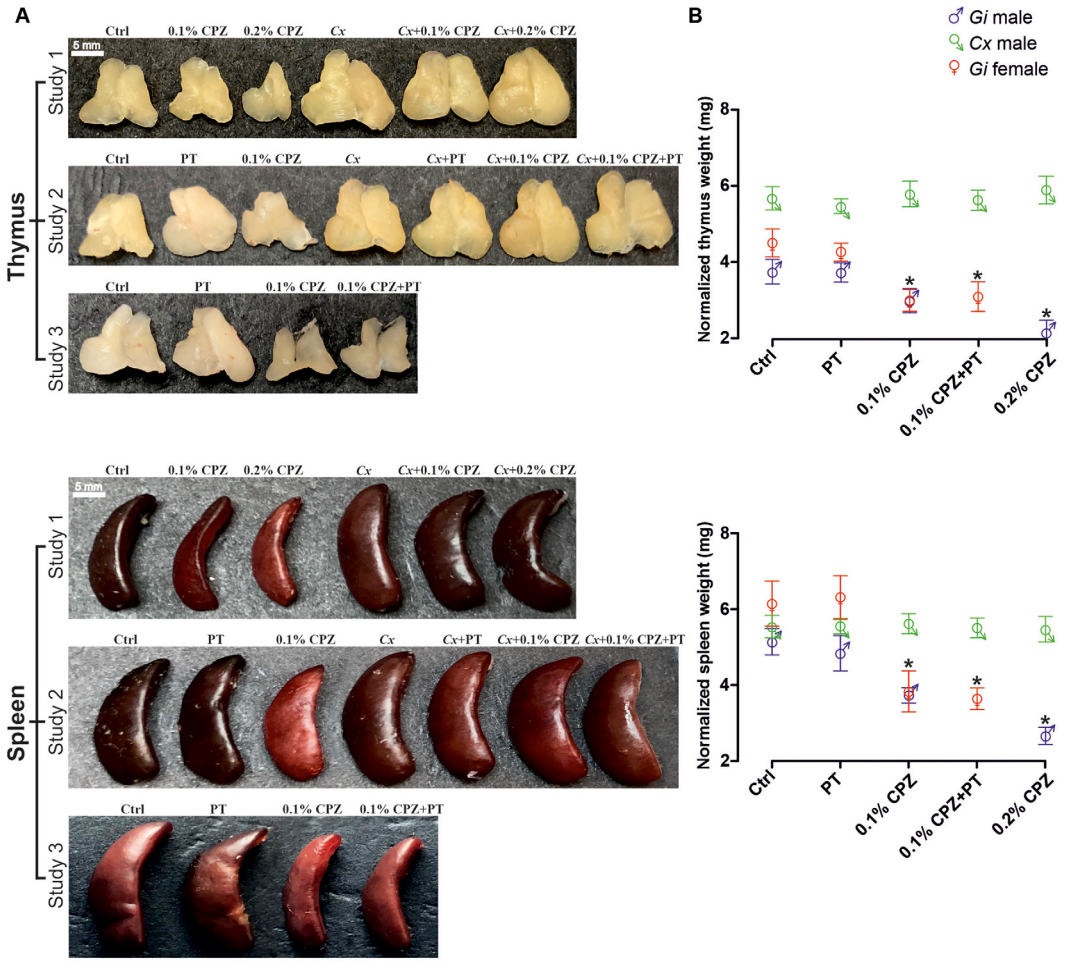

FIGURE 1 | Effects of cuprizone (CPZ)-feeding or castration (*Cx*) on thymus and spleen size and weight. Representative examples of the gross appearance of the thymus and spleen organs **(A)** and quantification of the wet weights **(B)** of the different treatment groups used in the three different studies. In gondally intact (*Gi*) males and females, CPZ-feeding produced a dose-dependent reduction in immune organ mass ($p < 0.05$). In the *Cx* groups, *Cx* significantly increased thymic mass compared to *Gi* males and females ($p < 0.05$) and prevented CPZ-induced thymic and splenic atrophy ($p > 0.05$). In *Gi* female mice CPZ-induced atrophy was indistinguishable to that observed in *Gi* males. Data are presented as mean ± SEM, one-way analysis of variance (ANOVA), $n = 10$ thymic or spleens/group. *Indicates a significant difference from Ctrl ($p < 0.05$).

antibody (CD4 and CD8 blots were incubated with goat anti-rabbit 1:2,000 and mouse anti-mouse, 1:500, respectively) for 1 h at RT. Protein signals were visualized using an enhanced chemiluminescence detection reagent (1 ml/10 cm^2 for 1 min, Luminata Crescendo Western HRP Substrate, Merck-Millipore, Burlington, MA, USA) and scanned using an ImageQuant™ FUJI LAS-4000 (GE Healthcare, Chicago, IL, USA). The intensity of each protein band was measured using ImageJ software[2] to calculate the arbitrary value of every single band and the local background was subtracted from these values. The intensity of each band ($n = 3$ bands/mouse, $n = 3$ mice/group) was expressed as a raw value and presented relative to the values obtained from Ctrl mice. The sensitivity of the Abs used in western blot analyses was confirmed by comparing the molecular weight and band size of the signals obtained from the brain, splenic and thymic samples to the signals of the standard purified CD4 or CD8 recombinant proteins.

Flow Cytometry Analysis

T-cell levels in Study 2 were also analyzed using flow cytometry of thymic, splenic and CNS tissue ($n = 3$ mice/group) to further confirm the western blot and immunohistochemistry results. A standardized application protocol for flow cytometric analysis of T-cell subsets (Miltenyi Biotec)[3] was applied to prepare a cell suspension suitable for single-cell detection. Briefly, following perfusion with PBS, each organ was placed in a Petri dish and covered with 5 ml of freshly prepared cold (∼5°C) PEB buffer (0.5% bovine serum albumin, and 2 mM EDTA dissolved in 0.01 M PBS) and then organs were subjected to mechanical

[2]https://imagej.nih.gov/ij/

[3]http://www.miltenyibiotec.com

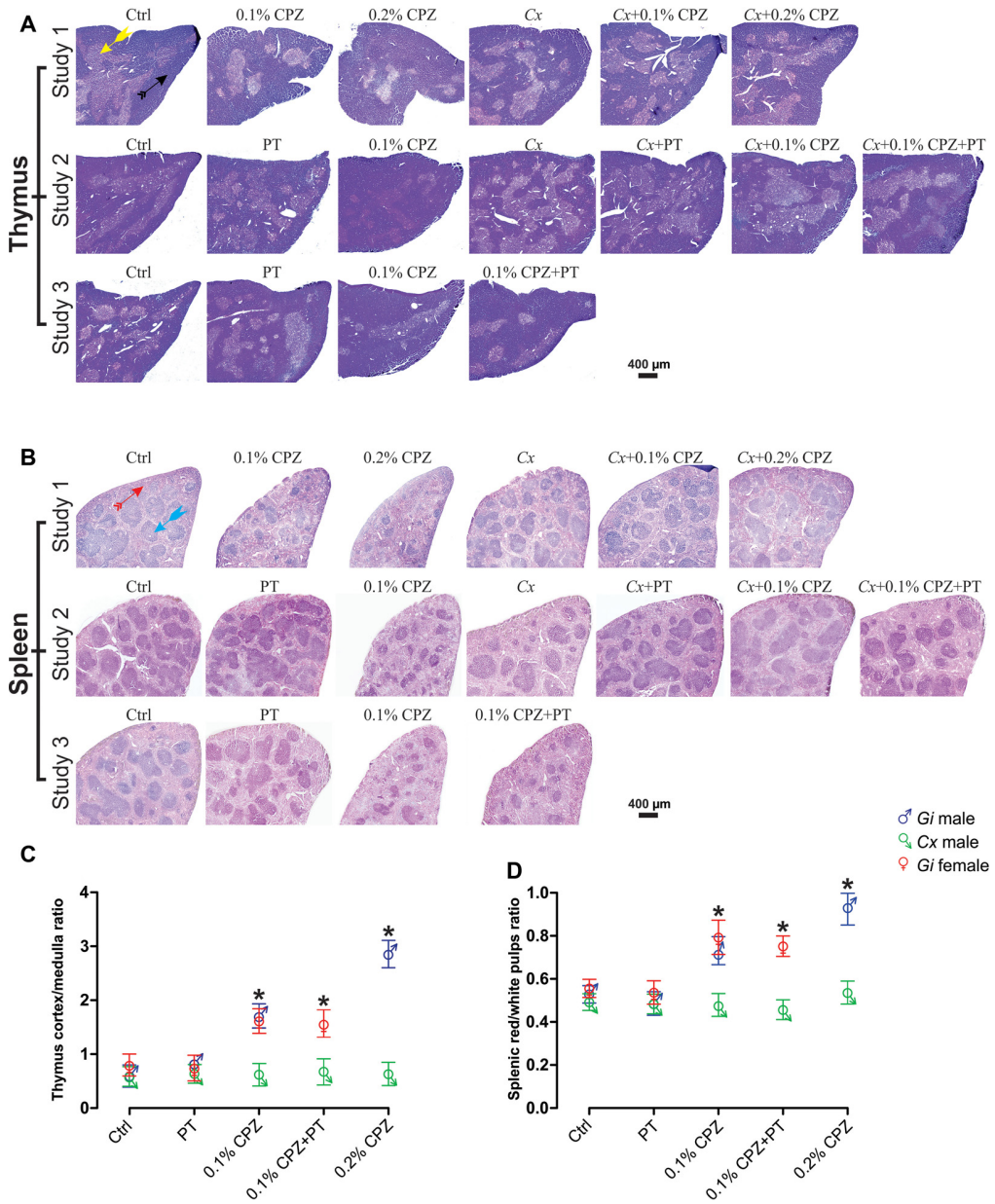

FIGURE 2 | Effects of CPZ-feeding or castration on peripheral immune organs histology. H&E images of the thymus **(A)** and spleen **(B)**, headed arrows identifying the thymic cortex (➶), medulla (➶), the splenic red pulp (➶) and white pulp (➶) regions, in the different groups of the three separate studies. Quantification of the mean ± SEM thymic cortex/medulla **(C)** and splenic red pulp/white pulp ratios **(D)**. Thymic cortex/medulla and splenic red pulp/white pulp ratios were significantly decreased by 0.1% CPZ in both *Gi* male and female mice and by 0.2% CPZ in *Gi* males compared to Ctrl whereas these ratios were unchanged in *Cx* groups. One-way ANOVA, $n = 3$ thymic or spleens/group, five sections/organ; *indicates significant difference from Ctrl ($p < 0.05$).

dissociation to obtain a cell suspension. A nylon mesh strainer (70 µm) was used to remove tissue debris and the cell suspension was centrifuged (300 *g*, 10 min, 4°C). Pellets were resuspended in PEB buffer, centrifuged (300 *g*, 10 min, 4°C), and washed with 2 ml 0.01 M PBS before resuspending cells in 1 ml of 0.01 M PBS. Cells (5 µl) were stained with Trypan Blue (Life Technologies, Carlsbad, CA, USA) and counted (Countess automated cell counter, Invitrogen). Each sample was divided into three aliquots: unstained aliquot (negative control) and stained aliquots (CD4 and 8). Cells were stained (~1 × 10^5 cells/ml) separately with either fluorochrome-conjugated FITC anti-mouse CD4 or PE/Cy7 anti-mouse CD8a antibodies (1:50 dilution, BioLegend, San Diego, CA, USA) for 1 h in the dark at RT while shaking. After adding 2 ml of 0.01 M PBS and centrifugation (300 *g*, 10 min, 4°C) the pellet was resuspended in 100 µl of 0.01 M PBS and analyzed using a MACSQuant® Flow Cytometer (Bergisch Gladbach, NRW, Germany). A total of 20,000 events were analyzed for each sample. The lymphocyte

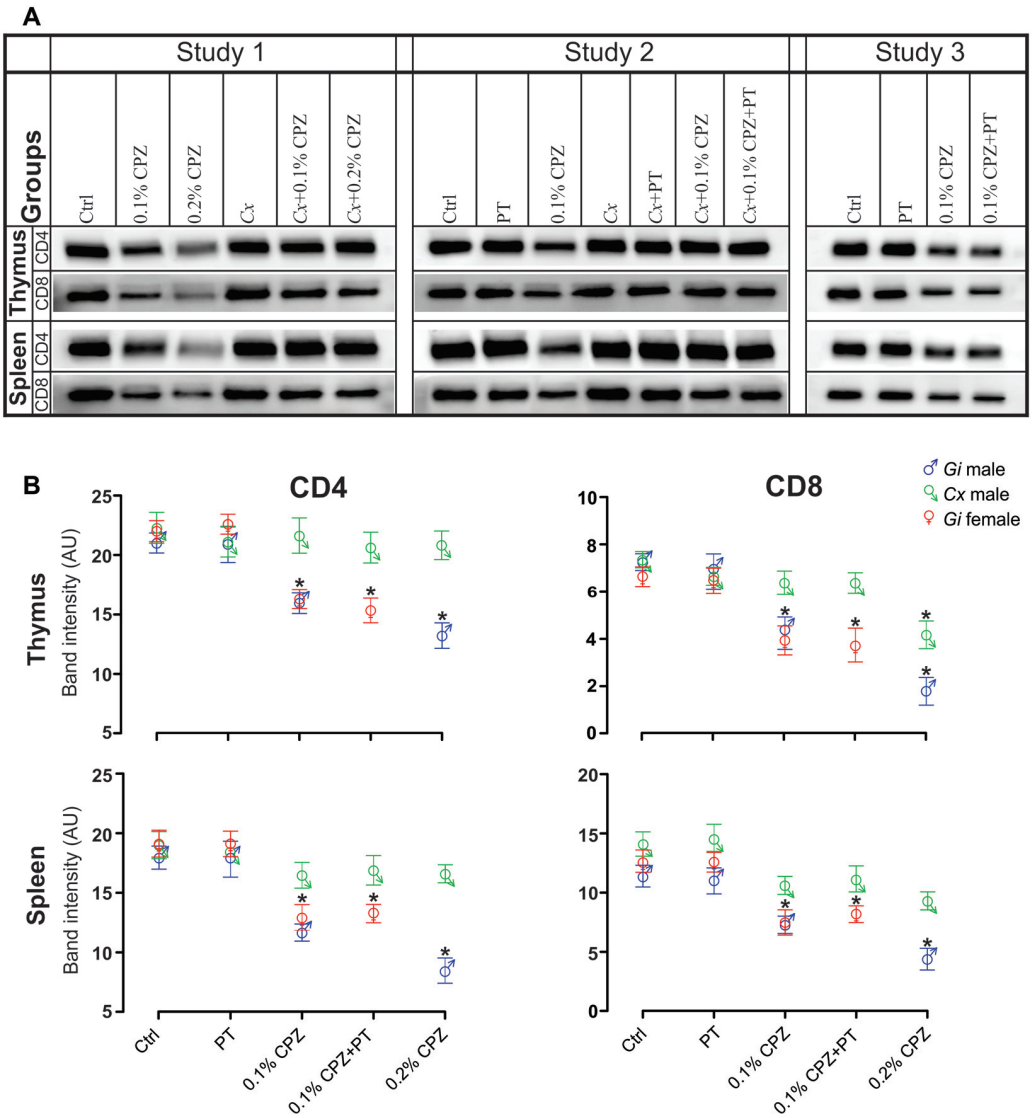

FIGURE 3 | Effects of CPZ-feeding or castration (*Cx*) on CD4 and CD8 signal intensity in the immune organs of male and female mice. Representative examples of western blot images of CD4 and CD8 signal intensities **(A)** and their quantification **(B)** in the different groups in the three separate studies. CD4/8 signal intensities were significantly reduced in the thymus and spleen of *Gi* CPZ-fed male and female mice, whereas CD4/8 signals were completely restored in all *Cx* groups in thymus and spleen except that CD8 signal of the thymus in *Cx*+0.2% CPZ group was markedly attenuated. SDS-PAGE gels were loaded with a 20 μg/well of total protein; one-way ANOVA, $n = 3$ thymic or spleens/group, all samples were processed in triplicate; *indicates significant difference from Ctrl ($p < 0.05$).

gate was defined by forward and side scatters and the $CD4^+$ and $CD8^+$ T-lymphocytes gates were defined by FITC and PE channels, respectively. Data were analyzed on FlowJo software (version 10, LLC, Ashland, OR, USA) and presented as the absolute number of dot blots/quadrant 1 (Q1) or 3 (Q3) for CD4 and CD8 T-cell populations, respectively and the ratio of CD4 to CD8 counts.

Histology and Immunohistochemistry

Tissue Preparation

Mice ($n = 5$/group in each study) were deeply anesthetized with isoflurane (2–3% in 100% oxygen) and perfused transcardially with cold 0.9% saline followed by 4% paraformaldehyde (in 0.1 M phosphate buffer, Sigma–Aldrich, St. Louis, MO, USA). Samples (CNS, thymic and spleens) were collected from the different groups and postfixed using 4% paraformaldehyde at 4°C for 3 days, then kept in 0.02% sodium azide (prepared in 0.01 M PBS, Sigma–Aldrich, St. Louis, MO, USA) at 4°C until processed for staining within 1 month. Whole CNS was immersed in a 30% sucrose solution for 48 h at RT until it sank, confirming cryoprotection. Tissue was then embedded in 4% gelatine (Chem-Supply, Gillman, SA, Australia) in cryomolds (Sakura, Torrance, CA, USA). Gelatine embedded tissue was then embedded in Tissue-Tek™ optimal cutting temperature compound (Sakura) and sectioned with a cryostat (Leica, Wetzlar, HE, Germany) at −20°C. Serial coronal sections of the CNS (40 μm) were either

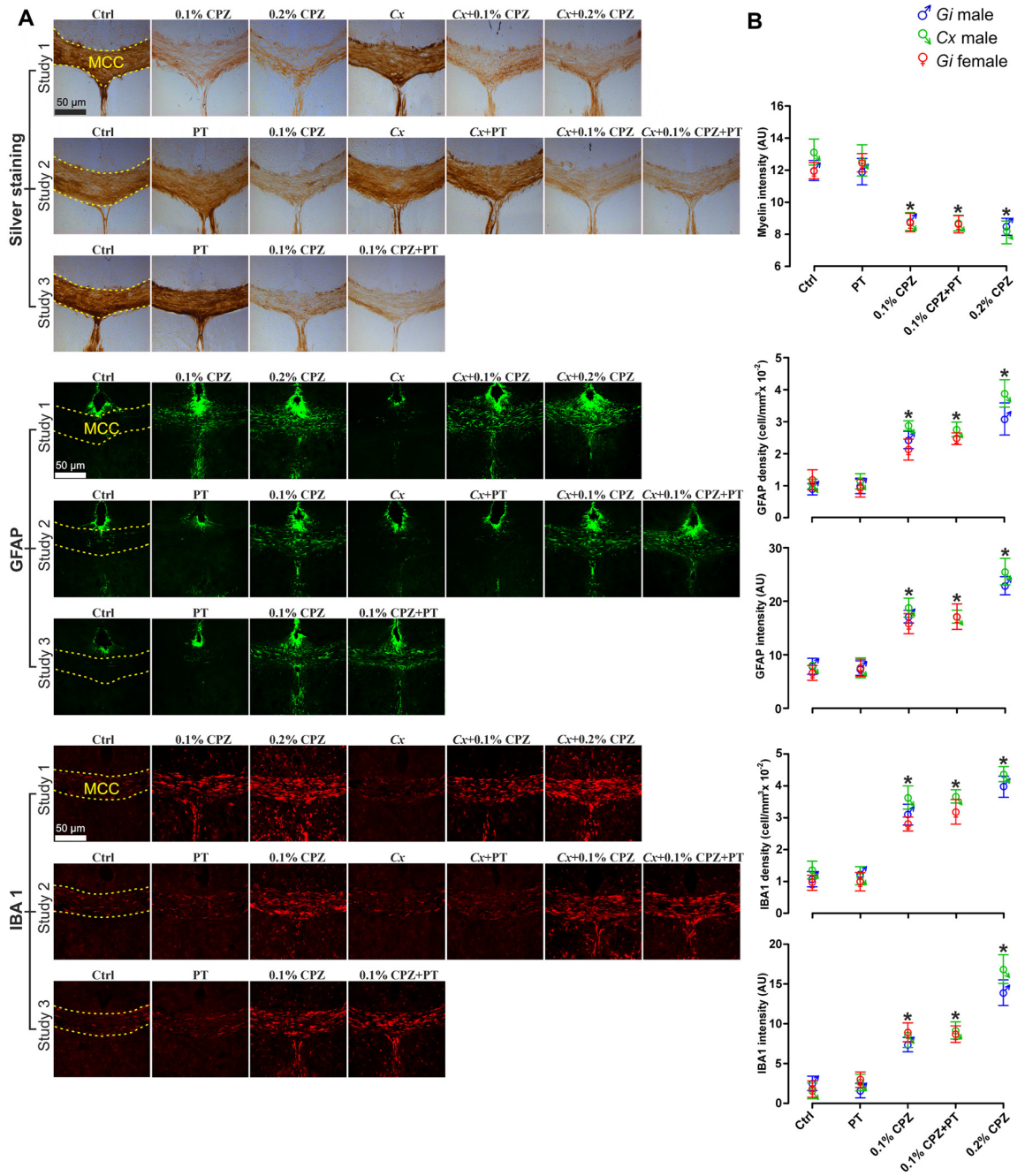

FIGURE 4 | Effects of CPZ-feeding or *Cx* on the central nervous system (CNS) histology. Representative silver, GFAP and IBA 1 staining images **(A)** and quantification **(B)** of silver staining intensity and astrocytes/microglia fluorescence intensity and cell density (cell/mm^3) in the midline corpus callosum (MCC). 0.1% and 0.2% CPZ-feeding produced identical loss ($p < 0.05$) of myelin intensity in *Gi* male mice. The silver intensity was unaffected following *Cx* in all castrated groups. 0.1% CPZ-feeding to *Gi* male and female mice induced comparable demyelination. Fluorescence intensity and cell density of GFAP and IBA 1 stained sections were significantly ($p < 0.05$) increased in a dose-dependent manner (0.1% < 0.2% CPZ) in *Gi* and *Cx* males. The increase in the fluorescence intensity and density were indistinguishable between males and females when mice were fed with 0.1% CPZ. One-way ANOVA, $n = 5$ mice/group, 10 sections/brain; *indicates significant difference from Ctrl ($p < 0.05$), and dashed yellow line indicates quantification area.

transferred to 6-well plates containing 0.01 M PBS (free-floating for immunohistochemistry) or mounted onto 0.5% gelatine-coated slides for silver staining. Sections were placed in an anti-freezing solution (glycerol, ethylene glycol and 0.01 M PBS at 1:1:2 by volume) at −20°C until stained (≥1 month), as described previously (Sen et al., 2019a). To prepare tissue for hematoxylin and eosin (H&E) staining, thymic and spleens were postfixed in 10% formalin for 3 days and then dehydrated in

ethanol (70%, 80%, 95%, and 100%) for 2 h each, cleared using xylene for 2 h and embedded in paraffin (SLEE medical GmbH, Mainz, Germany). Organs were placed in embedding cassettes (Sigma–Aldrich) and kept at 4°C to form solid paraffin blocks. Then tissue blocks were sectioned (10 μm) using a manual rotary microtome (Leica Microsystem, Wetzlar, Germany). A consecutive series of tissue sections were mounted onto glass gelatine coated slides and dried at RT for 1 h. Excess paraffin wax was removed from the slides by heating them at 55°C for 30 min).

Silver Myelin Staining and Quantification

Staining and quantification were performed as previously described (Sen et al., 2019a). Briefly, slide-mounted brain sections were air-dried for 48 h at RT and then immersed in 10% formalin (Sigma–Aldrich) for 14 days. Slides were incubated with a 2:1 solution of pyridine (VWR, Radnor, PA, USA) and acetic anhydride (Merck, Darmstadt, HE, Germany) followed by incubation with freshly prepared ammoniacal silver nitrate (Chem-Supply) for 45 min for staining. Mounting medium (DPX, Merck) and coverslips (Knittel Glass, Braunschweig, NI, Germany) were used to cover the sections and left to dry for 72 h at RT. All brain sections were imaged with bright field Olympus Carl Zeiss microscope (Zeiss, Jena, TH, Germany) using the same settings (i.e., exposure time, magnification and illumination intensity). Images were analyzed by ImageJ software as follows: for each section, the region of interest (midline corpus callosum, MCC) was contoured and the mean optical density was measured as mean gray value [i.e., summation of all the pixels in the region of interest divided by the number of pixels, with individual pixels ranging from black (0) to white (256)]. The results were plotted as the reciprocal of the light intensity to measure the amount of myelin. The anatomical landmark was identified as described previously (Paxinos and Franklin, 2012; Sen et al., 2019a).

Immunofluorescence Staining and Quantification

Staining and quantification were carried out as previously described (Sen et al., 2019a). In short, non-specific binding was blocked using 10% goat serum (Sigma–Aldrich) for 2 h at RT and sections were incubated overnight at RT with primary Abs: glial fibrillary acidic protein (anti-GFAP-AlexaFluor 488, 1:1,000, Merck-Millipore, Burlington, MA, USA), ionized calcium-binding adaptor molecule 1 (rabbit anti-IBA 1, 1:1,000, Wako, Japan), anti-CD4 (rabbit anti-CD4, 1:200, Abcam), or anti-CD8 (mouse anti-CD8, 1:100, Santa-Cruz Biotechnology, Dallas, TX, USA), then washed thrice with 0.01 M PBS. Sections were then incubated with secondary corresponding Abs [either goat anti-rabbit IgG, 1:500, Invitrogen (USA) or mouse anti-mouse IgGκ, 1:100 (Santa-Cruz Biotechnology)] for 2 h at RT and washed 3 × 10 min with 0.01 M PBS. Sections were counterstained with 1.5 mg/ml of nuclear counter-stain Vectashield plus 4′,6-diamidino-2-phenylindole (DAPI, Vector Laboratories, Burlingame, CA, USA) and imaged using a fluorescence Olympus Carl Zeiss microscope (Zeiss, Germany) using the same exposure time and magnification settings. Fluorescence intensity measurement of GFAP and IBA 1 stained sections was performed with ImageJ software as described above. Positively stained cells with GFAP and IBA 1 (and co-stained with DAPI) were counted using unbiased stereo investigator optical fractionator workflow software (see **Figure 4** and **Supplementary Stereology Excel File**) as described previously (Sen et al., 2019a). However, due to the low counts per unit area and regional heterogeneity of $CD8^+$ cell distribution; these cells were counted manually across the entirety of each section in the cerebrum, cerebellum, brainstem and spinal cord (three animals/group, 10 sections/brain or spinal cord, five sections/cerebellum or brainstem). In order to confirm that the $CD8^+$ expressing cells were a distinct population (i.e., from microglia) brain and spinal cords sections were double-labeled with CD8 and IBA 1 antibodies and co-stained with DAPI.

Assessment of BBB Integrity

To assess the permeability of the BBB following PT injection in Study 2, peroxidase-based immunohistochemistry was used to visualize immunoglobulin G (IgG) in the CNS. In Study 3, the same method was used to breach BBB and the results were consistent with Study 2 (*data not shown*). Free-floating coronal sections were washed as described above and non-specific binding and endogenous peroxidase activity were blocked using peroxidase blocking solution (Dako, Carpinteria, CA, USA). Sections were then incubated for 1 h at RT in biotinylated anti-mouse IgG secondary Ab (1:100 dilution, Vector Laboratories Inc., Burlingame, CA, USA). Sections were then incubated with avidin-biotin-peroxidase complex (1:200 dilution, ABC complex, Vector Laboratories) for 30 min at RT, and visualized using diaminobenzidine (DAB, Vector Laboratories Inc., Burlingame, CA, USA) solution (0.05% DAB in 0.005% H_2O_2). All incubation and reaction steps were performed in parallel for all sections, at RT, to ensure that the DAB staining was comparable (i.e., equal number of sections from each experimental group exposed to the same batch of DAB stain and incubated for the same amount of time). Sections were then mounted on slides and cover-slipped using DPX mounting medium and left to dry overnight. Sections were imaged by bright field Olympus Carl Zeiss microscope (Zeiss, Germany) and quantified using ImageJ software to measure the IgG color intensity as described above.

Haematoxylin and Eosin (H&E) Staining

Staining with H&E was performed in thymus and spleen tissue to assess the structural changes associated with CPZ-feeding. Following removal of excess paraffin from the tissue (see "Tissue Preparation" section), slides were rinsed in xylene for 10 min (to remove the remaining paraffin wax) and rehydrated by dipping in a series of alcohol washes (100%, 80%, 50% and 0%, five times each solution). In the next step, hematoxylin (4 g/l, Merck-Millipore, Burlington, MA, USA) was used for 3 min to stain the sections followed by washing with tap water. Slides were then dipped into acid alcohol for 30 s to differentiate the cytoplasm and transferred into Scott's Bluing solution to stain the nucleus. Then the tissue was stained with eosin (0.5%) to counterstain acidic components of cells (e.g., cytoplasmic proteins) and washed with tap water followed by ascending concentrations of alcohol (70%, 95%, and 100%) to dehydrate the tissue and xylene to clear it. Slides were covered with mounting medium (Merck) and sealed with coverslips (Cardiff et al., 2014).

Tissue sections were imaged with an Olympus Carl Zeiss bright field microscopy. ImageJ software was used to analyze various histomorphometric measurements of the thymus and spleen as previously described (Tryphonas et al., 2004). Briefly, the total area (mm^2) of each thymus section (three mice/group, five sections/mouse) was contoured and measured. All regions of the thymic medulla in each section were also contoured individually to obtain the area of each region; these values were summed to yield the total medullary size of each thymic section. The total section area was then subtracted from the medulla area to get the total thymic cortex area. Averages of cortical and medullary values of each mouse in all groups were calculated. Finally, the average values of cortex were divided by average medullary values to obtain the thymic cortex/medulla ratio. The same strategy was applied to spleen sections in order to measure the splenic red pulp/white pulp ratio.

Statistical Analysis and Graphing

All data were presented as mean ± standard error of the mean (SEM). Bodyweight data was analyzed using the two-way analysis of variance (ANOVA). All other data were analyzed using a one-way ANOVA and individual differences were determined using Newman–Keuls *post hoc* multiple comparison analyses. Statistically significant differences compared to Ctrl were considered when $p < 0.05$ and indicated by asterisks (*) in all graphs. Statistical analyses and graphing were performed using GraphPad Prism 7.03 software[4] (San Diego, CA, USA). Figures were assembled using the CorelDRAW graphics design software version 2019[5] (Ottawa, ON, Canada).

RESULTS

Study 1: Castration Counteracts the Peripheral Effects of CPZ

To quantify the impact of CPZ on the thymus and spleen, and to test whether *Cx* could protect these organs against the effects of CPZ-feeding, prepubescent male C57Bl/6 mice (i.e., 4 weeks old) were surgically castrated and subsequently fed with powdered chow containing 0.1% or 0.2% CPZ for 2 weeks, in parallel with Ctrl mice. Weight gain in all *Cx* males (*Cx*, *Cx*+0.1% CPZ, and *Cx*+0.2% CPZ groups) was significantly reduced compared to *Gi* CPZ-fed males and *Gi* Ctrl during the first 3 days of CPZ-feeding and this effect continued to the end of the study. During the second week of CPZ-feeding, significant reductions in body weight gain were observed in the CPZ-fed animals compared to healthy Ctrls (**Supplementary Figure S2**). By the end of the experiment, the weight differences between Ctrl mice and that fed 0.1% or 0.2% CPZ were approximately 9% and 15%, respectively. This rank order was preserved when comparing *Cx* alone and 0.1% or 0.2% CPZ *Cx* animals, in which the weight differences were approximately 8% and 15% respectively. Following 2 weeks of 0.1% or 0.2% CPZ-feeding, the size (**Figure 1A**) and weight of the thymus and spleen (normalized to body weight, **Figure 1B**, Study 1 panels) in *Gi* males was reduced ($p < 0.05$) in a dose-dependent manner (thymus: 13.3 ± 0.03% vs. 28.4 ± 0.03%, spleen: 27.6 ± 0.04% vs. 42.4 ± 0.04% for 0.1% vs. 0.2% CPZ) compared to their respective Ctrls. In contrast, thymic mass was increased by 69.0 ± 4.1%, ($p < 0.05$) following *Cx* compared to *Gi* Ctrls at 2 weeks and this effect remained despite CPZ-feeding. While the splenic mass of *Cx* mice was not different from *Gi* Ctrls, *Cx* did prevent the CPZ-induced reduction in splenic weight seen in the *Gi* group (**Figure 1B**).

Castration Restored the Histological Architecture of Thymus and Spleen

In *Gi* male mice, CPZ-feeding induced dose-dependent reductions in medulla area (0.2% CPZ: 18.5 ± 1.0 > 0.1% CPZ: 9.6 ± 1.0 mm^2) without any change in cortical area (**Figures 2A,C**, **Table 1**) resulting in a dose-dependent increase in the thymic cortex/medulla ratio (0.2% CPZ: 1 ± 0.03 > 0.1% CPZ: 0.7 ± 0.04 > Ctrl: 0.5 ± 0.03). In contrast, the thymic cortex/medulla ratio was unchanged by feeding 0.1% or 0.2% CPZ to *Cx* mice (**Table 1**). Similarly, H&E staining confirmed that feeding CPZ to *Gi* mice induced a dose-dependent (0.1% < 0.2% CPZ) reduction in splenic red pulp/white pulp ratio [**Figures 2B,D**; i.e., the white pulp size was affected by CPZ-feeding (**Table 1**)]. In contrast, CPZ-feeding had no effect on white pulp area following *Cx*, i.e., white pulp size of *Cx*+0.1% and *Cx*+0.2% CPZ groups were indistinguishable ($p < 0.05$) from *Gi* Ctrl spleens. Taken together, these results showed that *Cx* protected mice against the deleterious effects of CPZ-feeding on the spleen and thymus regardless of CPZ dose.

Castration Preserved CD4/8 Signal in the Thymus and Spleen Against the Impact of CPZ

Western blot analysis indicated a significant dose-dependent reduction (0.2% > 0.1% CPZ) in the signal intensity of CD4 and CD8 T-cells in both thymus and spleen of *Gi* CPZ males compared to *Gi* Ctrl males (**Figures 3A,B**). The effect of 0.1% or 0.2% CPZ on CD4 signals in both thymus and spleen was prevented by *Cx* despite feeding with CPZ. Moreover, the CD8 signal was indistinguishable from the Ctrl group when *Cx* combined with 0.1% or 0.2% CPZ in spleen but only with the *Cx*+0.1% CPZ group in the thymus. Although the effect of CPZ on thymic CD8 signal in the *Cx*+0.2% CPZ group was ameliorated by *Cx* (compared with the *Gi* male at the same dose), CD8 signal was significantly ($p < 0.05$) decreased in the *Cx*+0.2% CPZ group compared to the Ctrl group (**Figure 3B**). Overall, 0.2% CPZ had a significant ($p < 0.05$) suppressive impact on the levels of CD4/8 in both thymus and spleen compared to 0.1% CPZ in *Gi* mice. *Cx* induced preservation of thymic and splenic CD4/8 levels in both *Cx*+0.1% CPZ and *Cx*+0.2% CPZ groups compared to *Gi* Ctrl males.

CPZ-Induced Demyelination

Silver staining revealed that 0.1% and 0.2% CPZ-feeding induced a significant decrease in MCC myelin of *Gi* male mice compared to *Gi* Ctrl males (**Figures 4A,B**, Study 1 panel) and the extent of demyelination was indistinguishable between 0.1% or 0.2%

[4]www.graphpad.com
[5]www.coreldraw.com

TABLE 1 | Histomorphometric evaluation of thymus and spleens from *Gi* and *Cx* males, and *Gi* female mice, exposed to CPZ.

	Group	Thymic cortex	Thymic medulla		Splenic red pulp	Splenic white pulp	
Study 1	Ctrl	33.8 ± 3.3	40.1 ± 2.6		7.7 ± 0.9	14.5 ± 1.4	
	0.1% CPZ	32.6 ± 3.7	18.5 ± 1	↓	6.7 ± 0.5	9.5 ± 1.3	↓
	0.2% CPZ	27.1 ± 3	9.6 ± 1.1	↓	5.7 ± 0.6	5.9 ± 0.4	↓
	Cx	33.1 ± 4.3	56.6 ± 2.4	↑	8.1 ± 0.6	15.3 ± 1.5	
	Cx+0.1% CPZ	32.2 ± 0.8	51.7 ± 2.5	↑	7.9 ± 0.3	14.3 ± 1.1	
	Cx+0.2% CPZ	31.6 ± 3.8	49.8 ± 4.3	↑	7.8 ± 0.4	14.5 ± 0.5	
Study 2	Ctrl	33.8 ± 3.3	40.14 ± 2.57		7.7 ± 0.9	14.5 ± 1.5	
	PT	35.0 ± 3.9	39.37 ± 4.23		7.0 ± 1.1	13.9 ± 0.6	
	0.1% CPZ	32.6 ± 3.7	18.45 ± 0.97	↓	7.4 ± 0.5	8.5 ± 0.7	↓
	Cx	33.1 ± 4.3	56.62 ± 2.41	↑	8.1 ± 0.6	15.3 ± 1.5	
	Cx+PT	31.6 ± 4.3	44.94 ± 4.44	↑	8.4 ± 0.4	14.7 ± 0.5	
	Cx+0.1% CPZ	32.2 ± 0.8	51.67 ± 2.46	↑	7.9 ± 0.3	14.3 ± 1.1	
	Cx+0.1% CPZ+PT	32.4 ± 0.7	53.49 ± 6.39	↑	8.3 ± 0.2	15.9 ± 2.3	
Study 3	Ctrl	32.3 ± 3.4	41.19 ± 3.1		8.2 ± 0.8	15.2 ± 1	
	PT	28.8 ± 3.1	39.11 ± 4.2		8.4 ± 0.2	15.9 ± 1.5	
	0.1% CPZ	28.1 ± 1.8	17.39 ± 0.8	↓	7.9 ± 0.5	10.2 ± 1.4	↓
	0.1% CPZ+PT	26.8 ± 1.5	17.29 ± 1.1	↓	7.6 ± 0.2	10.1 ± 0.6	↓

Values are presented as mean area (mm^2) ± SEM (n = 3 thymic or spleens/group, five histological sections/organ). Statistically significant changes are indicated as higher (↑) or lower (↓) relative to Ctrl when $p < 0.05$.

CPZ. *Cx* alone, or when combined with 0.1% or 0.2% CPZ, did not affect the myelin staining intensity compared to *Gi* Ctrl males. Overall, 0.1% CPZ-feeding was as effective at producing demyelination as 0.2% CPZ in mice, with or without *Cx*.

Effects of CPZ and *Cx* on Glial Activation

GFAP and IBA 1 staining were used to quantify astrocytes and microglia, respectively, in the MCC. Following CPZ-feeding in *Gi* males, cell density (cell/mm^3) and fluorescence intensity of both GFAP and IBA 1 were significantly increased in a dose-dependent manner (0.2% > 0.1% CPZ) compared to *Gi* Ctrl (**Figures 4A,B**, Study 1 panels, GFAP, IBA 1). Combining *Cx* with 0.1% or 0.2% CPZ-feeding did not change the cell density or the fluorescence intensity of either GFAP or IBA 1 staining. Both 0.1% and 0.2% CPZ-feeding induced a strong glial response in the demyelinated areas in the MCC.

Study 2

Intraperitoneal injections of PT in male mice had no synergistic effect when combined with 0.1% CPZ in both the *Gi* and *Cx* males. As seen in Study 1, CPZ-feeding resulted in comparable reductions in weight gain (**Supplementary Figure S2**, Study 2) and a reduction in thymic and splenic mass (**Figures 1A,B**, Study 2 panels). *Cx* increased the thymic weight but the splenic mass remained unchanged compared to *Gi* Ctrl. Western blot analysis showed significant reductions ($p < 0.05$) in CD4/8 signals in *Gi* animals fed 0.1% CPZ compared to Ctrl whereas, in *Cx* groups, CD4/8 signals remained unchanged when fed 0.1% CPZ (**Figures 3A,B**, Study 2 panels). Likewise, flow cytometric analysis of thymocytes and splenocytes showed significant decreases ($p < 0.05$) in CD4/8 T-cell subpopulations in the 0.1% CPZ group compared to Ctrl, whereas in the *Cx* groups CD4/8 T-cell subpopulations were significantly increased ($p < 0.05$, **Figures 5A,B**). In addition, there were no changes in the ratio of CD4/CD8 across all groups ($p > 0.05$, **Figure 5C**). Myelin, GFAP and IBA 1 intensities in the PT group of *Gi* males were indistinguishable from Ctrl. PT injection did not change the amount of demyelination nor the extent of microglia and astrocyte activation when combined with *Cx*, 0.1% CPZ, or *Cx*+0.1% CPZ (**Figures 4A,B**, Study 2 panels). The PT-mediated breach of the BBB was confirmed by a significant increase in the intensity of IgG staining in the hippocampal region of the PT injected groups (**Supplementary Figures S3A,B**). Quantification was performed in the hippocampus because the intensity of the stain was highest there relative to regions (**Supplementary Figure S3**).

$CD8^+$ T-cell Number Increased in the CNS Following PT Injection in *Cx*-CPZ-Fed Mice

In a previous study, CD4 and/or CD8 were not detected following PT injection in the CNS of *Gi* male mice fed 0.1% CPZ (Sen et al., 2019a). In contrast, when 2 weeks of 0.1% CPZ-feeding was combined with *Cx* and PT treatment (*Cx*+0.1% CPZ+PT, **Figures 6A,B**) $CD8^+$ cell numbers in the CNS increased. The distribution of $CD8^+$ T-cells in the stained slices was not homogeneous, with $CD8^+$ cells appearing either as individual cells or in small groups of cells distributed widely throughout the CNS (cerebrum, cerebellum, brainstem, and spinal cord). In *Gi* and *Cx* animals, $CD8^+$ cells were rarely encountered and their numbers were unaffected by CPZ-feeding (range between 0–23 cells/section) compared to Ctrl. When CPZ-feeding and *Cx* were combined with PT, the number of $CD8^+$ cells increased (<2-fold) in multiple regions of the brain (whole parenchyma) and spinal cord (most notably in the gray matter and around the central canal, **Figures 6A,B**). Double labeling of CNS sections with CD8 and IBA 1 antibodies (and co-stained with nuclear DAPI staining) confirmed that CD8 and IBA 1 were expressed in distinct cell populations (**Figure 6C**).

In addition, using the same western blot analysis of the brain and spinal cord homogenate samples (three independent 60 μg sample loads per animal, three animals/group) we replicated the previous finding that neither CD4 nor CD8 signals were detected in the CNS homogenates of Ctrl, 0.1% CPZ and PT treated *Gi*

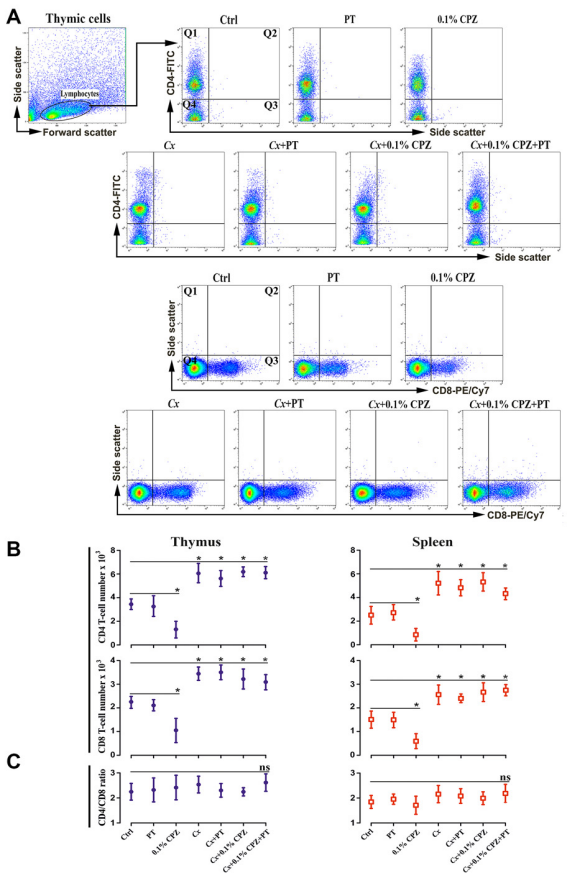

FIGURE 5 | Flow cytometric analysis of T-cell subpopulations ($CD4^+$ and $CD8^+$) in the immune organs of male mice. Representative flow cytometry dot blots of thymic CD4 and CD8 T-cells **(A)** and the quantification of their cell number in thymus and spleen tissue from Study 2 **(B)**. CD4/8 number was significantly reduced in the thymus and spleen of 0.1% CPZ-fed mice compared to Ctrl. The numbers of CD4/8 increased in all *Cx* groups compared to Ctrl and were unaffected by CPZ. Cell counts in the quadrant 1 (Q1) for CD4 and quadrant 3 (Q3) for CD8 were used to quantify cell number in each experimental group. No significant (ns, $p > 0.05$) changes in the ratio of CD4/CD8 were observed in thymus and spleen **(C)**. A one-way ANOVA ($n = 3$ thymic or spleens per group, 20,000 events/sample) was used to determine significant differences from Ctrl (*$p < 0.05$).

males (Sen et al., 2019a). However, in the *Cx*+0.1% CPZ+PT mice, CD8 signal was detected in the CNS homogenates, whereas the CD4 signal was not (**Figure 7**, Study 2). Furthermore, neither CD4 nor CD8 signals were detected in CNS homogenates in either Study 1 or Study 3 (**Figure 7**, Studies 1 and 3).

The increased $CD8^+$ T-cell signal intensity (western blot) and number (immunohistochemistry) in the brain and spinal cord tissue of the *Cx*+0.1% CPZ+PT mice were also confirmed using flow cytometric analysis (**Figures 8A,B**). Moreover, $CD4^+$ T-cells count via flow cytometry did not show any changes among all groups (i.e., CD4 cell number in Ctrls: brain 1,087 ± 314; spinal cord 834 ± 176). The ratio of CD4/CD8 was unchanged in all groups compared to Ctrl except in the *Cx*+0.1% CPZ+PT group, in which the ratio was significantly decreased ($p < 0.05$, **Figure 8C**).

Study 3

BBB disruption was applied in Study 3 to test whether $CD8^+$ T-cells could be increased in the CNS of *Gi* female mice as observed in *Cx*+0.1% CPZ+PT treated males. Feeding 0.1% CPZ to *Gi* female mice led to reduced body weight gain (**Supplementary Figure S2**), severe thymic and splenic atrophy (**Figures 1A,B**) and changes in histological architecture (thymic cortex/medulla and splenic red pulp/white pulp ratios). These effects were indistinguishable from those observed in *Gi* males (**Figures 2A,B**). Notably, the reductions in CD4/8 were comparable to those in *Gi* males (**Figures 3A,B**). Likewise, the levels of demyelination, and microglia and astrocyte activation were indistinguishable from those observed in age (and treatment) matched *Gi* and *Cx* males (**Figures 4A,B**). In contrast to the *Cx* males, following 0.1% CPZ+PT, CD4/8 T-cells were not detected in CNS tissue of *Gi* female mice (**Figure 6**).

DISCUSSION

To better understand why T-cells have been so infrequently found at sites of demyelination in the CPZ animal model, the impact of CPZ-feeding on the peripheral immune organs that are responsible for the maturation, differentiation and production T-cells, namely the thymus and spleen, was assessed (Cesta, 2006; Pearse, 2006). While previous studies have shown CPZ-induced thymic and splenic atrophy, they did not attempt to alleviate these effects (Solti et al., 2015; Martin et al., 2018; Sui et al., 2019; Sen et al., 2019a). The morphological and histopathological changes to the thymus following CPZ-feeding observed here and in other studies (Solti et al., 2015), are remarkably similar to those observed and attributed to androgen-dependent thymic involution that can be reversed by androgen depletion (Roden et al., 2004; Tang et al., 2012). Consistent with this observation, Study 1 demonstrated that *Cx* reversed the 0.1% or 0.2% CPZ-induced atrophy of the thymus and spleen and preserved CD4/8 signal intensity in both immune organs. In Study 2, *Cx*, when combined with 2 weeks of CPZ-feeding and disruption of the BBB (using PT), resulted in demyelination, gliosis and $CD8^+$ T-cell infiltration in the cerebrum, cerebellum, brainstem, and spinal cord. In female mice (Study 3), combining CPZ-feeding with BBB disruption resulted in CNS demyelination and gliosis, but no $CD8^+$ T-cell infiltration into the brain or spinal cord. Taken together, these results indicate that CPZ-induced demyelination in the CNS can trigger a $CD8^+$ T-cell-mediated central response when the peripheral immune system is preserved.

As previously documented, CPZ-feeding led to a significant reduction in weight gain (Franco-Pons et al., 2007; Torkildsen et al., 2009; Ye et al., 2013; Chang et al., 2017; Sen et al., 2019a) and a reduction in thymic and splenic weights (Solti et al., 2015; Martin et al., 2018; Sui et al., 2019; Sen et al., 2019a). Although *Cx* was timed to precede the onset of normal age-related thymic atrophy (Sheean et al., 2015), *Cx* did not prevent the CPZ-induced suppression of total body weight gain. However, *Cx* did counteract the CPZ-induced suppression of thymus size and weight, spleen weights, and changes in the thymic medulla and splenic white pulp

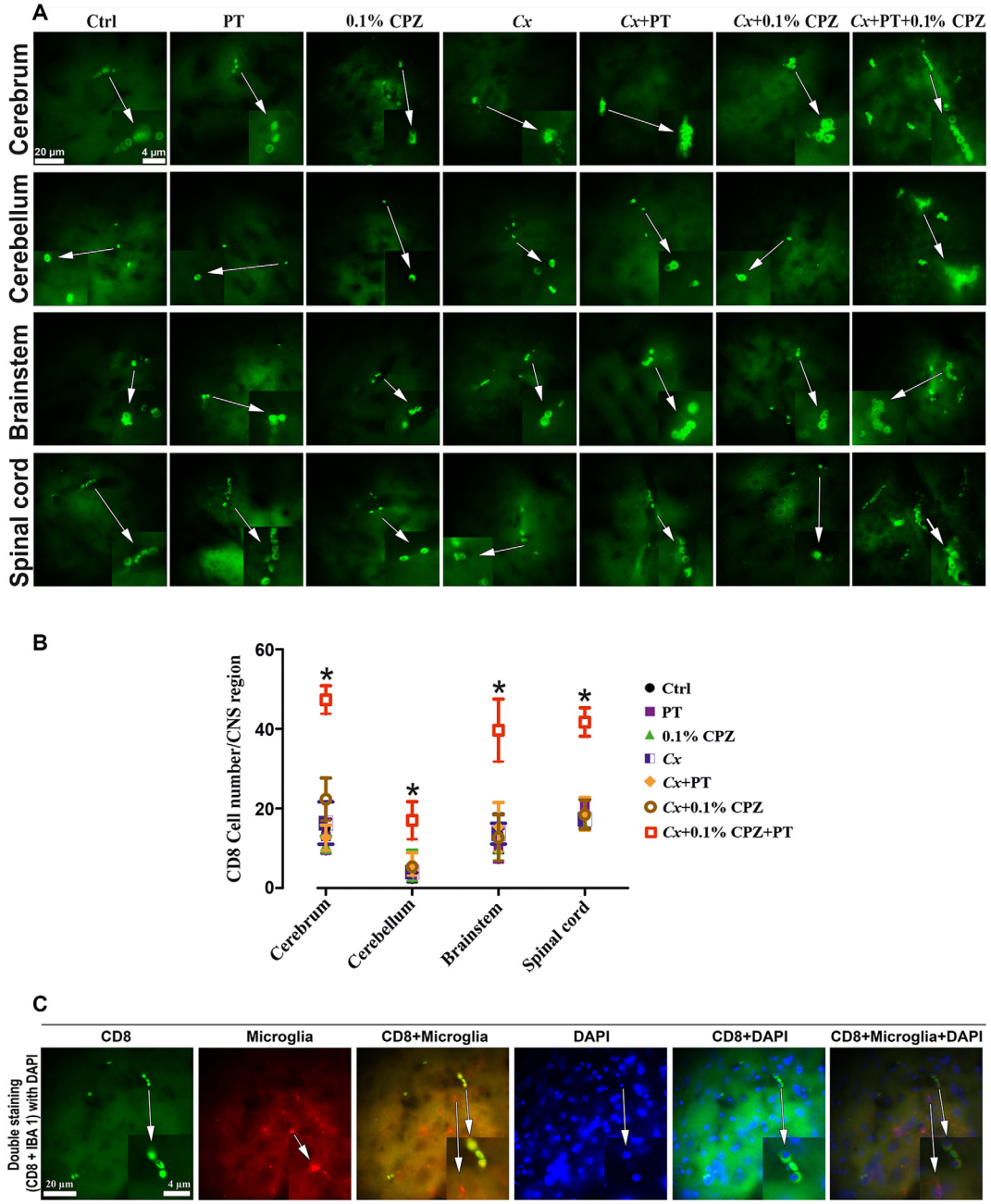

FIGURE 6 | Combined effects of CPZ-feeding and *Cx* with pertussis toxin (PT) on CD8$^+$ T-cells in the CNS. Representative images of CD8$^+$ T-cells detected in the CNS tissue **(A)** and quantification **(B)** of CD8$^+$ T-cell numbers in the CNS (cerebrum, cerebellum, brainstem, and spinal cord). In Study 2, the number of CD8$^+$ T cells was significantly ($p < 0.05$) higher in each part of the CNS in the *Cx*+0.1% CPZ+PT group than in all other groups. Section **(C)** shows representative images of double labeling with CD8 and IBA 1 antibodies in the brain tissue, nuclear DAPI staining, and merged images confirming the identity of CD8$^+$ T-cells. As indicated by white arrows, regions of the images were magnified five times and these appear as insets at the bottom of the image panel; one-way ANOVA, $n = 3$ mice/group, 10 sections/ brain or spinal cord, five sections/cerebellum or brainstem; *indicates significant difference from Ctrl ($p < 0.05$).

(structures responsible for T-cell development and production). Furthermore, western blot analysis confirmed that *Cx* countered all CPZ-induced suppression of CD4/8 signal in the thymus and spleen. In the absence of the protective effects of *Cx*, the direct effects of CPZ-feeding on the thymus and spleen provide a plausible explanation as to why prior studies did not show the involvement of T-cells in the CNS of CPZ-fed mice (Remington et al., 2007; Tejedor et al., 2017; Sen et al., 2019a). Likewise, the demonstration that CPZ ameliorates and/or prevents the clinical and pathological features of EAE and Theiler's virus

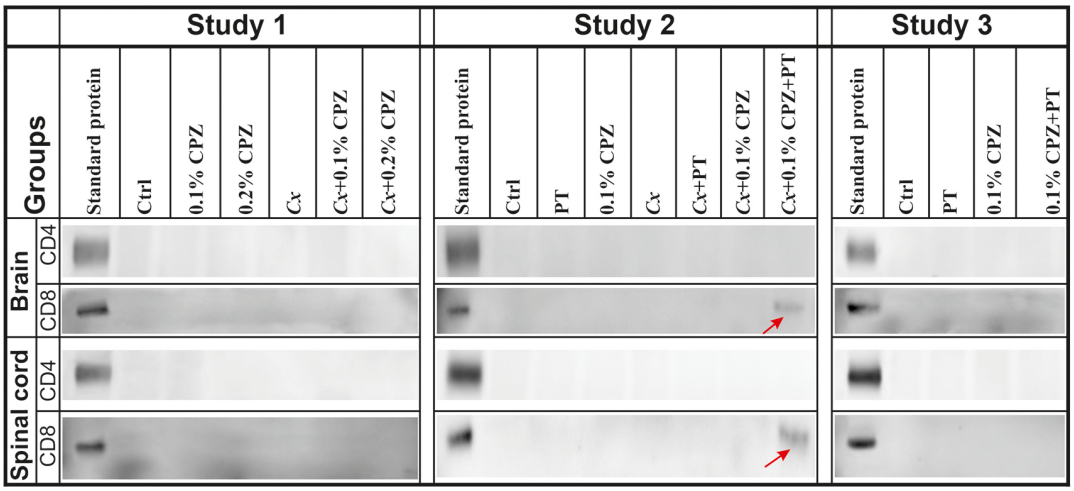

FIGURE 7 | Detection of CD4/8 signals in the CNS homogenate. Representative images of western blot analysis of CD4 and CD8 antigen detection in the brain and spinal cord. No CD4 signal was detected in the CNS tissue across all groups in Studies 1–3. In contrast, the CD8 signal band was detected only in brains and spinal cords of *Cx*+0.1% CPZ+PT mice in Study 2 (red arrows). SDS-PAGE gels were loaded with 60 μg/well of total protein, all samples were processed in triplicate, and standard purified CD4 and CD8 protein concentrations were 5 ng/well and 5 μg/well, respectively.

encephalomyelitis (Maña et al., 2009; Herder et al., 2012), is consistent with CPZ suppressing peripheral immune function and hence improving both clinical and pathological features driven by T-cells. Based on this, and prior work (Solti et al., 2015; Martin et al., 2018; Sui et al., 2019; Sen et al., 2019a), it is clear that suppressive effects of CPZ on the thymus and spleen, and thus T-cells ($CD4^+$ and $CD8^+$ lymphocytes), are not conducive to study effects mediated by peripheral immune cells *unless* strategies to protect and/or boost the peripheral immune system are employed.

Broadly speaking, the toxic effects of CPZ have been attributed to copper chelation that interferes with cellular and mitochondrial metabolism and results in the formation of mega- or enlarged-mitochondria in the liver and thymus of mice (Suzuki, 1969; Hoppel and Tandler, 1973; Solti et al., 2015). Likewise, in the mitochondria of oligodendrocytes, increased reactive oxygen species and decreased activity of respiratory chain complexes resulted from CPZ-feeding (Gudi et al., 2014; Faizi et al., 2016). Additionally, in the atrophied thymus, enlarged mitochondria, myelin bodies, enlarged lysosomes, and lipid droplets were observed following CPZ-feeding (Solti et al., 2015). The enlarged lysosomes are the result of increased membrane permeability, and the release of lysosomal proteases activates caspases, ultimately leading to thymocyte apoptosis (Zhang et al., 2009; Veto et al., 2010).

T-helper ($CD4^+$) cells require copper to transcribe interleukin-2 (Hopkins and Failla, 1999)-a process that may be suppressed due to the copper chelating action of CPZ (Emerson et al., 2001). These effects of CPZ on mitochondrial function and thymocyte apoptosis may explain why western blot and flow cytometry analyses of the thymus from CPZ-fed *Gi* mice identified a reduction in CD4/8 T-cell levels whereas *Cx* counteracted this effect, at least in part due to the hypertrophy resulting from the ablation of androgens. Supporting this, it has been suggested that androgen depletion may be involved in the regulation of mitochondrial dysfunction and toxic responses (Liu et al., 2019).

The suppressive effects of androgens on the structure and function of the thymus have been extensively investigated. The most prominent effects are mitochondrial dysfunction-induced thymocyte apoptosis and thymic atrophy, which result in a subsequent reduction of circulating T-cells (Olsen et al., 1994, 1998; Veto et al., 2010). However, *Cx* countered these effects. The preservation of thymic CD4/8 signal intensity in *Cx* groups, in the presence of CPZ, may not be limited to the effects of *Cx* on developing thymic cortical and medullary cells, but include effects on bone marrow-derived stem cells. *Cx* increased the number of thymocyte precursor cells in the bone marrow and enhanced their differentiation into mature thymocytes in the thymus, leading to thymic regeneration (Sutherland et al., 2005). These effects of *Cx* are consistent with other findings in young and aged animals in which orchiectomy induces rapid restoration of thymopoiesis, a significant increase in the proliferation of immature thymocytes, and a reduction in apoptosis (Olsen et al., 1994; Roden et al., 2004; Page et al., 2006; Sheean et al., 2015). In the current work, combining a 0.1% CPZ with *Cx* meant that the suppressive effects of CPZ on the peripheral immune system were counter-balanced by ablating the normal androgen-mediated involution of the thymus, thereby preserving peripheral immune function.

Immature T-cells are selected in the thymic tissue according to their specificity to T-cell receptors (e.g., $CD4^+$, $CD8^+$, and forkhead $P3^+$ regulatory T-cells), to develop functional and self-tolerant T-cell repertoires (positive selection), and induce a central tolerance to eliminate of autoreactive T-cells (negative selection). The maturation of thymocytes occurs in the thymic cortex, whereas the differentiation and negative selection of T-cells occurs in the thymic medulla (Klein et al., 2014;

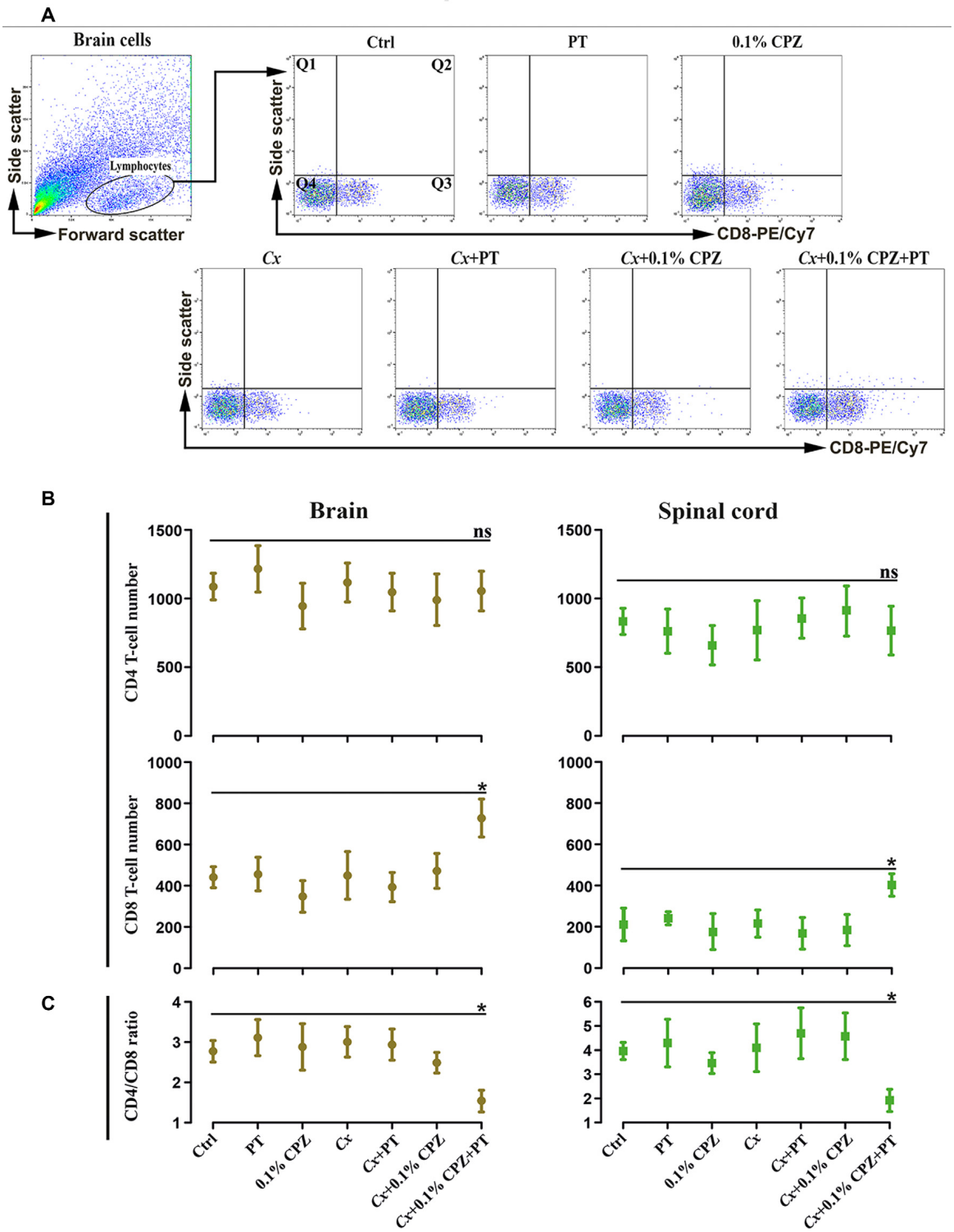

FIGURE 8 | Flow cytometric analysis of T-cell subpopulations (CD4 and CD8) in the brain and spinal cord of male mice. Representative $CD8^+$ T-cells dot blots in the brain **(A)** and quantification **(B)** of $CD4^+$ and $CD8^+$ T-cell numbers in the brain and spinal cord. In Study 2, no significant (ns) changes in the number of $CD4^+$ T-cell of the brain and spinal cord were observed, whereas the number of $CD8^+$ T-cells was significantly ($p < 0.05$) increased only in the brains and spinal cord of the *Cx*+0.1% CPZ+PT group. Cell counts in quadrant 3 (Q3) for CD8 were used to quantify cell number in each experimental group. The ratio of CD4/CD8 in the brain and spinal cord was unchanged (ns) in all groups except in the *Cx*+0.1% CPZ+PT group in which the ratio was significantly decreased in both brain and spinal cord **(C)**. A one-way ANOVA ($n = 3$ thymic or spleens per group, 20,000 events/sample) was used to determine significant differences from Ctrl (*$p < 0.05$).

Kurd and Robey, 2016). This suggests that the CPZ-mediated effects in the medulla (i.e., on maturation, differentiation, and selection of T lymphocytes) might decrease the capacity of the thymus to support a T-cell-mediated immune response in the CNS. In contrast, in the *Cx*-CPZ-fed animals, the increased thymic mass, particularly in the medulla, is still capable of initiating/sustaining a T-cell response through maturation, differentiation and selection processes.

The central role of androgen-mediated thymic atrophy has been suggested on the basis of the presence of androgen receptors on the thymic epithelial cells (Savino and Dardenne, 2000) and developing thymocytes (Viselli et al., 1995) that are stimulated by circulating androgens, thus resulting in thymic atrophy (Olsen et al., 2001). CD4 and CD8 T-cells are the major cell subsets that express androgen receptors (Sutherland et al., 2005), and are the major cell subsets that are reduced by CPZ-feeding. Therefore, the combined effects of androgen-dependent involution and CPZ-feeding in the *Gi* male mice resulted in a reduction in thymic mass and function, whereas in CPZ-fed *Cx* mice, thymic mass (and $CD4^+$ and $CD8^+$ thymocytes) are preserved.

As in the thymus, CPZ-feeding reduced splenic wet weight, the size of its white pulp (a site of B and T-cell production) and CD4/8 T-cell levels, effects that have been attributed to CPZ-induced mitochondrial dysfunction and oxidative stress (Martin et al., 2018). Furthermore, a highly sensitive top-down proteomic analysis of spleens from CPZ-fed *Gi* male mice identified a significant increase in arginase-I abundance as well as decreased levels of protein disulfide isomerase (Partridge et al., 2016). The increased level of arginase-I, expressed by myeloid-derived suppressor cells, may have contributed to the decreased T-cell levels in the CPZ-fed mice. Furthermore, protein disulfide isomerase is required for the appropriate assembly of major histocompatibility complex-I (Kang et al., 2009). A reduction in major histocompatibility complex-I molecules and consequent reduction in antigen presentation will impair cytotoxic T-cell ($CD8^+$) activity and thus limit subsequent T-cell activation and clonal expansion, thereby providing another mechanism by which T-cell activity in CPZ-fed mice was compromised. Following orchiectomy, spleens were enlarged with increased white pulp areas, an effect attributed to the mitotic expansion of splenic lymphoid cells capable of responding to immune stimuli (Dean et al., 1984). This increased mitotic division of splenic lymphoid cells in *Cx* groups may compensate for the loss of mass and cell number induced by CPZ-feeding.

In Studies 1 and 2, 2 weeks of CPZ-feeding led to extensive demyelination that was unaffected by androgen ablation in *Cx* mice. However, it has been shown that androgen depletion by *Cx* increased the severity of demyelination after 5 weeks of CPZ-feeding (Patel et al., 2013). The authors attributed this to the lack of protective androgen effects in the CNS following *Cx*. This suggests that at this early time point (i.e., 2 weeks of CPZ-feeding) lack of androgens does not have any deleterious effects on CNS demyelination. Androgens work as trophic factors to maintain the development and the plasticity of neuronal tissue regulates glial cell activity and enhances myelination (Melcangi et al., 2001; Garcia-Segura and Melcangi, 2006). These protective effects of androgens are sustained by androgen receptors that are found on all cell types in the CNS including astrocytes, microglia, oligodendrocytes, and neurons (Jung-Testas and Baulieu, 1998; Garcia-Ovejero et al., 2002). In contrast, others have argued that testosterone administration increases oligodendrocytosis by amplifying the toxic damage through α-amino-3-hydroxy-5-methyl-4-isoxazolepropionic acid (AMPA)/Kainate receptor activation (Marin-Husstege et al., 2004; Cerghet et al., 2006). Other studies have shown that as little as 2 weeks of CPZ-feeding can induce significant demyelination in the mouse CNS (Pfeifenbring et al., 2015; Caprariello et al., 2018). In the current work, short term (2 weeks) feeding of 0.1% CPZ produced comparable demyelination and gliosis to the standard 0.2% CPZ dose; yet 0.1% CPZ has a more limited effect on the peripheral immune structures. These findings are consistent with previous data showing that 0.1% CPZ-feeding was as effective at producing demyelination as 0.2% CPZ but with less impact on the spleen (Sen et al., 2019a).

Having demonstrated that *Cx* did not enhance CPZ-induced demyelination and gliosis, yet protected against the suppression of peripheral immune organs, Study 2 showed that combining *Cx* and CPZ-feeding with disruption of the BBB resulted in a $CD8^+$ T-cell immune response in the CNS. The disruption of the BBB was confirmed in Studies 2 and 3 by an increased presence of IgG in the brain parenchyma following PT injection. It has been argued that the disruption of the BBB increases the possibility of adaptive immune cells traversing the barrier leading to activation and recruitment of T-cells due to myelin antigen presentation by microglia following oligodendrocytosis and the degeneration of myelin induced by CPZ (Caprariello et al., 2018). Disruption of the BBB alone, even when combined with either CPZ-feeding or castration, was not sufficient to initiate a $CD8^+$ T-cell mediated response in the CNS. This means that the release of myelin antigens following CPZ-feeding is the key step to induce a peripheral immune response and provides strong evidence for the inside-out theory of MS disease initiation (Stys et al., 2012; Stys, 2013). The increase in the number of $CD8^+$ T-cells observed in the CNS using immunohistochemistry was further confirmed by flow cytometric analysis of brain and spinal cord tissue. Notably, the CD8 signal was also detected in brain and spinal cord tissue by western blot analysis when *Cx* was combined with 0.1% CPZ and PT. This preferential increase in CD8 levels was not observed in previous CPZ-feeding studies that did not include strategies to protect the peripheral immune system (Remington et al., 2007; Partridge et al., 2016; Traka et al., 2016; Tejedor et al., 2017; Sen et al., 2019a) or which the focus of analysis was on a pan T-cell marker (CD3; Caprariello et al., 2018). While it has been argued that "cellular sources of CD8 were reactive macrophages/microglia" (Zhang et al., 2009), here, double labeling of the brain and spinal cord sections with IBA 1 and CD8 showed distinct microglia and CD8 cell populations. Notably, as observed in human MS lesions (del Pilar Martin et al., 2008), most of the $CD8^+$ T-cells were observed in the CNS parenchyma surrounding the blood capillaries, suggesting recent infiltration of these cells into the CNS tissue. Previous studies showed that *Cx* significantly increases peripheral $CD8^+$ T-cell numbers and function in humans and mice (Page et al., 2006; Tang et al., 2012). The

exact mechanism of CD8 T-cell infiltration was not examined in this study but seems most likely to have occurred following BBB disruption with subsequent expansion in response to the CPZ-induced demyelination, consistent with the inside-out theory of MS (Stys et al., 2012; Stys, 2013).

Indeed, the process of infiltration may have been facilitated by the activation of innate immune cells (microglia and astrocytes), their presentation of myelin antigens and the release of tumor necrosis factor-γ and reactive oxygen species (Bonetto et al., 2017), that are known to increase the permeability of the BBB and attract $CD8^+$ T-cell (Suidan et al., 2006). Notably, the predominance of $CD8^+$ T-cell in the CNS of mice (Study 2) resembles that seen at MS lesion sites where the key steps include recruitment and clonal expansion (Hauser et al., 1986; Friese and Fugger, 2005), with $CD8^+$ outnumbering $CD4^+$ T-cells by 3–10 fold (Booss et al., 1983; Babbe et al., 2000). In contrast, $CD4^+$ and $CD8^+$ T-cell levels in the blood of MS patients are comparable to those observed in healthy individuals (Waschbisch et al., 2014), suggesting that the initiation of immune involvement in MS patients is a result of $CD8^+$ T-cell expansion at the site of the lesion (Crawford et al., 2004).

The inability to detect the CD4 antigen by western blot in the CNS did not appear to be due to failure of the techniques used as CD4 antigens were readily identified in the spleen, thymus, and in samples of brain tissue that were spiked with a recombinant CD4 protein standard (Sen et al., 2019a). Notably, the specificity of the CD4 antibody has been confirmed by others (Forlani et al., 2019; Zhao et al., 2019), and has been used to detect $CD4^+$ cells in the spinal cord of EAE animals (Sen et al., 2019a). In addition to the copper chelating actions of CPZ causing apoptosis of T-helper cells, the lack of CD4 detection in the CNS may, at least in part, be due to a PT-mediated inhibition of CD4 chemokine receptors (G_i protein-coupled receptors), which play a key role in migration and extravazation of $CD4^+$ T cell into target tissues (Su et al., 2001; Alt et al., 2002). Conversely, a PT-mediated inhibition of chemokine receptors that protect against apoptotic signaling in $CD4^+$ T-cells may also contribute to the absence of $CD4^+$ T-cells (Vlahakis et al., 2002; Rot and von Andrian, 2004). Although EAE (a widely used animal model of MS) has provided important insights into how $CD4^+$ T-cell responds to peripherally injected myelin antigens (Steinman and Shoenfeld, 2014), it does not address the role of central (e.g., *inside-out*), triggers of immune responses (Caprariello et al., 2018). Therefore, the EAE model does not replicate the same circumstances of disease *initiation* as seen in humans: namely, a response to a slow, long-term endogenous demyelination in the CNS, a predominance of brain and spinal cord pathology (vs predominance of spinal cord pathology), and CD8 (vs. CD4) mediated T-cell involvement (Wiendl and Hohlfeld, 2002). In contrast, here, Study 2 resulted in a pathological pattern that included focal demyelination *inside* the CNS and a subsequent *outside* infiltration of $CD8^+$ T-cell into the CNS, closely resembling the pattern observed in type III MS lesion in humans that is characterized by severe oligodendrocytosis and T-cell infiltration (presence of T-lymphocytes, macrophages and large numbers of oligodendrocytes loss; Lucchinetti et al., 2000).

The hypothesis underlying Study 3 was that combining CPZ-feeding with BBB disruption in females that have naturally lower testosterone levels, would result in $CD8^+$ T-cell infiltration into the CNS similar to that seen in *Cx* males (Study 2). However, the preservation of thymic and splenic mass (and their associated $CD4^+$ and $CD8^+$ thymocytes) seen in *Cx* males was not reproduced in *Gi* females. This indicates that the preservation of immunological function observed following *Cx* in males cannot be solely ascribed to the loss of androgen production but may be attributed to other gonadal hormones shared by males and females e.g., activin and inhibin (Licona et al., 2006). Indeed, testosterone production offers some protection against the development of immunological disorders in males, such as MS, an effect that may explain why the disease occurs more frequently (2–3-fold) in females (Compston and Coles, 2008; Orton et al., 2010; Wallin et al., 2012). The high incidence of the disease in females has been ascribed to the rapid response of their immune system to any immunological stimulus such as vaccination because the concentrations of serum immunoglobulin are higher than in males (Azar et al., 2017; Trend et al., 2018). Aspinall and Andrew reported that age-related involution of the thymus (thymic atrophy) occurred earlier in *Gi* male mice than in females due to the effects of androgens. Consequently, the numbers of $CD4^+$ and $CD8^+$ thymocytes were reduced prior to positive selection (Aspinall and Andrew, 2001). Additionally, CPZ-feeding to female mice induced a 2–3-fold reduction in the weights of their uterus and ovaries compared to Ctrls (Taylor et al., 2010). This means that androgens in normal female mice have a slower effect on age-related thymus atrophy than in males. In addition, CPZ-feeding effects on the uterus and ovaries may reduce the levels of circulating androgens in females, thereby somewhat alleviating their effects on peripheral immune organs.

In Study 3, it was found that feeding CPZ to prepubescent female mice induced similar effects on the CNS (demyelination and gliosis) and peripheral immune organs as seen in males, consistent with previous studies (Taylor et al., 2010; Martin et al., 2018). This indicates that there are no sex differences with regard to the deleterious effects of CPZ-feeding in juvenile or adult mice.

Overall, this work has addressed two important questions relevant to the etiology of MS. First, could demyelination and activation of innate immunity trigger an autoimmune response similar to that seen in MS? Second, might MS primarily be initiated by demyelination that then triggers peripheral T-cell recruitment to the CNS lesions? Concerning the first question, the data indicate that the peripheral actions of CPZ are an impediment to studying the role of the peripheral immune system in response to central demyelination, despite damage to the CNS that is quite reminiscent of MS. With regard to the second question, the data confirm that, subsequent to CPZ-induced demyelination, $CD8^+$ T-cells are recruited to the CNS following disruption of the BBB when the peripheral immune system is intact. The fact that peripheral $CD3^+$ T-cells are recruited into the CNS following CPZ-feeding and BBB disruption (with PT), when combined with strategies that protect or *"boost"* the peripheral immune system, i.e., peripheral CFA injections (Caprariello et al., 2018), provides further support for an "*inside-out*" initiation of MS.

Despite using multiple techniques (organ weight, western blot analysis, immunohistochemistry and flow cytometry) to confirm the interaction (and its reversal by *Cx*) between CPZ-feeding, peripheral immune structures and CD4/8 T-cell recruitment to the CNS, future activation and proliferation assays are required to determine the impact of individual or combined (*Cx*+0.1% CPZ+PT) treatments on T-cell function and their capacity to traverse the BBB. This need for detailed functional studies is reinforced by other work showing that the use of CFA injection to "boost" the peripheral immune system resulted in an enhanced infiltration of cells expressing the pan T-cell marker CD3 following CPZ-induced demyelination (Caprariello et al., 2018).

CONCLUSION

The findings fully establish that feeding juvenile male mice with 0.1% or 0.2% CPZ for 2 weeks produced equivalent levels of demyelination and gliosis in the corpus callosum. However, 0.1% CPZ-induced less thymic and splenic atrophy, histopathology and a more modest effect on T-cell levels than the standard CPZ dose (0.2%). Moreover, the suppression of peripheral immune structures by CPZ explains why the recruitment of peripheral immune cells into the CNS has not been reported in previous studies. Castration protected against CPZ-induced thymic and splenic atrophy and thus the loss of CD4/8 T-cells. Furthermore, the addition of PT to castrated CPZ-fed mice resulted in $CD8^+$ T lymphocyte infiltration into CNS parenchyma, providing strong supporting evidence for the "inside-out" hypothesis in the etiology of MS. Demonstration of $CD8^+$ T-cell recruitment into the CNS of CPZ-fed mice, albeit castrated male mice, provides a potential new variant of the CPZ model with which to explore the early events involved in CNS demyelinating diseases like MS and thus move beyond the focus on glia responses and pan T-cell markers in the literature. However, while 0.1% CPZ-feeding in *Gi* female mice induced peripheral immune organ atrophy, T-cell signal suppression, and CNS demyelination and gliosis identical to that seen in males, BBB disruption did not result in T-cell infiltration into the CNS, indicating that testosterone levels alone are not responsible for the central CD8 T-cell response.

DATA AVAILABILITY STATEMENT

All datasets generated for this study are included in the article/**Supplementary Material**.

ETHICS STATEMENT

The animal study was reviewed and approved by Western Sydney University animal ethics committee (A11938) in accordance with the Australian Code of Practice for the Care and Use of Animals for Scientific Purposes as laid out by the National Health and Medical Research Council of Australia.

AUTHOR CONTRIBUTIONS

MA, MS, PS, DM, and JC conceived the study and provided all resources. MA and MS carried out the lab work in collaboration. MA analyzed the data and drafted the original manuscript. All authors reviewed the different versions of the manuscript and approved the final version.

FUNDING

We acknowledge the Rotary Club of Narellan for Multiple Sclerosis research funding and Western Sydney University School of Medicine Animal Care for their support with this project. MA is grateful to the Higher Committee for Education Development in Iraq for sponsoring his Ph.D. scholarship. MS was the recipient of a WSU-International Postgraduate Research Scholarship.

SUPPLEMENTARY MATERIAL

The Supplementary Material for this article can be found online at: https://www.frontiersin.org/articles/10.3389/fncel.2020.00043/full#supplementary-material.

REFERENCES

Ahlgren, C., Odén, A., and Lycke, J. (2011). High nationwide prevalence of multiple sclerosis in Sweden. *Mult. Scler.* 17, 901–908. doi: 10.1177/1352458511403794

Alt, C., Laschinger, M., and Engelhardt, B. (2002). Functional expression of the lymphoid chemokines CCL19 (ELC) and CCL 21 (SLC) at the blood-brain barrier suggests their involvement in G-protein-dependent lymphocyte recruitment into the central nervous system during experimental autoimmune encephalomyelitis. *Eur. J. Immunol.* 32, 2133–2144. doi: 10.1002/1521-4141(200208)32:8<2133::aid-immu2133>3.0.co;2-w

Aspinall, R., and Andrew, D. (2001). Gender-related differences in the rates of age associated thymic atrophy. *Dev. Immunol.* 8, 95–106. doi: 10.1155/2001/17064

Azar, A., Rank, M. A., Zarka, M. A., Chang, Y. H., and Lal, D. (2017). Gender-specific differences *in serum* immunoglobulin E levels and prevalence of fungus in sinonasal tissue noted in patients with chronic rhinosinusitis who underwent endoscopic sinus surgery. *Am. J. Rhinol. Allergy* 31, 370–375. doi: 10.2500/ajra.2017.31.4471

Babbe, H., Roers, A., Waisman, A., Lassmann, H., Goebels, N., Hohlfeld, R., et al. (2000). Clonal expansions of CD8(+) T cells dominate the T cell infiltrate in active multiple sclerosis lesions as shown by micromanipulation and single cell polymerase chain reaction. *J. Exp. Med.* 192, 393–404. doi: 10.1084/jem.192.3.393

Bonetto, G., Charalampopoulos, I., Gravanis, A., and Karagogeos, D. (2017). The novel synthetic microneurotrophin BNN27 protects mature oligodendrocytes against cuprizone-induced death, through the NGF receptor TrkA. *Glia* 65, 1376–1394. doi: 10.1002/glia.23170

Booss, J., Esiri, M. M., Tourtellotte, W. W., and Mason, D. Y. (1983). Immunohistological analysis of T lymphocyte subsets in the central nervous system in chronic progressive multiple sclerosis. *J. Neurol. Sci.* 62, 219–232. doi: 10.1016/0022-510x(83)90201-0

Butt, R. H., and Coorssen, J. R. (2005). Postfractionation for enhanced proteomic analyses: routine electrophoretic methods increase the resolution of standard 2D-PAGE. *J. Proteome. Res.* 4, 982–991. doi: 10.1021/pr050054d

Caprariello, A. V., Rogers, J. A., Morgan, M. L., Hoghooghi, V., Plemel, J. R., Koebel, A., et al. (2018). Biochemically altered myelin triggers autoimmune

demyelination. *Proc. Natl. Acad. Sci. U S A* 115, 5528–5533. doi: 10.1073/pnas.1721115115

Cardiff, R. D., Miller, C. H., and Munn, R. J. (2014). Manual hematoxylin and eosin staining of mouse tissue sections. *Cold Spring Harb. Protoc.* 2014, 655–658. doi: 10.1101/pdb.prot073411

Carrillo-Salinas, F. J., Mestre, L., Mecha, M., Feliu, A., Del Campo, R., Villarrubia, N., et al. (2017). Gut dysbiosis and neuroimmune responses to brain infection with Theiler's murine encephalomyelitis virus. *Sci. Rep.* 7:44377. doi: 10.1038/srep44377

Cerghet, M., Skoff, R. P., Bessert, D., Zhang, Z., Mullins, C., and Ghandour, M. S. (2006). Proliferation and death of oligodendrocytes and myelin proteins are differentially regulated in male and female rodents. *J. Neurosci.* 26, 1439–1447. doi: 10.1523/jneurosci.2219-05.2006

Cesta, M. F. (2006). Normal structure, function, and histology of the spleen. *Toxicol. Pathol.* 34, 455–465. doi: 10.1080/01926230600867743

Chang, H., Liu, J., Zhang, Y., Wang, F., Wu, Y., Zhang, L., et al. (2017). Increased central dopaminergic activity might be involved in the behavioral abnormality of cuprizone exposure mice. *Behav. Brain. Res.* 331, 143–150. doi: 10.1016/j.bbr.2017.05.045

Churchward, M. A., Butt, R. H., Lang, J. C., Hsu, K. K., and Coorssen, J. R. (2005). Enhanced detergent extraction for analysis of membrane proteomes by two-dimensional gel electrophoresis. *Proteome Sci.* 3:5. doi: 10.3390/proteomes4030027

Compston, A., and Coles, A. (2008). Multiple sclerosis. *Lancet* 372, 1502–1517. doi: 10.1016/S0140-6736(08)61620-7

Crawford, M. P., Yan, S. X., Ortega, S. B., Mehta, R. S., Hewitt, R. E., Price, D. A., et al. (2004). High prevalence of autoreactive, neuroantigen-specific CD8+ T cells in multiple sclerosis revealed by novel flow cytometric assay. *Blood* 103, 4222–4231. doi: 10.1182/blood-2003-11-4025

Dean, D. H., Hiramoto, R. N., Ghanta, V. K., Hiramoto, N. S., and Wall, C. N. (1984). Effects of orchiectomy on spleen cell mitogen response and on the thymus of aged mice. *Exp. Aging Res.* 10, 189–191. doi: 10.1080/03610738408258462

del Pilar Martin, M., Cravens, P. D., Winger, R., Frohman, E. M., Racke, M. K., Eagar, T. N., et al. (2008). Decrease in the numbers of dendritic cells and CD4+ T cells in cerebral perivascular spaces due to natalizumab. *Arch. Neurol.* 65, 1596–1603. doi: 10.3410/f.1124248.581396

Emerson, M. R., Biswas, S., and LeVine, S. M. (2001). Cuprizone and piperonyl butoxide, proposed inhibitors of T-cell function, attenuate experimental allergic encephalomyelitis in SJL mice. *J. Neuroimmunol.* 119, 205–213. doi: 10.1016/s0165-5728(01)00394-0

Faizi, M., Salimi, A., Seydi, E., Naserzadeh, P., Kouhnavard, M., Rahimi, A., et al. (2016). Toxicity of cuprizone a Cu(2+) chelating agent on isolated mouse brain mitochondria: a justification for demyelination and subsequent behavioral dysfunction. *Toxicol. Mech. Methods* 26, 276–283. doi: 10.3109/15376516.2016.1172284

Forlani, G., Baratella, M., Tedeschi, A., Pique, C., Jacobson, S., and Accolla, R. S. (2019). HTLV-1 HBZ Protein Resides Exclusively in the Cytoplasm of Infected Cells in Asymptomatic Carriers and HAM/TSP Patients. *Front. Microbiol.* 10:819. doi: 10.3389/fmicb.2019.00819

Franco-Pons, N., Torrente, M., Colomina, M. T., and Vilella, E. (2007). Behavioral deficits in the cuprizone-induced murine model of demyelination/remyelination. *Toxicol. Lett.* 169, 205–213. doi: 10.1016/j.toxlet.2007.01.010

Friese, M. A., and Fugger, L. (2005). Autoreactive CD8+ T cells in multiple sclerosis: a new target for therapy? *Brain* 128, 1747–1763. doi: 10.1093/brain/awh578

Garcia-Ovejero, D., Veiga, S., Garcia-Segura, L. M., and Doncarlos, L. L. (2002). Glial expression of estrogen and androgen receptors after rat brain injury. *J. Comp. Neurol.* 450, 256–271. doi: 10.1002/cne.10325

Garcia-Segura, L. M., and Melcangi, R. C. (2006). Steroids and glial cell function. *Glia* 54, 485–498. doi: 10.1002/glia.20404

Glatigny, S., and Bettelli, E. (2018). Experimental Autoimmune Encephalomyelitis (EAE) as animal models of Multiple Sclerosis (MS). *Cold Spring Harb. Perspect. Med.* 8. doi: 10.1101/cshperspect.a028977

Gudi, V., Gingele, S., Skripuletz, T., and Stangel, M. (2014). Glial response during cuprizone-induced de- and remyelination in the CNS: lessons learned. *Front. Cell. Neurosci.* 8:73. doi: 10.3389/fncel.2014.00073

Harbo, H. F., Gold, R., and Tintoré, M. (2013). Sex and gender issues in multiple sclerosis. *Ther. Adv. Neurol. Disord.* 6, 237–248. doi: 10.1177/1756285613488434

Hauser, S. L., Bhan, A. K., Gilles, F., Kemp, M., Kerr, C., and Weiner, H. L. (1986). Immunohistochemical analysis of the cellular infiltrate in multiple sclerosis lesions. *Ann. Neurol.* 19, 578–587. doi: 10.1002/ana.410190610

Herder, V., Hansmann, F., Stangel, M., Schaudien, D., Rohn, K., Baumgartner, W., et al. (2012). Cuprizone inhibits demyelinating leukomyelitis by reducing immune responses without virus exacerbation in an infectious model of multiple sclerosis. *J. Neuroimmunol.* 244, 84–93. doi: 10.1016/j.jneuroim.2012.01.010

Hopkins, R. G., and Failla, M. L. (1999). Transcriptional regulation of interleukin-2 gene expression is impaired by copper deficiency in Jurkat human T lymphocytes. *J. Nutr.* 129, 596–601. doi: 10.1093/jn/129.3.596

Hoppel, C. L., and Tandler, B. (1973). Biochemical effects of cuprizone on mouse liver and heart mitochondria. *Biochem. Pharmacol.* 22, 2311–2318. doi: 10.1016/0006-2952(73)90012-9

Jung-Testas, I., and Baulieu, E. E. (1998). Steroid hormone receptors and steroid action in rat glial cells of the central and peripheral nervous system. *J. Steroid Biochem. Mol. Biol.* 65, 243–251. doi: 10.1016/s0960-0760(97)00191-x

Kang, K., Park, B., Oh, C., Cho, K., and Ahn, K. (2009). A role for protein disulfide isomerase in the early folding and assembly of MHC class I molecules. *Antioxid. Redox Signal.* 11, 2553–2561. doi: 10.1089/ars.2009.2465

Klein, L., Kyewski, B., Allen, P. M., and Hogquist, K. A. (2014). Positive and negative selection of the T cell repertoire: what thymocytes see (and don't see). *Nat. Rev. Immunol.* 14, 377–391. doi: 10.1038/nri3667

Kurd, N., and Robey, E. A. (2016). T-cell selection in the thymus: a spatial and temporal perspective. *Immunol. Rev.* 271, 114–126. doi: 10.1111/imr.12398

Licona, P., Chimal-Monroy, J., and Soldevila, G. (2006). Inhibins are the major activin ligands expressed during early thymocyte development. *Dev. Dyn.* 235, 1124–1132. doi: 10.1002/dvdy.20707

Liu, C., Ma, J., Zhang, J., Zhao, H., Zhu, Y., Qi, J., et al. (2019). Testosterone deficiency caused by castration modulates mitochondrial biogenesis through the AR/PGC1alpha/TFAM pathway. *Front. Genet.* 10:505. doi: 10.3389/fgene.2019.00505

Lucchinetti, C., Bruck, W., Parisi, J., Scheithauer, B., Rodriguez, M., and Lassmann, H. (2000). Heterogeneity of multiple sclerosis lesions: implications for the pathogenesis of demyelination. *Ann. Neurol.* 47, 707–717. doi: 10.1002/1531-8249(200006)47:6<707::aid-ana3>3.0.co;2-q

Maña, P., Fordham, S. A., Staykova, M. A., Correcha, M., Silva, D., Willenborg, D. O., et al. (2009). Demyelination caused by the copper chelator cuprizone halts T cell mediated autoimmune neuroinflammation. *J. Neuroimmunol.* 210, 13–21. doi: 10.1016/j.jneuroim.2009.02.013

Marin-Husstege, M., Muggironi, M., Raban, D., Skoff, R. P., and Casaccia-Bonnefil, P. (2004). Oligodendrocyte progenitor proliferation and maturation is differentially regulated by male and female sex steroid hormones. *Dev. Neurosci.* 26, 245–254. doi: 10.1159/000082141

Martin, N. A., Molnar, V., Szilagyi, G. T., Elkjaer, M. L., Nawrocki, A., Okarmus, J., et al. (2018). Experimental demyelination and axonal loss are reduced in MicroRNA-146a deficient mice. *Front. Immunol.* 9:490. doi: 10.3389/fimmu.2018.00490

Melcangi, R. C., Magnaghi, V., Galbiati, M., and Martini, L. (2001). Steroid effects on the gene expression of peripheral myelin proteins. *Horm. Behav.* 40, 210–214. doi: 10.1006/hbeh.2001.1678

Olsen, N. J., Olson, G., Viselli, S. M., Gu, X., and Kovacs, W. J. (2001). Androgen receptors in thymic epithelium modulate thymus size and thymocyte development. *Endocrinology* 142, 1278–1283. doi: 10.1210/endo.142.3.8032

Olsen, N. J., Viselli, S. M., Fan, J., and Kovacs, W. J. (1998). Androgens accelerate thymocyte apoptosis. *Endocrinology* 139, 748–752. doi: 10.1210/endo.139.2.5729

Olsen, N. J., Viselli, S. M., Shults, K., Stelzer, G., and Kovacs, W. J. (1994). Induction of immature thymocyte proliferation after castration of normal male mice. *Endocrinology* 134, 107–113. doi: 10.1210/endo.134.1.8275924

Oner, H., and Ozan, E. (2002). Effects of gonadal hormones on thymus gland after bilateral ovariectomy and orchidectomy in rats. *Arch. Androl.* 48, 115–126. doi: 10.1080/01485010231726742 7

Orton, S. M., Ramagopalan, S. V., Brocklebank, D., Herrera, B. M., Dyment, D. A., Yee, I. M., et al. (2010). Effect of immigration on multiple sclerosis sex ratio in Canada: the Canadian Collaborative Study. *J. Neurol. Neurosurg. Psychiatry* 81, 31–36. doi: 10.1136/jnnp.2008.162784

Page, S. T., Plymate, S. R., Bremner, W. J., Matsumoto, A. M., Hess, D. L., Lin, D. W., et al. (2006). Effect of medical castration on CD4+ CD25+ T cells, CD8+ T cell IFN-gamma expression, and NK cells: a physiological role for testosterone and/or its metabolites. *Am. J. Physiol. Endocrinol. Metab.* 290, E856–863. doi: 10.1152/ajpendo.00484.2005

Partridge, M. A., Gopinath, S., Myers, S. J., and Coorssen, J. R. (2016). An initial top-down proteomic analysis of the standard cuprizone mouse model of multiple sclerosis. *J. Chem. Biol.* 9, 9–18. doi: 10.1007/s12154-015-0138-0

Partridge, M. A., Myers, S. J., Gopinath, S., and Coorssen, J. R. (2015). Proteomics of a conundrum: thoughts on addressing the aetiology versus progression of multiple sclerosis. *Proteomics Clin. Appl.* 9, 838–843. doi: 10.1002/prca.201400141

Patel, R., Moore, S., Crawford, D. K., Hannsun, G., Sasidhar, M. V., Tan, K., et al. (2013). Attenuation of corpus callosum axon myelination and remyelination in the absence of circulating sex hormones. *Brain Pathol.* 23, 462–475. doi: 10.1111/bpa.12029

Paxinos, G., and Franklin, K. (2012). *Paxinos and Franklin's the Mouse Brain in Stereotaxic Coordinates, 4th Edn.* San Diego, CA: Academic Press.

Pearse, G. (2006). Normal structure, function and histology of the thymus. *Toxicol. Pathol.* 34, 504–514. doi: 10.1080/01926230600865549

Pfeifenbring, S., Nessler, S., Wegner, C., Stadelmann, C., and Bruck, W. (2015). Remyelination after cuprizone-induced demyelination is accelerated in juvenile mice. *J. Neuropathol. Exp. Neurol.* 74, 756–766. doi: 10.1097/nen.0000000000000214

Remington, L. T., Babcock, A. A., Zehntner, S. P., and Owens, T. (2007). Microglial recruitment, activation and proliferation in response to primary demyelination. *Am. J. Pathol.* 170, 1713–1724. doi: 10.2353/ajpath.2007.060783

Roden, A. C., Moser, M. T., Tri, S. D., Mercader, M., Kuntz, S. M., Dong, H., et al. (2004). Augmentation of T cell levels and responses induced by androgen deprivation. *J. Immunol.* 173, 6098–6108. doi: 10.4049/jimmunol.173.10.6098

Rot, A., and von Andrian, U. H. (2004). Chemokines in innate and adaptive host defense: basic chemokinese grammar for immune cells. *Annu. Rev. Immunol.* 22, 891–928. doi: 10.1146/annurev.immunol.22.012703.104543

Savino, W., and Dardenne, M. (2000). Neuroendocrine control of thymus physiology. *Endocr. Rev.* 21, 412–443. doi: 10.1210/er.21.4.412

Sen, M. K., Almuslehi, M. S. M., Gyengesi, E., Myers, S. J., Shortland, P. J., Mahns, D. A., et al. (2019a). Suppression of the peripheral immune system limits the central immune response following cuprizone-feeding: relevance to modelling multiple sclerosis. *Cells* 8:1314. doi: 10.3390/cells8111314

Sen, M. K., Mahns, D. A., Coorssen, J. R., and Shortland, P. J. (2019b). Behavioural phenotypes in the cuprizone model of central nervous system demyelination. *Neurosci. Biobehav. Rev.* 107, 23–46. doi: 10.1016/j.neubiorev.2019.08.008

Sheean, R. K., Weston, R. H., Perera, N. D., D'Amico, A., Nutt, S. L., and Turner, B.J. (2015). Effect of thymic stimulation of CD4+ T cell expansion on disease onset and progression in mutant SOD1 mice. *J. Neuroinflammation* 12:40. doi: 10.1186/s12974-015-0254-3

Skripuletz, T., Gudi, V., Hackstette, D., and Stangel, M. (2011). De- and remyelination in the CNS white and grey matter induced by cuprizone: the old, the new and the unexpected. *Histol. Histopathol.* 26, 1585–1597. doi: 10.14670/HH-26.1585

Solti, I., Kvell, K., Talaber, G., Veto, S., Acs, P., Gallyas, F. Jr., et al. (2015). Thymic atrophy and apoptosis of CD4+CD8+ thymocytes in the cuprizone model of multiple sclerosis. *PLoS One* 10:e0129217. doi: 10.1371/journal.pone.0129217

Sriram, S., and Steiner, I. (2005). Experimental allergic encephalomyelitis: a misleading model of multiple sclerosis. *Ann. Neurol.* 58, 939–945. doi: 10.1002/ana.20743

Steinman, L., and Shoenfeld, Y. (2014). From defining antigens to new therapies in multiple sclerosis: honoring the contributions of Ruth Arnon and Michael Sela. *J. Autoimmun.* 54, 1–7. doi: 10.1016/j.jaut.2014.08.001

Stys, P. K. (2013). Pathoetiology of multiple sclerosis: are we barking up the wrong tree? *F1000Prime. Rep.* 5:20. doi: 10.12703/p5-20

Stys, P. K., Zamponi, G. W., van Minnen, J., and Geurts, J. J. (2012). Will the real multiple sclerosis please stand up? *Nat. Rev. Neurosci.* 13, 507–514. doi: 10.1038/nrn3300

Su, S. B., Silver, P. B., Zhang, M., Chan, C. C., and Caspi, R. R. (2001). Pertussis toxin inhibits induction of tissue-specific autoimmune disease by disrupting G protein-coupled signals. *J. Immunol.* 167, 250–256. doi: 10.4049/jimmunol.167.1.250

Sui, R. X., Miao, Q., Wang, J., Wang, Q., Song, L. J., Yu, J. W., et al. (2019). Protective and therapeutic role of Bilobalide in cuprizone-induced demyelination. *Int. Immunopharmacol.* 66, 69–81. doi: 10.1016/j.intimp.2018.09.041

Suidan, G. L., Pirko, I., and Johnson, A. J. (2006). A potential role for CD8+ T-cells as regulators of CNS vascular permeability. *Neurol. Res.* 28, 250–255. doi: 10.1179/016164106x98116

Sutherland, J. S., Goldberg, G. L., Hammett, M. V., Uldrich, A. P., Berzins, S. P., Heng, T. S., et al. (2005). Activation of thymic regeneration in mice and humans following androgen blockade. *J. Immunol.* 175, 2741–2753. doi: 10.3410/f.1026418.329478

Suzuki, K. (1969). Giant hepatic mitochondria: production in mice fed with cuprizone. *Science* 163, 81–82. doi: 10.1126/science.163.3862.81

Tang, S., Moore, M. L., Grayson, J. M., and Dubey, P. (2012). Increased CD8+ T-cell function following castration and immunization is countered by parallel expansion of regulatory T cells. *Cancer Res.* 72, 1975–1985. doi: 10.1158/0008-5472.can-11-2499

Taylor, L. C., Gilmore, W., Ting, J. P., and Matsushima, G. K. (2010). Cuprizone induces similar demyelination in male and female C57BL/6 mice and results in disruption of the estrous cycle. *J. Neurosci. Res.* 88, 391–402. doi: 10.1002/jnr.22215

Tejedor, L. S., Wostradowski, T., Gingele, S., Skripuletz, T., Gudi, V., and Stangel, M. (2017). The effect of stereotactic injections on demyelination and remyelination: a study in the cuprizone model. *J. Mol. Neurosci.* 61, 479–488. doi: 10.1007/s12031-017-0888-y

Torkildsen, Ø., Brunborg, L. A., Milde, A. M., Mørk, S. J., Myhr, K. M., and Bø, L. (2009). A salmon based diet protects mice from behavioural changes in the cuprizone model for demyelination. *Clin. Nutr.* 28, 83–87. doi: 10.1016/j.clnu.2008.10.015

Traka, M., Podojil, J. R., McCarthy, D. P., Miller, S. D., and Popko, B. (2016). Oligodendrocyte death results in immune-mediated CNS demyelination. *Nat. Neurosci.* 19, 65–74. doi: 10.3410/f.726006903.793519431

Trend, S., Jones, A. P., Cha, L., Byrne, S. N., Geldenhuys, S., Fabis-Pedrini, M. J., et al. (2018). Higher serum immunoglobulin G3 levels may predict the development of multiple sclerosis in individuals with clinically isolated syndrome. *Front. Immunol.* 9:1590. doi: 10.3389/fimmu.2018.01590

Tryphonas, H., Cooke, G., Caldwell, D., Bondy, G., Parenteau, M., Hayward, S., et al. (2004). Oral (gavage), *in utero* and post-natal exposure of Sprague–Dawley rats to low doses of tributyltin chloride. Part II: effects on the immune system. *Food Chem. Toxicol.* 42, 221–235. doi: 10.1016/j.fct.2003.08.019

Vargas, D. L., and Tyor, W. R. (2017). Update on disease-modifying therapies for multiple sclerosis. *J. Investig. Med.* 65, 883–891. doi: 10.1136/jim-2016-000339

Veto, S., Acs, P., Bauer, J., Lassmann, H., Berente, Z., Setalo, G. Jr., et al. (2010). Inhibiting poly(ADP-ribose) polymerase: a potential therapy against oligodendrocyte death. *Brain* 133, 822–834. doi: 10.1016/j.clim.2010.03.094

Viselli, S. M., Olsen, N. J., Shults, K., Steizer, G., and Kovacs, W. J. (1995). Immunochemical and flow cytometric analysis of androgen receptor expression in thymocytes. *Mol. Cell. Endocrinol.* 109, 19–26. doi: 10.1016/0303-7207(95)03479-q

Vlahakis, S. R., Villasis-Keever, A., Gomez, T., Vanegas, M., Vlahakis, N., and Paya, C. V. (2002). G protein-coupled chemokine receptors induce both survival and apoptotic signaling pathways. *J. Immunol.* 169, 5546–5554. doi: 10.4049/jimmunol.169.10.5546

Wallin, M. T., Culpepper, W. J., Coffman, P., Pulaski, S., Maloni, H., Mahan, C. M., et al. (2012). The gulf war era multiple sclerosis cohort: age and incidence rates by race, sex and service. *Brain* 135, 1778–1785. doi: 10.3410/f.717949355.793454506

Waschbisch, A., Sammet, L., Schroder, S., Lee, D. H., Barrantes-Freer, A., Stadelmann, C., et al. (2014). Analysis of CD4+ CD8+ double-positive T cells in blood, cerebrospinal fluid and multiple sclerosis lesions. *Clin. Exp. Immunol.* 177, 404–411. doi: 10.1111/cei.12345

Wiendl, H., and Hohlfeld, R. (2002). Therapeutic approaches in multiple sclerosis: lessons from failed and interrupted treatment trials. *BioDrugs* 16, 183–200. doi: 10.2165/00063030-200216030-00003

Ye, J. N., Chen, X. S., Su, L., Liu, Y. L., Cai, Q. Y., Zhan, X. L., et al. (2013). Progesterone alleviates neural behavioral deficits and demyelination with reduced degeneration of oligodendroglial cells in cuprizone-induced mice. *PLoS One* 8:e54590. doi: 10.1371/journal.pone.0054590

Zhang, L., Sheng, R., and Qin, Z. (2009). The lysosome and neurodegenerative diseases. *Acta. Biochim. Biophys. Sin (Shanghai)* 41, 437–445. doi: 10.1093/abbs/gmp031

Zhao, W., Zhou, P., Gong, C., Ouyang, Z., Wang, J., Zheng, N., et al. (2019). A disinhibitory mechanism biases *Drosophila* innate light preference. *Nat. Commun.* 10:124. doi: 10.1038/s41467-018-07929-w

Conflict of Interest: The authors declare that the research was conducted in the absence of any commercial or financial relationships that could be construed as a potential conflict of interest.

frontiers in Cellular Neuroscience

REVIEW
published: 03 April 2020
doi: 10.3389/fncel.2020.00078

Dissecting the Dual Role of the Glial Scar and Scar-Forming Astrocytes in Spinal Cord Injury

Tuo Yang[1,2], *YuJuan Dai*[2], *Gang Chen*[3,4]* *and ShuSen Cui*[1]*

[1]Department of Hand Surgery, China-Japan Union Hospital of Jilin University, Changchun, China, [2]Medical School of Nantong University, Nantong, China, [3]Department of Tissue and Embryology, Medical School of Nantong University, Co-innovation Center of Neuroregeneration, Nantong University, Nantong, China, [4]Department of Anesthesiology, Affiliated Hospital of Nantong University, Nantong, China

OPEN ACCESS

Edited by:
Stefania Ceruti,
Università Degli Studi di Milano, Italy

Reviewed by:
Roberta Brambilla,
University of Miami, United States
Igor Jakovcevski,
German Center for Neurodegenerative Diseases (DZNE), Germany
Seiji Okada,
Kyushu University, Japan

***Correspondence:**
Gang Chen
chengang6626@ntu.edu.cn
ShuSen Cui
cuiss@jlu.edu.cn

Specialty section:
This article was submitted to Non-Neuronal Cells, a section of the journal Frontiers in Cellular Neuroscience

Received: 28 November 2019
Accepted: 18 March 2020
Published: 03 April 2020

Citation:
Yang T, Dai Y, Chen G and Cui S (2020) Dissecting the Dual Role of the Glial Scar and Scar-Forming Astrocytes in Spinal Cord Injury. Front. Cell. Neurosci. 14:78. doi: 10.3389/fncel.2020.00078

Recovery from spinal cord injury (SCI) remains an unsolved problem. As a major component of the SCI lesion, the glial scar is primarily composed of scar-forming astrocytes and plays a crucial role in spinal cord regeneration. In recent years, it has become increasingly accepted that the glial scar plays a dual role in SCI recovery. However, the underlying mechanisms of this dual role are complex and need further clarification. This dual role also makes it difficult to manipulate the glial scar for therapeutic purposes. Here, we briefly discuss glial scar formation and some representative components associated with scar-forming astrocytes. Then, we analyze the dual role of the glial scar in a dynamic perspective with special attention to scar-forming astrocytes to explore the underlying mechanisms of this dual role. Finally, taking the dual role of the glial scar into account, we provide several pieces of advice on novel therapeutic strategies targeting the glial scar and scar-forming astrocytes.

Keywords: spinal cord injury, glial scar, astrocyte, scar-forming astrocyte, regeneration

INTRODUCTION

The past decades have witnessed a rapid increase in studies on the pathology and molecular mechanisms of and therapeutic strategies for spinal cord injury (SCI). The clinical management of SCI, including surgical interventions, supportive therapies and rehabilitation methods, markedly improves functional recovery and reduces disability (Fehlings et al., 2017). Due to the high complexity and limited recoverability of the human central nervous system (CNS), however, more than 27 million SCI patients worldwide remain disabled and experience decades of life with permanent disabilities and suffering (James et al., 2019). The reasons why the outcomes of human SCI remain so poor are complex and varied. The glial scar, a dense limiting border around the SCI lesion core (the lesion core is also known as the fibrotic scar) formed predominately by scar-forming astrocytes after SCI, has long been considered one of the primary causes of the failure of spinal cord regeneration.

Astrocytes, a major CNS component, are glial cells characterized by a star shape. Astrocytes provide essential physiological insulation and support for neurons. Their pathological importance was underestimated at first. In recent decades, however, astrocytes have been found to not only extensively participate in biological activities in the CNS, including the regulation of the blood-brain barrier, synaptic function and glutamate uptake (Füchtbauer et al., 2011; Haj-Yasein et al., 2011; Murai and Pasquale, 2011; Min and Nevian, 2012; Murphy-Royal et al., 2015), but also play crucial roles in pathological processes, including neurodegenerative diseases, stroke and CNS injuries (Bradford et al., 2009; Kuchibhotla et al., 2009; Wanner et al., 2013; Khakh and Sofroniew, 2015; Malik et al., 2020). After SCI, astrocytes are activated, and some of them rapidly proliferate to form an astrocytic scar border, traditionally referred to as the glial scar. The glial scar and scar-forming astrocytes play key roles in the recovery of SCI. A thorough analysis of the roles of the glial scar in SCI may help provide new views of SCI and identify novel therapeutic strategies. For decades, the glial scar was thought to be a primary inhibitor of SCI recovery (Sugar and Gerard, 1940; Clemente and Windle, 1954). However, this concept has been continually challenged in recent years since several studies have shown that the radical ablation of the glial scar failed to promote SCI recovery (Anderson et al., 2016; Gu et al., 2019). It is increasingly accepted that the glial scar plays a dual role in the pathological process of SCI, both protective and inhibitory. However, the complexity of this dual role has been underestimated. Many components of the glial scar, such as astrocytes, microglia, and oligodendrocyte precursor cells, are highly plastic. They not only directly contribute to the dual role of the glial scar but also interact with other components, increasing its complexity. Furthermore, this dual role is dynamic and changes as SCI progresses. This diverse and dynamic nature makes it difficult to target the glial scar for therapeutic purposes, resulting in a need to understand and take into account the dual role of the glial scar.

In the context of SCI, we dissect the dual role of the glial scar over time to explore the underlying mechanisms of its diverse and dynamic nature, with a focus on the disparity, variation, and interactions of scar-forming astrocytes. Taking the dual role of the glial scar into account, we analyze some potential interventions targeting the glial scar (especially scar-forming astrocytes) and offer several pieces of advice for novel therapeutic strategies.

TIMELINE OF GLIAL SCAR FORMATION AND THE TRANSFORMATION OF SCAR-FORMING ASTROCYTES

Astrocytic Activation Within Hours

Regardless of the cause of SCI, injury directly damages neural tissue and induces tissue ischemia, which is caused by vascular trauma and tissue swelling (Tator and Koyanagi, 1997; Mautes et al., 2000; Norenberg et al., 2004). These damaged cells release ATP, which acts on a variety of purinergic receptors expressed by astrocytes, microglia, oligodendrocytes and oligodendrocyte precursor cells (OPCs) and triggers the activated states of these cells (Franke et al., 2001; James and Butt, 2002). Additionally, astrocyte activation can also be triggered and amplified by multiple inflammatory factors, including TNF, IFN-γ, IL-6, and IL-1β (Liddelow et al., 2017). Astrocyte activation may occur immediately after SCI, since many studies show that some indicators of astrocyte activation [glial fibrillary acidic protein (GFAP), GFAP mRNA, pSTAT3, NF-κB and chondroitin sulfate proteoglycans (CSPGs)] significantly increase within a few hours of CNS insults, in both brain injuries and SCI (Brambilla et al., 2005, 2009; O'Callaghan et al., 2014; Takano et al., 2014). The early astrocyte activation in SCI is even stronger than that in brain injuries (Schnell et al., 1999). Morphologically, most reactive astrocytes are essentially similar to normal astrocytes in the uninjured spinal cord, but reactive astrocytes differ from normal ones in cellular hypertrophy and overexpression of GFAP (Wanner et al., 2013).

Glial Scar Formation Within Days

Beginning at 1–2 days after injury, some reactive astrocytes rapidly proliferate and densely populate the area around the lesion core within a 7–10-day period of glial scar formation (Wanner et al., 2013). The proliferation of these astrocytes is the fastest 3–5 days after injury, slows 7 days after injury and is nearly stopped 14 days after injury. During this process, these astrocytes begin to extend elongated processes perpendicularly towards the lesion core. They gradually lose their domains and become dense to form a narrow (only several cell layers) limiting border (the glial scar) surrounding the lesion core (Herrmann et al., 2008; Wanner et al., 2013; Hara et al., 2017). Thus, these astrocytes transform into scar-forming astrocytes, which are quite different from reactive astrocytes in adjacent neural tissue (Khakh and Sofroniew, 2015). It is worth mentioning that most scar-forming astrocytes are newly proliferated (Zai and Wrathall, 2005). A recent quantitative analysis confirmed this view and showed that the number of astrocytic cell bodies in the glial scar is nearly twice that in the uninjured spinal cord. Additionally, this study also found a diminishing gradient of the proliferation and density of scar-forming astrocytes as the distance to the lesion core increases (Wanner et al., 2013). This topographical heterogeneity of scar-forming astrocytes and directionality of elongated processes indicate that reactive astrocytes may receive signals from the lesion core and phenotypically change into scar-forming astrocytes in response.

Glial Scar Maturation Within Weeks

The rapid proliferation of reactive astrocytes gradually stops approximately 2 weeks after injury. From 1 to 2 weeks to several weeks after injury, the glial scar becomes completely mature (Ren et al., 2017). Scar-forming astrocytes complete their phenotypic change and no longer orient their processes perpendicularly towards the lesion core but instead become more parallel and overlap with each other. Thus, they completely lose their domains and form a compact mature glial scar (Wanner et al., 2013). After this point, the SCI lesion begins to stabilize, and a long chronic phase of regeneration begins. It is worth

mentioning that the STAT3 pathway, a master regulator of astrocyte activation and glial scar formation, also controls glial scar maturation (Ceyzériat et al., 2016; Escartin et al., 2019). In STAT3-KO mice, the elongated processes of scar-forming astrocytes remain perpendicular to the lesion core and do not become parallel to form a dense astrocytic scar border after SCI (Wanner et al., 2013).

OTHER REPRESENTATIVE COMPONENTS ASSOCIATED WITH SCAR-FORMING ASTROCYTES

In addition to astrocytes, other components of the glial scar also play important roles in its formation. These components interact extensively with astrocytes. Some of them directly act on astrocytes, some are regulated by astrocytes and some are released by astrocytes. Although they are in the minority compared with scar-forming astrocytes, these components influence the activity and function of scar-forming astrocytes as well as other cell types and molecules in the glial scar. Following is a discussion of several representative components associated with scar-forming astrocytes and the interactions between them.

Microglia

As the most sensitive responders to CNS injuries, microglia have a relatively low activation threshold and are the first reactive cell type in the cascade reactions following injuries (David and Kroner, 2011; Bellver-Landete et al., 2019). Microglia reach the maximum level of proliferation in the first week after SCI and are more beneficial during this period (Bellver-Landete et al., 2019). During the acute and subacute phase, microglia participate in the inflammatory response, phagocytosis for debris clearance (Greenhalgh and David, 2014), and in interactions with monocyte-derived macrophages to regulate inflammation (Greenhalgh et al., 2018). Glial scar formation highly depends on the interactions between reactive astrocytes and reactive microglia (Shinozaki et al., 2017). When activated, microglia release cytokines that trigger and maintain the activation of astrocytes. Microglia induce glial scar formation by releasing IGF-1, which triggers astrocytic activation and proliferation (Bellver-Landete et al., 2019). The *in vivo* inhibition of IGF-1 results in attenuated astrocytic activation and proliferation. The depletion of microglia also leads to attenuated glial scar formation and worse functional recovery, suggesting a crucial role for microglia in glial scar formation (Bellver-Landete et al., 2019). Another study demonstrates that microglia may downregulate the astrocytic P2Y1 receptor to improve glial scar formation after CNS injury (Shinozaki et al., 2017). There have also been reports indicating that microglia are responsible for inducing a neurotoxic phenotype of astrocytes (Liddelow et al., 2017). In the chronic phase, microglia remain remarkably activated across the entire spinal axis up to 180 days after SCI and participate in the chronic neuropathic pain (Chen et al., 2018).

Macrophages

The astrocyte-macrophage axis in SCI is complex, dynamic and crucial for recovery. In the acute phase, reactive astrocytes participate in the early inflammatory response including recruiting monocytes from peripheral blood to the lesion site by releasing multiple cytokines and chemokines (e.g., CCL2, CCL5, CXCL8; Mildner et al., 2009; Shechter et al., 2013; Zhou et al., 2018). These monocytes will further differentiate into macrophages including two main subtypes, the pro-inflammatory subtype M1 and the anti-inflammatory subtype M2. This recruitment of macrophages lays a crucial foundation for recovery from SCI since these macrophages not only clear toxic debris from injured tissues through phagocytosis but also remove dying neutrophils through efferocytosis (Hawthorne and Popovich, 2011). Reactive astrocytes induce chemotaxis and polarization of macrophages to manipulate their fates (Li et al., 2020). In the subacute phase, macrophages amplify astrocytic activity and promote glial scar formation. *In vitro*, M1 macrophages are essential inducers of astrocytic activation (Haan et al., 2015). On the other hand, M2 macrophages secrete TGF-β to induce glial scar formation *in vitro* (Song et al., 2019). M2 macrophages may also enhance the polarization of reactive astrocytes after SCI (Sonn et al., 2019). Inhibition of the centripetal migration of macrophages impairs the migration of astrocytes and glial scar formation, resulting in exacerbated neuronal loss and decreased functional recovery (Kobayakawa et al., 2019). However, excessive macrophage activity also contributes to damaging cascade reactions, secondary damage and axonal dieback (Evans et al., 2014). M1 macrophages induce necroptosis of reactive astrocytes, which may be an important mechanism of secondary damage of SCI (Fan et al., 2016). Meanwhile, reactive astrocytes may act as negative feedback regulators that in turn inhibit macrophages' activity. *In vitro*, M2 macrophage-stimulated astrocytes can inhibit the proliferation of both M1 and M2 macrophages and decrease the production of proinflammatory factors (Haan et al., 2015).

All of these results indicate that macrophages have a critical influence on glial scar formation and scar-forming astrocytes. Astrocytes also influence macrophages in turn, but the exact roles of M1 and M2 macrophages require more investigation. It is worth mentioning that most studies on macrophages in SCI focus on their roles in the acute and subacute phase, but they may still be active (Beck et al., 2010) and influence axonal regeneration in the chronic phase (Zukor et al., 2013).

Chondroitin Sulfate Proteoglycans

After SCI, extracellular matrix (ECM) molecules undergo differential regulation, as some, like hyaluronan are degraded, some, like CSPGs, are upregulated and some, like tenascin-C, are newly expressed (Haggerty et al., 2017). These changes lead to the emergence and enrichment of some key inhibitory molecules and eventually make the ECM an inhibitory environment for regeneration after injury. Among these key inhibitory molecules, CSPGs are the most prominent. CSPGs, a proteoglycan family characterized by chondroitin sulfate side chains, are thought to be released predominantly from neurons and scar-forming astrocytes (Quraishe et al., 2018). It has long been thought that CSPGs are crucial inhibitory factors of CNS axonal regeneration, making them a primary

cause of the inhibitory roles of the glial scar (McKeon et al., 1991). CSPGs mainly act on oligodendrocytes and neurons to exert their inhibitory function. Recent studies have proven that CSPGs inhibit axonal regeneration through excessive adhesion but not repulsion (McTigue et al., 2006; Filous et al., 2014; Silver and Silver, 2014; Lang et al., 2015). Mediated by several receptors, including phosphatase leukocyte common antigen-related (LAR), protein tyrosine phosphatase σ (PTPσ) and nogo receptors 1, 2, and 3 (NgR), CSPGs adhere to and immobilize regenerating axons to function as inhibitory factors (Sapieha et al., 2005; Schwab and Strittmatter, 2014; Lang et al., 2015; Dyck et al., 2018, 2019). Many studies have focused on the development of therapeutic strategies against CSPGs, including interventions targeting their chondroitin sulfate side chains or downstream receptors. These studies showed satisfactory results, making CSPGs a promising therapeutic target for SCI (further discussion is in "Strategies Targeting CSPGs" section). However, whether scar-forming astrocytes are the primary producers of CSPGs remains controversial (see "Scar-Forming Astrocytes Are Major, but Not Predominant, Producers of CSPGs" section).

NG2-OPCs

NG2-OPCs, another cellular component of the glial scar, refer to OPCs that express neuron-glial antigen 2 (NG2; mainly on their cell membrane). OPCs rapidly react after SCI and exhibit cell process retraction, cell hypertrophy and increased expression of NG2 (Levine, 2016). As a member of the CSPG family, NG2 is a powerful axonal regeneration inhibitor (Ughrin et al., 2003), which makes NG2-OPC another major inhibitory CSPG producer besides scar-forming astrocytes in the glial scar (Dou and Levine, 1994). The inhibition of NG2 by an NG2 neutralizing antibody after SCI can improve spinal cord recovery (Tan et al., 2006; Petrosyan et al., 2013). Despite evidence indicating the inhibitory roles of the NG2 CSPG, NG2-OPCs themselves may not be inhibitory since several studies have indicated that NG2-OPCs are closely related to axonal regeneration (Yang et al., 2006; Filous et al., 2014; Hackett and Lee, 2016). NG2-OPCs may also play fundamental roles in glial scar formation, since the glial scar exhibits discontinuous morphology and decreased GFAP density after inhibition of NG2-OPCs (Rodriguez et al., 2014; Hesp et al., 2018). The inhibition of NG2-OPCs in these studies moderately reduces the density of the glial scar, but not as radically as in other studies of glial scar ablation (Anderson et al., 2016; Gu et al., 2019). Interestingly, this relatively moderate glial scar disruption induced by the NG2-OPC inhibition results in increased axon regeneration, which is quite different from the radical ablation (Rodriguez et al., 2014; Anderson et al., 2016; Hesp et al., 2018; Gu et al., 2019). When the inhibition of NG2+ cells was discontinued, the glial scar became compact again (Hesp et al., 2018). These studies on NG2-OPCs may provide us with clues to new interventions targeting the glial scar which moderately reduces its density without interrupting its integrity. It is worth mentioning that it is not known whether the axon regeneration results from NG2 inhibition itself or follows glial scar disruption. Also, NG2-OPCs can differentiate into astrocytes in injured CNS including in SCI (Raff et al., 1983; Sellers et al., 2009; Hackett et al., 2016). Interestingly, this differentiation of NG2-OPCs into astrocytes is mainly induced by the expression of bone morphogenetic proteins (BMPs) by reactive astrocytes, contributing to glial scar formation (Wang et al., 2011). Taken together, these studies on NG2-OPCs deepen our understanding of the complexity of the glial scar and provide us with new ideas to modulate the glial scar by manipulating the fate of NG2-OPCs.

THE DUAL ROLE OF THE GLIAL SCAR IN SCI RECOVERY

Many studies have attempted to demonstrate the roles of the glial scar in SCI in recent years (**Table 1**). While the exact roles of the glial scar in SCI remain unclear, it has become widely accepted that the glial scar plays a dual role in SCI, both protective and inhibitory. According to the timeline of SCI development and glial scar formation, we summarize the dual role of the glial scar (**Figure 1**).

Inhibitory Roles

The Glial Scar as a Physical Barrier to Inhibit Axonal Regrowth

For decades, the glial scar had been considered a critical inhibitor of CNS regeneration. Some early observations showed that regenerating axons fail to grow past the glial scar, leading to the hypothesis that the glial scar forms a physical barrier that obstructs axonal regeneration (Sugar and Gerard, 1940; Brown and McCouch, 1947). Several studies provided more evidence for this hypothesis, thus making it prevalent (Clemente and Windle, 1954). However, it has also been challenged for decades due to the inability to replicate the beneficial effects of glial scar attenuators (Arteta, 1956; Matthews et al., 1979) and more recent observations that the ablation of the glial scar fails to facilitate spinal cord regeneration (Anderson et al., 2016). However, although many researchers have already focused on other inhibitory mechanisms, the notion of the glial scar as a physical barrier has persisted until today and remains controversial. The confirmation or rejection of this notion may be challenging but is necessary.

Scar-Forming Astrocytes Are Major, but Not Predominant, Producers of CSPGs

Another reason why the glial scar was previously considered a crucial inhibitor is that the glial scar participates in building an inhibitory ECM for axonal regeneration by permanently producing several inhibitory molecules, including CSPGs. Astrocytes express increased levels of CSPGs after SCI and were previously thought to be the predominant producers of CSPGs (McKeon et al., 1999; Jones et al., 2003). Selectively isolated scar-forming astrocytes also exhibit high levels of expression of CSPGs, which provides additional evidence for this line of thought (Hara et al., 2017). However, scar-forming astrocytes may not be the predominant producers of CSPGs since the radical ablation of scar-forming astrocytes fails to reduce the total CSPG level in SCI lesions; the lesion area fills with GFAP-negative but CSPG-positive cells after astrocyte ablation (Anderson et al., 2016). Other cell types,

TABLE 1 | Recent studies demonstrating the roles of the glial scar in SCI.

Role of the glial scar in SCI	SCI model	Intervention	Results	Reference
Aids regeneration	T10 forceps crush injury (mice)	Inhibition of the glial scar by STAT3 knockout, TK/GCV, and diphtheria toxin-mediated astrocyte ablation	Failed to result in spontaneous axonal regrowth	Anderson et al. (2016)
	T8 forceps crush injury (mice)	Selective ablation of the glial scar by the HSV-TK/GCV system	Failed to improve spontaneous functional recovery	Gu et al. (2019)
	C5 contusion (mice)	Glial scar disruption by NG2 ablation	Impaired forelimb locomotion	Hesp et al. (2018)
Restricts inflammatory and fibrotic cells	L1/L2 forceps crush injury (mice)	Selective deletion of STAT3	Increased the spread of inflammatory and fibrotic cells; increased neuronal loss	Wanner et al. (2013)
	T10 aneurysm clip crush injury (mice)	Conditional ablation of astrocytic BMPR1a	Reduced astrocytic hypertrophy, increased inflammatory infiltration and reduced axon density	Sahni et al. (2010)
	L1/L2 longitudinal stab injury and moderate crush injury	Ablation of reactive astrocytes by the HSV-TK/GCV system	Failure of blood-brain barrier repair, leukocyte infiltration, local tissue disruption, severe demyelination, neuronal and oligodendrocyte death and pronounced motor deficits	Faulkner et al. (2004)
Provides permissive bridges for axonal regeneration	T8 forceps crush injury (mice)	shRNA-mediated PTEN suppression	Most axons regrew along the astrocytic bridge	Zukor et al. (2013)
Induces A1 astrocytes, which kill neurons and mature oligodendrocytes	T10 weight-drop impact injury (rats)	Notch signaling pathway blockage	Suppresses A1 astrocyte transition	Qian et al. (2019)
	T10 impactor contusion injury (rats)	Intravenous injection of mesenchymal stem cells or their exosomes	Decreased lesion area and improved motor function	Wang L. et al. (2018)
Inhibits axonal regeneration	T10 impactor contusion injury (mice)	Reduction in glial scar formation through the pharmacological blockade of astrocytic type I collagen interaction	Improved axonal regeneration and functional recovery	Hara et al. (2017)
Produces CSPGs to inhibit spinal cord regeneration	T10 impactor contusion injury (mice)	Chondroitin sulphate N-acetylgalactosaminyl-transferase-1 gene knockout	Improved recovery compared to that of chondroitinase ABC-treated mice and wild-type mice	Takeuchi et al. (2013)
	T8 impactor contusion injury (rats)	CSPG receptor blockade by a CSPG receptor PTPσ mimetic peptide	Facilitated functional recovery	Lang et al. (2015)
	C7 hemisection (rhesus monkeys)	Intraparenchymal injections of chondroitinase	Improved hand function	Rosenzweig et al. (2019)
	C2 hemisection (rats)	A combined chondroitinase ABC and intermittent hypoxia conditioning treatment	Led to a rapid and robust respiratory and motor recovery	Warren et al. (2018)
	T8 hemisection (rats)	Decreasing CSPGs and fibrotic scarring by microtube stabilization	Promoted axonal regeneration	Hellal et al. (2011)

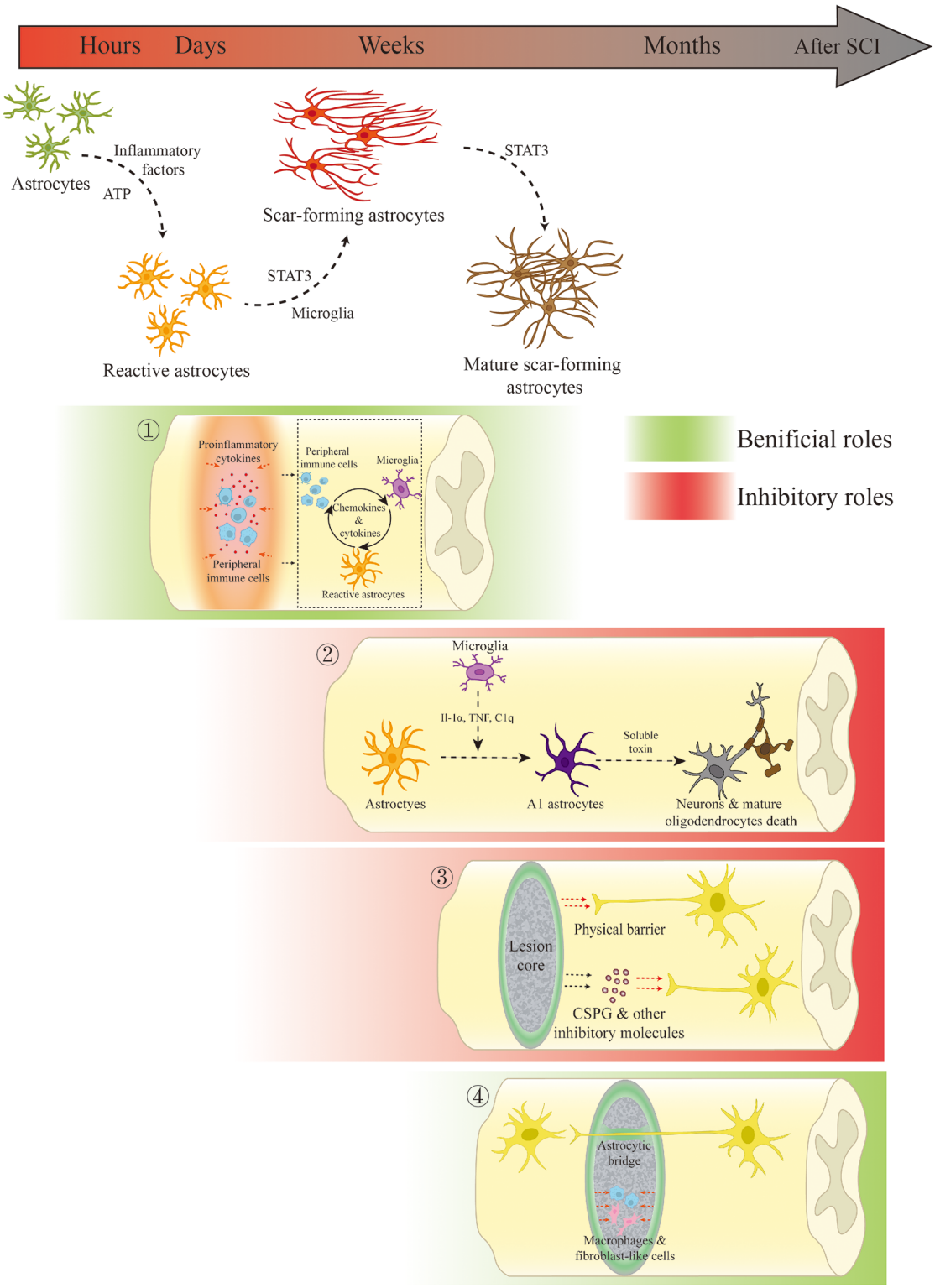

FIGURE 1 | Scar-forming astrocyte transformation and the dual role of the glial scar and scar-forming astrocytes in spinal cord injury (SCI). ① In the acute and subacute phases of SCI, the glial scar and scar-forming astrocytes not only restrict the spread of inflammation but also regulate inflammation through interactions with innate and peripheral immune cells. ② Microglia-mediated A1 phenotypic changes result in neuronal and mature oligodendrocytic death through the release of soluble toxins. ③ The glial scar inhibits spinal cord regeneration through physical obstruction and the release of inhibitory molecules. ④ In the chronic phase, the glial scar persistently limits the fibrotic tissue and macrophages. Scar-forming astrocytes may serve as bridges for axonal growth under certain conditions.

such as NG2-OPCs, macrophages, and oligodendrocytes also contribute to CSPG enrichment (Uhlin-Hansen et al., 1993; Asher et al., 2002; Tan et al., 2005). Some studies ablating particular CSPG-producing cell types (including scar-forming astrocytes and NG2-OPCs) failed to improve axonal regeneration (Kucharova et al., 2011; Filous et al., 2014; Anderson et al., 2016). These findings may be explained by the observations that: (1) there is no dominant CSPG producer, but most of the cellular components of the glial scar contribute to CSPG enrichment; and (2) scar-forming astrocytes and other glial cells are highly plastic and may be complementary in expressing CSPGs. Thus, directly targeting CSPGs or targeting the downstream receptors of CSPGs would be a better choice than the ablation of particular CSPG-producing cell types for therapeutic interventions to regulate CSPGs.

The Neurotoxic Phenotype of Reactive Astrocytes

Based on the plasticity and heterogeneity of astrocytes that accumulating evidence has suggested (Adams and Gallo, 2018), it is reasonable to infer that there may be particular astrocytic phenotypes playing a neurotoxic or neuroprotective role which contribute to the dual role of the glial scar. A neurotoxic subgroup of reactive astrocytes, which was termed the A1 phenotype, has been found in brain injuries and neurodegenerative disorders recently (Liddelow et al., 2017). The study by Liddelow et al. (2017) indicates that reactive microglia releases cytokines such as Il-1α, TNF and C1q to induce A1 astrocytes. The powerful neurotoxicity of A1 astrocytes can kill oligodendrocytes and neurons *in vitro*. The *in vivo* blockade of A1 astrocyte formation through a total KO of C1qa/TNF/IL1a prevents the death of CNS neurons. Similar to the results in brain injury models, a recent study demonstrated the existence and neurotoxic function of A1 astrocytes in an SCI model (Qian et al., 2019). In this study, the immunofluorescence of C3 (a marker of A1 astrocytes) increases as early as 3 days after SCI. At 28 days after SCI, it shows a large area of increased immunofluorescence of C3 around the lesion core, which is consistent with the distribution and topographical heterogeneity of scar-forming astrocytes. This finding indicates that A1 astrocytes may comprise part of the scar-forming astrocytes in SCI. Like the transition of scar-forming astrocytes, reactive astrocytes may receive inflammatory factors from the lesion site to transform into a neurotoxic phenotype in the context of SCI, which is consistent with the findings of Liddelow et al. (2017). In another study of A1 astrocytes in SCI, mesenchymal stem cells (MSC) and MSC-exosomes were used to reduce A1 astrocytes through downregulating inflammatory factors (Wang L. et al., 2018). Wang L. et al. (2018) also found a better functional recovery by reduction of A1 astrocytes. However, it is worth mentioning that in these studies, the single marker C3 which the authors used may not be sufficient to qualify astrocytes as "A1" and neurotoxic. The direct relationship between the reduction of A1 astrocytes and functional recovery also needs more proof. Qian et al. (2019) changed the astrocytic state through interventions on the Notch-STAT3 axis, which was quite different from the study of Liddelow et al. (2017). Regardless, these findings suggest that: (1) the existence of a neurotoxic/neuroprotective phenotype of astrocytes in the context of SCI is reasonable; (2) the A1 astrocytes may be a part of the scar-forming astrocytes and contribute to the inhibitory roles of the glial scar; (3) the A1 astrocytes are closely related to inflammation and are induced as early as the acute phase of SCI; and (4) although the existence, biomarkers, and behavior of A1 astrocytes remain controversial, it may provide a new way to understand the neuronal loss and axonal dieback in SCI. The identification and remodeling of A1 astrocytes in SCI are worth further investigation.

Beneficial Roles

The Glial Scar and Reactive Astrocytes Contribute to the Balance of Inflammatory Activities in the Acute and Subacute Stages of SCI

Debris clearance mediated by inflammatory cells is essential for recovery. However, the uncontrolled spread of cytotoxic inflammation can be devastating for spared neural tissues. Although the roles of the glial scar are still unclear, there is a consensus that the glial scar restricts the spread of inflammation to protect spared neural tissues (Sofroniew, 2015). Previous studies have demonstrated a key role of astrocytic migration in the healing process after SCI. Limiting astrocytic migration by conditional ablation of STAT3 leads to an enlarged lesion area, increased inflammatory infiltration and impaired recovery of motor function, whereas facilitating astrocytic migration by conditional ablation of SOCS3 results in enhanced contraction of the lesion area and improved functional recovery (Okada et al., 2006). Ablation of the glial scar in the acute or subacute phase also leads to an increased lesion range and worse recovery (Anderson et al., 2016). These studies show a critical role of the glial scar in limiting inflammation and indicate that inhibition of glial scar formation in the acute or subacute phase does not help or even worsens recovery. However, the glial scar is not only anti-inflammatory. After SCI, reactive astrocytes, microglia and peripheral immune cells release proinflammatory cytokines and interact with each other, which contributes to the inflammation in the acute and subacute stage (Escartin et al., 2019). Reactive astrocytes also have negative feedback regulation for inflammation after SCI (Haan et al., 2015; Zhang et al., 2019). In summary, the glial scar and reactive astrocytes are not mere limiters of the inflammation but rather balancers which are not only limiting but also contributing to the inflammation.

The Glial Scar Serves as a Restrictive Border to Limit Fibrotic Tissue and Macrophages After the Acute Stage of SCI

Many scientists have proposed that the glial scar may become more harmful than beneficial in the chronic phase of SCI. The early ablation of the glial scar fails to improve recovery, but are delayed interventions feasible? It is unlikely, based on the findings of Anderson and colleagues, who found that the ablation of the chronic glial scar mediated by diphtheria toxin 5 weeks after injury fails to help axons regenerate (Anderson et al., 2016). This result, however, may not lead to the conclusion that the chronic glial scar directly aids SCI recovery. The ablation of the chronic glial scar and adjacent reactive astrocytes causes enlarged

lesions and tissue degeneration (Anderson et al., 2016). This finding may tell us that the fibrotic tissues and macrophages in the lesion core stay active and are influential not only in the acute and subacute phase but also in the chronic phase; they may also be inhibitory factors for axonal regeneration, since regenerating CST axons avoid clusters of these cells (Zukor et al., 2013) and decreased chronic fibrotic response improves axonal regeneration and functional recovery (Cooper et al., 2018). Therefore, after the radical ablation of the chronic glial scar, fibrotic tissues and macrophages in the lesion core may impair axonal regeneration and enlarge the lesion without limitation by the glial scar and adjacent reactive astrocytes. This inference is consistent with the results of Anderson et al. (2016). Interestingly, many studies indicate that the removal of chronic scar tissue improves axonal regeneration (Li et al., 2018; Patil et al., 2018; Wang N. et al., 2018). However, the scar tissue removed in these studies includes both the glial scar and the fibrotic scar. This scar removal eliminates the harmful effects from the fibrotic scar, and no more limitation is needed for them, promoting axonal regeneration.

In summary, fibrotic tissues and macrophages in the lesion core are still active and detrimental in the chronic phase of SCI. The glial scar and adjacent reactive astrocytes may contribute to limit the detrimental effects of fibrotic tissue and macrophages. The radical ablation of the chronic glial scar may fail to help since the benefits provided by the ablation may not be sufficient to overcome the inhibitory factors of uncontrolled fibrotic tissues and macrophages. It is worth mentioning that this inference may need more direct evidence and the roles of the chronic glial scar deserve more attention.

Scar-Forming Astrocytes Exhibit Environment-Dependent Plasticity and Could Serve as Bridges for Axonal Regrowth Under Certain Conditions

Previous studies have found the following: in physiological development, axons grow along immature astroglia (Mason et al., 1988; Raper and Mason, 2010); the glial scar is mostly formed by newly proliferated astrocytes with immature astroglia properties (Wanner et al., 2013); in lower vertebrates, axons regenerate along newly proliferated immature astroglia (Mokalled et al., 2016); immature astroglia grafts support axonal regrowth across the lesion core (Davies et al., 2006; Shih et al., 2014). According to these findings, it is reasonable to infer that scar-forming astrocytes could be permissive for axonal growth or even serve as bridges.

The bridge formed by astrocytes is more like a short "drawbridge (Silver, 2016)." Scar-forming astrocytes could lay down their "drawbridge" to let regenerating axons pass through only if the lesion core is artificially made to be thin enough (e.g., if it is induced by spinal cord crush with extremely fine forceps; Zukor et al., 2013). This study also shows that astrocytes that form astrocytic bridges are not derived from ependymal stem cells but are more likely derived from mature scar-forming astrocytes (Zukor et al., 2013). Thus, some scar-forming astrocytes are transformed into beneficial bridge-forming astrocytes through the artificial regulation of the environment, indicating that glial cells may have high environment-dependent plasticity. This environment-dependent plasticity was supported by another study in which the sequential phenotypic change in scar-forming astrocytes was demonstrated to be reversible, since reactive astrocytes could be reverted to naïve astrocytes when transplanted into the naïve spinal cord after SCI. On the other hand, naïve astrocytes formed astrocytic scars when transplanted into injured spinal cords (Hara et al., 2017). These findings provide us with a novel strategy for astrocytic reprogramming through environmental interventions instead of the direct manipulation of astrocytes.

POTENTIAL THERAPEUTIC STRATEGIES TARGETING SCAR-FORMING ASTROCYTES

Although the glial scar is more than merely scar-forming astrocytes, most current studies still focus on manipulating astrocytes. Here, we pose some promising strategies for discussion.

Environmental Regulation of Astrocytic Fate

Accumulating findings have suggested the critical role of the ECM in SCI (Klapka and Müller, 2006; Schwab and Strittmatter, 2014; Yokota et al., 2017). ECM molecules not only directly participate in neuronal loss, inflammatory infiltration and axonal dieback/regrowth but also determine the outcomes of SCI by modulating scar-forming astrocytes and other cell types (Gaudet and Popovich, 2014; Didangelos et al., 2016; Bradbury and Burnside, 2019). As mentioned before, astrocytes exhibit high environment-dependent plasticity and are highly influenced by ECM molecules. For example, periostin, a type of ECM protein, is a key promotor of glial scar formation. Glial scar formation can be inhibited by the pharmacological blockade of periostin to improve functional recovery after SCI (Yokota et al., 2017). In another study, the pharmacological activation of Epac2 modulates the lesion environment and remodels reactive astrocytes to guide regenerating axons (Guijarro-Belmar et al., 2019). Also, changes in physical structure may influence astrocytic functions since scar-forming astrocytes could serve as bridges to allow regenerating axons to pass through when the injury width is sufficiently narrow (Zukor et al., 2013). Thus, remodeling astrocytes through environmental interventions is promising for therapeutic use.

Direct Cell Reprogramming Strategies

In vivo direct cell reprogramming strategies once surprised us and have been widely investigated in CNS disorders (Guo et al., 2014; Trudler and Lipton, 2019). Since irreversible neuronal loss is another primary problem in SCI recovery, cell reprogramming may solve this problem by converting other cell types into neurons. Previous studies showed that *in vivo*, astrocytes can be reprogrammed into functional neurons after SCI through a single transcription factor (Su et al., 2014; Zarei-Kheirabadi et al., 2019). These reprogramming strategies exhibit limited efficiency in transforming astrocytes, thereby avoiding

excessive attenuation of the glial scar. Therefore, with a more appropriate design, these astrocytic reprogramming strategies may be promising to not only supply functional neurons for the axonal relay but also modestly attenuate the density of the glial scar without interrupting its integrity. Unfortunately, few current studies have provided exciting behavioral results. One possible reason is that the time required for gene delivery and astrocytic reprogramming to provide functional neurons exceeds that required for the irreversible degeneration of target muscles. Rehabilitation strategies can provide use-dependent plasticity and reduce muscle degeneration, making them potential complementary therapies for astrocytic reprogramming strategies.

Astrocytic Phenotype Remodeling Strategies

As mentioned before, the sequential phenotypic change in astrocytes is reversible (Hara et al., 2017). It is possible to attenuate neuronal loss and improve regeneration by remodeling astrocytic phenotypes. For instance, A1 astrocytes may widely participate in multiple pathological processes in CNS injuries and disorders (Liddelow et al., 2017). In models of neurodegenerative diseases, the neuronal loss and behavioral deficits were reduced by blocking microglia-mediated A1 astrocytic conversion (Yun et al., 2018). In the context of SCI, remodeling A1 astrocytes also led to better functional recovery (Wang L. et al., 2018). For future studies in this area, new markers for accurately identifying different phenotypes of astrocytes, detailed mechanisms of astrocytic phenotype conversion and the role of specific phenotypes in SCI may need further investigation.

Strategies Targeting CSPGs

As mentioned before, CSPGs as the representative inhibitory molecules produced by scar-forming astrocytes are promising therapeutic targets for SCI. Current strategies mainly aim to target their chondroitin sulfate side chains or downstream receptors. Chondroitinase ABC, an enzyme that degrades the CSPG glycosaminoglycan chains, is a representative intervention targeting CSPGs. Chondroitinase ABC can attenuate the inhibitory activity of CSPGs and promote axonal regeneration (Bradbury et al., 2002; Pakulska et al., 2017). It can significantly propel functional recovery in many kinds of SCI models and can also be combined with other treatments (e.g., stem cell transplantation, peripheral nerve autografts, and conditioning treatment) to achieve better results (Alilain et al., 2011; DePaul et al., 2015; Suzuki et al., 2017; Warren et al., 2018). Other studies on chondroitinase ABC aim to innovate the delivery route to promote clinical applications (Burnside et al., 2018; Hu et al., 2018). The receptors of CSPGs are also potential targets for therapeutic strategies. Many studies show that manipulating these receptors can improve SCI recovery (Lang et al., 2015; Dyck et al., 2018). In general, therapeutic strategies targeting CSPGs are expected to provide a permissive microenvironment for spinal cord regeneration and become an important part of the comprehensive management of SCI.

Comprehensive Management of SCI Through Combination Therapy Including Astrocytic Regulation

Many interventions are effective individually in the more regenerative rodent CNS. The regeneration of the human CNS, however, is more complex and challenging. More and more scholars propose that SCI may require comprehensive therapies and management to maximize recovery (Courtine and Sofroniew, 2019; Yu and Gu, 2019; Griffin and Bradke, 2020). Strategies targeting the glial scar may also require complementary strategies, because: (1) satisfactory spinal cord regeneration may need a combination of several key factors (Anderson et al., 2018) and (2) strategies targeting the glial scar may provide a permissive microenvironment for axonal regeneration, but several studies indicate that robust axonal regeneration may be insufficient to result in significant functional improvement because it also requires synaptic reorganization and use-dependent plasticity provided by rehabilitation or other engineering strategies (Zukor et al., 2013; Du et al., 2015; Anderson et al., 2018; Courtine and Sofroniew, 2019). As a relatively mature strategy targeting the glial scar, chondroitinase ABC has been used in many studies to investigate combination therapies (Griffin and Bradke, 2020). By removing the inhibitory microenvironment, chondroitinase ABC treatments amplify the effects of other treatments, leading to better recovery (Alilain et al., 2011; DePaul et al., 2015; Suzuki et al., 2017; Warren et al., 2018). Other strategies targeting the glial scar may also apply to combination therapy, and in general, combinations of glial scar manipulations may help to overcome some of the key challenges in enhancing SCI recovery.

SUMMARY AND RECOMMENDATIONS FOR FUTURE STUDY

Accumulating evidence has suggested that the glial scar may not be entirely harmful but may be a potential therapeutic target or may even provide new hope for spinal cord regeneration. Based on the aforementioned roles of the glial scar, a summary and recommendations for future study follow:

(1) Glial scar formation and scar-forming astrocytes may offer more benefits in the acute and subacute stages of SCI. Radical interventions on glial scar formation in the acute phase or even genetic ablation may not contribute to recovery (Anderson et al., 2016; Gu et al., 2019). Additionally, multiple factors (e.g., fractures, bleeding, tissue oedema, compression, risks of infection and inflammation) limit the clinical application of early interventions on the glial scar. Novel therapeutic strategies should be more cautious in manipulating astrocytes in the acute phase.
(2) Radical ablation of the glial scar may not help spinal cord regeneration since the glial scar is playing a dual role. The integrity of the glial scar provides a critical barrier to limit the spread of inflammation and the detrimental effects of fibrotic tissue and macrophages in the chronic phase. However, several studies resulted, intentionally or unintentionally, in a moderate reduction of the density of the glial scar.

This reduction of the glial scar led to improved axonal regeneration and functional recovery (Rodriguez et al., 2014; Hesp et al., 2018; Zarei-Kheirabadi et al., 2019). These studies may provide us with clues as to how to manipulate the glial scar; that is, to reduce its density modestly without interrupting its integrity.

(3) Glial cells are highly plastic, which means they are highly influenced by environmental changes and exhibit different functions and roles. Functional changes in scar-forming astrocytes are not only causes but also consequences. Direct interventions on scar-forming astrocytes may fail to help regeneration without fundamentally regulating the cellular environment. It may be a better idea to modulate scar-forming astrocytes through manipulations on the microenvironment or downstream receptors.

(4) Recovery from SCI requires a combination of multiple essential factors, among which the least effective one may decide the outcome. *Anderson et al.* have once offered evidence for this theory by a study in which combined use of three facilitators significantly improved axon regeneration after SCI (Anderson et al., 2018). These facilitators are all required individually since the absence of any one element significantly reduces the effect and results in poor axon regeneration. As mentioned before, several studies have indicated that robust axonal regeneration may also be insufficient to result in significant functional improvement (Zukor et al., 2013; Du et al., 2015; Anderson et al., 2018; Courtine and Sofroniew, 2019). One possible reason is the absence of other essential factors for recovery, including synaptic reorganization and use-dependent plasticity. Based on this theory, it seems impractical to conquer multiple deficiencies in spinal cord regeneration through single interventions. The human CNS is more complex and less regenerative than the CNS of rodents, and single interventions may be effective in rodents but not in humans. To accelerate clinical translation, a more comprehensive management of SCI is worthy of consideration. Combined applications of complementary interventions that act on multiple targets at various time points deserve further investigation. The regulation of the glial scar may also serve as a critical part of the comprehensive management of SCI.

CONCLUSIONS

The critical role of the glial scar in SCI has been gradually and widely accepted. The glial scar, however, is more complex than we initially thought. It contains multiple cellular components and a complex ECM. It plays multifaceted roles in SCI that are highly dynamic and change based on time, position, environment and therapeutic intervention. These properties of the glial scar and scar-forming astrocytes provide tremendous therapeutic potential. Since the glial scar plays a dual role, novel therapeutic strategies should attenuate its inhibitory roles while maintaining or amplifying its beneficial roles. To accelerate clinical translation, combination therapies involving glial scar interventions deserve consideration.

AUTHOR CONTRIBUTIONS

SC and GC contributed to the conception and design of the review. TY drafted the manuscript. TY and YD contributed to the revision of the manuscript.

FUNDING

This work was supported by the National Key Research and Development Program of China (2017YFA0104700, 2017YFA0104704), National Natural Science Foundation of China (31872773), Basic Research Program of the Education Department of Jiangsu Province (17KJA180009), Jiangsu Province Natural Science Foundation of China (BK20181460), Jiangsu Province innovation and entrepreneurship training program for college students (201810304031Z) and Priority Academic Program Development of Jiangsu Higher Education Institutions (PAPD).

REFERENCES

Adams, K. L., and Gallo, V. (2018). The diversity and disparity of the glial scar. *Nat. Neurosci.* 21, 9–15. doi: 10.1038/s41593-017-0033-9

Alilain, W. J., Horn, K. P., Hu, H., Dick, T. E., and Silver, J. (2011). Functional regeneration of respiratory pathways after spinal cord injury. *Nature* 475, 196–200. doi: 10.1038/nature10199

Anderson, M. A., Burda, J. E., Ren, Y., Ao, Y., O'Shea, T. M., Kawaguchi, R., et al. (2016). Astrocyte scar formation aids central nervous system axon regeneration. *Nature* 532, 195–200. doi: 10.1038/nature17623

Anderson, M. A., O'Shea, T. M., Burda, J. E., Ao, Y., Barlatey, S. L., Bernstein, A. M., et al. (2018). Required growth facilitators propel axon regeneration across complete spinal cord injury. *Nature* 561, 396–400. doi: 10.1038/s41586-018-0467-6

Arteta, J. L. (1956). Research on the regeneration of the spinal cord in the cat submitted to the action of pyrogenous substances (5 or 3895) of bacterial origin. *J. Comp. Neurol.* 105, 171–184. doi: 10.1002/cne.901050202

Asher, R. A., Morgenstern, D. A., Shearer, M. C., Adcock, K. H., Pesheva, P., and Fawcett, J. W. (2002). Versican is upregulated in CNS injury and is a product of oligodendrocyte lineage cells. *J. Neurosci.* 22, 2225–2236. doi: 10.1523/JNEUROSCI.22-06-02225.2002

Beck, K. D., Nguyen, H. X., Galvan, M. D., Salazar, D. L., Woodruff, T. M., and Anderson, A. J. (2010). Quantitative analysis of cellular inflammation after traumatic spinal cord injury: evidence for a multiphasic inflammatory response in the acute to chronic environment. *Brain* 133, 433–447. doi: 10.1093/brain/awp322

Bellver-Landete, V., Bretheau, F., Mailhot, B., Vallières, N., Lessard, M., Janelle, M. E., et al. (2019). Microglia are an essential component of the neuroprotective scar that forms after spinal cord injury. *Nat. Commun.* 10:518. doi: 10.1038/s41467-019-08446-0

Bradbury, E. J., and Burnside, E. R. (2019). Moving beyond the glial scar for spinal cord repair. *Nat. Commun.* 10:3879. doi: 10.1038/s41467-019-11707-7

Bradbury, E. J., Moon, L. D. F., Popat, R. J., King, V. R., Bennett, G. S., Patel, P. N., et al. (2002). Chondroitinase ABC promotes functional recovery after spinal cord injury. *Nature* 416, 636–640. doi: 10.1038/416636a

Bradford, J., Shin, J. Y., Roberts, M., Wang, C. E., Li, X. J., and Li, S. (2009). Expression of mutant huntingtin in mouse brain astrocytes causes

age-dependent neurological symptoms. *Proc. Natl. Acad. Sci. U S A* 106, 22480–22485. doi: 10.1073/pnas.0911503106

Brambilla, R., Bracchi-Ricard, V., Hu, W. H., Frydel, B., Bramwell, A., Karmally, S., et al. (2005). Inhibition of astroglial nuclear factor κB reduces inflammation and improves functional recovery after spinal cord injury. *J. Exp. Med.* 202, 145–156. doi: 10.1084/jem.20041918

Brambilla, R., Hurtado, A., Persaud, T., Esham, K., Pearse, D. D., Oudega, M., et al. (2009). Transgenic inhibition of astroglial NF-κB leads to increased axonal sparing and sprouting following spinal cord injury. *J. Neurochem.* 110, 765–778. doi: 10.1111/j.1471-4159.2009.06190.x

Brown, J. O., and McCouch, G. P. (1947). Abortive regeneration of the transected spinal cord. *J. Comp. Neurol.* 87, 131–137. doi: 10.1002/cne.900870204

Burnside, E. R., De Winter, F., Didangelos, A., James, N. D., Andreica, E. C., Layard-Horsfall, H., et al. (2018). Immune-evasive gene switch enables regulated delivery of chondroitinase after spinal cord injury. *Brain* 141, 2362–2381. doi: 10.1093/brain/awy158

Ceyzériat, K., Abjean, L., Carrillo-de Sauvage, M. A., Ben Haim, L., and Escartin, C. (2016). The complex STATes of astrocyte reactivity: how are they controlled by the JAK-STAT3 pathway? *Neuroscience* 330, 205–218. doi: 10.1016/j.neuroscience.2016.05.043

Chen, G., Zhang, Y. Q., Qadri, Y. J., Serhan, C. N., and Ji, R. R. (2018). Microglia in pain: detrimental and protective roles in pathogenesis and resolution of pain. *Neuron* 100, 1292–1311. doi: 10.1016/j.neuron.2018.11.009

Clemente, C. D., and Windle, W. F. (1954). Regeneration of severed nerve fibers in the spinal cord of the adult cat. *J. Comp. Neurol.* 101, 691–731. doi: 10.1002/cne.901010304

Cooper, J. G., Jeong, S. J., McGuire, T. L., Sharma, S., Wang, W., Bhattacharyya, S., et al. (2018). Fibronectin EDA forms the chronic fibrotic scar after contusive spinal cord injury. *Neurobiol. Dis.* 116, 60–68. doi: 10.1016/j.nbd.2018.04.014

Courtine, G., and Sofroniew, M. V. (2019). Spinal cord repair: advances in biology and technology. *Nat. Med.* 25, 898–908. doi: 10.1038/s41591-019-0475-6

David, S., and Kroner, A. (2011). Repertoire of microglial and macrophage responses after spinal cord injury. *Nat. Rev. Neurosci.* 12, 388–399. doi: 10.1038/nrn3053

Davies, J. E., Huang, C., Proschel, C., Noble, M., Mayer-Proschel, M., and Davies, S. J. A. (2006). Astrocytes derived from glial-restricted precursors promote spinal cord repair. *J. Biol.* 5:7. doi: 10.1186/jbiol35

DePaul, M. A., Lin, C. Y., Silver, J., and Lee, Y. S. (2015). Peripheral nerve transplantation combined with acidic fibroblast growth factor and chondroitinase induces regeneration and improves urinary function in complete spinal cord transected adult mice. *PLoS One* 10:e0139335. doi: 10.1371/journal.pone.0139335

Didangelos, A., Puglia, M., Iberl, M., Sanchez-Bellot, C., Roschitzki, B., and Bradbury, E. J. (2016). High-throughput proteomics reveal alarmins as amplifiers of tissue pathology and inflammation after spinal cord injury. *Sci. Rep.* 6:21607. doi: 10.1038/srep21607

Dou, C. L., and Levine, J. M. (1994). Inhibition of neurite growth by the NG2 chondroitin sulfate proteoglycan. *J. Neurosci.* 14, 7616–7628. doi: 10.1523/JNEUROSCI.14-12-07616.1994

Du, K., Zheng, S., Zhang, Q., Li, S., Gao, X., Wang, J., et al. (2015). Pten deletion promotes regrowth of corticospinal tract axons 1 year after spinal cord injury. *J. Neurosci.* 35, 9754–9763. doi: 10.1523/JNEUROSCI.3637-14.2015

Dyck, S., Kataria, H., Akbari-Kelachayeh, K., Silver, J., and Karimi-Abdolrezaee, S. (2019). LAR and PTPσ receptors are negative regulators of oligodendrogenesis and oligodendrocyte integrity in spinal cord injury. *Glia* 67, 125–145. doi: 10.1002/glia.23533

Dyck, S., Kataria, H., Alizadeh, A., Santhosh, K. T., Lang, B., Silver, J., et al. (2018). Perturbing chondroitin sulfate proteoglycan signaling through LAR and PTPσ receptors promotes a beneficial inflammatory response following spinal cord injury. *J. Neuroinflammation* 15:90. doi: 10.1186/s12974-018-1128-2

Escartin, C., Guillemaud, O., and Carrillo de Sauvage, M. (2019). Questions and (some) answers on reactive astrocytes. *Glia* 67, 2221–2247. doi: 10.1002/glia.23687

Evans, T. A., Barkauskas, D. S., Myers, J. T., Hare, E. G., You, J. Q., Ransohoff, R. M., et al. (2014). High-resolution intravital imaging reveals that blood-derived macrophages but not resident microglia facilitate secondary axonal dieback in traumatic spinal cord injury. *Exp. Neurol.* 254, 109–120. doi: 10.1016/j.expneurol.2014.01.013

Fan, H., Zhang, K., Shan, L., Kuang, F., Chen, K., Zhu, K., et al. (2016). Reactive astrocytes undergo M1 microglia/macrohpages-induced necroptosis in spinal cord injury. *Mol. Neurodegener.* 11:14. doi: 10.1186/s13024-016-0081-8

Faulkner, J. R., Herrmann, J. E., Woo, M. J., Tansey, K. E., Doan, N. B., and Sofroniew, M. V. (2004). Reactive astrocytes protect tissue and preserve function after spinal cord injury. *J. Neurosci.* 24, 2143–2155. doi: 10.1523/JNEUROSCI.3547-03.2004

Fehlings, M. G., Tetreault, L. A., Wilson, J. R., Kwon, B. K., Burns, A. S., Martin, A. R., et al. (2017). A clinical practice guideline for the management of acute spinal cord injury: introduction, rationale, and scope. *Global Spine J.* 7, 84S–94S. doi: 10.1177/2192568217703387

Filous, A. R., Tran, A., Howell, C. J., Busch, S. A., Evans, T. A., Stallcup, W. B., et al. (2014). Entrapment *via* synaptic-like connections between NG2 proteoglycan+ cells and dystrophic axons in the lesion plays a role in regeneration failure after spinal cord injury. *J. Neurosci.* 34, 16369–16384. doi: 10.1523/JNEUROSCI.1309-14.2014

Franke, H., Krügel, U., Schmidt, R., Grosche, J., Reichenbach, A., and Illes, P. (2001). P2 receptor-types involved in astrogliosis *in vivo*. *Br. J. Pharmacol.* 134, 1180–1189. doi: 10.1038/sj.bjp.0704353

Füchtbauer, L., Groth-Rasmussen, M., Holm, T. H., Løbner, M., Toft-Hansen, H., Khorooshi, R., et al. (2011). Angiotensin II type 1 receptor (AT1) signaling in astrocytes regulates synaptic degeneration-induced leukocyte entry to the central nervous system. *Brain Behav. Immun.* 25, 897–904. doi: 10.1016/j.bbi.2010.09.015

Gaudet, A. D., and Popovich, P. G. (2014). Extracellular matrix regulation of inflammation in the healthy and injured spinal cord. *Exp. Neurol.* 258, 24–34. doi: 10.1016/j.expneurol.2013.11.020

Greenhalgh, A. D., and David, S. (2014). Differences in the phagocytic response of microglia and peripheral macrophages after spinal cord Injury and its effects on cell death. *J. Neurosci.* 34, 6316–6322. doi: 10.1523/JNEUROSCI.4912-13.2014

Greenhalgh, A. D., Zarruk, J. G., Healy, L. M., Baskar Jesudasan, S. J., Jhelum, P., Salmon, C. K., et al. (2018). Peripherally derived macrophages modulate microglial function to reduce inflammation after CNS injury. *PLoS Biol.* 16:e2005264. doi: 10.1371/journal.pbio.2005264

Griffin, J. M., and Bradke, F. (2020). Therapeutic repair for spinal cord injury: combinatory approaches to address a multifaceted problem. *EMBO Mol. Med.* 12:e11505. doi: 10.15252/emmm.201911505

Gu, Y., Cheng, X., Huang, X., Yuan, Y., Qin, S., Tan, Z., et al. (2019). Conditional ablation of reactive astrocytes to dissect their roles in spinal cord injury and repair. *Brain Behav. Immun.* 80, 394–405. doi: 10.1016/j.bbi.2019.04.016

Guijarro-Belmar, A., Viskontas, M., Wei, Y., Bo, X., Shewan, D., and Huang, W. (2019). Epac2 elevation reverses inhibition by chondroitin sulfate proteoglycans *in vitro* and transforms post-lesion inhibitory environment to promote axonal outgrowth in an ex vivo model of spinal cord injury. *J. Neurosci.* 39, 8330–8346. doi: 10.1523/JNEUROSCI.0374-19.2019

Guo, Z., Zhang, L., Wu, Z., Chen, Y., Wang, F., and Chen, G. (2014). *In vivo* direct reprogramming of reactive glial cells into functional neurons after brain injury and in an Alzheimer's disease model. *Cell Stem Cell* 14, 188–202. doi: 10.1016/j.stem.2013.12.001

Haan, N., Zhu, B., Wang, J., Wei, X., and Song, B. (2015). Crosstalk between macrophages and astrocytes affects proliferation, reactive phenotype and inflammatory response, suggesting a role during reactive gliosis following spinal cord injury. *J. Neuroinflammation* 12:109. doi: 10.1186/s12974-015-0327-3

Hackett, A. R., and Lee, J. K. (2016). Understanding the NG2 glial scar after spinal cord injury. *Front. Neurol.* 7:199. doi: 10.3389/fneur.2016.00199

Hackett, A. R., Lee, D. H., Dawood, A., Rodriguez, M., Funk, L., Tsoulfas, P., et al. (2016). STAT3 and SOCS3 regulate NG2 cell proliferation and differentiation after contusive spinal cord injury. *Neurobiol. Dis.* 89, 10–22. doi: 10.1016/j.nbd.2016.01.017

Haggerty, A. E., Marlow, M. M., and Oudega, M. (2017). Extracellular matrix components as therapeutics for spinal cord injury. *Neurosci. Lett.* 652, 50–55. doi: 10.1016/j.neulet.2016.09.053

Haj-Yasein, N. N., Vindedal, G. F., Eilert-Olsen, M., Gundersen, G. A., Skare, Ø., Laake, P., et al. (2011). Glial-conditional deletion of aquaporin-4 (Aqp4) reduces blood-brain water uptake and confers barrier function on

perivascular astrocyte endfeet. *Proc. Natl. Acad. Sci. U S A* 108, 17815–17820. doi: 10.1073/pnas.1110655108

Hara, M., Kobayakawa, K., Ohkawa, Y., Kumamaru, H., Yokota, K., Saito, T., et al. (2017). Interaction of reactive astrocytes with type i collagen induces astrocytic scar formation through the integrin-N-cadherin pathway after spinal cord injury. *Nat. Med.* 23, 818–828. doi: 10.1038/nm.4354

Hawthorne, A. L., and Popovich, P. G. (2011). Emerging concepts in myeloid cell biology after spinal cord injury. *Neurotherapeutics* 8, 252–261. doi: 10.1007/s13311-011-0032-6

Hellal, F., Hurtado, A., Ruschel, J., Flynn, K. C., Laskowski, C. J., Umlauf, M., et al. (2011). Microtubule stabilization reduces scarring and causes axon regeneration after spinal cord injury. *Science* 331, 928–931. doi: 10.1126/science.1201148

Herrmann, J. E., Imura, T., Song, B., Qi, J., Ao, Y., Nguyen, T. K., et al. (2008). STAT3 is a critical regulator of astrogliosis and scar formation after spinal cord injury. *J. Neurosci.* 28, 7231–7243. doi: 10.1523/JNEUROSCI.1709-08.2008

Hesp, Z. C., Yoseph, R. Y., Suzuki, R., Jukkola, P., Wilson, C., Nishiyama, A., et al. (2018). Proliferating NG2-cell-dependent angiogenesis and scar formation alter axon growth and functional recovery after spinal cord injury in mice. *J. Neurosci.* 38, 1366–1382. doi: 10.1523/JNEUROSCI.3953-16.2017

Hu, H. Z., Granger, N., Pai, S. B., Bellamkonda, R. V., and Jeffery, N. D. (2018). Therapeutic efficacy of microtube-embedded chondroitinase ABC in a canine clinical model of spinal cord injury. *Brain* 141, 1017–1027. doi: 10.1093/brain/awy007

James, G., and Butt, A. M. (2002). P2Y and P2X purinoceptor mediated Ca^{2+} signalling in glial cell pathology in the central nervous system. *Eur. J. Pharmacol.* 447, 247–260. doi: 10.1016/s0014-2999(02)01756-9

James, S. L., Theadom, A., Ellenbogen, R. G., Bannick, M. S., Montjoy-Venning, W., Lucchesi, L. R., et al. (2019). Global, regional, and national burden of traumatic brain injury and spinal cord injury, 1990–2016: a systematic analysis for the Global Burden of Disease Study 2016. *Lancet Neurol.* 18, 56–87. doi: 10.1016/S1474-4422(18)30415-0

Jones, L. L., Margolis, R. U., and Tuszynski, M. H. (2003). The chondroitin sulfate proteoglycans neurocan, brevican, phosphacan, and versican are differentially regulated following spinal cord injury. *Exp. Neurol.* 182, 399–411. doi: 10.1016/s0014-4886(03)00087-6

Khakh, B. S., and Sofroniew, M. V. (2015). Diversity of astrocyte functions and phenotypes in neural circuits. *Nat. Neurosci.* 18, 942–952. doi: 10.1038/nn.4043

Klapka, N., and Müller, H. W. (2006). Collagen matrix in spinal cord injury. *J. Neurotrauma* 23, 422–435. doi: 10.1089/neu.2006.23.422

Kobayakawa, K., Ohkawa, Y., Yoshizaki, S., Tamaru, T., Saito, T., Kijima, K., et al. (2019). Macrophage centripetal migration drives spontaneous healing process after spinal cord injury. *Sci. Adv.* 5:31106270. doi: 10.1126/sciadv.aav5086

Kucharova, K., Chang, Y., Boor, A., Yong, V. W., and Stallcup, W. B. (2011). Reduced inflammation accompanies diminished myelin damage and repair in the NG2 null mouse spinal cord. *J. Neuroinflammation* 8:158. doi: 10.1186/1742-2094-8-158

Kuchibhotla, K. V., Lattarulo, C. R., Hyman, B. T., and Bacskai, B. J. (2009). Synchronous hyperactivity and intercellular calcium waves in astrocytes in Alzheimer mice. *Science* 323, 1211–1215. doi: 10.1126/science.1169096

Lang, B. T., Cregg, J. M., Depaul, M. A., Tran, A. P., Xu, K., Dyck, S. M., et al. (2015). Modulation of the proteoglycan receptor PTPσ promotes recovery after spinal cord injury. *Nature* 518, 404–408. doi: 10.1038/nature13974

Levine, J. (2016). The reactions and role of NG2 glia in spinal cord injury. *Brain Res.* 1638, 199–208. doi: 10.1016/j.brainres.2015.07.026

Li, L., Ni, L., Heary, R. F., and Elkabes, S. (2020). Astroglial TLR9 antagonism promotes chemotaxis and alternative activation of macrophages *via* modulation of astrocyte- derived signals: implications for spinal cord injury. *J. Neuroinflammation* 17, 1–73. doi: 10.1186/s12974-020-01748-x

Li, X., Yang, B., Xiao, Z., Zhao, Y., Han, S., Yin, Y., et al. (2018). Comparison of subacute and chronic scar tissues after complete spinal cord transection. *Exp. Neurol.* 306, 132–137. doi: 10.1016/j.expneurol.2018.05.008

Liddelow, S. A., Guttenplan, K. A., Clarke, L. E., Bennett, F. C., Bohlen, C. J., Schirmer, L., et al. (2017). Neurotoxic reactive astrocytes are induced by activated microglia. *Nature* 541, 481–487. doi: 10.1038/nature21029

Malik, A. R., Lips, J., Gorniak-Walas, M., Broekaart, D. W. M., Asaro, A., Kuffner, M. T. C., et al. (2020). SorCS2 facilitates release of endostatin from astrocytes and controls post-stroke angiogenesis. *Glia* doi: 10.1002/glia.23778 [Epub ahead of print].

Mason, C. A., Edmondson, J. C., and Hatten, M. E. (1988). The extending astroglial process: development of glial cell shape, the growing tip and interactions with neurons. *J. Neurosci.* 8, 3124–3134. doi: 10.1523/JNEUROSCI.08-09-03124.1988

Matthews, M. A., St Onge, M. F., Faciane, C. L., and Gelderd, J. B. (1979). Spinal cord transection: a quantitative analysis of elements of the connective tissue matrix formed within the site of lesion following administration of piromen, cytoxan or trypsin. *Neuropathol. Appl. Neurobiol.* 5, 161–180. doi: 10.1111/j.1365-2990.1979.tb00617.x

Mautes, A. E., Weinzierl, M. R., Donovan, F., and Noble, L. J. (2000). Vascular events after spinal cord injury: contribution to secondary pathogenesis. *Phys. Ther.* 80, 673–687. doi: 10.1093/ptj/80.7.673

McKeon, R. J., Jurynec, M. J., and Buck, C. R. (1999). The chondroitin sulfate proteoglycans neurocan and phosphacan are expressed by reactive astrocytes in the chronic CNS glial scar. *J. Neurosci.* 19, 10778–10788. doi: 10.1523/JNEUROSCI.19-24-10778.1999

McKeon, R. J., Schreiber, R. C., Rudge, J. S., and Silver, J. (1991). Reduction of neurite outgrowth in a model of glial scarring following CNS injury is correlated with the expression of inhibitory molecules on reactive astrocytes. *J. Neurosci.* 11, 3398–3411. doi: 10.1523/JNEUROSCI.11-11-03398.1991

McTigue, D. M., Tripathi, R., and Wei, P. (2006). NG2 colocalizes with axons and is expressed by a mixed cell population in spinal cord lesions. *J. Neuropathol. Exp. Neurol.* 65, 406–420. doi: 10.1097/01.jnen.0000218447.32320.52

Mildner, A., MacK, M., Schmidt, H., Brück, W., Djukic, M., Zabel, M. D., et al. (2009). $CCR2^{+}Ly\text{-}6C^{hi}$ monocytes are crucial for the effector phase of autoimmunity in the central nervous system. *Brain* 132, 2487–2500. doi: 10.1093/brain/awp144

Min, R., and Nevian, T. (2012). Astrocyte signaling controls spike timing-dependent depression at neocortical synapses. *Nat. Neurosci.* 15, 746–753. doi: 10.1038/nn.3075

Mokalled, M. H., Patra, C., Dickson, A. L., Endo, T., Stainier, D. Y. R., and Poss, K. D. (2016). Injury-induced ctgfa directs glial bridging and spinal cord regeneration in zebrafish. *Science* 354, 630–634. doi: 10.1126/science.aaf2679

Murai, K. K., and Pasquale, E. B. (2011). Eph receptors and ephrins in neuron-astrocyte communication at synapses. *Glia* 59, 1567–1578. doi: 10.1002/glia.21226

Murphy-Royal, C., Dupuis, J. P., Varela, J. A., Panatier, A., Pinson, B., Baufreton, J., et al. (2015). Surface diffusion of astrocytic glutamate transporters shapes synaptic transmission. *Nat. Neurosci.* 18, 219–226. doi: 10.1038/nn.3901

Norenberg, M. D., Smith, J., and Marcillo, A. (2004). The pathology of human spinal cord injury: defining the problems. *J. Neurotrauma* 21, 429–440. doi: 10.1089/089771504323004575

O'Callaghan, J. P., Kelly, K. A., VanGilder, R. L., Sofroniew, M. V., and Miller, D. B. (2014). Early activation of STAT3 regulates reactive astrogliosis induced by diverse forms of neurotoxicity. *PLoS One* 9:e102003. doi: 10.1371/journal.pone.0102003

Okada, S., Nakamura, M., Katoh, H., Miyao, T., Shimazaki, T., Ishii, K., et al. (2006). Conditional ablation of Stat3 or Socs3 discloses a dual role for reactive astrocytes after spinal cord injury. *Nat. Med.* 12, 829–834. doi: 10.1038/nm1425

Pakulska, M. M., Tator, C. H., and Shoichet, M. S. (2017). Local delivery of chondroitinase ABC with or without stromal cell-derived factor 1α promotes functional repair in the injured rat spinal cord. *Biomaterials* 134, 13–21. doi: 10.1016/j.biomaterials.2017.04.016

Patil, N., Truong, V., Holmberg, M. H., Lavoie, N. S., McCoy, M. R., Dutton, J. R., et al. (2018). Safety and efficacy of rose bengal derivatives for glial scar ablation in chronic spinal cord injury. *J. Neurotrauma* 35, 1745–1754. doi: 10.1089/neu.2017.5398

Petrosyan, H. A., Hunanyan, A. S., Alessi, V., Schnell, L., Levine, J., and Arvanian, V. L. (2013). Neutralization of inhibitory molecule NG2 improves synaptic transmission, retrograde transport, and locomotor function after spinal cord injury in adult rats. *J. Neurosci.* 33, 4032–4043. doi: 10.1523/JNEUROSCI.4702-12.2013

Qian, D., Li, L., Rong, Y., Liu, W., Wang, Q., Zhou, Z., et al. (2019). Blocking Notch signal pathway suppresses the activation of neurotoxic A1 astrocytes

after spinal cord injury. *Cell Cycle* 18, 3010–3029. doi: 10.1080/15384101.2019.1667189

Quraishe, S., Forbes, L. H., and Andrews, M. R. (2018). The extracellular environment of the CNS: influence on plasticity, sprouting, and axonal regeneration after spinal cord injury. *Neural Plast.* 2018:2952386. doi: 10.1155/2018/2952386

Raff, M. C., Miller, R. H., and Noble, M. (1983). A glial progenitor cell that develops *in vitro* into an astrocyte or an oligodendrocyte depending on culture medium. *Nature* 303, 390–396. doi: 10.1038/303390a0

Raper, J., and Mason, C. (2010). Cellular strategies of axonal pathfinding. *Cold Spring Harb. Perspect. Biol.* 2:a001933. doi: 10.1101/cshperspect.a001933

Ren, Y., Ao, Y., O'Shea, T. M., Burda, J. E., Bernstein, A. M., Brumm, A. J., et al. (2017). Ependymal cell contribution to scar formation after spinal cord injury is minimal, local and dependent on direct ependymal injury. *Sci. Rep.* 7:41122. doi: 10.1038/srep41122

Rodriguez, J. P., Coulter, M., Miotke, J., Meyer, R. L., Takemaru, K. I., and Levine, J. M. (2014). Abrogation of β-catenin signaling in oligodendrocyte precursor cells reduces glial scarring and promotes axon regeneration after CNS injury. *J. Neurosci.* 34, 10285–10297. doi: 10.1523/JNEUROSCI.4915-13.2014

Rosenzweig, E. S., Salegio, E. A., Liang, J. J., Weber, J. L., Weinholtz, C. A., Brock, J. H., et al. (2019). Chondroitinase improves anatomical and functional outcomes after primate spinal cord injury. *Nat. Neurosci.* 22, 1269–1275. doi: 10.4021/jnr209w

Sahni, V., Mukhopadhyay, A., Tysseling, V., Hebert, A., Birch, D., Mcguire, T. L., et al. (2010). BMPR1a and BMPR1b signaling exert opposing effects on gliosis after spinal cord injury. *J. Neurosci.* 30, 1839–1855. doi: 10.1523/JNEUROSCI.4459-09.2010

Sapieha, P. S., Duplan, L., Uetani, N., Joly, S., Tremblay, M. L., Kennedy, T. E., et al. (2005). Receptor protein tyrosine phosphatase sigma inhibits axon regrowth in the adult injured CNS. *Mol. Cell. Neurosci.* 28, 625–635. doi: 10.1016/j.mcn.2004.10.011

Schnell, L., Fearn, S., Klassen, H., Schwab, M. E., and Perry, V. H. (1999). Acute inflammatory responses to mechanical lesions in the CNS: differences between brain and spinal cord. *Eur. J. Neurosci.* 11, 3648–3658. doi: 10.1046/j.1460-9568.1999.00792.x

Schwab, M. E., and Strittmatter, S. M. (2014). Nogo limits neural plasticity and recovery from injury. *Curr. Opin. Neurobiol.* 27, 53–60. doi: 10.1016/j.conb.2014.02.011

Sellers, D. L., Maris, D. O., and Horner, P. J. (2009). Postinjury niches induce temporal shifts in progenitor fates to direct lesion repair after spinal cord injury. *J. Neurosci.* 29, 6722–6733. doi: 10.1523/JNEUROSCI.4538-08.2009

Shechter, R., Miller, O., Yovel, G., Rosenzweig, N., London, A., Ruckh, J., et al. (2013). Recruitment of beneficial M2 macrophages to injured spinal cord is orchestrated by remote brain choroid plexus. *Immunity* 38, 555–569. doi: 10.1016/j.immuni.2013.02.012

Shih, C. H., Lacagnina, M., Leuer-Bisciotti, K., and Pröschel, C. (2014). Astroglial-derived periostin promotes axonal regeneration after spinal cord injury. *J. Neurosci.* 34, 2438–2443. doi: 10.1523/JNEUROSCI.2947-13.2014

Shinozaki, Y., Shibata, K., Yoshida, K., Shigetomi, E., Gachet, C., Ikenaka, K., et al. (2017). Transformation of astrocytes to a neuroprotective phenotype by microglia *via* P2Y1 receptor downregulation. *Cell Rep.* 19, 1151–1164. doi: 10.1016/j.celrep.2017.04.047

Silver, J. (2016). The glial scar is more than just astrocytes. *Exp. Neurol.* 286, 147–149. doi: 10.1016/j.expneurol.2016.06.018

Silver, D. J., and Silver, J. (2014). Contributions of chondroitin sulfate proteoglycans to neurodevelopment, injury, and cancer. *Curr. Opin. Neurobiol.* 27, 171–178. doi: 10.1016/j.conb.2014.03.016

Sofroniew, M. V. (2015). Astrocyte barriers to neurotoxic inflammation. *Nat. Rev. Neurosci.* 16, 249–263. doi: 10.1038/nrn3898

Song, G., Yang, R., Zhang, Q., Chen, L., Huang, D., Zeng, J., et al. (2019). TGF-β secretion by M2 macrophages induces glial scar formation by activating astrocytes *in vitro*. *J. Mol. Neurosci.* 69, 324–332. doi: 10.1007/s12031-019-01361-5

Sonn, I., Nakamura, M., Renault-Mihara, F., and Okano, H. (2019). Polarization of reactive astrocytes in response to spinal cord injury is enhanced by M2 macrophage-mediated activation of Wnt/β-catenin pathway. *Mol. Neurobiol.* doi: 10.1007/s12035-019-01851-y [Epub ahead of print].

Su, Z., Niu, W., Liu, M. L., Zou, Y., and Zhang, C. L. (2014). *In vivo* conversion of astrocytes to neurons in the injured adult spinal cord. *Nat. Commun.* 5:3338. doi: 10.1038/ncomms4338

Sugar, O., and Gerard, R. W. (1940). Spinal cord regeneration in the rat. *J. Neurophysiol.* 3, 1–19. doi: 10.1152/jn.1940.3.1.1

Suzuki, H., Ahuja, C. S., Salewski, R. P., Li, L., Satkunendrarajah, K., Nagoshi, N., et al. (2017). Neural stem cell mediated recovery is enhanced by Chondroitinase ABC pretreatment in chronic cervical spinal cord injury. *PLoS One* 12:e0182339. doi: 10.1371/journal.pone.0182339

Takano, T., He, W., Han, X., Wang, F., Xu, Q., Wang, X., et al. (2014). Rapid manifestation of reactive astrogliosis in acute hippocampal brain slices. *Glia* 62, 78–95. doi: 10.1002/glia.22588

Takeuchi, K., Yoshioka, N., Higa Onaga, S., Watanabe, Y., Miyata, S., Wada, Y., et al. (2013). Chondroitin sulphate N-acetylgalactosaminyl-transferase-1 inhibits recovery from neural injury. *Nat. Commun.* 4:2740. doi: 10.1038/ncomms3740

Tan, A. M., Colletti, M., Rorai, A. T., Skene, J. H. P., and Levine, J. M. (2006). Antibodies against the NG2 proteoglycan promote the regeneration of sensory axons within the dorsal columns of the spinal cord. *J. Neurosci.* 26, 4729–4739. doi: 10.1523/JNEUROSCI.3900-05.2006

Tan, A. M., Zhang, W., and Levine, J. M. (2005). NG2: a component of the glial scar that inhibits axon growth. *J. Anat.* 207, 717–725. doi: 10.1111/j.1469-7580.2005.00452.x

Tator, C. H., and Koyanagi, I. (1997). Vascular mechanisms in the pathophysiology of human spinal cord injury. *J. Neurosurg.* 86, 483–492. doi: 10.3171/jns.1997.86.3.0483

Trudler, D., and Lipton, S. A. (2019). Novel direct conversion of microglia to neurons. *Trends Mol. Med.* 25, 72–74. doi: 10.1016/j.molmed.2018.12.005

Ughrin, Y. M., Chen, Z. J., and Levine, J. M. (2003). Multiple regions of the NG2 proteoglycan inhibit neurite growth and induce growth cone collapse. *J. Neurosci.* 23, 175–186. doi: 10.1523/JNEUROSCI.23-01-00175.2003

Uhlin-Hansen, L., Wik, T., Kjellén, L., Berg, E., Forsdahl, F., and Kolset, S. O. (1993). Proteoglycan metabolism in normal and inflammatory human macrophages. *Blood* 82, 2880–2889. doi: 10.1182/blood.v82.9.2880.bloodjournal8292880

Wang, Y., Cheng, X., He, Q., Zheng, Y., Kim, D. H., Whittemore, S. R., et al. (2011). Astrocytes from the contused spinal cord inhibit oligodendrocyte differentiation of adult oligodendrocyte precursor cells by increasing the expression of bone morphogenetic proteins. *J. Neurosci.* 31, 6053–6058. doi: 10.1523/JNEUROSCI.5524-09.2011

Wang, L., Pei, S., Han, L., Guo, B., Li, Y., Duan, R., et al. (2018). Mesenchymal stem cell-derived exosomes reduce A1 astrocytes *via* downregulation of phosphorylated NFκB P65 subunit in spinal cord injury. *Cell. Physiol. Biochem.* 50, 1535–1559. doi: 10.1159/000494652

Wang, N., Xiao, Z., Zhao, Y., Wang, B., Li, X., Li, J., et al. (2018). Collagen scaffold combined with human umbilical cord-derived mesenchymal stem cells promote functional recovery after scar resection in rats with chronic spinal cord injury. *J. Tissue Eng. Regen. Med.* 12, e1154–e1163. doi: 10.1002/term.2450

Wanner, I. B., Anderson, M. A., Song, B., Levine, J., Fernandez, A., Gray-Thompson, Z., et al. (2013). Glial scar borders are formed by newly proliferated, elongated astrocytes that interact to corral inflammatory and fibrotic cells *via* STAT3-dependent mechanisms after spinal cord injury. *J. Neurosci.* 33, 12870–12886. doi: 10.1523/JNEUROSCI.2121-13.2013

Warren, P. M., Steiger, S. C., Dick, T. E., MacFarlane, P. M., Alilain, W. J., and Silver, J. (2018). Rapid and robust restoration of breathing long after spinal cord injury. *Nat. Commun.* 9:4843. doi: 10.1038/s41467-018-06937-0

Yang, Z., Suzuki, R., Daniels, S. B., Brunquell, C. B., Sala, C. J., and Nishiyama, A. (2006). NG2 glial cells provide a favorable substrate for growing axons. *J. Neurosci.* 26, 3829–3839. doi: 10.1523/JNEUROSCI.4247-05.2006

Yokota, K., Kobayakawa, K., Saito, T., Hara, M., Kijima, K., Ohkawa, Y., et al. (2017). Periostin promotes scar formation through the interaction between pericytes and infiltrating monocytes/macrophages after spinal cord injury. *Am. J. Pathol.* 187, 639–653. doi: 10.1016/j.ajpath.2016.11.010

Yu, B., and Gu, X. (2019). Combination of biomaterial transplantation and genetic enhancement of intrinsic growth capacities to promote CNS axon regeneration

after spinal cord injury. *Front. Med.* 13, 131–137. doi: 10.1007/s11684-018-0642-z

Yun, S. P., Kam, T. I., Panicker, N., Kim, S., Oh, Y., Park, J. S., et al. (2018). Block of A1 astrocyte conversion by microglia is neuroprotective in models of Parkinson's disease. *Nat. Med.* 24, 931–938. doi: 10.1038/s41591-018-0051-5

Zai, L. J., and Wrathall, J. R. (2005). Cell proliferation and replacement following contusive spinal cord injury. *Glia* 50, 247–257. doi: 10.1002/glia.20176

Zarei-Kheirabadi, M., Hesaraki, M., Kiani, S., and Baharvand, H. (2019). *In vivo* conversion of rat astrocytes into neuronal cells through neural stem cells in injured spinal cord with a single zinc-finger transcription factor. *Stem Cell Res. Ther.* 10:380. doi: 10.1186/s13287-019-1448-x

Zhang, Y., Zhou, Y., Chen, S., Hu, Y., Zhu, Z., Wang, Y., et al. (2019). Macrophage migration inhibitory factor facilitates prostaglandin E 2 production of astrocytes to tune inflammatory milieu following spinal cord injury. *J. Neuroinflammation* 16:85. doi: 10.1186/s12974-019-1468-6

Zhou, Y., Guo, W., Zhu, Z., Hu, Y., Wang, Y., Zhang, X., et al. (2018). Macrophage migration inhibitory factor facilitates production of CCL5 in astrocytes following rat spinal cord injury. *J. Neuroinflammation* 15:253. doi: 10.1186/s12974-018-1297-z

Zukor, K., Belin, S., Wang, C., Keelan, N., Wang, X., and He, Z. (2013). Short hairpin RNA against PTEN enhances regenerative growth of corticospinal tract axons after spinal cord injury. *J. Neurosci.* 33, 15350–15361. doi: 10.1523/JNEUROSCI.2510-13.2013

Conflict of Interest: The authors declare that the research was conducted in the absence of any commercial or financial relationships that could be construed as a potential conflict of interest.

Advantages of publishing in Frontiers

OPEN ACCESS
Articles are free to read for greatest visibility and readership

FAST PUBLICATION
Around 90 days from submission to decision

HIGH QUALITY PEER-REVIEW
Rigorous, collaborative, and constructive peer-review

TRANSPARENT PEER-REVIEW
Editors and reviewers acknowledged by name on published articles

Frontiers
Avenue du Tribunal-Fédéral 34
1005 Lausanne | Switzerland

Visit us: www.frontiersin.org
Contact us: frontiersin.org/about/contact

REPRODUCIBILITY OF RESEARCH
Support open data and methods to enhance research reproducibility

DIGITAL PUBLISHING
Articles designed for optimal readership across devices

FOLLOW US
@frontiersin

IMPACT METRICS
Advanced article metrics track visibility across digital media

EXTENSIVE PROMOTION
Marketing and promotion of impactful research

LOOP RESEARCH NETWORK
Our network increases your article's readership